LOW PROFILE, WIDEBAND AND HIGH POWER CAPABLE ANTENNAS FOR DIVERSE MILITARY PLATFORMS

by

Saurabh Ashok Sanghai
B.E. (Electronics), University of Mumbai, Mumbai, INDIA, 2012
M.S., University of Colorado Boulder, USA, 2017

A thesis submitted to the
Faculty of the Graduate School of the
University of Colorado in partial fulfillment
of the requirement for the degree of
Doctor of Philosophy
Department of Electrical, Computer and Energy Engineering
2018

This thesis entitled:

Low-Profile, Wideband and High Power Capable Antennas for Diverse Military Platforms

written by Saurabh Sanghai

has been approved for the Department of Electrical Computer and Energy Engineering

____
Prof. Dejan S. Filipović

____
Dr. Maxim Ignatenko

Date__________________

The final copy of this thesis has been examined by the signatories, and we

Find that both the content and the form meet acceptable presentation standards

Of scholarly work in the above mentioned discipline.

Saurabh Sanghai (Ph.D., Electrical, Computer and Energy Engineering)
Low-Profile, Wideband and High Power Capable Antennas for Diverse Military Platforms
Thesis directed by Professor Dejan S. Filipović

This thesis presents the analysis, design, and measurements of antennas and antenna systems across three frequency bands with attention to the practical aspects of antenna design and deployment on specific platform of interest. Low profile, wideband support, and high-power operation form the underlying elements that bind all the research areas together.

The first research area deals with the design of vehicular HF antenna for use over the 3 MHz to 30 MHz frequency range. Antenna performance for both scaled and full scaled HF antenna models using full wave electromagnetic analysis tools is shown for a vehicular platform of interest. Recent standardization of wideband HF waveforms has pushed the development of electrically small, vehicular HF antennas with 24 kHz tuned bandwidth. The antenna performance specifications are set to be at par or better than the existing vehicular HF antennas. The antenna must support zenith gain better than -20 dBi and bandwidth of better than 24 kHz. Antenna profile is a major motivating factor for this research. Traditional 3 kHz vehicular HF antennas have profiles of 1 m or higher. The design requirement for antenna profile lower than 1 m over the vehicle roof is inspired from the review of existing HF antennas. 3D printing and scaled prototyping is shown to validate the computational modeling and the proposed design process.

The second area of research showcased in this work focuses on the design, fabrication and field testing of a full scaled antenna on an actual military platform. Antenna design process developed in the first part is used to develop the full scaled antenna prototype. Special attention is given to practical design of the antenna to ease fabrication and integration on the military platform. The antenna design is approached as a modular kit so that it can be easily reconfigured into different modes of operation. A COTS tuner is interfaced with the antenna and tunability is demonstrated over the HF frequencies. Validation of the developed HF antenna system is achieved through measurement data and link establishment during field tests. The implementation of switched reconfigurable HF antenna with support for all three modes of HF propagation is discussed in the end as an extension of the reconfigurable antenna concept to increase the versatility of the antenna system.

The third part of research outlined in this work deals with the integration strategies for isolation improvement in cylindrical RF payloads operating at the millimeter wave frequencies. Cutting the horn antenna at its throat is proposed for ease of fabrication and integration inside a space constrained payload. The antenna performance in case of a realistic air gap at the cut interface between the top and bottom parts of the horn antenna is shown. Following the antenna level analysis, a system level impact of integration strategies on the RF leakage and coupling between the RF front ends in a cylindrical payload is shown. Measurements show the impact of internal RF leakages from components on deterioration in the system level isolation. Use of a conductive mesh as an RF sleeve placed over the component is discussed. Technique for improving system isolation from 65 dB worst case to 95 dB worst case using the proposed RF sleeves, across 18 GHz to 45 GHz is shown through a series of exhaustive measurements.

The practical considerations for platform integration of wideband antennas are covered in subsequent appendix sections at the end of the thesis body. The use of a low cost radome is proposed using a COTS Frisbee disc for a planar log periodic aperture in appendix section A. A spiral helix antenna is considered as a candidate for the study of antenna breakdown under high power conditions in appendix section B. Appendix section C discusses about the inspection of RF components for identification of fabrication artifacts that may lead to RF leakages when assembled in a system.

Dedication

To my parents Ashok Adinathrao Sanghai and Vaishali Ashok Sanghai
my brother Rishabh Ashok Sanghai and my wife Vinita Deepak Shah.

Acknowledgements

I would like to begin with extending my gratitude to my advisor, prof. Dejan Filipović, for his guidance and perseverant support throughout my Ph.D. journey. He has spent countless hours teaching me about a large and varied list of topics under the sun, both technical and non-technical. His passion for knowledge and excellence has been a major inspiration and guiding force throughout the course of scientific explorations related to this work. Filip has been instrumental in molding my work in its current form and providing me with ideas, and motivation for all the required elements for my Ph.D. Filips work ethics, managerial skills, and personal interaction over the years have been an inspiration. I consider myself very fortunate and feel immense pride to have been trained under Filip in this regard. I am thus very happy and grateful to have Filip as my academic advisor and guide for my Ph.D.

I would like to take this opportunity to thank the members of my Preliminary examination, Comprehensive examination and Thesis Defense committees: Prof. Zoya Popović, Prof. Edward Kuester, Prof. Albin Gasiewski, Prof. Dimitra Psychogiou, Prof. Robert Marshall, Dr. Maxim Ignatenko for taking the time to serve on my committees; your guidance has helped me grow as a student, a researcher and grow into an efficient engineer.

The courses I have taken with the Faculty at CU Boulder have significantly added to my knowledge base. I would like to thank Prof. Linden Mc.Clure, Prof. Sam Siewert, Prof. John Pratt, and Prof. Eric Bogatin for their training and contributions towards attainment of the Professional Certification in Embedded Systems as part of my tenure at CU.

I would like to thank all the graduate students and the post-docs from the prestigious P-Club from Prof. Filipović's research group. Dr. Rohit Sammeta, and Dr. Jaegeun Ha, have helped me greatly in adjusting to the graduate student life during my initial stages. They thought me how to efficiently use all the tools at hand and gave me an insight into the fundamentals of RF and electrical engineering during our late night lab discussions. I would like to give special vote of thanks to my lab mate, post-doctoral guide, friend and inspiration Dr. Mohamed Elmansouri, who has been a constant motivator and a great resource to learn and look up to. He has been a great team player throughout the progress of this work. I would like to thank my project leader and my manager, Dr. Maxim Ignatenko for maintaining his expert supervision over my work and making it better with every suggestion and correction over time. I would like to thank Prof. Gregor Lasser for his participation and guidance in countless hours of HF antenna measurements on the roof of the Engineering Building as well as for his critical yet vital evaluation of my work and for the suggestions that followed thereafter. I would like to thank Dr. Nathan Jastram for his support and constant constructive discussions that shaped the last part of my thesis work. I would like to thank Dr. Muhannad Tarifi for the insightful discussions and suggestions about the direction of my research over time. I would like to thank the large team of graduate students and post-doctoral researchers who participated with me in numerous discussion, fabrication and testing sessions related to the HF antennas including but not limited to: Mr. Sushant Sreshtha, Ms. Milica Notaros, Mr. Richard Smith, Mr. Bradley Allen, Mr. Matthew Arendall, Mr. Conrad Andrews, and Mr. Varun Joshi. I would like to recognize the contributions and participation of the rest of the members of my research group, past and present, towards this thesis in the form of team meetings, project reviews, as well as fabrication and research suggestions: Dr. Matthew Radway, Dr. Ahmed Abdelrahman, Dr. Nahid Rahman, Dr.

David Garrido-Lopez, Mr. Ehab Etellisi, Mr. Elie Tianang, Mr. Prathap Valaleprasannakumar, Mr. Ljubodrag Boskovic, Mr. Timothy Samson, Mr. Aman Samaiyar, Mr. Roger Hasse, Mr. Riley Pack, Mr. Andrew Kee, Mr. Carlos Mulero-Hernandez, Mr. Varun Joshi, Mr. Brian Simakauskas, Mr. Emanuel Valentin, and Mr. Nathan Sutton. I would like to thank ARG affiliates Mrs. Kim Hassett for her guidance and contribution towards the scaled HF antenna measurements and Mrs. Karina Viera-Hoel for her interaction, discussions, valued comments and concerns related to 3D printed antennas. I would also like to thank Prof. Popovic's research group members for discussions about active circuits and the relevance of antenna design from an active circuits and system level design perspective.

I would like to thank my parents, Mr. Ashok Adinathrao Sanghai, Vaishali Ashok Sanghai and my brother Rishabh Ashok Sanghai for being a constant resource to talk to during graduate school, and for encouraging me to follow my dreams. I would like to thank my grandparents, late Mr. Adinathrao Abaji Sanghai, late Mrs. Gayabai Adinathrao Sanghai, Dr. Subhashchandra Gopalrao Bidkar and Mrs. Vidyulata Subhashchandra Bidkar for their kind blessings and love since childhood and for inspiring me through their hard work to achieve success in life. A sincere thank you to all the friends and family that have been there for me during this process, especially my new parents and the extended family, Deepak Ramanlal Shah and Neepa Deepak Shah. Finally, words cannot express how my wife, Vinita Deepak Shah, has helped me along this journey. She has inspired me throughout the last five years as a friend, class mate and wife to continue my journey, strive for the best and to believe in my capabilities in times of distress and to remind me that there is a light at the end of the graduate school tunnel. Her constant support was needed this entire duration, and I thank her for that. I love you, Vini.

I would like to thank the various program managers, funding sources and entities that financially supported my work throughout the course of this thesis. This list includes Maj. Jack Holloway, Capt. Benjamin Pimentel, John Moniz, Dr. Bradley Binder, Dr. Gary Roan, and Tim Wasilition from the Office of Naval Research; Dr. Michael Daly from SPAWAR Systems Center, Pacific. Without all your financial and programmatic support, none of this work would have been performed.

I would like to thank the University of Colorado Boulder staff, Mr. Adam Sadoff, Mr. Wayne Gardener and Mr. David Kraft for their unwavering support and cooperation in administrative and academic matters.

I would like to extend my sincere respect and heartfelt thanks to the Indian Embassy for their help and support in facilitating my participation in the Office of Naval Research (ONR), annual technology demonstration event – Agile Bloodhound 2015. The interaction between ONR and the Indian embassy made it possible for me to put my research onto an actual military platform and get valuable research and scientific data supporting my research hypothesis. It is notable to mention the role of Capt. Benjamin Pimentel, Dr. Tarun Mohindra, and Mr. Anilkumar Yeningala in this regard. Without your support, a major chunk of the practical contribution of this work would not have been possible.

CONTENTS

LIST OF TABLES

LIST OF FIGURES

Chapter 1

Introduction

Antennas and RF systems are increasingly being populated on various platforms across the defense, industrial, and commercial sectors in recent times. The intended use cases for such antennas vary from communication, telemetry, remote sensing, surveillance, automotive, mobile, broadcast and satellite-based applications. The successful integration of an antenna system on the desired platform depends on many factors that are influenced by the size, shape, electrical, and mechanical properties and features of the host platform. In majority of the situations, the platform is populated with a number of preexisting systems that cannot be moved or altered. The antenna design in these cases needs to account for the presence and functional requirements of the existing systems. The antenna design and deployment on the platform becomes more challenging when the antenna is expected to achieve desired performance parameters without detrimentally affecting the performance of existing systems. Since the antenna is directly in contact with the host platform, the radiation from the antenna induces currents on the host platform may cause the platform to become a part of the larger antenna-platform structure which contributes towards radiation. In these scenarios, it is imperative to perform antenna design and validation with the inclusion of the critical platform features. A huge emphasis must be laid on the practical design aspects in this regard to maintain antenna operation while maintaining platform functionality. In general, the concept of operation of the host platform must be considered carefully during the antenna design phase. Seamless platform integration of antennas and antenna systems is therefore, a major challenge. Platform integration challenge is exacerbated after factoring in the exposure to extreme environments for long operational cycles. Naturally, antenna design for a specific host platform would eventually be a tradeoff between the electrical performance of the antenna, platform integration considerations, ease of operation, and co-existence with other systems.

This chapter introduces the reader to these challenges of antenna design and integration on specific host platforms. The research motivation for each case is elaborated, followed by the description of the research methodology adopted to address these antenna design challenges. The chapter is organized into four major sections as given below:

- Section 1.1 discusses the research motivation for the work presented in this thesis.
- Section 1.2 gives an overview of the connotation of terms that form the three underlying pillars for this research work. The terminology of antenna profile, wide bandwidth and high-power operation is elaborated for the understanding of the reader in this section.
- Section 1.3 outlines the research questions addressed through this work.
- Section 1.4 discusses the overview of the research methodology to analyze and address the research questions. An overview of the research process is discussed with brief discussion of the design tools, software packages and test facilities used for research.
- Section 1.5 discusses the thesis organization and lays out a brief description of the research work showcased in the following chapters.

1.1 Research Motivation

The research motivation for the HF antenna work showcased in this thesis is based on the requirement of achieving improved electrical performance from antennas while simultaneously pushing towards a decrease in their physical size. The recent trend of moving

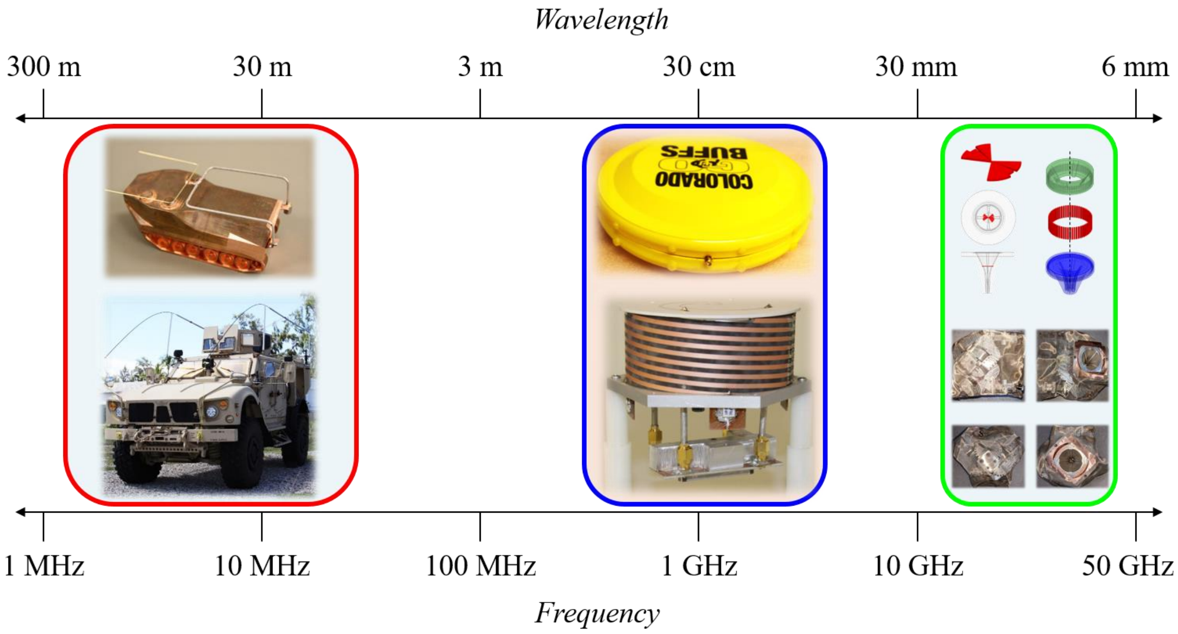

Figure 1.1 : Pictorial representation of the work showcased in this thesis and its placement on the frequency scale. The thesis work covers the antenna design for HF frequency range, the antenna integration approaches in the millimeter wave frequencies, and the appendix sections that cover antennas for UHF frequencies.

towards HF antennas with support for higher bandwidth is highlighted by the need for antennas with 24 kHz bandwidth, which is higher than the traditional 3 kHz bandwidth requirement of legacy HF antennas. For antennas and RF systems working at the millimeter wave frequencies, investigating the impact of possible internal RF leakages from components and RF assemblies inside a cylindrical payload is a major concern. The desire to quantify the leakage and prove its impact on the system level coupling and its mitigation thereafter, is motivated by the imminent requirement for the use of such millimeter wave repeaters in commercial and military networks as the use of these frequencies becomes more widespread and prevalent. For antennas addressed in the appendix section working at the UHF frequency range, the research motivation primarily comes from the power domain where antennas are expected be able to handle large input powers for sustained periods of time for applications related to communication, jamming, EW and electronic support. Improving the antenna robustness while maintaining electrical performance is also a motivating factor for practical antenna deployment.

1.2 Connotation of terms related to this thesis

This work revolves around three concepts of low profile, wideband support and high-power operation for different variety of antennas and RF systems discussed in the following chapters. The antennas discussed in this research are distributed across three set of frequencies from HF through the millimeter wave band, they have different design goals and potential end applications. The frequencies of interest for the HF antenna research proposed in this work is from 3 MHz to 30 MHz. The research related to passive RF front ends for millimeter wave repeater payload is focused on the frequency range of 18 GHz to 45 GHz. The frequencies from 500 MHz to 5 GHz are the focus of the work on wideband frequency independent antennas showcased in the appendix sections. The illustration of the scope of the research showcased in this thesis is outlined in Figure 1.1

It is important to observe that the three concepts of low profile, wideband support and high-power operation, together form the basic underlying theme that binds the research work showcased in this thesis. The subtle nuances of these three governing concepts need to be understood as and when the body of this research progresses across different host platforms, undergoes change in the frequency band of interest and moves across three independently unique applications. To introduce the reader to these underlying unifying concepts, and to provide the relevant understanding of their importance in the three proposed antenna design topics addressed in this work, the connotation for each of the underlying term is explained in detail in the following text below.

1.2.1 Antenna Profile

Antenna size is a major factor governing antenna performance. The antenna size constraints ensure that the antenna meets the physical expectations for effective integration with the host platform. It is important to understand the implications of the term ‘antenna profile’ for the antenna designs discussed in this work. The size of the antenna is fundamentally governed by the operating frequency. HF antennas are typically very large and bulky because of the large wavelengths involved. The wavelength at 3 MHz for instance is 100 m. The size of a traditional half wavelength dipole at 3 MHz would be 50 m. Such large antennas would not be acceptable for all practical vehicular mounting scenarios. The platform size also adds size constraints on the antenna. The vertical height of the antenna above the roof of the host vehicle is referred to as the ‘antenna profile’ for the part of research on HF antennas. The antenna profile of most common vehicular HF antennas is 1 m or higher. The design goal of profile is set to be less than 1 m in order to have a practical vehicular antenna with smaller or comparable antenna profile as the existing vehicular HF antennas. The two HF antenna designs proposed herein have a profile of 0.25 m (λ/400 at 3 MHz) and 0.8 m (λ/125 at 3 MHz) respectively, making them truly low-profile.

The millimeter wave RF front ends described in this work are intended to be mounted inside a cylindrical repeater payload. The term ‘profile’ in this case refers to the conformal features of the antenna aperture and the RF front end that allow it to be mounted inside the tight space constraints of a small cylinder. The wave guide transmission lines used for the RF front ends have complex routing, different contours and shapes to achieve the fit inside the cylinder and to maintain good phase match between the two channels that combine at the ortho mode transducer (OMT) connected to the antenna. The performance of the transmission lines as well as the electrical performance of the RF front end is desired to be preserved in spite of such complex profile and integration requirements.

For wideband antennas in the UHF frequencies, the radial size of the antenna is defined by the lowest frequency of operation. The thickness or the height of the antenna is influenced by the antenna form factor which includes the antenna cavity, the beamforming network or feed structure under the cavity and placement of radome or superstrates on the antenna aperture. The term ‘antenna profile’ for this part of research refers to the physical height of the antenna as well as its visual appearance in the deployed configuration. An expendable planar log periodic antenna is proposed for mounting in a rhino configuration on the front of the vehicle or used as a standalone bidirectional antenna with a design that has a low observable profile. The antenna profile in this case means the thickness of the antenna with the radome. Low profile is also interpreted as the antennas ability to be disguised and not be recognized as a typical antenna. In the case of the UHF antennas showcased in the appendix, a spiral-helix antenna is described. This antenna is intended to be flush mounted on a planar surface. The antenna profile in this case is the antenna height above the planar surface in the flush mounted configuration on the host platform.

1.2.2 Wideband Operation

Legacy HF infrastructure is designed to support 3 kHz bandwidth. Typically, HF radios are used with SSB modulation for carrying voice transmissions. The limited data transmission capabilities of legacy HF infrastructure are due to the use of some form of tone based encoding schemes. Operation with 3 kHz bandwidth limits the robustness and versatility of HF communication systems in the field. To address this, recent standardization of wideband HF waveforms has been defined with 24 kHz channel bandwidth for HF systems.

This is 8 times more bandwidth compared to traditional HF systems. 3 kHz channel bandwidth means a 0.1% bandwidth at 3 MHz. Although 0.1% bandwidth seems small, it is challenging to achieve 3 kHz bandwidth on practical vehicle mounted HF antennas due to their small electrical size. The migration to a 24 kHz capable system in this perspective is hence rightfully justified to be addressed as 'wideband' for the research of HF antennas in this work.

In the research segmented focused on millimeter wave system, integration techniques for mounting horn antenna are proposed followed by the investigation of internal RF leakages for RF front ends inside cylindrical payload and its mitigation thereafter. In both these cases, consistent antenna performance is shown over the 18 GHz to 45 GHz band. This bandwidth is considered 'wideband' as it spans over three traditional waveguide bands – WR 42 (18 GHz to 26.5 GHz), WR 28 (26.5 GHz to 40 GHz) and a quarter of the band covered by WR 19 (40 GHz to 60 GHz). In a more direct, physical sense, the 18 GHz to 45 GHz band represents a 2.5:1 bandwidth coverage which is also considered wideband for typical antenna applications.

The term 'wideband' is used in a more traditional sense for the antennas discussed in the appendix sections for operation over UHF bands. The expendable planar log periodic antenna is shown to work over 500 MHz to 5 GHz which is a 10:1 bandwidth, while the spiral helix antenna described for the antenna autopsy works from 500 MHz to 3 GHz, thus supporting a 6:1 bandwidth.

1.2.3 High power capability

The design requirement for the proposed HF antenna is set at a minimum input power of 400 W under continuous wave (CW) operation. Traditional vehicular HF antennas are rated up to 250 W CW operation. Thus, the antenna design requirement shown in this work is 1.6 times the existing power handling requirement, making it realistic to be addressed as high-power from a platform mounted HF antenna perspective.

The impact of internal RF leakage on the coupling inside a repeater payload is addressed for the millimeter wave frequency range in this thesis. RF leakage is approached from an at the antenna and system level perspective. High power operation is considered as a desired feature for the repeater payload. Improvement in system isolation levels would allow for operation of the repeater at higher power levels. The proposed mitigation technique for RF leakage allows the coupling inside the payload to be improved from 65 dB worst case to 90 dB worst case over the 18 to 45 GHz band. The improvement in isolation is a design improvement that would enable stable high power operation of the repeater payload.

The work on UHF antennas covered in the appendix section also looks into high power operating capabilities. The expendable planar log periodic antenna is based on the design guidelines established for high power operation for planar log periodic antennas. Special design considerations for the feed region and the resonating teeth are incorporated to attain the desired high-power capability. The spiral helix antenna is directly aimed at investigating the antenna performance under high input powers to understand the antenna failure mechanism. Deficiencies observed in the design through the analysis are then used to improve the antenna design and to make it capable of operating under high power conditions.

1.3 Research Questions

The three main research questions addressed in this work are outlined below:

- How to design low profile, 24 kHz wideband, electrically small HF antennas for vehicular on the move platform applications?

- How to address the platform integration and practical design challenges for the full scaled HF antenna prototype for operation on an actual military platform?
- How to address the platform integration for isolation improvement of millimeter wave and quasi millimeter wave RF front ends designed for space constrained cylindrical repeater payloads?

1.4 Research methodology

The work presented herein follows a step by step progression of antenna design starting from fundamental theory and eventually maturing into practically realizable antenna designs, test beds and prototypes. The approach for initial studies is based on exploring the fundamental physical bounds and limitations to set the realistic expectations on antenna or RF system performance for a specific platform. Computational studies and modeling is used to guide the antenna design process. The focus of the research revolves around the size, performance and practicality of the systems proposed in this work. The computational studies shown are performed using two numerical simulation packages employing full wave electromagnetic simulation tools – namely the method of moments code Altair FEKO, and the finite element code Ansys HFSS [1] [2]. The data post processing is performed using custom scripts written in MATLAB [3]. NI AWR software package is used for circuit simulations related to tuning, post processing measured data and embedding, and de-embedding transmission lines and other component data as needed [4]. The far field radiation patterns and gain is measured for antennas in the 500 MHz to 45 GHz range in the in-house antenna measurement chamber using an NSI 700S-30, fully automated and computer controlled antenna measurement system operated by the Antenna Research Group, at the

University of Colorado Boulder [5]. All the antenna S-parameter measurements are performed on an Agilent 8719ES network analyzer. All the antenna fabrication is done in house or at the various University of Colorado machine shops. The 3-D printing and additive manufacturing is done in-house while the plating and post processing of 3-D printed models is done through a variety of specialized vendors. Majority of the PCB fabrication for antenna apertures and prototypes is performed at a local PCB manufacturing shop [6]. All measurement and test locations accessed throughout the research phase of this work are explicitly mentioned in the appropriate sections in the following chapters in the case that the research was conducted at locations other than the University of Colorado Boulder.

1.5 Thesis Organization

The work presented in this thesis is organized as follows:

- Chapter 2: The design, analysis and scaled model prototyping of an ultra-low-profile, two arm, offset fed inverted-L antenna for the amphibious assault vehicle (AAV) is shown. The focus of this research is to achieve wideband 24 kHz tuned bandwidth and antenna operation in the NVIS favored frequency ranges (3 MHz to 10 MHz). To set the research relevance, the chapter overviews the fundamentals of HF communication followed by a brief introduction to electrically small antennas. The numerical and analytical tools used are encapsulated followed by an overview of the inverted-L antenna along with comparison with other similar antennas reported in literature. The antenna evolution from a whip to an electrically small vehicular antenna is achieved using a parametric study. Antenna performance is reported based on the adopted computational model followed by the scaled prototyping and impedance and pattern measurements. The final antenna dimensions presented at 3 MHz are λ/13 (L), λ/31 (B), λ/400 (H), making it truly electrically small and low profile.

- Chapter 3: The transition from scaled prototyping of vehicular HF antennas to full scaled prototype for the M-ATV platform is addressed in this chapter. This chapter builds on the antenna design process laid down in Chapter 2, while adding practical relevance and fabrication details required for the large antenna build. Numerical studies for the antenna design are reviewed before the fabrication details. The process adopted for achieving incremental testing goals is showcased where the antenna is matured through initial testing, multiple platform integrations and specialized full scaled HF antenna testing at various locations elaborated in the chapter. The culmination of these research efforts ends in the form of field demonstration of the antenna on the proposed M-ATV platform. Following the field demonstration, the antenna superstructure is re-used to develop a proof of concept for a switched mode HF antenna. The chapter is concluded with a summary and brief discussion on the practical realization of the proposed switched mode HF antenna.

- Chapter 4: The assembly strategies for isolation improvement of a millimeter wave repeater is presented. The research work is motivated through current requirements and expectations from millimeter wave front ends and space constrained platforms. An overview of the fundamentals of RF shields is followed by computational analysis of a horn antenna. Computational model is first validated against the measurements performed on a prefabricated horn antenna. The impact of introducing a cut plane along the throat of the horn antenna is presented with the proposed assembly strategy for the integration of the horn antenna inside a cylindrical payload. System level coupling analysis is performed and proof of internal RF leakages affecting the coupling is presented. The method for mitigating the impact of internal RF leakage on the coupling is demonstrated through measurements using proposed conductive RF sleeves. Discussion about the methods for component inspection are briefly discussed towards the end of this chapter.

- Chapter 5: A thesis overview with the highlights of research contributions is presented. The concluding remarks are presented and a pathway towards the future work is shown.

- Appendix A: Low cost, expendable planar log periodic antenna design comprising of radome made from COTS Frisbee discs is discussed. The antenna design, computational modeling and fabrication is shown. The main USP of the antenna is that it uses Frisbee disc as an effective radome without much detrimental impact on its consistent wideband performance.

- Appendix B: The investigation of a compact spiral helix antenna as part of the antenna autopsy is shown in the second half of the chapter. The autopsy probes into the antenna failure mechanism and suggestions to improve the weak design aspects of the antenna are presented thereafter.

- Appendix C: Preliminary component inspection techniques to detect miniature air gaps and fabrication artifacts in the component seams are described. The possibility of unintentional RF leakage from such small air gaps is a major concern for looking into these techniques.

Chapter 2

Ultra-Low Profile Inverted-L Antenna for Vehicular HF Communications

2.1 Introduction

High Frequency (HF) communication in the 3-30 MHz frequency range enables link establishment over thousands of kilometers without the use of satellites or land based repeating infrastructure [7]. HF communications is regarded as the last line of communication for local and nationwide networks to coordinate relief efforts after natural disasters, even in this modern satellite age [8][9][10][11]. Three modes of propagation are distinguished, namely, ground wave, long range sky wave and near vertical incidence skywave (NVIS). Legacy HF radio systems and antennas support 3 kHz bandwidth; however, recent standardization of wideband 24 kHz HF waveforms promotes migration towards wideband HF systems and necessitates development of wideband HF antennas supporting new waveforms [12]. The antenna proposed in this chapter deals with the NVIS mode of HF communication operating over 3 to 10 MHz, wherein the signal is launched at high angles towards the zenith [13].

The host platform for the antenna deployment is the Amphibious Assault Vehicle (AAV) [14]. The AAV is 8 m long and 3.3 m wide. The vehicle height from the base to the roof on the rear side is 2.6 m. The roof of the vehicle has a slight upwards gradient as we move towards the front. There are three personnel hatches on the vehicle roof for the crew. Each track on the AAV is 1.1 m in height and 0.7 m wide. The tracks maintain intimate electrical contact of the vehicle body with the ground beneath. The rear of the AAV has slanted side panels. The rectangular shaped flat roof top on the AAV is 3.5 m long and 2.1 m wide. The center of two of the crew hatches are located 4.8 m away from the rear edge of the roof on the AAV. The center to center distance between the two hatches located along the length of the vehicle is 1.3 m. These hatches protrude 0.25 m above the vehicle roof. Across different variants of the AAV, these hatches serve varied functions such as an observation window, turret mount for weapons and so on. The dimensions of the AAV are shown in Figure 2.1.

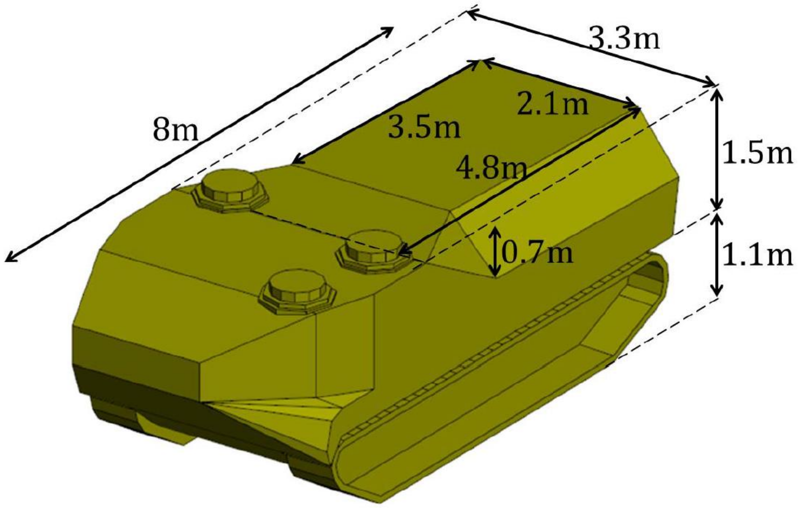

Figure 2.1: Detailed Dimensions of the AAV platform.

This chapter discusses the design of a low profile, on-the-move (OTM) NVIS inverted-L configuration operating from 3 to 10 MHz. The antenna has profile of λ/400 at 3 MHz and supports 24 kHz instantaneous bandwidth. The proposed design approach can be used to design antennas operating on various vehicular platforms, whereas this chapter shows design and performance of the antenna mounted over the AAV (Figure 2.2). The slanted side panels on the AAV help maintain clearance for the antenna structure from the vehicle body.

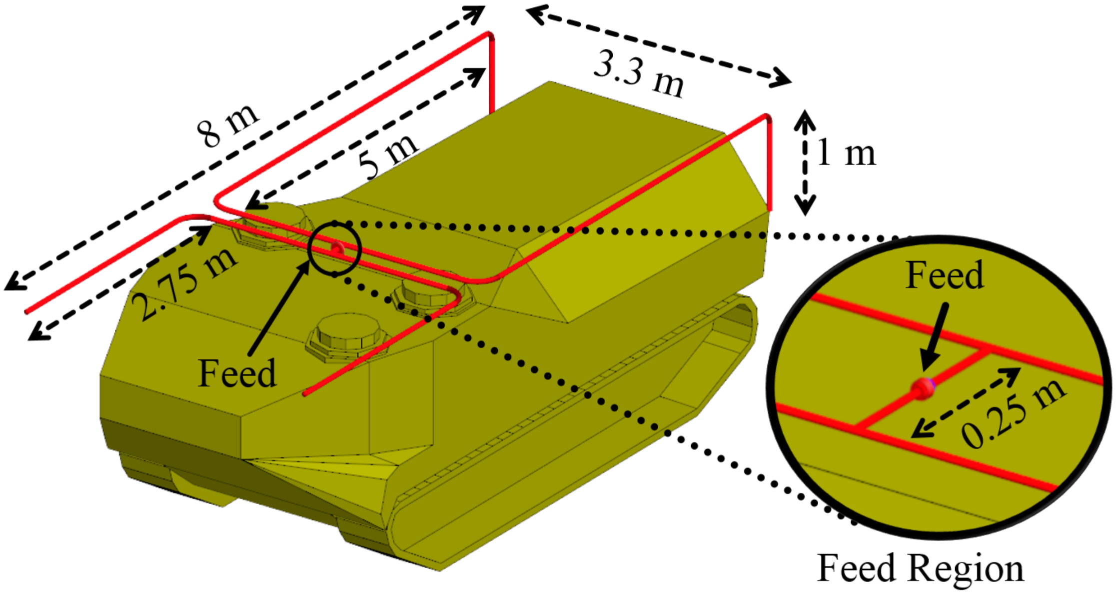

Figure 2.2: Isometric view of the proposed antenna over AAV.

An overview of some of the state of the art vehicular on-the-move HF antennas is shown in Figure 2.3. These antennas are currently fielded and commonly used in OTM operations on various vehicular platforms. Most of these antennas can be classified into a loop type or whip type configuration. These antennas are typically designed to support the legacy 3 kHz HF radios with 150 W of nominal input power. The Shakespeare 120-99 is a traditional whip antenna, commonly mounted on the aft sections of the host platform [15]. It has a profile as high as 9 m in one of its variant with an operating range of 1.6 to 30 MHz using a proprietary HF coupler/tuner [15]. The Cobham 3160-99 is a half-loop HF OTM antenna system with a proprietary tuner which requires two mounting points on the host platform and relies on good grounding for reliable operation [16]. The stealth 9400c (Super Skyrider™) is a Mobile HF NVIS magnetic loop antenna with continuous variable tuning from built in antenna tuner unit (ATU), catered towards covert HF mobile operation by shaping the antenna structure as a vehicular roof rack and operates over 4.5 to 22 MHz [17].

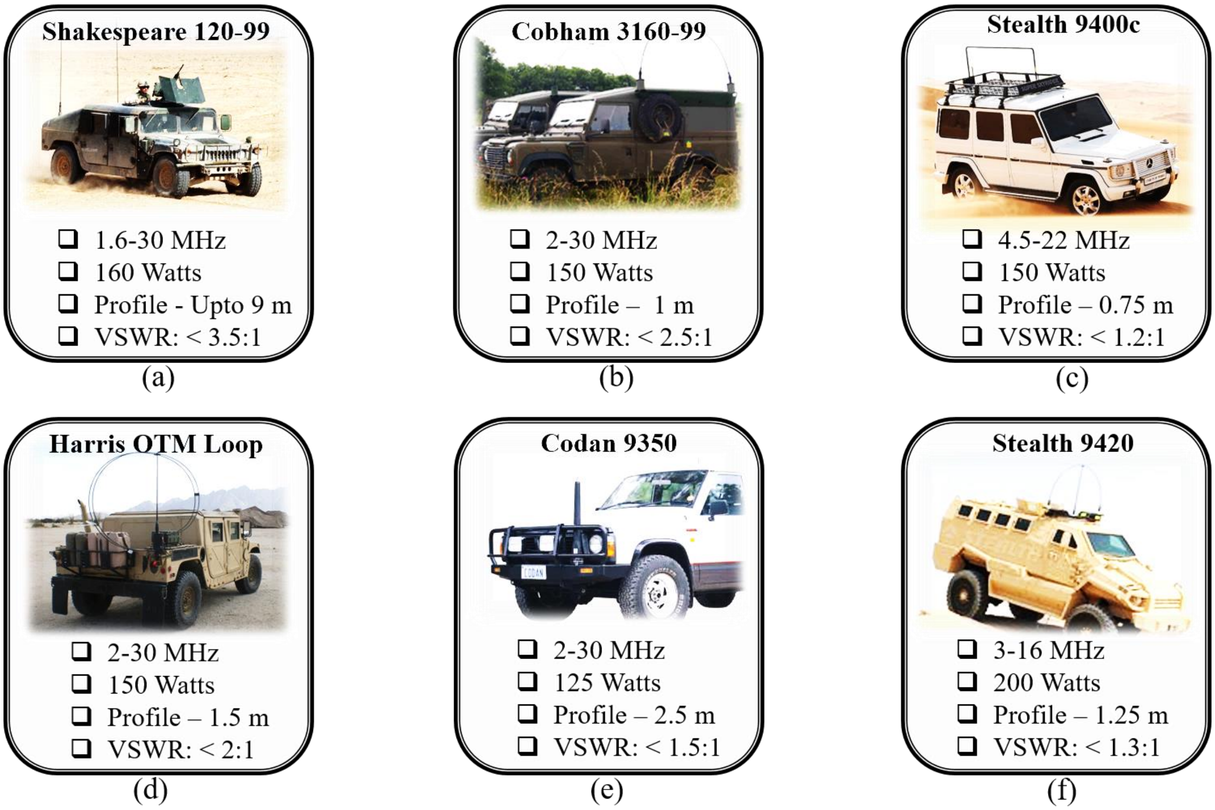

Figure 2.3: Overview of currently fielded state of the art vehicular HF antennas from different vendors: (a) Shakespeare 120-99 mobile HF whip antenna [15], (b) Cobham 3160-99 half loop OTM Antenna [16]. (c) Stealth 9400c actively tuned half loop antenna [17], (d) Harris OTM loop antenna [18], (e) Codan 9350 automatic tuning whip antenna [19], (f) Stealth 9420 Half Loop antenna[20].

The Harris OTM HF loop is a tuned full loop antenna with a proprietary coupler operating over 2 to 30 MHz [18]. The Codan 9350 is an automatic tuning HF bent whip antenna with the tuning element built into the base of the whip antenna for HF operation over 2 to 30 MHz [19]. The long length of the Codan whip is bent over the vehicle roof and secured using a harnessing rope for this antenna to achieve a lower profile. The Stealth 9420 is a autotuned NVIS HF mobile antenna with a half loop profile operating over 3 to 15 MHz in transmit mode with an integrated tuner at its base [20]. Most of these antennas have a profile higher than 1 m while they also need provisions for DC power, radio and data interface cables running to and from the antenna / tuner for tuning operation and stable vehicular grounding at the mounting interfaces.

The design of the HF antenna prototype described in this chapter is benchmarked against the size, features and performance of the commercial vehicular HF antennas reviewed above. The requirement on the antenna profile is set at less than 1m and the power handling requirement is set to be at a minimum of 400 W CW. The focus of this chapter is to demonstrate a design approach for developing a practical HF antenna with capability to support 24 kHz wideband HF waveforms while still maintaining the low-profile criterion when deployed on the AAV platform. The antenna design efforts are followed by scaled prototyping of the proposed concept to validate the adopted approach.

Having low profile is vitally important for OTM antennas. High profile antennas may obstruct the on-board sensors and / or weapon systems on a vehicular platform as well as yield large radar cross section (RCS) profiles that may inhibit much desired stealth operation [21]. High antenna profile also causes difficulty in vehicular operation in micro terrains, underpasses and near high tension electric utility distribution lines making the antennas impractical for on-the-move use [22]. Commercially available off the shelf (COTS), state of the art 3 kHz Harris vehicular HF OTM loop antenna has profile of 1.5 m and -15 dBi gain at 3.5 MHz [23]. Profile of the legacy Cobham half-loop is 0.9 m; it has gain of -26 dBi at 2 MHz and -17 dBi at 3.5 MHz [21] [24]. Performance of existing COTS antennas augments the design requirement for new wideband antennas: the profile should be less than 1 m and gain at zenith better than –20 dBi at 3 MHz.

Recently, new 24 kHz capable wideband HF antennas have been reported in literature. A half loop antenna with profile of 0.5 m and gain better than -25 dBi at 2 MHz is shown to support tunable bandwidth of better than 24 kHz [25]. However, this antenna requires a few access points to vehicle ground potentially complicating practical realization. Cobham has reported a 24 kHz capable half loop antenna with a profile of 1.25 m [26], which is higher than its existing 3 kHz antenna variant.

This chapter demonstrates the antenna design, computational modeling and scaled prototyping of vehicular HF antenna design. The focus of the design is for the HF frequency bands over 3 to 10 MHz with greater detail to the near vertical incidence skywave (NVIS) mode of propagation. The chapter is organized into four sections as described below, followed by the conclusion.

- Section 2.2 discusses the basic overview of an inverted-L antenna followed by fundamental studies for the inverted-L antenna with size relevance to the AAV.
- Section 2.3 discusses the evolution of the antenna design described in this chapter. The performance of a single arm and two arm inverted-L antenna are discussed.
- Section 2.4 describes the antenna performance in the NVIS band. Discussion about the antenna tuning, and performance of the proposed antenna under considered mechanical failure is shown. This section also discusses the omnidirectional performance of the antenna and about the impact of flaring the antenna arms to conform to the AAV body.
- Section 2.5 discusses the scaled prototyping and measurements performed to validate the computational design process.
- Section 2.6 talks about the practical aspects of the proposed antenna.
- The overall summary of the chapter is laid down in Section 2.7.

2.1.1 Ionospheric Model

HF Radio links are typically established over thousands of kilometers by bouncing the radio waves from different parts of the Earth's ionosphere. This phenomenon of bouncing signals from the earths ionosphere is temporal and often influenced by operating conditions related to spatial and frequency domains. This special and complex behavior of HF radio waves as they travel through the propagation channel of the ionosphere is commonly referred to through the term called HF propagation.

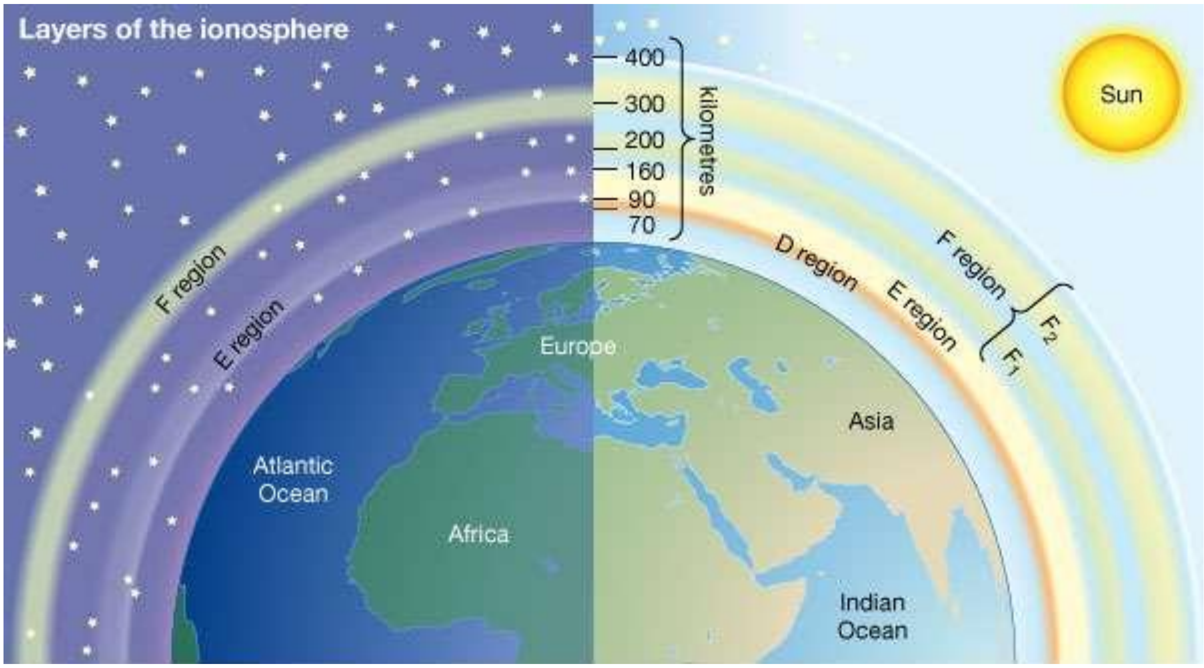

Figure 2.4: General representation of the ionospheric composition over day and night [27].

The ionosphere formed around the earth is divided into a few regions called as layers. The D layer, E layer and the F layer together comprise majority of the ionospheric regions. Each of these layers exhibit distinct behavior due to their interaction and exposure to different levels of solar radiation. These different layers are distinguished based on their ion density and altitude from the surface of the earth. It must be noted that these layers do not have sharp boundaries but rather dynamic interfaces that move based on the level of solar radiation which in turn is influenced by factors such as the time of the day, the tilt of the rotational axis of the earth and the season of the year. A general representation of the composition of the ionosphere is shown in Figure 2.4 with the ionospheric variations depicted across day and night [27].

The D-layer is the lowest of these ionospheric regions and typically occupies altitudes between 75 and 95 km. It appears at daytime but diminishes significantly during night due to reduced solar radiation levels. The D-layer is mainly responsible for absorption and attenuation of high frequency radio waves. The E-layer is the next ionospheric region above the D-layer. The E-layer typically manifests between about 95 and 150 km and is responsible for reflecting radio waves lower than 10 MHz while it offers moderate levels of attenuation to frequencies higher than 10 MHz. In situations of high ionic content cloud formation during the day, a sporadic E-layer is also observed. The formation of the sporadic E-layer is short lived and may be seen over intervals of few minutes to a couple of hours. The ionospheric region above the E-layer is called as the F-layer. The F-layer starts from 150 km and higher [28]. The F-layer can extend all the way to 500 km from the surface of the earth. The F-layer has the highest electron density among the three layers. During the day, the F-layer splits into two sub layers of high electron density concentration called as the F1-layer and F2-layer due to the high exposure to solar radiation. At night, the two sub layers fuse into one relatively smaller layer, commonly referred to as the F2-layer.

2.1.2 HF Propagation

HF radio infrastructure typically consists of the transmitter equipment comprised of the radio transmitter or source coupled to a transmitting antenna, the channel through which the signal travels and the receiving end equipment consisting of a receiving antenna and a radio receiver unit. In the case of the HF radio links, the channel for transfer of energy between the transmitter and the receiver includes the ionosphere. The ionosphere is a region of Earth's atmosphere, where atmospheric gas is partially ionized by solar radiation as described above. The existence of charged ions in the ionosphere favors communication by reflecting obliquely incident radio signals under specific operating conditions. The signal reflection occurs when the incident radio signal is lower in frequency than the electron plasma frequency for a set of existing ionospheric conditions defined by the electron density, the electron mass, and the charge of an individual electron. The highest frequency signal which will be reflected to the earth for a specific ionospheric layer under normal incidence consideration is called as the critical frequency. The critical frequency can be mathematically represented as [29]:

$$f_c = 9\sqrt{N_{max}}, \tag{2.1}$$

where, $'f_c'$ represents the critical frequency represented in Hz, and $'N_{max}'$ represents the maximum electron density per unit volume expressed in number of electrons per m^3. The reflection of radio signal from the ionosphere is also a function of the angle of incidence of the radio signal at the ionospheric layer measured from the normal to the ionospheric layer subtended towards the line representing the arriving radio signal. The highest frequency for a given angle of incidence $'\theta'$ above which the ionosphere can no longer reflect the incident radio signal is termed as the maximum usable frequency (MUF). MUF is mathematically represented as [29]:

$$MUF = f_c\, Sec(\theta), \tag{2.2}$$

The MUF often proves to be challenging to adhere to as an upper bound for practical HF operations for a given set of operating conditions. Since the ionosphere has a predominantly dynamic nature, the MUF changes with the corresponding change in the ionospheric conditions. To provide a more stable upper bound on the operating frequency for a given set of ionospheric conditions, a more conservative parameter called as the optimum working frequency (OWF) is defined. Operating at or below the OWF would ideally provide stable HF link between two points provided there are not too many drastic changes in the ionospheric conditions. Mathematically, OWF is represented as [29]:

$$OWF = 0.85 * MUF, \tag{2.3}$$

The cutoff frequency is referred to the frequency below which a radio wave fails to pass through a layer of ionosphere at a given angle of incidence required for link establishment between two specified points by refraction from that layer. Most of the time the cutoff frequency falls within the HF band for typical ionospheric and link establishment conditions. This makes it possible to establish long range and short-range links in the HF frequency band by conducting multiple signal bounces through the ionosphere.

2.1.3 Modes of HF Communication

Three modes of HF communication are generally distinguished based on the propagation characteristics employed to close the link between two points. The near vertical incidence skywave (NVIS), long range skywave, and ground wave modes are appropriately named after the propagation principles they exploit [29] [30] [31] [32]. NVIS links rely on near vertical incidence communication, typically within 2-10 MHz frequency range. The launch angles required to support NVIS communication are high, ranging between 60° and 90° from the horizon. Long range skywave and ground wave modes typically propagate at shallow launch angles close to horizon as shown in Figure 2.5. Long range skywave links require frequencies typically higher than NVIS link frequencies; whereas ground waves often utilize frequencies at lower end of the HF frequency range. Each propagation mode also has its typical link coverage characteristics. The ground wave propagation mode relies on the use of vertically polarized antennas that support high gain close to the horizon for achieving longer link distances without much attenuation of the signal from the earth. Since ground wave links are made of surface waves, they do not rely on the reflection from ionosphere. The ground wave mode is used for local communications typically less than 100 km. The ground wave link distances are influenced by the curvature of the earth and the severe attenuation of signal by the signal interaction with the ground. The NVIS mode of communication is used to send the signals overhead where they are bounced back from the ionosphere. To achieve this, the antennas used for NVIS communication must have significant part of the radiated energy directed towards the zenith. This allows for establishing communication in the urban environments over few tens of kilometers where obstructions near the antenna and undulating terrain might prohibit conventional point to point and ground based links. The long-range sky wave mode of operation is most commonly used for global communications. In this case, the signals can travel between two points of the HF link after multiple bounces from the ionosphere and the earth. Unlike the ground wave mode of propagation, antenna polarization does not play a significant role in the NVIS mode or the long-range sky wave mode of communication since the signal gets split into two polarizations as it is reflected from

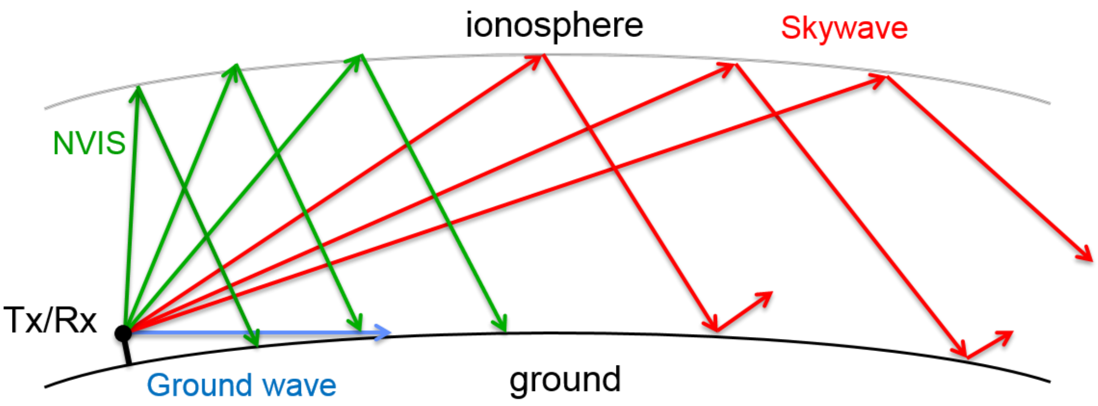

Figure 2.5: Different modes of propagation used in HF communication.

the ionosphere. Since long range sky wave and ground wave communication require low take off angles close to horizon, whip antennas are often utilized on vehicles to serve these modes.

The distance between the farthest link closed by the ground wave propagation mode and the shortest link distance offered by the long-range sky wave mode using a single bounce from the ionosphere is called as the skip zone. The skip zone does not receive any energy from either the ground wave mode or the long-range sky wave mode. No link can be established if a point lies in the skip zone for a given set of operating conditions such as operating frequency, transmit power, ionospheric conditions, antenna gain and the launch angle. However, when all three modes of HF propagation can be supported and intelligently set up, standalone and seamless coverage over 1000's of kilometers can be achieved using simple HF communication infrastructure.

2.1.4 Channel Capacity Considerations

Traditionally, HF communication systems have been used with 3 kHz bandwidth for voice, command and control, and limited data capabilities. Recent standardization of wideband waveforms paved a path towards practical HF systems using more complex waveforms ranging from 3 kHz bandwidth up to 24 kHz bandwidth with 3 kHz steps [12] [33]. Widening signal bandwidth may help to improve channel capacity or/and link robustness. The estimation of channel capacity bound for various antenna gains and waveform bandwidths for a typical NVIS link is considered in the analysis shown in this section. The procedure follows to that discussed in [34]. In all cases, favorable ionospheric conditions are assumed.

The channel capacity bound outlined by the Shannon – Hartley theorem is used for the channel capacity analysis. The Shannon – Hartley theorem states that channel capacity C is determined by the channel bandwidth B in hertz and signal-to-noise ratio SNR as:

$$C = B\, log_2(1 + SNR), \tag{2.4}$$

where, the channel is assumed to be a subject of additive white Gaussian noise, and bandwidth B corresponds to the signal waveform bandwidth. To find SNR, the received power P_r and noise power level N should be determined. The power of received signal P_r is given by modified Friis transmission formula as:

$$P_r = P_t + G_{Tx} - L + G_{Rx}, \tag{2.5}$$

where P_t is the transmitting power, G_{Tx} is the gain of transmitting antenna, L is a total propagation loss, and G_{Rx} is the gain of receiving antenna. All terms are given in the dB scale.

For the estimation, the total loss 'L' consists of free-space path loss ($FSPL$), D-layer loss at day time (L_D) and polarization mismatch loss (L_P)

$$L = FSPL + L_D + L_P, \tag{2.6}$$

The expression for free space path loss can be mathematically represented as:

$$FSPL = 20\log_{10}\frac{4\pi d}{\lambda}, \tag{2.7}$$

where d is the path length, and λ is the signal wavelength.

The expression for Noise power is given with respect to thermal noise N_{thrm} as:

$$N_{thrm} = -204 + 10\log_{10} B, \tag{2.8}$$

where, the unit of N_{thrm} is dBW and temperature of 300 K is assumed. Noise figure contribution of radio noise is given as [35]:

$$NF = 67.2 - 27.7\log_{10} f_{MHz}, \tag{2.9}$$

The relationship between thermal noise N_{thrm}, noise figure NF, and total noise power N is:

$$N = N_{thrm} + NF. \tag{2.10}$$

TABLE 2.1

Channel capacity for communication between stationary and portable radio.

		Night	Day	Night	Day
Signal:					
Frequency	MHz	3	7	3	7
Bandwidth	kHz	3		24	
Transmitter:					
Power	dBW	20		20	
Antenna gain	dBi	5		5	
EIRP	dBW	25	25	25	25
Channel Specs:					
NVIS height	km	100	300	100	300
Ground range	km	100		100	
Free space path loss	dB	89	105	89	105
D-layer loss	dB	0	10	0	10
Receiver:					
Polarization mismatch	dB	3		3	
Antenna gain	dBi	-25	-10	-25	-10
Receiving signal:					
Power	dBW	-92	-103	-92	-103
Noise:					
Thermal noise	dBW	-169		-160	
Noise figure	dB	54	44	54	44
Noise power	dBW	-115	-125	-106	-116
SNR	**dB**	**23**	**22**	**14**	**13**
Channel capacity	**kbps**	**22.94**	**21.95**	**112.96**	**105.33**

Example of calculated channel capacity for a stationary base station radio setup with a 100 W of radiating power and 5 dBi antenna gain communicating to a portable vehicular radio setup with a low gain antenna is shown in Table 2.1. Gain of the receive antenna corresponds to typical gain of an existing 3 kHz OTM NVIS antennas. Clearly, wider bandwidth leads to higher channel capacity in this case. Channel capacities for day and night links are nearly the same because the higher loss at day time in the ionosphere is compensated by the higher antenna gain at corresponding higher operating frequency (7 MHz) used during the day time for the calculations; however, this is not a general rule.

The results for a detailed parametric study are shown in Figure 2.6. Transmitter is a stationary antenna with 5 dBi gain and radiating power of 100 W. Channel capacity is estimated for a range of gain values supported by receive antennas. As seen, at nighttime channel capacity is getting larger for wider bandwidth for all G_{Rx}. At daytime, the same effect holds when G_{Rx} is higher than -15 or -10 dBi approximately. With lower gain receiving antennas, there is an indication of saturation of the channel capacity even when wider bandwidth is used. In this case, the deterioration of SNR due to higher thermal noise level overcomes the benefit offered using wider bandwidth for enhanced channel capacity. With lower transmitting power, e.g. P_t = 20 W corresponding to a portable radio and various transmitter antenna gains and fixed 5 dBi receiver antenna gain, the saturation becomes more apparent (Figure 2.7). In another case, when a link is stablished between two portable radios (P_t = 20 W) with the same gain antennas (Figure 2.8), the channel capacity is saturated in most cases, unless the gain of antennas is positive. This example clearly demonstrates that higher antenna gain is desirable, when high throughput between portable radios is required.

From the results of channel capacity considerations mentioned above, it must be noted that for a typical vehicular OTM communication scenario, the antenna gain is low at lower end of the HF spectrum due to their small electrical size. Operationally, there will be cases involving the vehicle communicating to another vehicle, to the base station or to a manpack portable unit on the ground. The channel capacity is directly proportional to the bandwidth of the channel in such cases. With an electrically small antenna with low gain, having a larger channel bandwidth would allow for more noise to enter the system and saturate the channel capacity. It must be noted that for such electrically small antennas with low gain, the system is thus externally noise limited. However, the wider channel bandwidth would allow for use of more complex and robust signal encoding which is currently desired and is being addressed in the new wideband standard for HF communication.

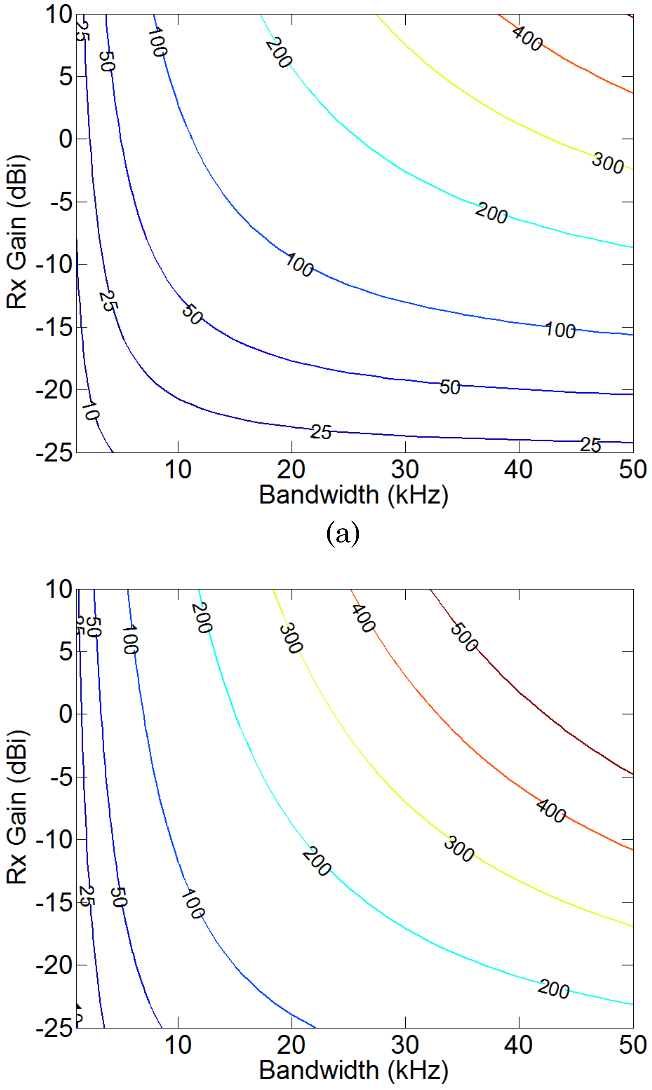

(a)

(b)

Figure 2.6: Channel capacity in kbps for communication between a stationary radio (G_{Tx} = 5 dBi, P_t = 100 W) and receiving stations with various gains for (a) daytime and (b) nighttime propagation conditions [34].

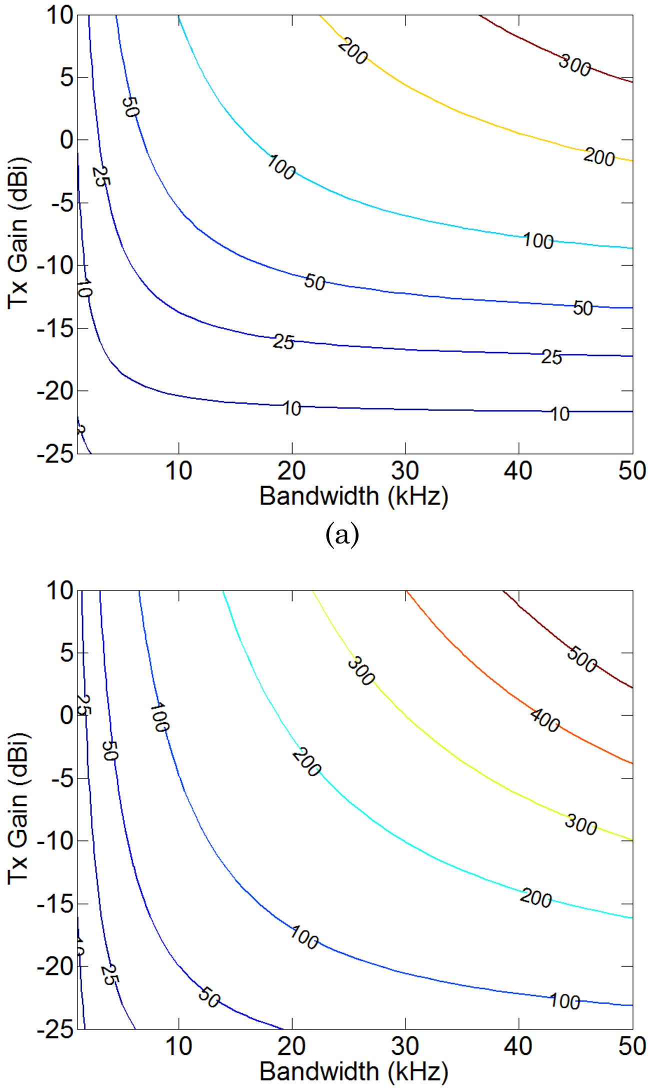

(a)

(b)

Figure 2.7: Channel capacity in kbps for communication between a radio with reduced transmitting power with varying transmitter antenna gains (P_t = 20 W) and receiving stations with G_{Rx} = 5 dBi for (a) daytime and (b) nighttime propagation conditions [34].

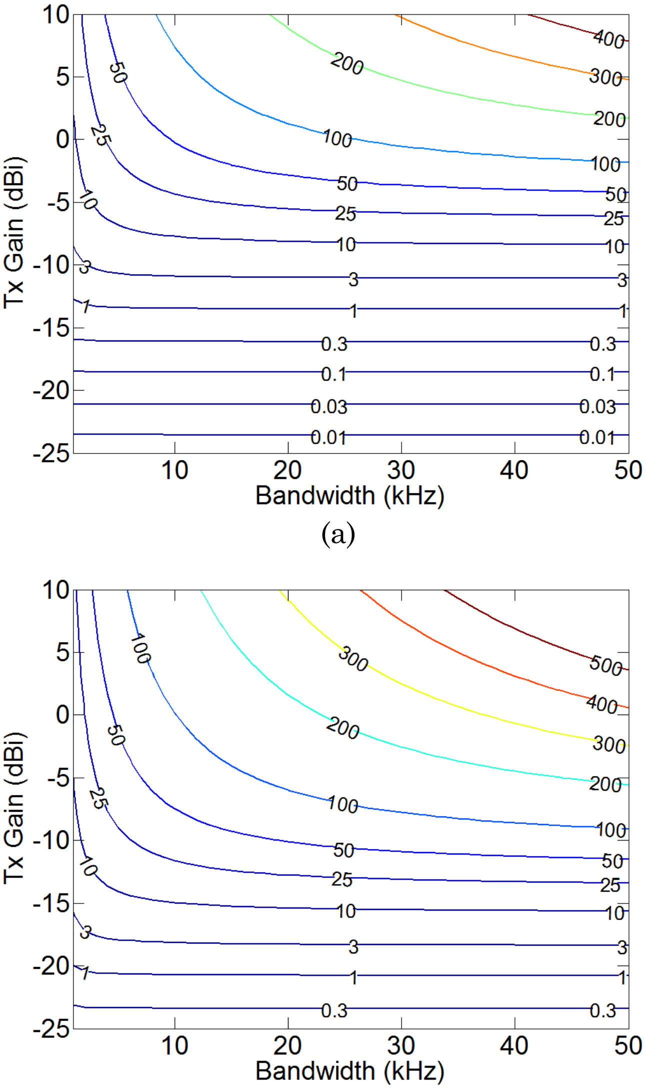

(a)

(b)

Figure 2.8: Channel capacity in kbps for communication between two radios with the same antennas ($G_{Tx} = G_{Rx}$, P_t = 20 W) for (a) daytime and (b) nighttime propagation conditions [34].

HF antennas and communication systems are typically large and have associated mechanical, electrical and practical implementation challenges. Apart from these challenges, these systems also need to adapt to the dynamic nature of the ionosphere due to changes in the solar radiation levels, atmospheric activity, and seasonal changes on a time scale that can span from a few minutes to a few months at end. Among the top challenges that need to be encountered and addressed in real time over a typical HF link are events of fading, ionospheric noise, spurious noise caused by solar activity and so on. Addressing these challenges in electrically large antennas for HF communication is often a major engineering problem. The use of electrically small OTM antennas for HF communication makes this an even greater engineering challenge.

2.1.5 Electrically Small Antennas

The special class of antennas whose entire radiating structure including its image can be confined inside a volume smaller than a sphere of radius 'a' such that the size of the sphere is smaller than the inverse of the wavenumber at the lowest frequency of operation are called electrically small antennas [36][37].

The relationship for the radius 'a' of the enclosing sphere and the wavelength for electrically small antennas can be represented as:

$$a < \frac{\lambda}{2\pi}, \tag{2.11}$$

This radius at which we characterize the electrically small nature of the antenna is called the radian sphere. The physical significance of the radian sphere is that it is at this distance that the energy stored in the reactive near field of the antenna is equal to the radiating far field of the antenna in magnitude. Inside the radian sphere, the near field terms are dominant meaning the antenna stores energy and outside the sphere, the radiating far field terms are dominant meaning the antenna radiates that energy. Historically, the concept of electrically small antennas was first proposed by H. A. Wheeler in 1947 where he discussed the lumped circuit equivalence of electrically small antennas [36]. According to his proposition, the small electric dipole was represented as a parallel plate capacitor and the small magnetic dipole was represented by an inductive coil. Wheeler laid down the basis that antenna Q is inversely proportional to the antenna volume in this work. L.J. Chu in 1948 further made contributions to the electrically small antenna theory by treating the antenna as a lumped circuit model, similar to the approach laid down by Wheeler. Chu added the consideration of spherical modes to establish the optimum performance bounds from an antenna enclosed in a radian sphere [38]. Like Wheeler, Chu defined a simple geometric boundary called the *'Chu Sphere'* which separated the distinct field behavior of the antenna. The Chu Sphere was defined to have a radius 'a' and the maximum linear dimension of the antenna was set to '$2a$' including its image. The spatial treatment of antenna was used by Chu to establish the lower bound on the Q for an electrically small linearly polarized antenna of a given size as [38]:

$$Q = \frac{1}{(ka)} + \frac{1}{(ka)^3}, \tag{2.12}$$

This chapter adopts the definition of electrically small antennas as [38]:

$$ka < 1, \tag{2.13}$$

where, $k = 2\pi/\lambda$ is the wavenumber and 'a' is the radius of the smallest sphere that encloses the antenna, the host vehicle platform and their image.

Most vehicular HF OTM antennas are electrically small in the lower HF band due to size constraints. Consequently, they tend to be narrowband and have very small radiation resistance leading to low radiation efficiency. Increasing their bandwidth while keeping efficiency as high as possible is thus a challenging engineering problem.

2.1.6 Numerical Tools

Since the performance of the electrically small antenna is influenced by different types of losses, the antenna, vehicle body and grounds need to be considered carefully during the design process. For accurate loss analysis, the vehicular body is made of steel (electrical conductivity $\sigma_{steel} = 1.45\times10^{6}$ S/m) while the antenna structure is made up of copper (electrical conductivity $\sigma_{copper} = 5.93\times10^{7}$ S/m). Range of lossy grounds are modeled with parameters given in Table 2.2 [39]. The real part of permittivity for the dry ground used for modeling is ε_r = 2.5 and its electric conductivity is $\sigma = 10^{-4}$ S/m. For the wet ground, the real part of permittivity used for modeling is ε_r = 35 and its electric conductivity is $\sigma = 10^{-2}$ S/m. The

TABLE 2.2

Parameters for grounds used in the analysis

Ground	$Re\ (\varepsilon_r)$	σ, $[S/m]$
Dry	2.5	0.0001
Wet	35	0.01

antenna is made up of 5 cm thick wire for this study. In all cases, the antenna corners are modeled with a 0.1 m (4 in) radius of curvature to accommodate for cable routing.

2.2 Inverted-L Antenna

The theory of inverted-L antenna was proposed by Harrison in 1958 [40]. The treatment of the Inverted – L antenna as a transmission line was introduced by King, et al. in 1960 [41]. They showed the approach towards a circuit level analysis of the inverted-L antenna in the form of a transmission line loaded with a shunt driven element placed at one of its ends. A simple analysis of the inverted-L antenna with the consideration of its image

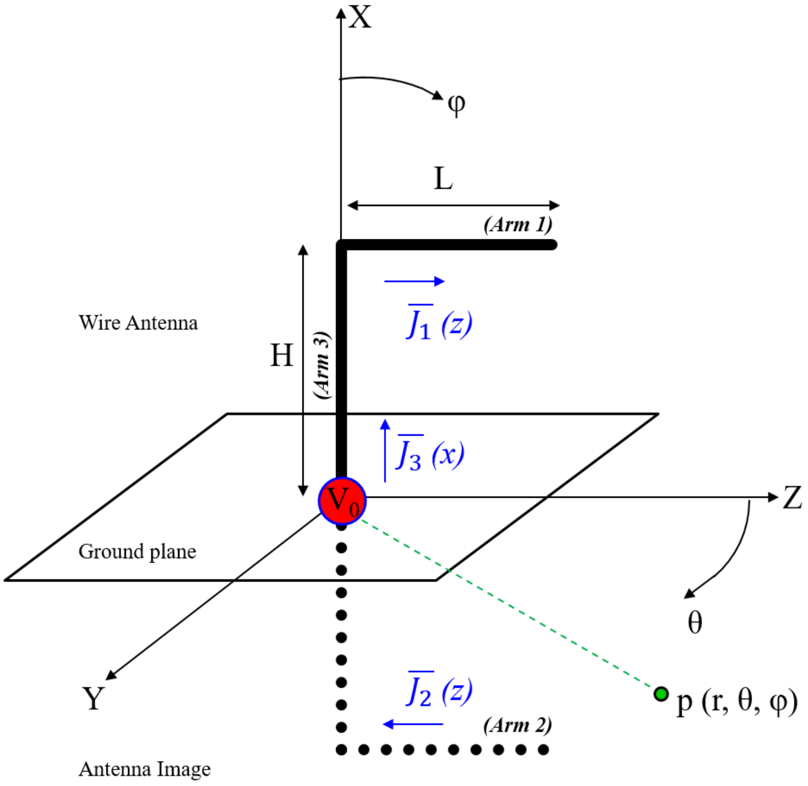

Figure 2.9: Simple model of the inverted-L antenna placed over a ground plane.

formed below the ground was shown by Fujimoto, et al. in 1987 [42]. The model of the inverted-L antenna considered for this analysis is shown in Figure 2.9.

The vertical element of the inverted-L antenna with an arbitrary height *'H'* is fed against the ground and oriented along the X axis. The folded section of the antenna arm with a length *'L'* forms the overhanging capacitive load and is oriented along the Z axis. The antenna image is formed below the ground plane and is represented with a dotted line in the illustration. The currents flowing on the folded section of the antenna and its image; viz arm 1 and arm 2 are in the opposite direction. The current distributions on each of the antenna arms are considered to be sinusoidal at resonance. The respective currents for each arm can be represented as:

$$J_1(z) = J_z \, sin\,[k(L - z')]\, cos\,(kH)\, \hat{a}_z\,, \tag{2.14}$$

$$J_2(z) = J_z \, sin\,[k(L - z')]\, cos\,(kL)\, (-\hat{a}_z)\,, \tag{2.15}$$

$$J_3(z) = J_z \, cos\,(kx')\, sin\,(kL)\, \hat{a}_x\,, \tag{2.16}$$

where, *'k'* is the wavenumber. Using the above described current distributions, the field contribution from each arm can be expressed by calculating its magnetic vector potential A [42]. Using the magnetic vector potentials, the current and field distribution information, the normalized pattern factors for the three planes can be found.

The normalized pattern factors for E_θ are represented with the appropriate mathematical expressions as given below:

In the XY plane,

$$F(\phi) = \ cos\ \phi\ , (From\ arms\ 1\ and\ 2) \tag{2.17}$$

In the YZ plane,

$$F(\theta) = \ 0\ , (From\ arms\ 1\ and\ 2) \tag{2.18}$$

In the XZ plane,

$$F(\theta) = cos\left(\frac{\pi}{2}cos\theta\right) + j\left(sin\left(\frac{\pi}{2}cos\theta\right) - cos\theta\right), \\ (From\ arms\ 1\ and\ 2) \tag{2.19}$$

Similarly, the normalized pattern factors for E_{ϕ} are:

In the XY plane,

$$F(\phi) = \ sin\ \phi\ , (From\ arm\ 3) \tag{2.20}$$

In the YZ plane,

$$F(\theta) = 1\ , (From\ arm\ 3) \tag{2.21}$$

In the XZ plane,

$$F(\theta) = \cos\theta, (From\ arm\ 3) \tag{2.22}$$

The corresponding radiation patterns for the inverted-L antenna obtained from the pattern factors represented above are shown in Figure 2.10. The radiation patterns are omnidirectional in the azimuthal plane and resemble that of a monopole in Y-Z and X-Y plane. Two E_θ components are generated, one by arm 1 and 2 and another by arm 3. These components vary in phase and in magnitude accordingly for corresponding variation in θ and ф. When these two aforementioned electric field components combine, the resultant electric field pattern results in a pattern that is close to omnidirectional in nature [42].

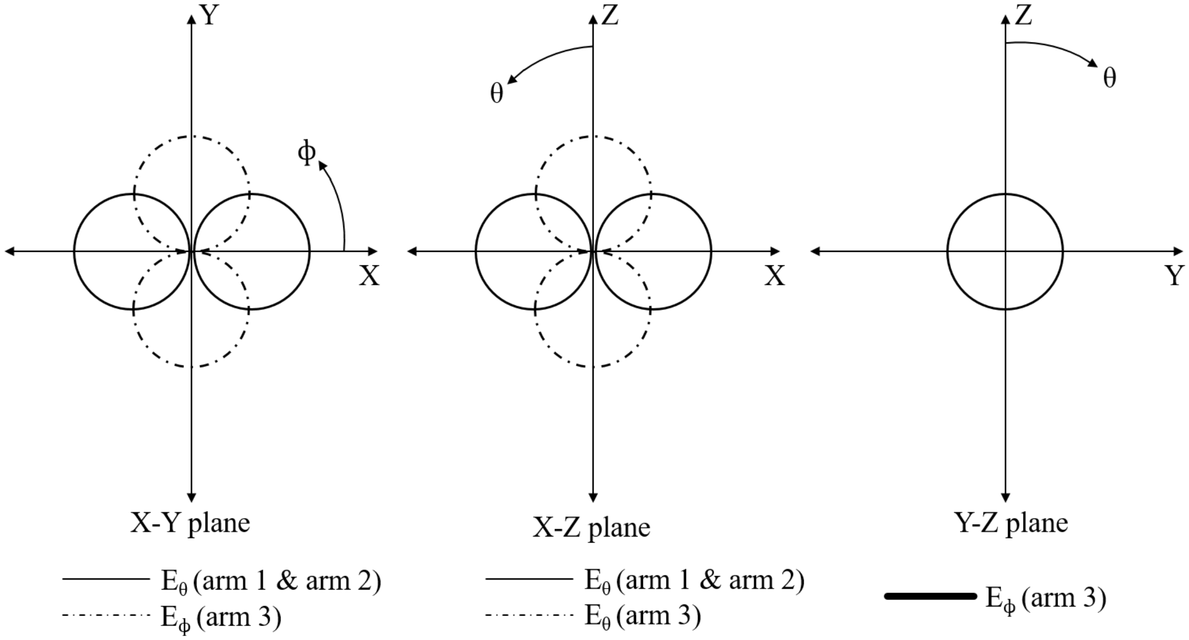

Figure 2.10: Inverted-L antenna patterns from the fundamental analysis of the case presented for the antenna placed over a ground plane.

The analytical approach shown above is based on the consideration that the inverted-L antenna height is small compared to the wavelength. It must be noted that the radiation pattern of the inverted-L antenna changes accordingly as the ratio of H/L is varied [43]. The antenna supports a predominantly vertical monopole type pattern for high H/L ratios where contribution from the vertical section *'H'* is greater than that of the horizontal section *'L'*. Conversely, the antenna has a predominantly horizontal dipole type of pattern for lower H/L ratio. The use of this property will be extensively exploited in the following studies and design processes to favor NVIS type patterns from the inverted-L antenna while maintaining decent support for long range sky wave and ground wave modes of operation over a wide range of frequencies in the HF band.

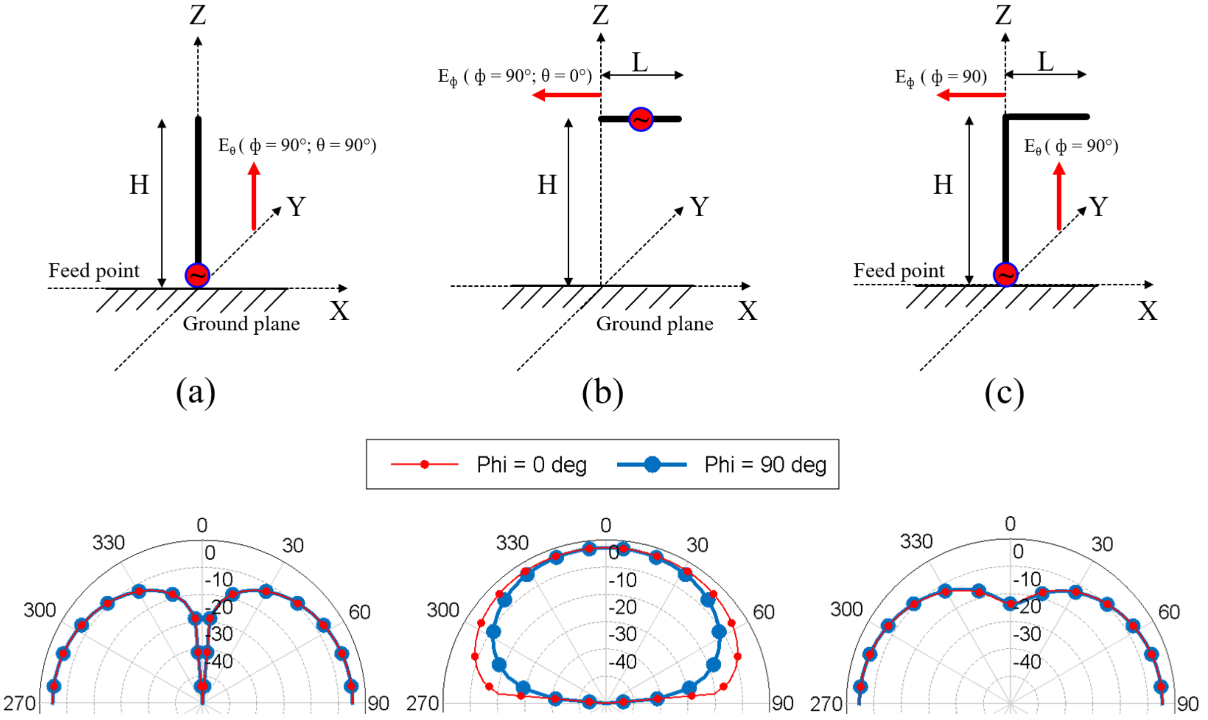

Figure 2.11: The inverted-L antenna pattern expressed as contribution from the monopole component and the horizontal dipole component over an infinite PEC ground [43]. H/L ratio of 3 is used for this illustration. (a) The monopole pattern contribution to the inverted-L radiation pattern from the vertical arm, (b) The patch antenna type contribution from the horizontal arm, (c) Pattern supported by the inverted-L antenna as a combination of the patterns supported by the vertical and horizontal arms.

Figure 2.11 shows the contributions of the individual arms towards the total radiation for an antenna with an H/L ratio of 3. This proves that by choosing the appropriate H/L ratio, we can engineer the patterns of the inverted-L antenna to suit our needs [43]. The pattern can be made to favor either a monopole, an isotropic radiator in the azimuthal plane or a patch type radiation.

The analytical approach for investigating the impedance characteristics of the inverted-L antenna was laid down by Wunsch in 1996 [44]. The impedance of an electrically small inverted-L antenna with the criterion of 'kH' < 0.5 and 'kL' < 0.5 is explained using Pocklington's integral equation and the integral of the far field Pointing vector. Both these approaches assume a known current distribution on the antenna arms.

The current established on an electrically small dipole is distributed along the length of the antenna as we move away from the feed with an almost triangular current distribution. The general assumption that this current distribution holds good for the inverted-L antenna is based on the continuity equation where the currents on the ends of the antenna arms must be equal to zero. Thus, the currents can be represented as:

$$I_z\,(Z) = I_0\left(1 - \frac{|z|}{H+L}\right), for - H \leq Z \leq H \tag{2.23}$$

$$I_x\,(x) = \pm I_0\left(1 - \frac{x - a + H}{H+L}\right), for\ a \leq x \leq L + a \tag{2.24}$$

where, 'a' is the radius of the wire forming the antenna arms, 'H' is the vertical height and 'L' is the horizontal length of the bent section of the antenna. The Pocklington equation uses a phasor vector potential **A** from the known currents [45]. Using the Pocklington equation and some algebraic operations shown in [44], we arrive at the resistance of the inverted-L antenna which is expressed as:

$$R_L\,(\Omega) = 15(kH)^2\left(2 - \frac{H}{H+L}\right)\left[2 - \frac{10}{9}\,\frac{\left(H^2 + \frac{3}{5}\,L^2 + \frac{6}{5}\,HL_a\right)}{(H+L)^2}\right], \qquad (2.25)$$

where, 'L_a' = L + a. For test of consistency, if we set L = 0, the input resistance can be represented as:

$$R_L\,(L=0) = 10(kH)^2\left(1.\overline{33} - \left(\frac{2a}{H}\right)\right), \qquad (2.26)$$

The input resistance of an infinitesimally small monopole is represented as:

$$R_M = 10(kH)^2\,, \qquad (2.27)$$

this means that the formula for the input resistance of an inverted-L antenna has a small deviation from the formula for infinitesimally small dipole for the special case of L = 0, and that the discrepancy is dependent on the value of the ($2a/H$) term.

The input resistance of the inverted-L antenna derived using the far-field Pointing vector used to extract the total radiated power from the antenna is given as [44]:

$$R_{LP} = 40(kH)^2\left(1 - \left(\frac{1}{2}\right)\frac{H}{H+L}\right)^2, \qquad (2.28)$$

this expression is independent of the wire radius *'a'* used to make the antenna arms. For the special case of L = 0, this expression for the input resistance of an inverted-L antenna converges to the input resistance for an infinitesimally small dipole. It is worth noting that the input resistance of the inverted-L antenna will be equal to the radiation resistance of the antenna for a lossless case. In both the Pocklington approach and the far-field Pointing vector approach, the input resistance of the antenna is proportional to the square of the electrical height of the monopole represented by the factor $(kH)^2$. Thus, the input resistance for an electrically small, low profile inverted-L antenna will be small. The addition of the folded horizontal, overhanging arm to the vertical arm improves the input resistance of the inverted-L antenna when compared to a monopole of the same height. The addition of the horizontal section also reduces the reactance of the antenna compared to the monopole case, making it potentially easy to match in the use case adopted in this research.

Offset feeding can be used as a technique to change the ratio of the voltage and currents at the feed. It improves the current density on the horizontal section of the antenna when compared to a base fed inverted-L antenna and it enhances the contribution of radiation from the horizontal section of the antenna to help direct more energy towards the zenith [46] [47]. The inverted-L antenna resonates for a total length (H+L) equal to a quarter of a wavelength at the desired frequency of operation. When such a quarter wavelength inverted-L antenna is fed at its base against the ground, there is high current flow at the feed location as the currents travel outwards from the feed into the ground and onto the resonant length of the antenna. By translating the feed to a location on the vertical or horizontal arms of the antenna, the currents flowing at the feed reduce in magnitude as compared to the base fed case since they are bounded by the continuity equation at the end of the antenna arm. Consequently, this helps to improve the input resistance of the antenna and makes it easier to feed and match. It must be noted however, that introducing offset feeding to the antenna improves the input impedance of the antenna but does not help in miniaturizing the antenna in any way or does not alter the quarter wavelength resonance frequency of the antenna.

2.2.1 Antenna Overview

The inverted-L antenna proposed herein has both, lower profile, and simplified vehicle grounding requirements. Improved performance is accomplished by using two arms and offset feed, so that the antenna name is two arm offset fed inverted-L antenna which is abbreviated as TAO-ILA. Typically inverted-L antennas possess nulls at zenith in radiation patterns, which is not desirable for NVIS communication. Herein, the null at zenith is significantly reduced by using offset feed and long horizontal antenna section. The offset feed improves current density on the horizontal sections, and thus facilitates stronger radiation

TABLE 2.3

Comparison of the state of the art inverted – L antennas with proposed antenna

Performance Parameter	ILA [47]	Aircraft ILA [48]	Broadband PILA [49]	DFILA [50]	TAO-ILA (This Work)
Frequency	2.45 GHz	20 MHz	2.75 GHz	2.4 GHz	3 MHz
Bandwidth (%)	2.71 $^{@}$	51.5 *	50 $^{@}$	40 $^{@}$	0.8 $^{@}$
Electrical size on platform '*ka*'	1.72	6.3	13	1.67	0.28
Electrical height	λ/30	λ/50	λ/10	λ/4.7	λ/400
Electrical length	λ/4	λ/17	λ/17	λ/4.3	λ/13
Gain (dBi)	4.14 (peak)	1.75 (peak)	0 (peak)	3.24 (peak)	-20 ┼; -14 (peak);
Mounting Platform Size	2 λ × λ	1.5 λ × 1.3 λ	3λ × 3λ	λ/2.6 × λ/4.3	λ/13 × λ/31

*VSWR 6:1 @VSWR 2:1 ┼Zenith gain

at zenith direction. Two arms improve bandwidth and enhance mechanical robustness. In recent times, many designs were published with the inverted-L antenna for various applications. A summary of reported performance figures of inverted-L antennas compared to the TAO-ILA is shown in Table 2.3. The antennas chosen for comparison include reported compact designs of inverted-L antenna on an aerial platform [48], planar inverted-L antenna [49] and wire inverted-L antennas [47] [50]. As seen from the comparison in Table 2.3, vehicle mounting constraints and low-profile requirement make the proposed antenna to be smallest in terms of the electrical size and profile. Clearly, very small size and profile force the antenna to be narrowband with low realized gain when compared to other electrically large antennas reported in literature, and this makes antenna design to be extremely challenging.

2.2.2 Fundamental Limits

The minimal quality factor 'Q' supported by a lossless, electrically small antenna with a given fractional bandwidth 'BW' and center frequency 'f_o' can be derived from the expression for bandwidth estimate shown in [51]:

$$Q_{min} = 0.71\left(\frac{f_o}{BW\ (10\ dB)}\right), \qquad (2.29)$$

where, 'f_o' = 3 MHz and BW(10 dB) is the 10 dB impedance bandwidth (VSWR 2:1). The size of an antenna can be based on one of the known fundamental limits equations. For the purposes of this work, we use the expression laid down by Gustaffson et al. [52] [53]:

$$Q \; = \left(\frac{1.5}{(ka)^3 \; \gamma_1^{norm}}\right), \tag{2.30}$$

plugging the value of 'Q_{min}' in the above expression, we can arrive at the minimum physical antenna size 'L_{min}' that is required to support the desired bandwidth criterion as:

$$L_{min} = \; 2a = \frac{\lambda}{\pi}\left(\frac{1.5}{Q_{min} \; \gamma_1^{norm}}\right)^{\frac{1}{3}}, \tag{2.31}$$

The summary for the results of minimum physical antenna size required to support 3 kHz and 24 kHz bandwidth at 3 MHz for lossless antennas with form factors corresponding to a solid sphere, a loop and a dipole are listed in Table 2.4. From the results, it is clear that a lossless antenna would have to be impractically large to support the required bandwidth of 3 kHz at 3 MHz. The results for 24 kHz bandwidth further stress the huge size required for a lossless antenna to be able to support 24 kHz bandwidth down at 3 MHz. For instance, the minimum size of a dipole antenna to support 24 kHz bandwidth at 3 MHz is 22.2 m while the minimum size for a loop antenna to achieve the same 24 kHz bandwidth would be 13.2 m. Such large antenna sizes suggest that the lossless antennas with 24 kHz bandwidth support

TABLE 2.4

Antenna dimensions to achieve 3 kHz and 24 kHz bandwidth at 3 MHz.

Antenna Type	γ_1^{norm}	Q_{min}: 3 kHz bandwidth	L_{min}[m]: 3 kHz bandwidth	Q_{min}: 24 kHz bandwidth	L_{min}[m]: 24 kHz bandwidth
Spherical	1	710	4.1	88.75	8.2
Loop	0.24	710	6.6	88.75	13.2
Dipole	0.05	710	11.1	88.75	22.2

would be out of the realm of practicality for potential installations and operation on small vehicular platforms.

While the discussion of minimum antenna size does not consider any losses, the actual application scenarios are associated with practical losses that cannot be avoided. These losses inherently contribute to an increase in the VSWR bandwidth. They include, but are not limited to ohmic losses in the antenna and vehicle body, losses due to the ground and matching network and the losses from other impacts and contributions from the antenna environment. It is hence imperative to consider a fundamental approach for the antenna with the inclusion of losses to move towards a more practical consideration of our problem. By

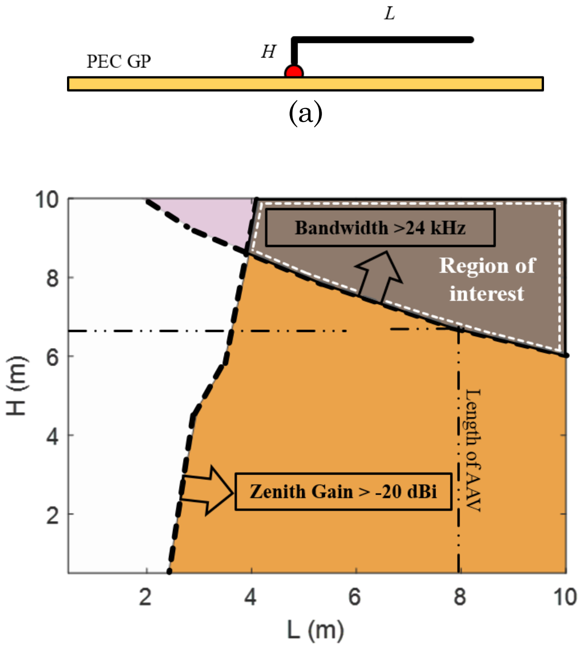

(a)

(b)

Figure 2.12: Antenna performance for lossless case over PEC ground with variation in height and length of the folded section: (a) geometric representation of the parametric setup, (b) Parametric region of interest where the antenna satisfies both the bandwidth and gain criteria. Antenna height and length are limited to 10 m. (λ/10 at 3 MHz) for this analysis.

including the impact of losses on the fundamental performance of the antenna, we can set realistic performance expectations thereafter.

To verify if a lossless inverted-L antenna can achieve the required performance over an infinite PEC ground, the parametric study for varying the antenna size is performed by means of method of moments (MoM) code Altair FEKO [1]. An inverted-L antenna is formed from a simple monopole by folding part of the monopole orthogonal to its vertical height to introduce a capacitive load as shown in Figure 2.12 (a). This capacitive load helps to improve antenna radiation resistance and bandwidth when compared to a regular monopole of the same vertical height [41] [44]. The antenna tuned bandwidth is estimated based on the untuned input impedance [51]. The variation of antenna bandwidth and the zenith gain for various antenna heights (H) and the lengths of the bent segment (L) are shown in Figure 2.12 (b). Zenith gain is considered as a design parameter as it impacts the NVIS link quality. The study is conducted at 3 MHz, where the antenna is electrically the smallest. The wire thickness is maintained at 5 cm which compares to that of most commercially available HF whips [54] [55]. Clearly, in lossless case the antenna should be tall to have bandwidth wider than 24 kHz and gain higher than -20 dBi. For example, when $L = 8$ m (AAV length), the antenna should be at least 6.5 m tall to satisfy gain and bandwidth requirements. For shorter platforms, the required height should be even higher. Such lossless, tall antennas with long folded sections would not be structurally stable and they therefore prove to be impractical for vehicular deployment.

With an assumed highest profile of antenna over the AAV platform as 1 m, the size of the Chu sphere that encompasses the antenna and the vehicle is ≈ 4.7 m. This size would correspond to an electrical size of 'ka' ≈ 0.3 at 3 MHz. The product of fractional bandwidth 'B' and linear efficiency 'η' for a lossy antenna is given as [56]:

$$(B\eta)_{max} = \frac{1}{\sqrt{2}\,Q}, \qquad (2.32)$$

The Q factor for an inverted – L antenna is given as [57]:

$$Q = \frac{6\left\{\left[ln\left(\frac{H}{r}\right) - 1\right] + L\left[ln\left(\frac{2L}{r}\right) - 1\right]\right\}}{k^3H^2(H+L)^2}, \qquad (2.33)$$

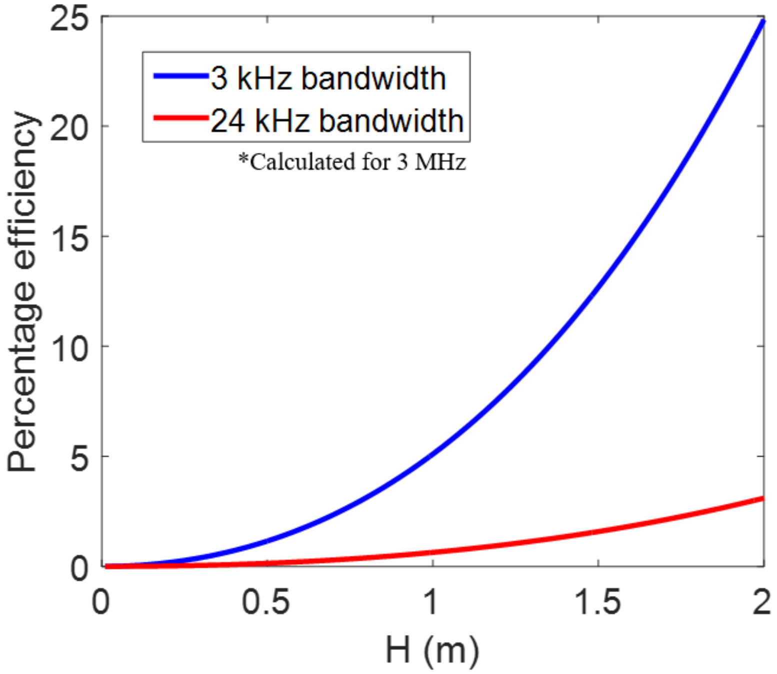

Figure 2.13: Calculated efficiency for an inverted-L antenna to support 3 kHz and 24 kHz bandwidth with varying antenna profiles. The antenna is made from wire of radius 2.5 cm and the length of horizontal section of the antenna ‘L’ is kept at 8 m for this study.

where, '*H*' is the antenna profile, '*L*' is the length of the horizontal section, '*r*' is the radius of the antenna wire, and '*k*' is the wave number. A study of the percentage efficiency for the antenna with corresponding change in its vertical height '*H*' for L = 8 m, is shown in Figure 2.13. Keeping profile H = 1 m, the length of horizontal section L = 8 m, and wire radius r = 2.5 cm, we can see that the antenna efficiency should be 0.6% to support 24 kHz bandwidth at 3 MHz. Note that in the legacy case, when bandwidth is 3 kHz, the same antenna structure will need to be 5% efficient, which is 8 times higher efficiency when compared to the 24 kHz case. Such low efficiency figures indicate that antenna gain will be very low to support the desired bandwidth. Low efficiency also indicates that accurate loss analysis is critical for the antenna design.

For practical vehicular deployment, ohmic losses in antenna and platform together with losses in grounds are unavoidable. In addition, electrically small antennas require tuners (couplers) to operate over a wide frequency range. The tuner losses impact system performance and must be included in the design analysis. Consequently, a design parameter referred to as 'effective tuner resistance' is introduced, which accounts for the tuner losses in the form of a series resistance modeled at the feed point of the antenna. It is important to recognize that the effective tuner resistance is a means to facilitate antenna design. However, it can be used to estimate the associated tuner loss, and thus sets the design guidelines for tuners for low profile wideband HF OTM antennas [58].

2.3 Antenna Evolution

The evolution of the proposed design of the inverted-L antenna from a simple whip is shown in Figure 2.14 (a). Typical HF whips have 5 or 10 m profile and cannot be used for OTM operation. To support NVIS communication and reduce profile, whip antennas are

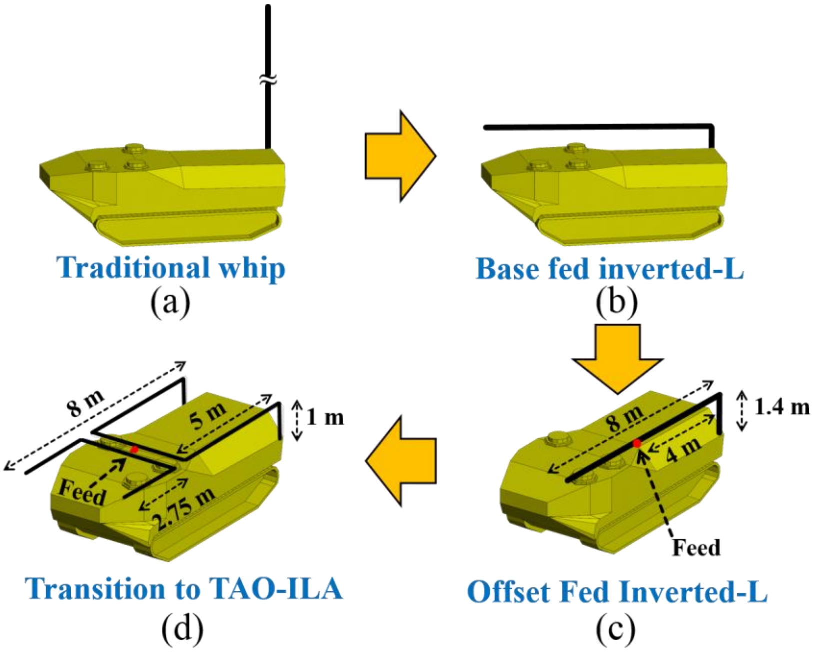

Figure 2.14: The step by step design evolution of the antenna from a traditional whip concept to the two arm offset fed inverted – L antenna. (a): Traditional whip antenna shown mounted on the AAV, (b) Transition to a base fed inverted-L configuration, (c) Introduction of offset feed with single arm inverted-L antenna, (d) Proposed two arm offset fed inverted-L antenna design.

physically bent and secured into horizontal orientations [59]. Tilting the whip orthogonally to its vertical section above the vehicle yields a simple base fed inverted-L (Figure 2.14 (b)). With offset feed, impedance match can be improved, and in addition, the feed location on the horizontal section of the antenna makes horizontal current density more uniform, therefore improving zenith gain (Figure 2.14 (c)). Introducing the second arm effectively increases antenna volume, leading to better bandwidth performance (Figure 2.14 (d)). Herein, a parametric study of the antenna gain and bandwidth values against changing profile and feed location is described to evaluate the performance of the antenna for NVIS operation.

2.3.1 Single Arm Inverted-L Antenna Configuration

Gain at zenith and bandwidth of the single arm inverted-L antenna mounted on AAV is evaluated at 3 MHz for different profiles and offset feed locations (Figure 2.15). The horizontal length of the antenna is kept at 8 m, which corresponds to the length of AAV. Antenna performance is reported in terms of the minimum antenna profile required to achieve the desired 24 kHz bandwidth and gain of -20 dBi. The study is performed over dry, wet and PEC grounds, and the worst case results are shown. As seen, the antenna satisfies the performance criteria with a profile higher than 0.625 m (λ/150 @ 3 MHz), and thus this configuration satisfies the desired study objectives. However, it is beneficial to have as low a profile as possible to facilitate improved vehicle maneuverability and reduced visual signature during operation.

2.3.2 Two arm Offset fed ILA Configuration

Two arms make the antenna effectively larger, and thus help to improve its bandwidth performance [60]. Geometry of this configuration is shown in Figure 2.16. The decision of using two arms is based on the reasons of practicality. Increased number of arms with offset feed pose severe obstructions on the AAV roof where the cargo loading doors are located and make the antenna impractical. Consequently, a practical two arm design wherein the two arms run along the edge of the vehicle is adopted. The analysis is performed using a similar parametric study as described for a single arm case (Figure 2.16). Clearly, with two arms the antenna profile can be reduced to 0.25 m. In this way, the profile is reduced by 63% compared to the single arm configuration. The antenna satisfies set gain and bandwidth requirements, when feed is offset by 5 m from the rear of the vehicle and the effective tuner resistance is 5 Ω.

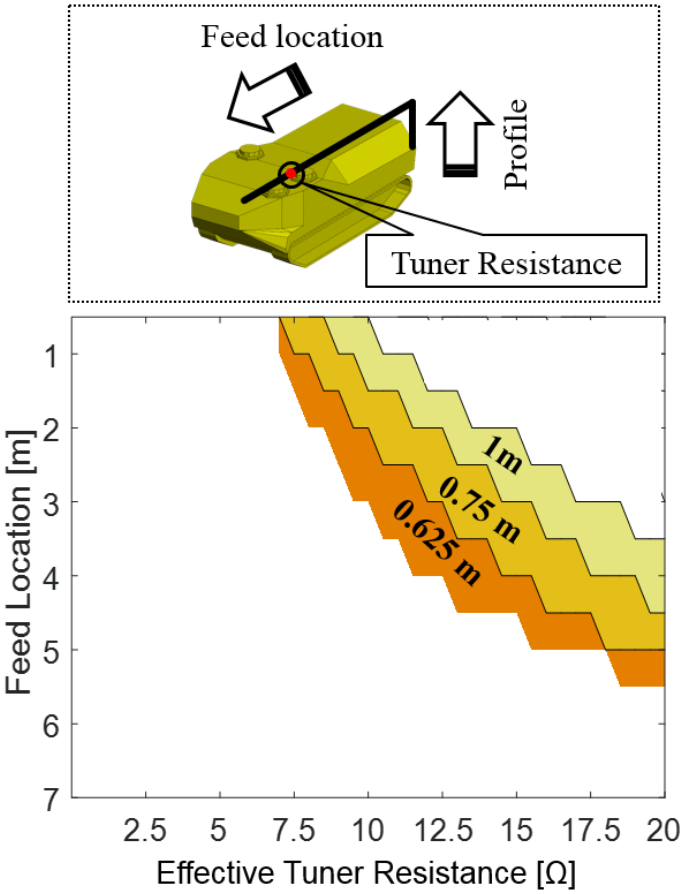

Figure 2.15: Parametric study results for a single arm inverted – L antenna having gain at zenith better than -20 dBi and 24 kHz bandwidth. The results indicate that the single arm antenna requires a minimum profile of 0.625 m in the worst case above dry, wet and PEC grounds. Inset above shows geometrical modifications considered in this study.

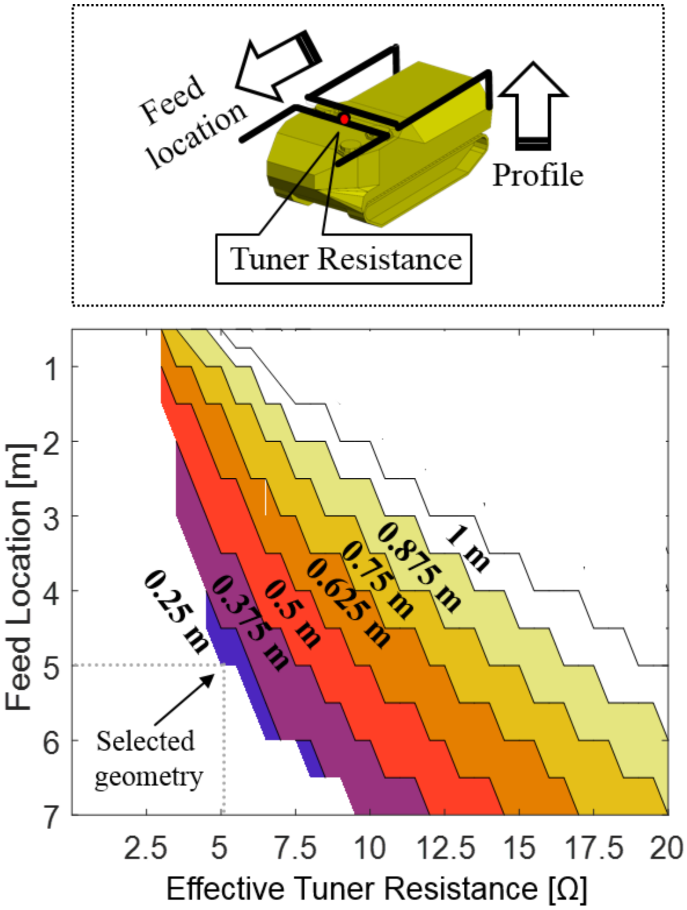

Figure 2.16: Parametric study results for proposed TAO-ILA satisfying gain criterion of better than -20 dBi and 24 kHz bandwidth. The results indicate that the TAO-ILA requires a minimum profile of 0.25 m in the worst case above dry, wet and PEC grounds. Inset above shows geometrical modifications considered in this study.

2.4 Antenna Performance in the NVIS Range

The calculated input resistance and reactance of the TAO-ILA obtained from MoM code Altair FEKO, with the tuner effective resistance taken into account is shown in Figure 2.17 and Figure 2.18, respectively. Also shown alongside is the result for the dry ground case obtained from the finite element method (FEM) code Ansoft HFSS [2].

The antenna has a resonance at ~6.3 MHz and anti-resonance at ~9.2 MHz. As expected, the input resistance of the antenna is very small at the low frequency end and it increases with frequency where the antenna becomes electrically larger. Also, the input

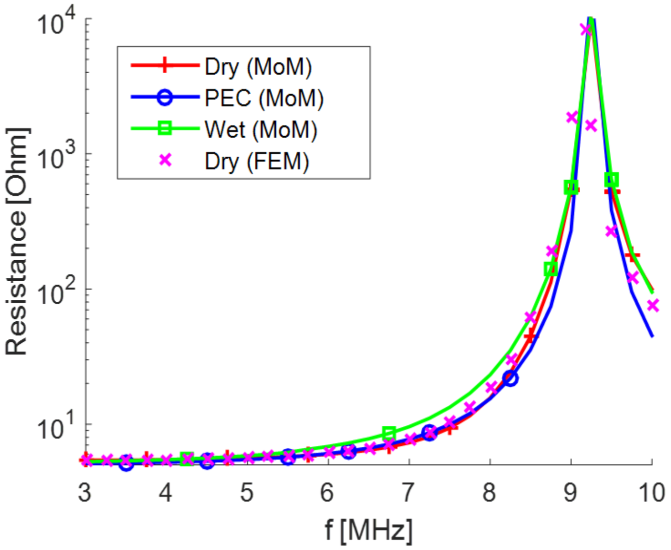

Figure 2.17: Input resistance of the TAO-ILA with 0.25 m profile and offset feed at 5 m from the rear. Additional 5Ω effective tuner resistance is taken into account.

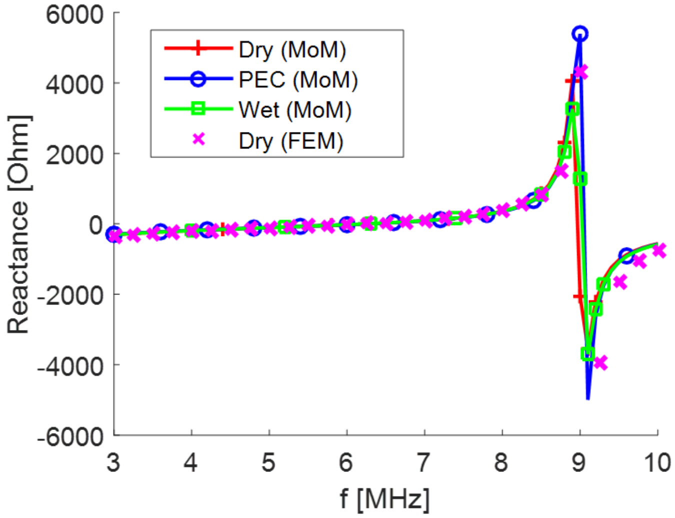

Figure 2.18: Input reactance of the TAO-ILA with 0.25 m profile and offset feed at 5 m from the rear. Additional 5Ω effective tuner resistance is taken into account.

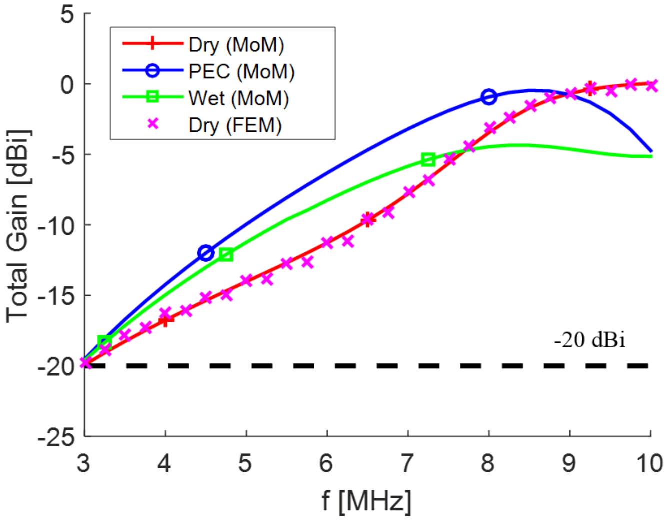

Figure 2.19: Total zenith gain for the TAO-ILA loaded with 5 Ω of effective tuner resistance. Results show that antenna is satisfying the gain criterion for all the frequencies between 3 and 10 MHz. Antenna performance over dry ground is the worst at low frequency end.

resistance profile remains consistent over different grounds which suggests that same tuning

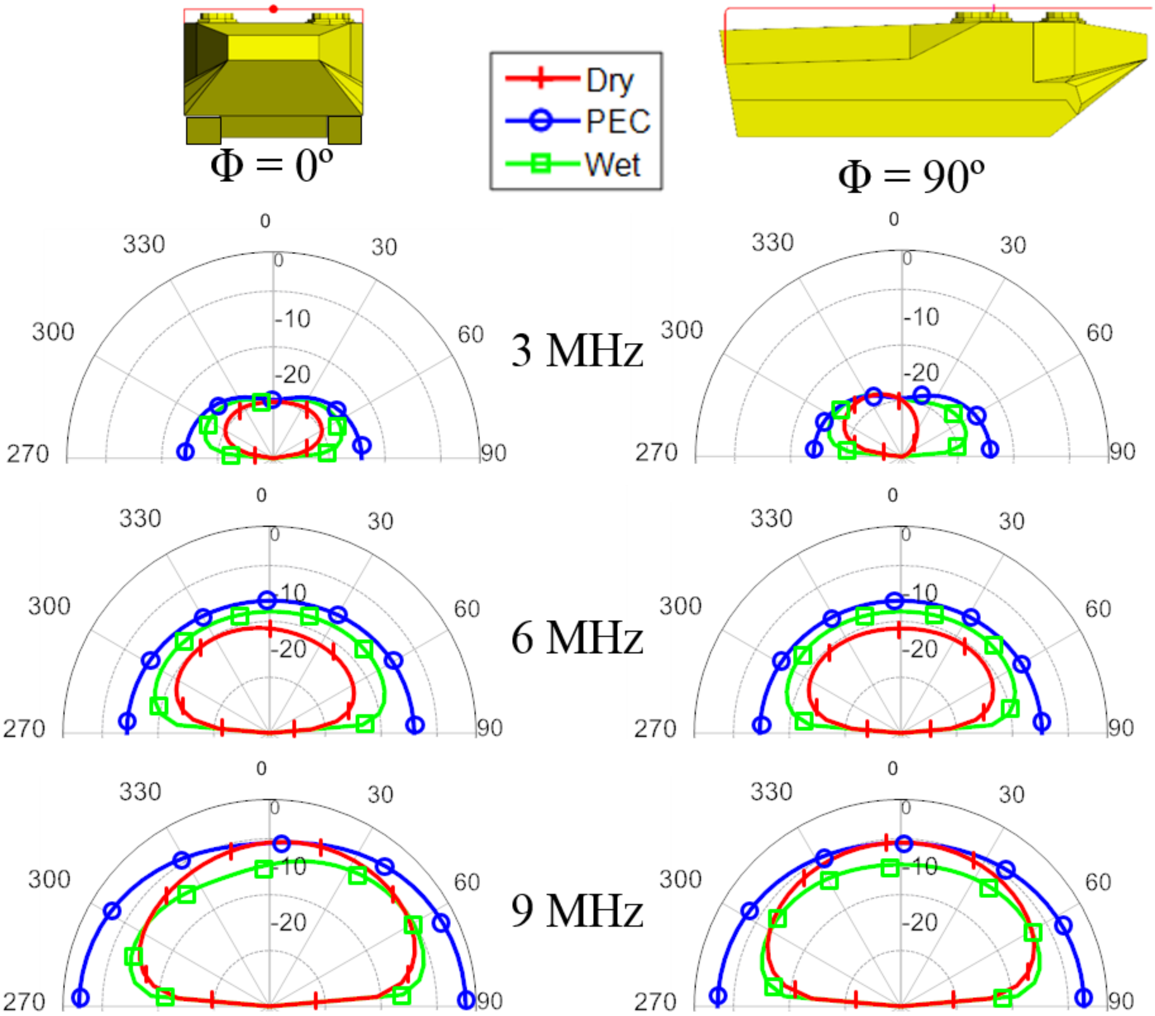

Figure 2.20: Simulated total gain patterns for the TAO-ILA over dry, wet and PEC grounds.

approach can be used to tune this antenna over different grounds.

Zenith gain result plotted in Figure 2.19 shows that the best gain performance is over PEC ground (as expected) since the ground redirects a large amount of energy towards the upper hemisphere in this case. Overall, there is very good agreement between the MoM and FEM codes for the input impedance and zenith gain shown for the dry ground case. The total gain patterns for the antenna are shown in Figure 2.20. From the patterns it can be seen that antenna favors NVIS type communication.

2.4.1 Antenna Tuning

Typically, OTM HF antennas are operated over specific frequencies in the HF band as permitted by the operational and licensing arrangements. Most of the HF antennas have a tuning element connected at the feed to tune the antenna to the desired frequency of operation. Given the electrically small size of the vehicular HF antennas, the changing environment and grounds over which they must work and the wide range of frequencies that need to be covered by these antennas, use of a tuning network is imperative. Among the possible tuning techniques, a two-element tuning network represents the simplest tuning approach.

The tuned bandwidth estimates for the TAO-ILA with real grounds are shown in Figure 2.21 along with the calculated bandwidth supported by a lossless L-matching network.

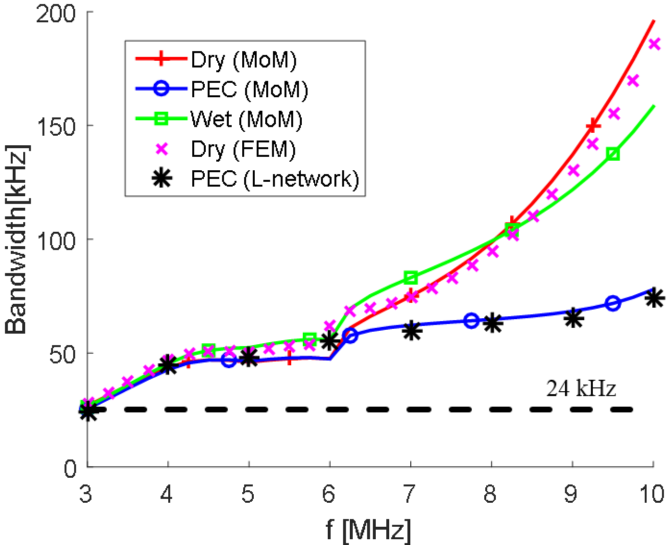

Figure 2.21: Bandwidth estimate for the TAO-ILA loaded with 5Ω of effective tuner resistance. The antenna supports bandwidth better than 24 kHz over different grounds for the entire frequency range from 3 MHz to 10 MHz.

The loss in the tuner elements is embedded in the antenna impedance with the effective tuner resistance when the lossless L-matching network is used. From the bandwidth estimates, it is clear that the antenna can support bandwidth better than 24 kHz over the entire frequency range. It can also be seen that bandwidth estimate and the bandwidth supported by the L-matching network over the PEC ground are in agreement thus validating the bandwidth estimation. It is important to note that the comparison with the L-matching network is a mere fundamental approach for validation of the bandwidth estimate. A single two element matching network will not be able to practically tune the antenna over such a wide frequency range especially when the antenna reactance changes from capacitive at the low end to inductive after the first resonance and then back to capacitive after the antiresonance. Tuning such an antenna over these reactance values as they changes across frequency is out of the scope of this work but would ideally demand for a typical three element tuning network like a T-network or a π – network as discussed in [61].

The tuner efficiency with the consideration of the effective tuner resistance 'R_T' can be given as:

$$\eta_{T(Estimated)} = \frac{1}{1 + R_T/R_A}, \tag{2.34}$$

where, 'R_A' is the unloaded antenna input resistance. For our case, the value of R_T = 5Ω. At 3 MHz, the unloaded antenna input resistance is 0.4 Ω over dry ground. The tuner efficiency is very low and estimated to be around -11.3 dB. Nevertheless, such low tuner efficiency widens the antenna bandwidth while maintaining the antenna zenith gain better than -20 dBi as desired. The measured tuner efficiency from the actual prototype can be expressed as [62]:

$$\eta_{T(Measured)} = \frac{|s_{12}|^2(1-|\Gamma_L|^2)}{|1-s_{22}\Gamma_L|^2}, \qquad (2.35)$$

where S_{12} and S_{22} are the tuner s-parameters with port 2 facing to the antenna load, and Γ_L is the antenna reflection coefficient.

2.4.2 Antenna Performance in Case of Mechanical Failure

The bandwidth and gain performance of the TAO-ILA is evaluated in the event of a mechanical failure (Figure 2.22). The analysis of mechanical failure of the TAO-ILA considers that the antenna sustains a hit at the front section between the antenna feed and the nose of the AAV or at the rear section between the feed and the mounting base as shown in **Error! Reference source not found.**. In case of the frontal impact, it is considered that the arm falls off after impact while in case of the rear section hit, the arm is electrically broken but is mechanically held in place as part of the antenna structure thereby acting as a vestigial parasitic element. Bandwidth estimate and gain at zenith are shown in Figure 2.23 and Figure 2.24, respectively. Clearly, the TAO-ILA can support communication at a reduced bandwidth but with similar gain performance even after such impact. The TAO-ILA satisfies zenith gain and wide bandwidth requirements over 96% of the NVIS frequency band in case of the front failure. For the case of rear failure, the antenna supports wider than 12.5 kHz bandwidth and zenith gain better than -20 dBi over the entire NVIS band. Consistent performance under failure thereby adds to reliability and robustness of the proposed antenna.

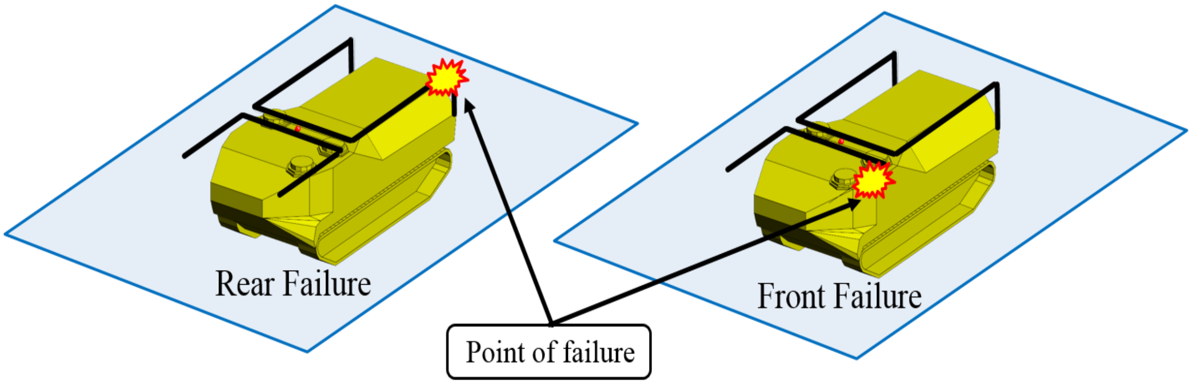

Figure 2.22: Considered cases of mechanical failure for the TAO-ILA.

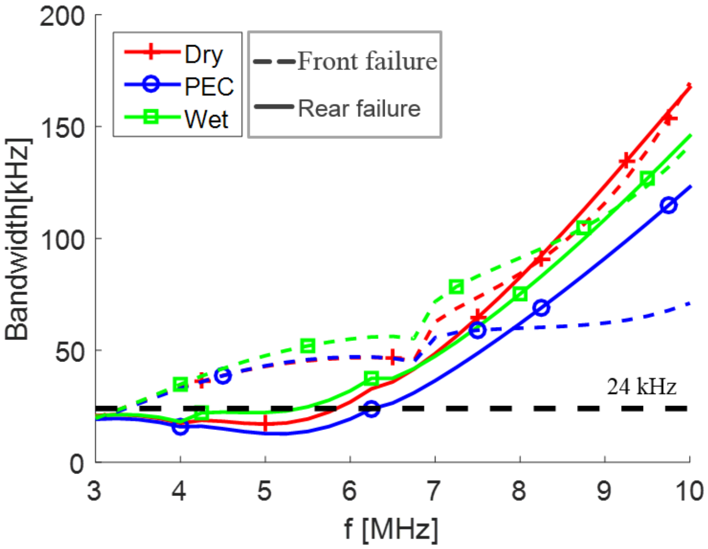

Figure 2.23: Bandwidth estimate of TAO-ILA under mechanical failure. The worst case bandwidth supported is at 5.25 MHz and equal to 12.7 kHz over PEC ground for the rear failure scenario.

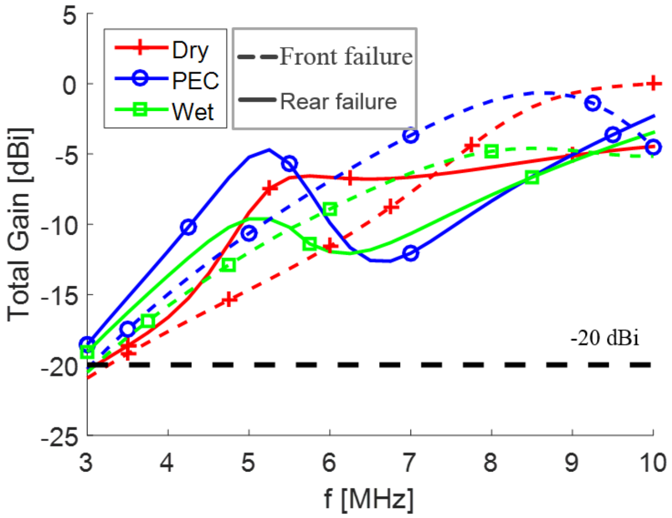

Figure 2.24: Simulated gain at zenith of the antenna under mechanical failure. From the gain performance it can be seen that the antenna supports gain of better than -20 dBi over majority of the frequency band of interest.

2.4.3 Wobble of Wave (WoW)

The omnidirectional behavior of the antenna is characterized by means of the wobble of the wave (WoW) which is defined as:

$$WoW = D_{max,dB} - D_{min,dB}, \tag{2.36}$$

where, directivity D is calculated in the pattern cut of interest. The WoW is particularly important for a vehicular HF antenna as it shows the antennas potential to support ground wave and long-range sky wave communications in all directions. As seen from Figure 2.25, the WoW of the TAO-ILA is compared to that of a legacy 9.8 m HF whip antenna mounted vertically.

The WoW comparison is made at an angle close to the horizon. We see that over dry ground, the WoW of the TAO-ILA is less than that of the whip from 5 MHz to 10 MHz. Over wet ground, the WoW of the TAO-ILA is better than of the whip from 4 MHz to 8 MHz. Thus, over majority of the frequency band, the TAO-ILA will provide similar or slightly better omni-directional coverage as compared to a whip that is routinely used for long range skywave and ground wave communications.

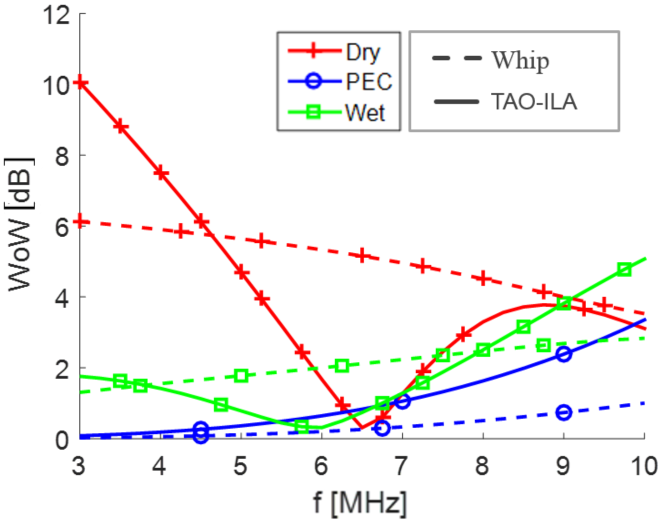

Figure 2.25: Omni-directionality of the TAO-ILA over dry, PEC and wet ground in terms of the WoW measured at 10° from the horizon and plotted across frequency. The smaller the WoW, better is the antenna in terms of omni-directional performance for ground wave and long range skywave communications.

2.4.4 Flared Antenna Arms

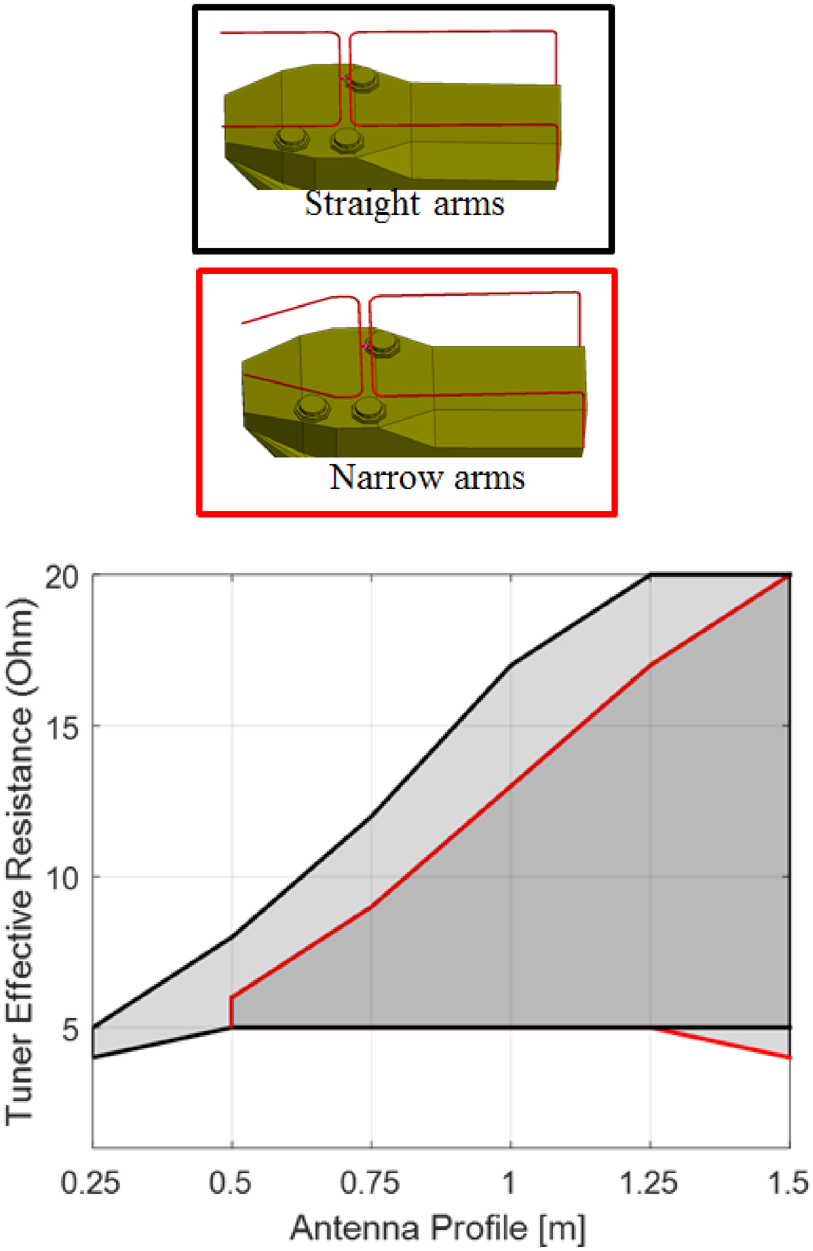

Figure 2.26: Analysis of antenna flaring and its impact on the operational range of the antenna performed at 3 MHz. We see that the antenna configuration with straight arms has a performance benefit of 0.25 m lower profile over the configuration with flared arms.

Flaring the antenna arms at the front of the AAV is studied as part of the various design aspects considered for the proposed antenna to make it more practical. The proposed antenna over the AAV has straight arms along the length of the vehicle. The antenna profile above the vehicle is given the highest importance in this design approach as the antenna profile is one of the most challenging and important parameters for practical use in this design. However, an antenna which has the arm tips at the front of the AAV bending inwards so that they match the AAV body shape may be desired under certain considerations related to operations, fleet management, stowage, shipping and deployment. It is also vital to acknowledge that from practical implementation viewpoint, any bending above vehicle top for better conformal shape may block the view of the crew through the hatches.

The antenna shape is made conformal to the AAV body by flaring the arms outwards at the front of the vehicle as we move towards the feed from the nose based on the above discussion. The results of operational range analysis for straight and flared arm configurations are shown in the Figure 2.26. As seen, the antenna configuration with bent arms achieves 24 kHz bandwidth and objective gain at zenith, only with profile of higher than 0.5 m contrasting to the 0.25 m profile of the straight arm geometry. This result is expected, since antenna with flared arms has more metal underneath forcing strong interaction between the currents on the arms and the currents on the roof of the AAV, thereby deteriorating its performance.

2.5 Prototyping and Measurements

The fabrication and testing of a full-scale HF antenna system on a vehicular platform is an expensive and time consuming process. Instead, a 50 times smaller prototype is utilized, where the vehicle is built by means of 3D printing.

2.5.1 Additive Manufacturing

The scaled AAV model is 3d printed by using fused deposition modeling (FDM) method on MakerBot Replicator 5th Generation Desktop 3D printer [63]. Accuracy of the FDM method is acceptable, while fabrication time is fast, and the cost is low. The base material used for the vehicular model fabrication is the 1.75mm diameter MakerBot PLA filament. The vehicular model for the AAV used in fabrication is sourced from the online open source repository – “3D Warehouse” [64]. The model is scaled and prepared for print in three parts [65]. Printing by parts allows for achieving better control over the quality at relatively fast print time. The non-critical features of the vehicle are eliminated. The tracks are printed as a separate part with the highest print resolution settings. The upper and the lower hull of the vehicle are printed as two separate parts with relatively coarse resolution. Printing the

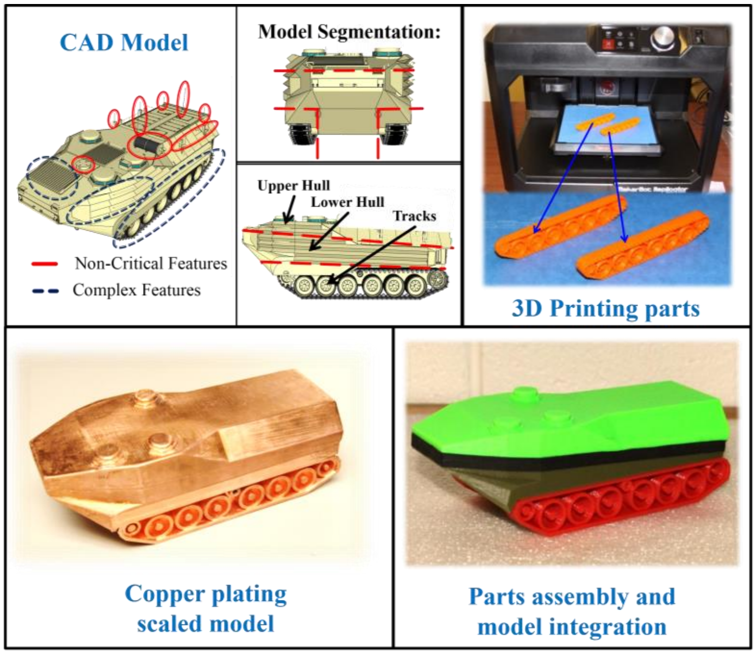

Figure 2.27: Description of the fabrication of the scaled vehicle model. The model was 3D printed by means of FDM additive manufacturing process and copper plated afterwards.

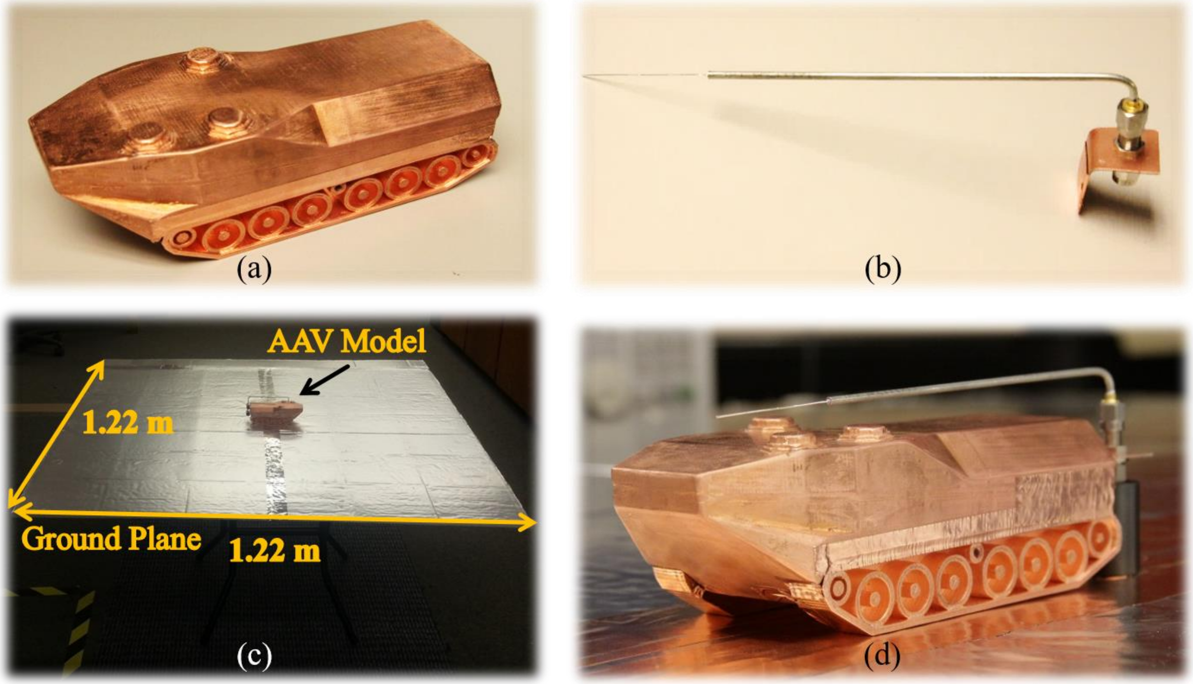

Figure 2.28: Description of the fabrication and installation of the single arm offset fed inverted-L antenna on the scaled AAV model. (a) 3D printed ad copper plated, 50 times scaled model of the AAV, (b) One arm offset fed inverted-L antenna fabricated from a 2.2 mm diameter coaxial cable, (c) Scaled model of the AAV with the single arm offset fed antenna mounted on a 1.2 m x 1.2 m (0.4 λ x 0.4 λ at f_{low}) ground plane for impedance measurements, (d) A close up photo of the single arm inverted-L antenna mounted on the scaled AAV model.

parts separately also allows for post processing and finishing on each part. Once the individual parts are finished, they are bonded together using commercial epoxy-resin mixture. The finished vehicular model is prepared for copper plating which is done using a commercial electroplating process [66]. The model is sealed before plating. Plating is done

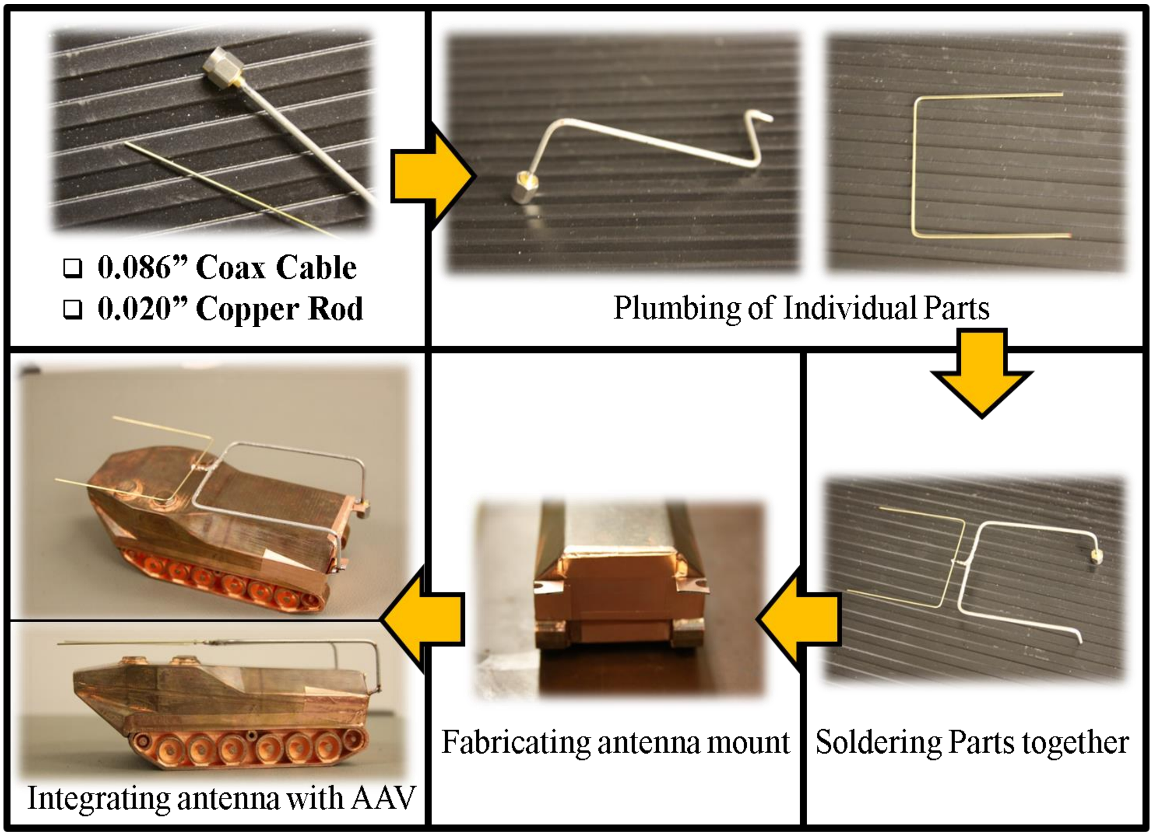

Figure 2.29: Description of the antenna integration on the vehicular platform.

using 2 ounce copper deposition per square foot. The thickness of plated layer of copper is 70 μm. The detailed additive manufacturing process to fabricate the copper plated 3D printed vehicular model is shown in Figure 2.27. The frequency range of 3-10 MHz translates to a scaled frequency range of 150-500 MHz. The skin depth at the scaled frequency range varies from 5.3 μm at 150 MHz to 2.9 μm at 500 MHz, and thus the copper thickness is much larger than the skin depth.

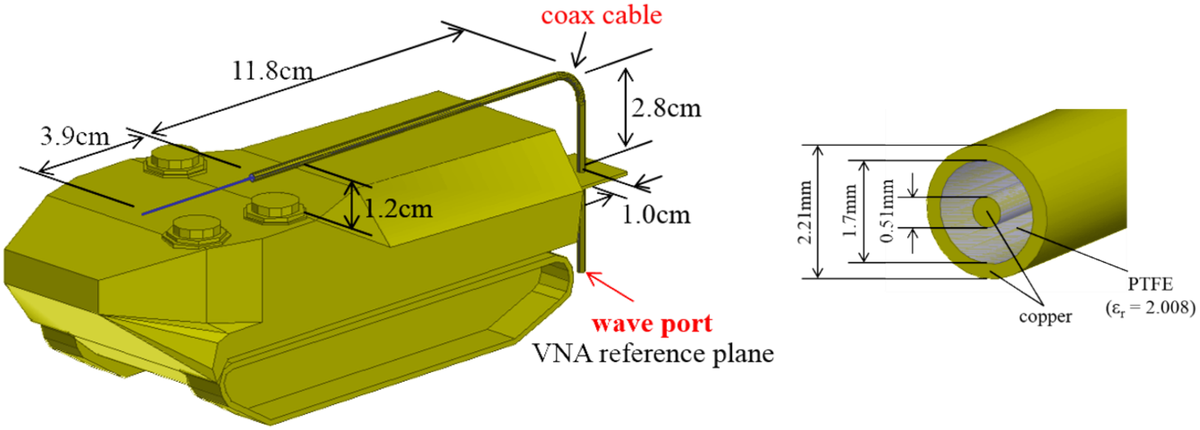

Figure 2.30: Computational model (FEM) of the single arm offset fed inverted-L antenna mounted on the AAV scaled prototype.

2.5.2 Scaled Antenna Fabrication

Scaled antenna models for a single arm offset fed inverted-L antenna as well as the more complex two arm offset fed antenna are fabricated. The single arm offset fed inverted – L model is made from a single 2.2 mm (0.086”) diameter coaxial cable. The offset feed is established by stripping the coaxial cable shield from the center conductor at the desired feed location. The scaled model for the single arm offset fed inverted-L antenna is shown in Figure 2.28. The fabrication details of the two-arm offset fed antenna are shown in detail here. The scaled antenna structure is made of sections of 2.2 mm (0.086”) diameter semi rigid coaxial cable and 0.5 mm (0.020”) diameter copper rod. The plumbing and cutting of each section of the antenna is done with precision to match the scaled dimensions as close as possible to the reference full scale design. All the individual sections are soldered together, and the complete antenna structure is tested for continuity. The antenna is then mounted on the scaled vehicular platform using custom fabricated copper mounting brackets and fastened using copper tape. The mounting bracket assembly allows for a modular setup such that multiple

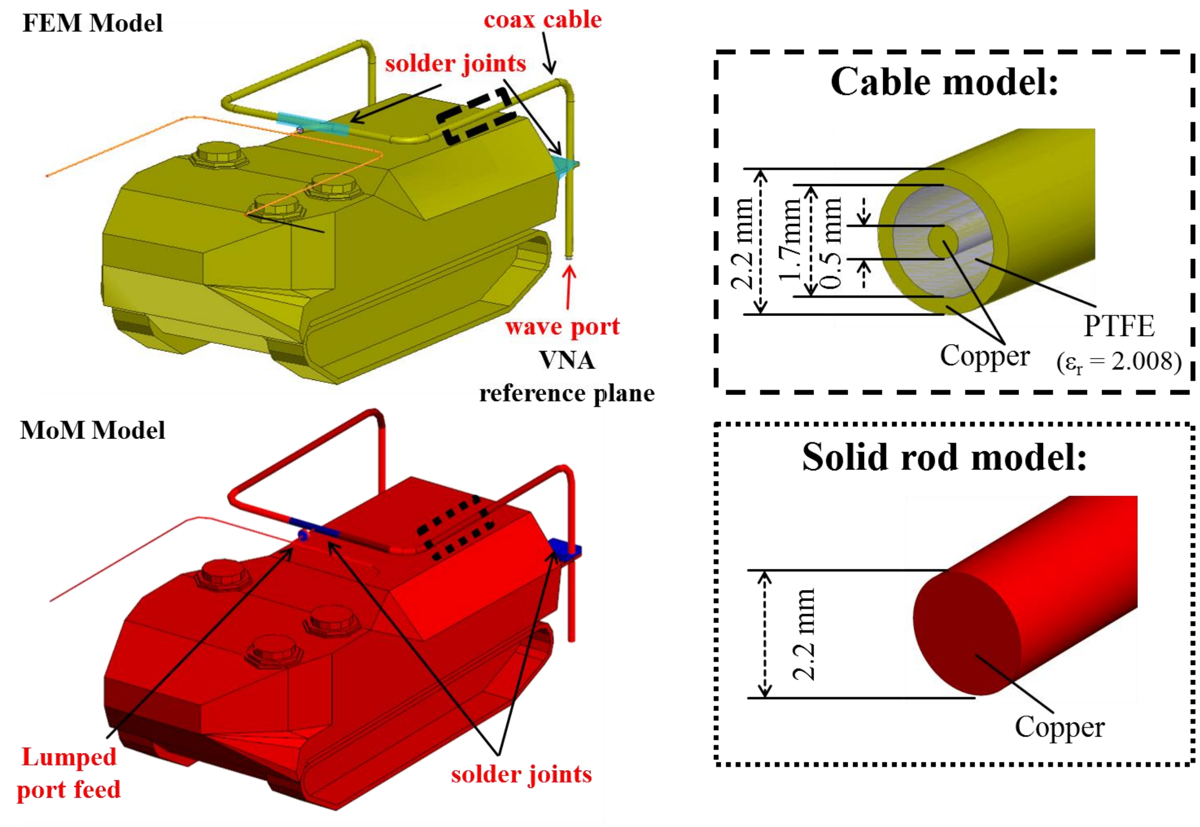

Figure 2.31: Computational models used to validate prototype measurements.

antennas can be mounted and tested on the same vehicular platform. The vehicle antenna integration is illustrated for the two arm antenna in detail in Figure 2.29.

2.5.3 Computational Modeling

The computational model for the vehicle is created using ANSYS HFSS and Altair FEKO. The details of the computational model for the single arm offset fed inverted-L antenna are shown in Figure 2.30. This model is kept computationally simple to prove the concept of offset feed using the stripped outer conductor of a coaxial cable. The detailed computational models for the scaled TAO-ILA on the AAV prototype are shown in Figure 2.31.

The vehicle is made from copper in both, FEKO and HFSS models. In the HFSS model, the antenna deployed on the vehicle is modeled out of 2.2 mm diameter copper coaxial cable and 0.5 mm diameter copper rod is used for the front section of the antenna after the feed. The soldering blobs formed at the antenna feed and the mounting brackets at the rear side of the vehicle are modeled by means of 1 mm thick solder coating layer set on the base metal that forms the solder joint. Antenna is fed with a wave port at the base of the mounting bracket and sealed with a PEC puck enclosure. This resembles the actual coaxial feed used in the measurements performed on the scaled model. In the FEKO model, wire port is used at the feed location. The vehicle and antenna is made up of copper. Solder patches are introduced at the joints. Coaxial cable of 165 mm length and 2.2 mm diameter is embedded to move the reference plane to the rear bottom side of the antenna in the results.

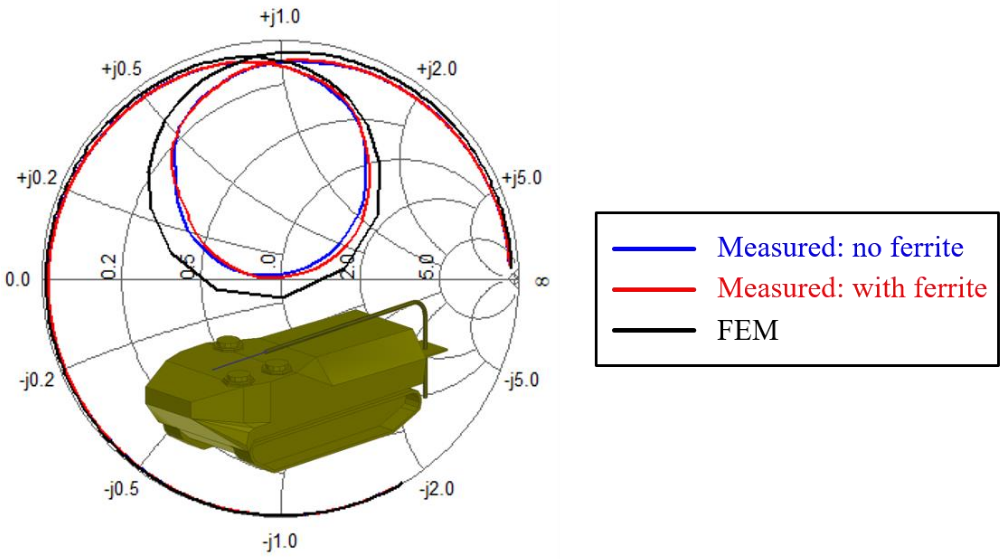

Figure 2.32: Measured and simulated impedance of the single arm offset fed scaled prototype.

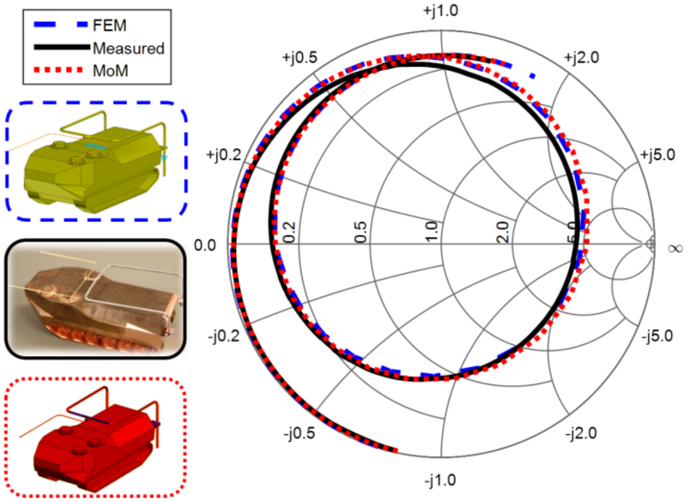

Figure 2.33: Measured and simulated impedance of the scaled prototype.

2.5.4 Impedance Measurements of Scaled Prototype

The impedance measurement of the scaled model is performed on a 1.22 m × 1.22 m square ground plane. The size of the ground plane corresponds to an electrical size of 0.4 λ × 0.4 λ at the lowest frequency of operation for the scaled prototype. The vehicle is placed in the center of the ground plane and fed through a coaxial cable from the bottom. Stable and solid electrical grounding is established by connecting the base of the vehicle and its tracks to the ground plane surface by use of copper tape. The outer shield of the coaxial cable feeding the scaled model is connected to the ground plane. Measurements with and without ferrite beads are conducted for the single arm configuration to make sure there are no return currents that may radiate from the VNA coaxial cable that feeds the antenna during the measurements. Once the stability of results with and without the ferrite beads is verified, the measurement on the two arm prototype is performed without the ferrite beads. The impedance measurement results for the single arm offset fed inverted-L antenna are shown in Figure 2.32. Good stability in the results can be seen between the measurement with and without ferrite beads. The slight difference in the FEM simulation and the measured results is attributed to small differences in the fabricated model as compared to the computational model which are later fixed in the two-arm prototype measurement as shown below.

The results of the measurement for the two-arm prototype are shown in Figure 2.33. Excellent agreement between the measurements and simulated results makes us confident in the used computational setup for such an electrically small problem. The results also establish good correlation with the physical measurement setup and demonstrate the validity of additive manufacturing process adopted for quick and cost-effective fabrication.

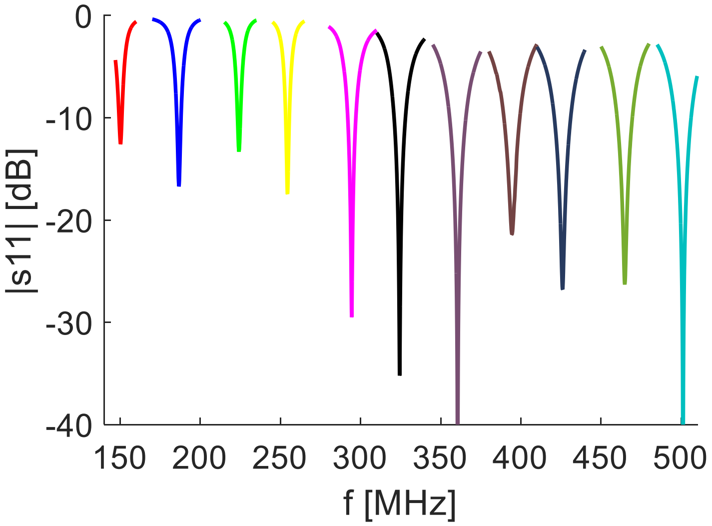

Figure 2.34: Tuned reflection coefficients obtained analytically based on measured impedance of the scaled prototype. L-matching network with COTS elements was used.

TABLE 2.5

Matching network specifications for scaled prototype

Freq. (MHz)	Tuning Inductor (nH)	ATC Part No (Q factor)	Tuning Capacitor (pF)	ATC Part No. (Q factor)	Tuned Bandwidth (MHz)
150.3	51.11	0603WL510JT (28.22 @150 MHz)	130	ATC800C131 (726 @150 MHz)	1.7
186.8	27.06	0402WL270JT (28.41 @185 MHz)	110	ATC800C111 (589.2 @185 MHz)	2.7
224.3	11.02	0402WL110JT (28.94 @220 MHz)	120	ATC800C121 (439.5 @220 MHz)	1.8
254.5	2.4	0402WL2R4JT (21.06 @255 MHz)	100	ATC800C101 (386.3 @255 MHz)	2.3
294.3	43.38	0402WL430JT (25.07 @290 MHz)	27	ATC600L270 (389.3 @290 MHz)	5

TABLE 2.5 (Cont.)

Matching network specifications for scaled prototype

Freq. (MHz)	Tuning Inductor (nH)	ATC Part No (Q factor)	Tuning Capacitor (pF)	ATC Part No. (Q factor)	Tuned Bandwidth (MHz)
324.3	51.29	0402WL510JT (19.08 @325 MHz)	11	ATC600L110 (987.3 @325 MHz)	7.1
360.5	36.42	0402WL360JT (34.77 @360 MHz)	2	ATC600S2R0 (3.77k @360 MHz)	10.2
394.5	11.06	0402WL110JT (41.04 @395 MHz)	20	ATC800R200 (698.4)	9.9
426	1	0402WL1R0JT (27.95 @430 MHz)	24	ATC800R240 (530.4 @ 430 MHz)	10.2
464.8	33.93	0805WL330JT (57.78 @ 465 MHz)	13	ATC800R130 (889 @ 465 MHz)	9.5
501.3	44.59	0805WL430JT (60.0 @ 500 MHz)	7.5	ATC800R7R5 (1398 @ 500 MHz)	10.2

2.5.5 Scaled Prototype Tuning Analysis

The plot with tuned impedance for the scaled prototype at various frequencies is shown below in Figure 2.34. Values of *L*'s and *C*'s for matching elements together with tuned bandwidth are listed in Table 2.5. Tuning studies were performed in AWR. The parameters of reactive tuning elements correspond to the respective available COTS parts listed in Table 2.5. The expected bandwidth of this prototype is better than 1.2 MHz which maps to a full scale tuned bandwidth of 24 kHz. As seen, in all cases bandwidth is wider than 1.7 MHz, which corresponds to 34 kHz for the full-scale antenna. The higher bandwidth in the prototype is due to thicker wire radius used for the antenna arms, the contributions of losses from the Q factors of the chosen tuning elements, and the addition of some losses due to the use of solder at various antenna interfaces.

It is important to note that wide impedance bandwidth can be easily achieved by introducing loss at the expense of reduced radiation efficiency. However, the work highlighted in this chapter shows the approach to achieve the required bandwidth together with the required gain, which is a more complicated task. It also considers fundamental limits and estimates if the design objectives are practically realizable.

2.5.6 Pattern Measurements of Scaled Prototype

The pattern measurements for the described scaled model are performed over the available 350 MHz to 500 MHz range. The vehicle is mounted on a 0.5 m diameter circular ground plane. Using a larger ground plane can help reducing the impact of the ground plane on the radiation patterns however the size is limited by the specifications of the measurement chamber used. Figure 2.35 shows the measured and simulated normalized patterns of the scaled prototype. The patterns are seen to be symmetric over the cut plane that runs along the width of the vehicle. For the plane along the length of the vehicle, there is some squint in the patterns towards the back of the vehicle due to the influence of the small size ground plane used for the measurements. Overall good agreement between the measured and simulated patterns is seen. Some deviation is observed at the low frequency end where the measurements are the most challenging because of the small electrical size of the antenna and vehicle system, and chamber imperfections.

2.6 Discussion on Practical Aspects

The proposed antenna on the AAV is shown to support 24 kHz bandwidth and on the move operation over 3 to 10 MHz with a profile of 0.25 m. NVIS performance with radiation towards the zenith is discussed. The antenna has omni-directionality (WoW) that is comparable to the whip antennas, and thus it also supports long range sky wave and ground wave communications. At higher frequencies from 10 MHz to 30 MHz the antenna has consistent radiation patterns over the upper hemisphere leading to a better support of long range skywave and ground wave modes [58]. For frequencies lower than 3 MHz, the antenna becomes electrically very small. The gain dip at zenith becomes more prominent, and thus it becomes very challenging to address the required zenith gain criterion. Possible extension of the antenna operation down to the lower frequencies can be done by increasing the zenith gain with an increase in the antenna profile. The practical realization of the proposed antenna can be achieved by a structure made from hollow tubes, appropriate adapters and fixtures [58]. The offset feed can be implemented in a similar way as it is implemented in the scaled model design where the coaxial cable center conductor and the shield are split at the feed such that the signal carrying conductor is connected to the front side of the antenna structure while the shield of the cable is connected to the aft side of the antenna structure.

The front side of the antenna may need a support to ensure no mechanical stress is developed at the feed region, for instance, using nonconductive load bearing support sections. The coaxial cable can be fed through the hollow tubes that form the antenna arms and routed from the back of the vehicle through a grommet assembly made in the roof. Chokes must be installed at the feed to eliminate any undesired return currents from flowing on the shield of the feed cable. High power capable, low loss cables like the LMR-400 can be used in this assembly [67]. Presence of two arms allows for redundancy in the design such that a spare coaxial feed cable can be embedded in the second arm. In the case that the primary feed cable fails, the antenna can be fed using the auxiliary feed cable. A coaxial switch can be implemented at the antenna feed to switch between the feed cables under such situations. This specific implementation of the described antenna with the provision for an auxiliary feed mechanism will further add to its reliability and robustness.

2.7 Summary

The entire research and development process resulting in a novel design of an electrically small, low profile, on the move capable vehicular HF antenna, with increased bandwidth is discussed. The overview of ionosphere and HF propagation shows that HF links can provide a possibility for long and short-range communication established without satellites or repeaters. Traditional ionosphere communication relies on 3 kHz links, whereas wider bandwidth waveforms with upto 24 kHz bandwidth have been standardized recently. Channel capacity estimates of ionospheric NVIS links typically improve with wider bandwidth links, when at least one of nodes has a high gain antenna (GTx ~ 5dBi) and high transmission power is used (Pt = 100 W). When communication between two portable nodes

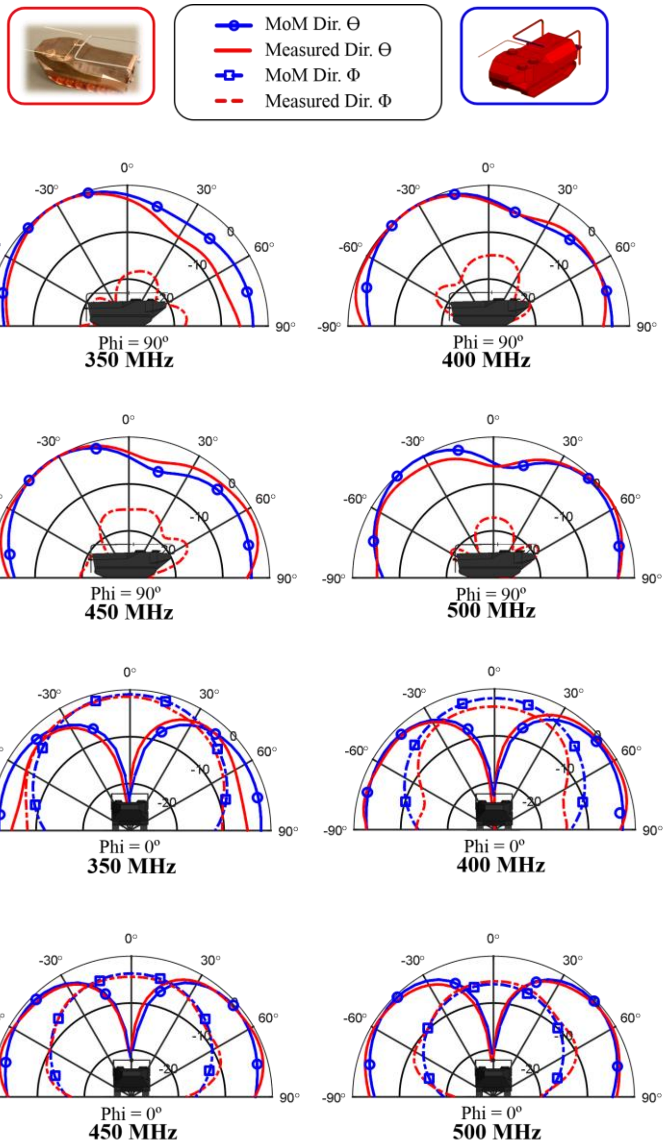

Figure 2.35: Measured and simulated normalized patterns of the scaled prototype.

with low gain antennas and limited transmitting power (Pt = 20 W) is considered, channel capacity is almost independent of bandwidth, indicating a saturation in the channel capacity. For the overall performance with the set bandwidth and gain criterion in mind, studies show that the inclusion of losses is necessary to assess the realistic performance for an electrically small antenna. The antenna evolution shows that a low profile inverted-L antenna can potentially replace the existing whip antennas for purposes of on-the-move operation with better performance for NVIS mode of operation. The proposed antenna has gain better than -20 dBi above 3 MHz and bandwidth better than 24 kHz over different grounds with a profile of only 0.25 m (λ/400 at 3 MHz). Two-arm configuration is more robust, improves antenna performance and enables profile reduction of 63% as compared to a single arm topology. The antenna design process developed in this thesis can be adopted for various platforms and the desired performance criterion for gain and bandwidth can be achieved by adjusting the effective tuner resistance, profile and offset feed parameters favorably. The design is validated by means of scaled prototyping. Additive manufacturing is shown to be a time and cost-effective approach to model and test scaled HF antenna prototypes over a vehicular platform. The measurement results for impedance as well as the patterns provide confidence in the computational approach used throughout this work.

Chapter 3

Full Scale Prototyping and Platform Integration of Vehicular HF Antennas

3.1 Introduction

The development of HF antennas for vehicular platforms requires a multi-dimensional design approach focusing on the electrical and mechanical performance of the antenna structure over the selected vehicular platform. At HF frequencies, ranging from 3 to 30 MHz [7], the vehicular antennas tend to be electrically small, owing to the large wavelengths and the relatively small size of the desired vehicular platform. The small electrical size of the antenna forces strong currents to flow onto the vehicular platform from where they radiate, making the vehicular platform an integral part of the antenna. Besides, the HF antennas considered herein are expected to support radiation at zenith for NVIS and at horizon for long range and ground communication, which is extremely challenging. This means that taking a specific vehicular platform into account during design is beneficial and may be necessary for successful accomplishment of the design goal.

Vehicular HF antennas with low vertical profile are desired for ease operation in micro terrains, underpasses and in urban environments. These antennas often need to support on the move (OTM) operation. Vehicular HF antennas are also expected to integrate seamlessly with the vehicular superstructure and co-exist with other on-board infrastructure on the platform. They need to be easy to maintain and repair and be low cost and light weight. These expectations add to the practical design constraints of the antenna and limit the volume available for the antenna deployment on the vehicular platform. The culmination of all these design requirements across various domains make the design of HF antennas on vehicular platforms extremely challenging.

The maximum dimension of low-profile HF OTM antennas is restricted by the size of the vehicular platform which is typically 3 to 10 m in length and 2.5 to 5 m in width. The wavelength at 3 MHz is 100 m. Since the total size of the antenna – vehicle system is very small compared to the wavelength at HF frequencies, they are electrically small and support impedances with small input resistance and high reactance. These electrically small antennas support fundamental mode radiation patterns like the Hertzian electric dipoles or a Hertzian magnetic dipole at the low frequency end. As the antenna grows larger in electrical size with increase in operating frequency, these patterns change. This means that the antenna patterns need to be studied and engineered to favor the different modes of HF propagation at different frequencies.

This chapter discusses the design, fabrication, integration, and field testing of a low profile, 24 kHz capable, vehicular HF antenna that has the potential to support near vertical incidence skywave (NVIS), groundwave as well as long range sky wave propagation modes over 3 to 30 MHz. Fabrication details for the antenna structure are illustrated. The antenna has built in tuner housed at its feed. Tuning with a COTS tuner is demonstrated. Impedance and pattern measurements for the full-scale HF antenna are shown and the challenges related to measurements are also discussed. The design approach described in Chapter 2 is used to design the antenna over the desired platform of the Oshkosh Mine Resistant Ambush Protected – All Terrain Vehicle (M-ATV) [68]. The focus of this chapter is the inverted-L mode of operation for the proposed antenna over the M-ATV. However, the same antenna structure can also be reconfigured into loop mode or top loaded monopole mode of operation as may be required in different applications and operational scenarios [69].

The design of the full scaled HF antenna prototype described in this chapter is benchmarked against the size, features and performance of commercial vehicular HF antennas reviewed in Chapter 2. The requirement on the antenna profile is set at less than 1 m and the power handling requirement is set to be higher than 400 W CW. The focus of this chapter is to design, fabricate, and discuss details about the field test for a practical prototype antenna with capability to support 24 kHz wideband HF waveforms while maintaining the desired low-profile criterion when deployed on the M-ATV platform.

The chapter is organized into five sections followed by the summary as described below.

- Section 3.2 discusses the features of M-ATV, the vehicular platform of interest, to lay the foundation for the antenna design process.
- Section 3.3 discusses the antenna design process and the computational modeling details and results.
- Section 3.4 shows the full-scaled prototype fabrication and integration over the steel pedestal platform at The University of Colorado Boulder.
- Section 3.5 shows antenna measurements and field demonstration performed on the M-ATV platform mockup to validate the design.
- Section 3.6 talks about the details of the vehicular integration of the full scaled antenna on the M-ATV platform, impedance measurement results and field demonstration performed thereafter.
- Section 3.7 discusses the concept of an electrically switched reconfigurable HF antenna.
- The extract of the chapter is summarized in Section 3.8

3.2 M-ATV Vehicular Platform

The vehicular platform of interest for the design and demonstration of the full scale wideband HF antenna prototype is the Oshkosh Mine Resistant Ambush Protected-All Terrain Vehicle (M-ATV) [68]. This platform is designed to be the near future replacement for the currently used light weight all terrain platforms. The vehicle is 6.2 m long and 2.5 m wide with a height of 2.7 m. The prominent features of the vehicle that need to be considered in the HF antenna design include the presence of a crossed dipole for satellite communications in the rear, fog lamps on the front side of the roof, presence of personnel and weapons mounting hatch on the roof top, VHF antenna mounts on the front side near the A pillars, and a full size spare tire in the rear mounted high above the bumper.

With a 1 m profile of antenna over the M-ATV platform, the size of the Chu sphere that encompasses the antenna and the vehicle is ≈ 3.8 m. This size would correspond to an electrical size of 'ka ≈ 0.24' at 3 MHz. For a single arm inverted-L antenna with a height of 1 m and length equal to the length of the M-ATV platform (~6 m), the efficiency of the antenna needs to be less than 4.2% to support legacy 3 kHz bandwidth and less than 0.5% to support 24 kHz wideband instantaneous tuned bandwidth at 3 MHz, based on the analytical approach for bandwidth and efficiency of electrically small antennas, discussed in chapter 2. Such low efficiency suggests that antenna gain performance will be sacrificed. As seen from the review of vehicular HF antennas in chapter 2, practical vehicle mounting constraints and low-profile requirement limit the best achievable antenna performance. The proposed antenna with the details of the M-ATV platform are shown in Figure 3.1.

3.3 Antenna Design

The design of the proposed antenna prototype was performed as per the design process described in chapter 2. The antenna design is evolved from the traditional whip type HF antenna, mounted on the rear of the M-ATV. The performance of the bent whip was analyzed before transitioning to a single arm base fed inverted-L antenna. A second arm was added to enhance the bandwidth performance of the antenna without increasing its feed complexity. Tuner box was added to the rear of the vehicle and directly integrated with the antenna structure for the two-arm antenna model mounted on the M-ATV platform. The step by step antenna evolution is described in Figure 3.2.

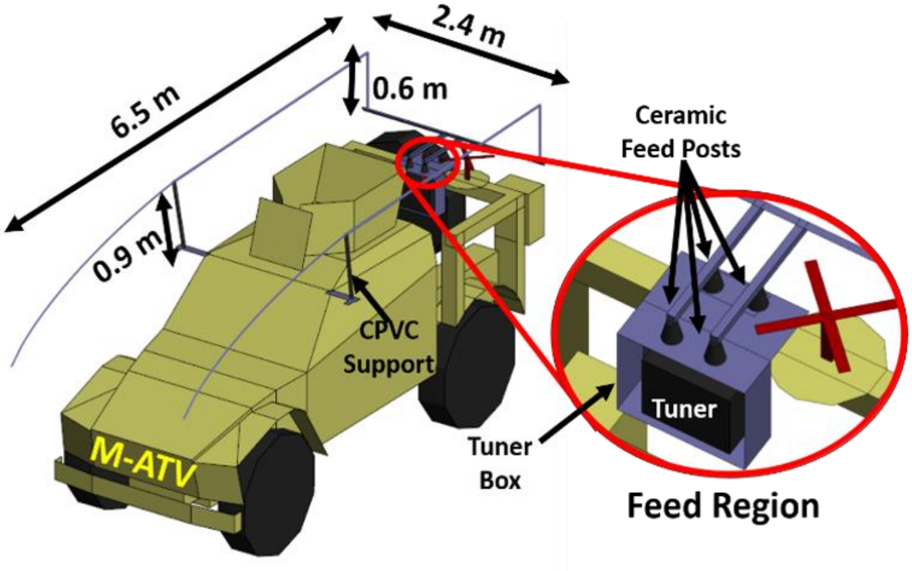

Figure 3.1: Full scale antenna prototype mounted on the M-ATV platform.

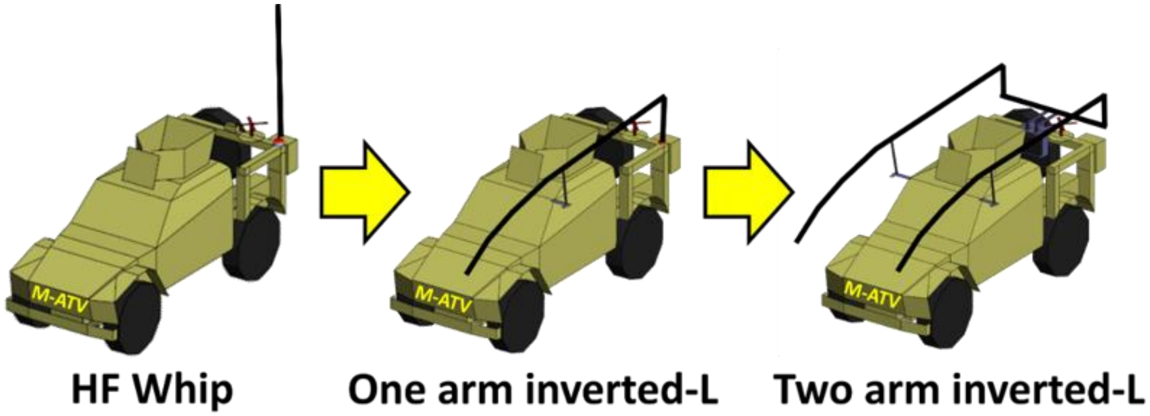

Figure 3.2: Antenna evolution for the full-scale prototype mounted on the M-ATV.

3.3.1 Mechanical Reconfigurability

The full scaled prototype antenna is built with a structure that can mechanically reconfigure into an inverted-L mode, loop mode, and top loaded monopole mode of operation as shown in Figure 3.3. Each mode has its own set of benefits that could be exploited for the antenna to adapt to diverse communication requirements, and platform scenarios. Monopole based antennas (inverted-L or top loaded monopole antennas) require a single electrical ground point for mounting leading to easier platform integration. Additionally, monopole based antennas are less sensitive to losses from the surroundings. The input impedance of a monopole does not show anti-resonance behavior within the NVIS frequency range, with the considered antenna size on the M-ATV platform. This means that the considered monopole type antenna would have has less impedance variation as we move higher in frequencies, making it easier for tuning. The loop type of antenna on the other hand has better NVIS performance at the cost of requiring two ground points, and higher sensitivity to tuner and environment losses.

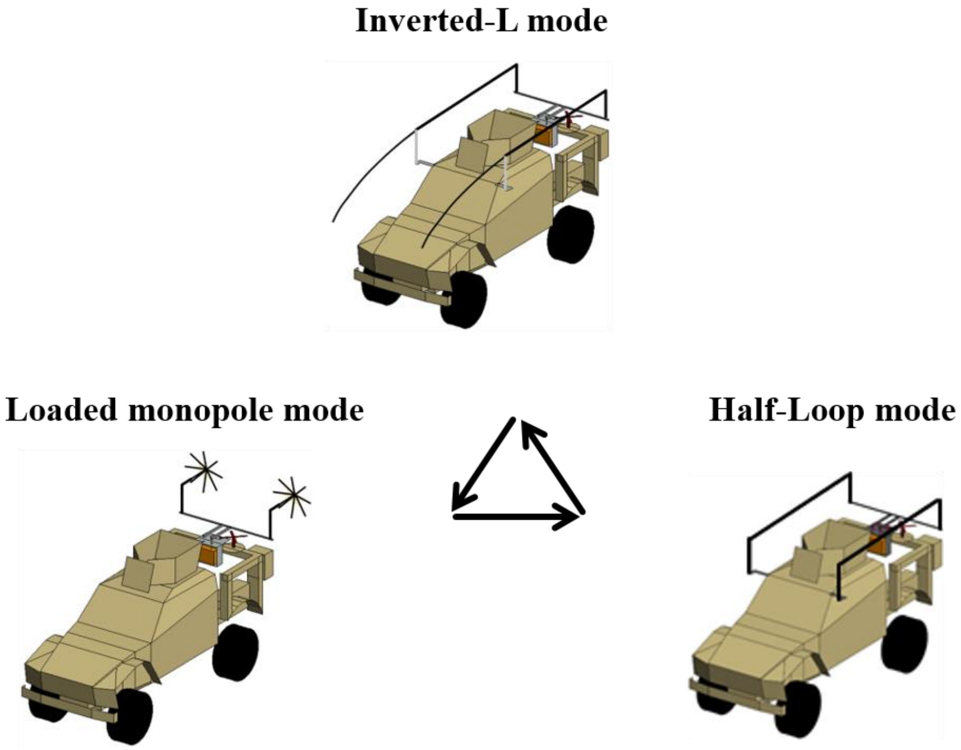

Figure 3.3: Mechanical reconfiguration of the antenna from Inverted-L mode of operation to loop mode and top loaded monopole mode of operation on the M-ATV [34].

The proposed inverted-L antenna on the M-ATV was specifically designed to share most of the basic hardware between itself and its loop or top loaded monopole counterparts. The decision of having a base fed inverted-L antenna was influenced by the practical necessity for the prototyping campaign to demonstrate and evaluate performance of different antennas types on the selected vehicle. Base feeding also allows for the tuner integration right at the antenna feed, which is important as the impedance seen by the tuner is an accurate representation of the antenna input impedance. The ability of the antenna to be reconfigured into different modes of operation was also approached as a risk mitigation strategy for the prototyping campaign because much details about the vehicular platform were not available in the open domain literature.

3.3.2 Numerical Studies

The antenna design is performed in MoM code Altair FEKO [1]. The vehicular body and the tuner box are made of steel (electrical conductivity $\sigma_{\text{steel}} = 1.45\times10^{6}$ S/m). The antenna arms are built from 3.175 cm (1.25 in) diameter aluminum tubes (electrical conductivity $\sigma_{\text{aluminum}} = 3.8\times10^{7}$ S/m). Lossy grounds, defined in chapter 2 are used to compute antenna performance. The tires are modeled as rubber (dielectric constant $\varepsilon_r = 3.0$; relative permeability $\mu_r = 1$; electrical conductivity $\sigma_{\text{rubber}} = 1\times10^{-15}$ S/m). The non-conductive arms at the front that support the inverted-L antenna arms are made from chlorinated polyvinyl chloride (CPVC) pipe of 3.81 mm (1.5 in) diameter (dielectric constant $\varepsilon_r = 3.7$; $\tan(\delta) = 0.0096$) [70]. The calculated input resistance and the reactance of the proposed two arm inverted-L

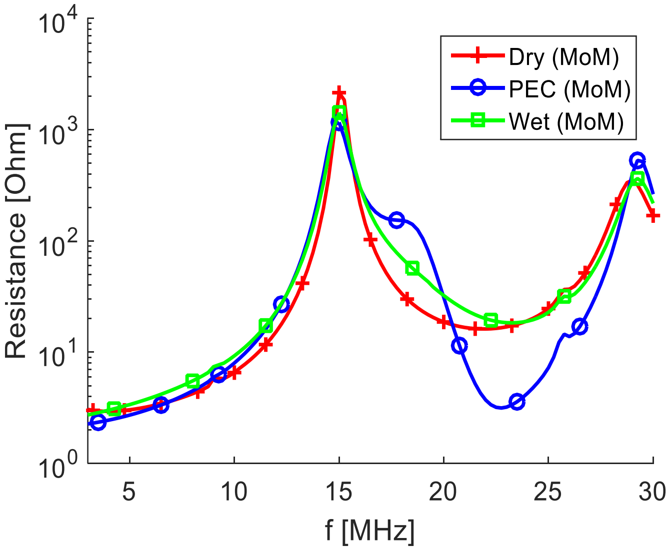

Figure 3.4: Input resistance of the two arm Inverted-L antenna mounted on the M-ATV with 0.8 m profile and 6 m length. Additional 2Ω effective tuner resistance is taken into account.

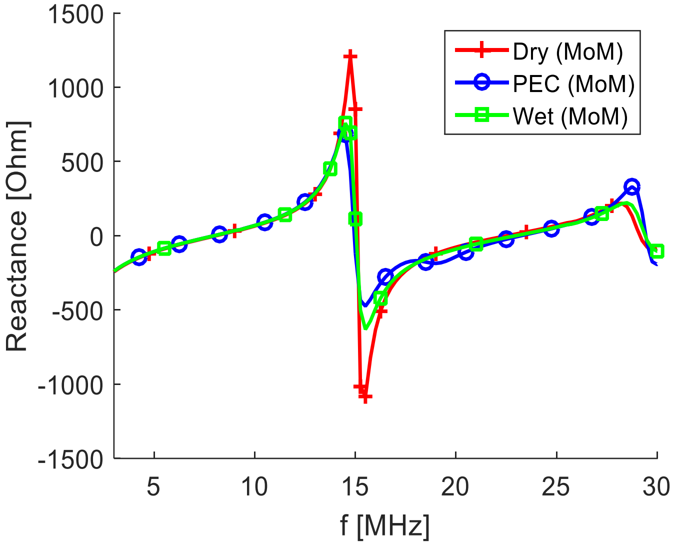

Figure 3.5: Input reactance of the two arm inverted-L antenna mounted on the M-ATV with 0.8 m profile and 6 m length. Additional 2Ω effective tuner resistance is taken into account.

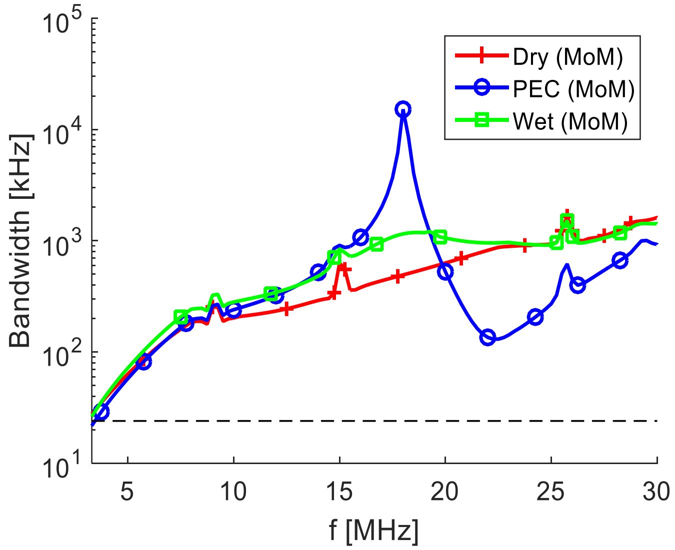

Figure 3.6: Bandwidth estimate for the two arm inverted-L antenna mounted on the M-ATV loaded with 2Ω of effective tuner resistance. The antenna supports bandwidth better than 24 kHz over different grounds for the entire frequency range from 3 to 30 MHz.

antenna deployed on the M-ATV is shown in Figure 3.4 and Figure 3.5 respectively.

Bandwidth performance is shown in Figure 3.6. The antenna performance with additional 2 Ω of effective tuner resistance, considered as part of the antenna system is reported herein. This 2 Ω effective tuner resistance value sets the requirements for the tuner performance to achieve the desired bandwidth and gain goals with the proposed antenna.

The antenna impedance shows a resonance around 8 MHz on the low end and around 23 MHz on the high end. The antenna has an antiresonance around 15 MHz on the low end and around 29.5 MHz on the high end. The input resistance of the antenna is small at the low end and progressively increases as we go higher in frequency till the first antiresonance. Over the entire frequency range of interest spanning from 3 MHz to 30 MHz, the antenna wraps around the Smith chart two times as we move up in frequency.

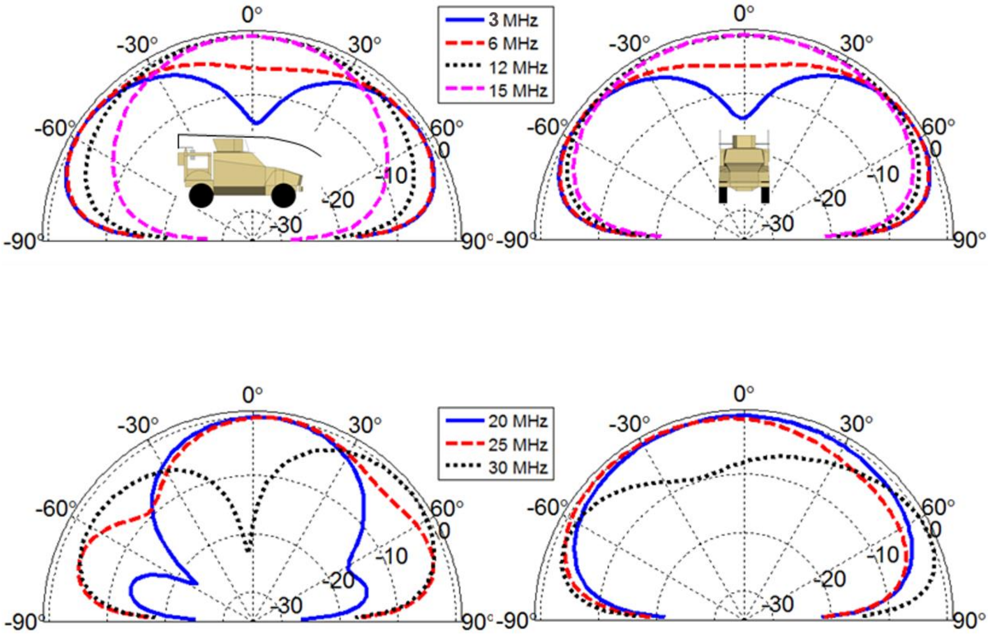

Figure 3.7: Simulated total gain patterns for the two-arm inverted-L antenna mounted on the M-ATV over dry, wet and PEC grounds.

The input reactance of the antenna over different ground follows similar trend showing that this antenna can be tuned using the same tuning topology at a given point in frequency over different types of grounds. The tuned fractional impedance bandwidth is estimated based on the untuned antenna input resistance R and reactance X as described in chapter 2. The bandwidth estimation of the antenna over different grounds, as shown in Figure 3.6 demonstrates that PEC ground is the worst case in terms of bandwidth. The simulated antenna gain performance over dry grounds is shown in Figure 3.7. Dry ground is the worst-case scenario for gain of the two-arm inverted-L antenna mounted over the M-ATV. The patterns show that in the NVIS frequency range (3 to 10 MHz) the antenna is capable of supporting NVIS, ground wave and long-range sky wave patterns. At frequencies above 15 MHz, the antenna favors long range sky wave and ground wave modes of communication. With the given profile of 0.8 m, this antenna satisfies the design requirements of 24 kHz bandwidth starting from 3 MHz with the considered 2 Ω of effective tuner resistance. However, performance at 2 MHz can be improved by using a higher profile or by making current distribution in the horizontal sections more uniform, for example, with an offset feed as shown in chapter 2, or by the use of reactive loading, which is the part of future study.

3.4 Full Scale Prototype

After designing the antenna with computational tools mentioned in the previous sections, the antenna design was transitioned from the digital design files into a full scaled prototype. The antenna fabrication was carried out in form of an incremental process where every functional element of the antenna was tested and validated one at a time. Every element was tested for mechanical fit and functionality before moving to the electrical tests.

The simulated input resistance and reactance of the two-arm inverted-L antenna for the M-ATV emphasized the importance of good fabrication for the success of the antenna since every possible loss in the antenna was desired to be minimized. Measurement and fabrication capabilities required for realizing such electrically small antenna on a vehicular platform were developed and verified as part of the process. The developed capabilities were eventually used towards the realization of the full scaled design on the M-ATV.

3.4.1 Antenna Fabrication

The full-scale prototype fabrication was conducted at the University of Colorado Boulder. Since accurate vehicle dimensions were not available at the time of fabrication, and access to the M-ATV could not be granted, the antenna was built out of interconnecting

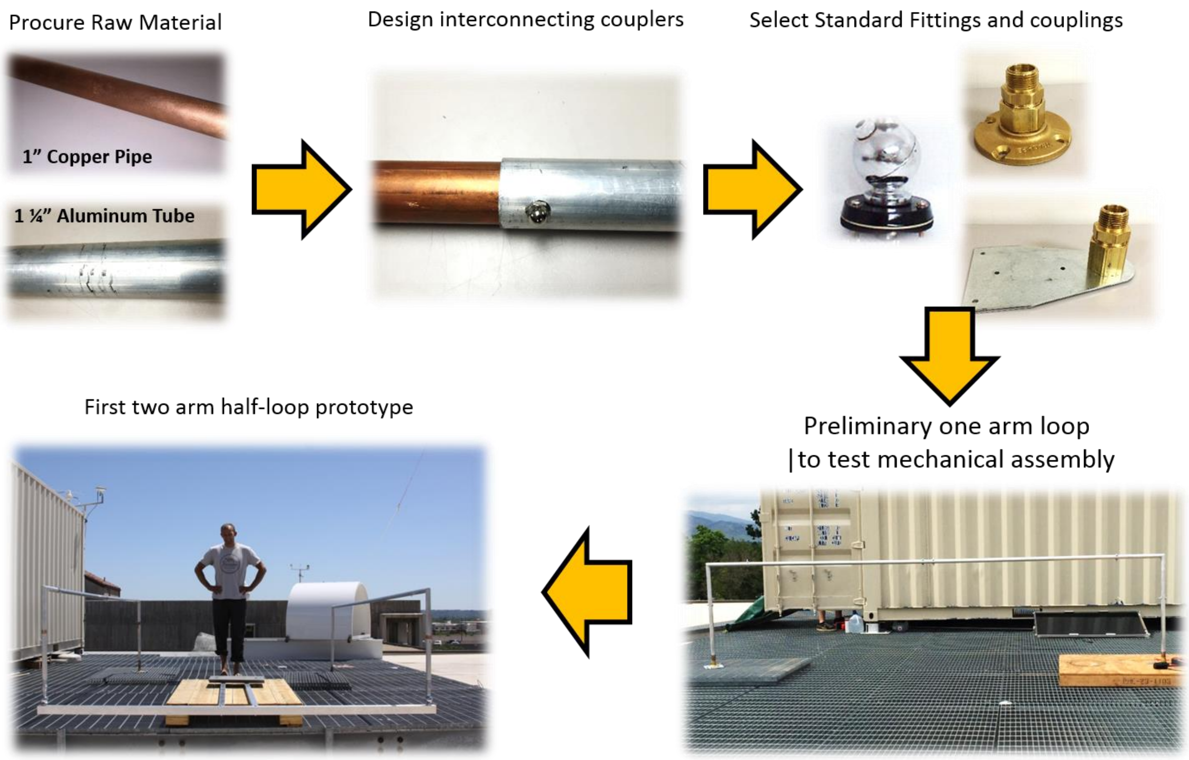

Figure 3.8: Fabrication and assembly of the proposed antenna full scaled prototype.

modules. These modules were designed to be connected and realigned with respect to each other to enable flexible adjustment of the antenna dimensions to fit on the vehicle. The ability of the individual antenna sections and modules to be flexible to adapt to the vehicle dimensions added a lot of confidence in the fabrication stage as the antenna had a high likelihood of easy platform integration compared to a rigid structure made from fixed lengths.

The step by step fabrication and assembly of the full scaled antenna is shown in Figure 3.8. The antenna superstructure was chosen to be made from 3.175 cm (1.25") diameter aluminum tube sections which are interconnected with 1" copper pipe sections. The selection of a tube and pipe combination was made so that the outer diameter of the copper pipe matched the inner diameter of the aluminum tube to give a high tolerance sleeve contact between the aluminum – copper – aluminum interface. Standard COTS plumbing and structural parts such as flanges, elbows and reducers were used in the model to ensure ease of fabrication, achieve low development cost and to minimize the number of custom parts required for the antenna. While the two arms of the antenna were chosen to be made from cylindrical tubular structures with 4 feet long sections connected with the copper pipe sleeves, the right-angled sections of the arms were made from 1 feet long, welded sections of the aluminum tubes. The rear base of the antenna was fabricated with 6.35 cm (2.5 in) square busbar sections. The use of busbars allowed the antenna mount and the base to bear the entire structural load of the antenna and transfer it effectively onto the vehicle chassis while maintaining good structural integrity. Custom adapters were developed for the transition between the rear busbar section and the tubes forming the antenna arms. The antenna feed was established between the busbar sections and the antenna base using 7.62 cm (3 in) thick and 11.43 cm (4.5 in) tall insulating ceramic support posts. The details of the different parts of the prototype are shown in Figure 3.9.

Welding the right angle sections of the antenna

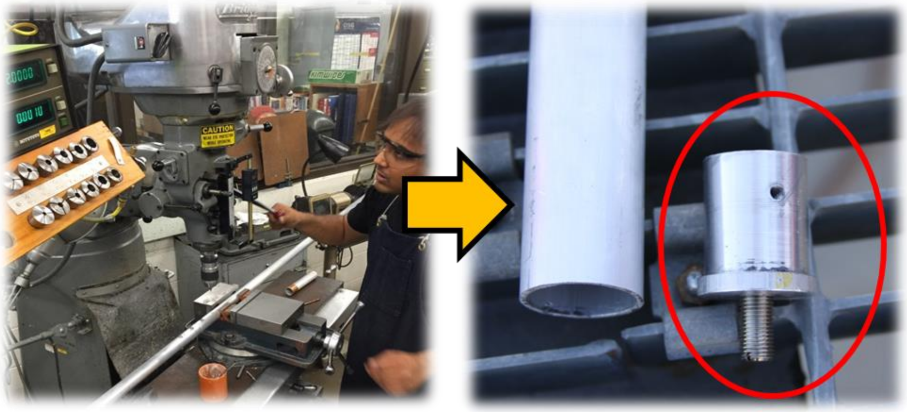

Fabricating custom adapters for the antenna transitions

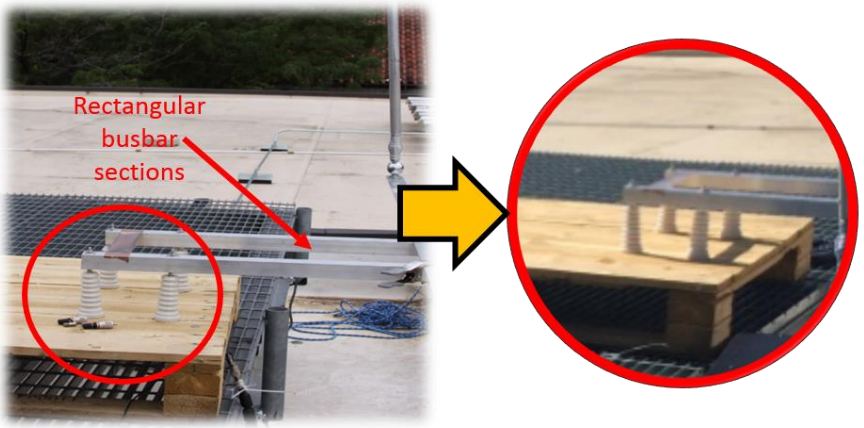

Building the feed with feed through and solid ceramic posts

Figure 3.9: Fabrication details for the full scaled half-loop prototype showing the welding process to form the right-angled sections of the loop arms, the fabrication of custom adapters and the build details of the feed.

3.4.2 Preliminary Testing

The first set of tests with the fully assembled antenna system was performed at the University of Colorado Boulder. The test aimed to assess the integration of the antenna parts along with the COTS tuner and radio, and to acquire the experience for measurement, tuning integration, and operation of such electrically small antennas. A number of links at various frequencies and with various power levels were established with a remote test site in order to perform system integration tests and to acquire NVIS communication experience. Majority of these tests focused on working with the antenna in the loop mode as it was the most challenging variant to tune and operate due to its small input resistance. There were two

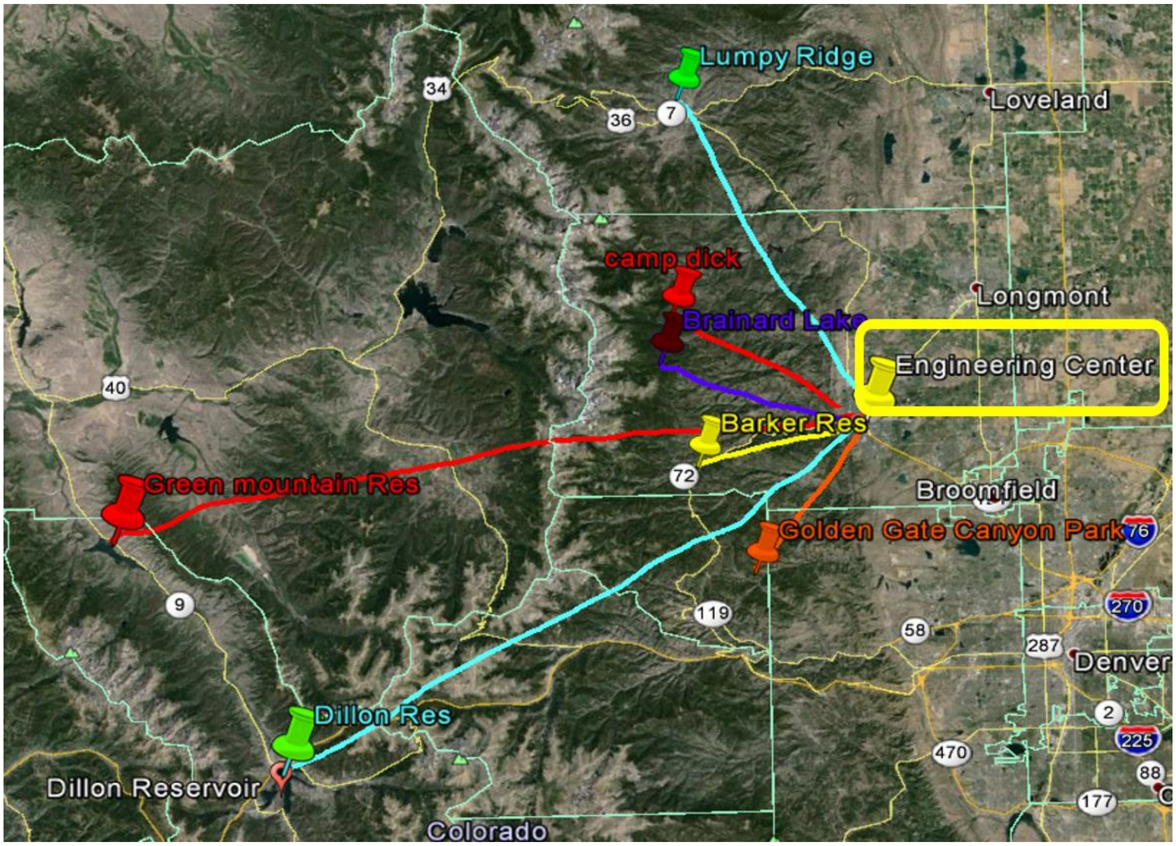

Figure 3.10: Map of Boulder, Colorado, showing the various test locations considered for the preliminary NVIS link tests.

Figure 3.11: Setup for the HF station atop the roof of the engineering center at the University of Colorado Boulder. Seen in the top inset is the structure of the antenna configures in the Dual Arm Half Loop Antenna (DHLA) mode. The top right inset shows the details of the tuner box, the feed region and the COTS tuner installed inside the tuner box [34].

operation sites established to perform the testing. One site was responsible for the operation of the loop antenna from the Engineering building at the University of Colorado Boulder, while the other group set up an HF station with a tri-band fan dipole at a remote location in the mountains close to Boulder, Colorado. A few locations were considered for this test. All the selected locations were across mountains so that the ground wave component would be severely suppressed (Figure 3.10). The Barker reservoir location, 12.8 mi away from the University location was chosen for the further tests after surveying the selected locations.

The setup for the two arm half-loop antenna atop the engineering center at the University of Colorado Boulder is shown in Figure 3.11**.** The setup consists of the prototype configured in the dual arm half loop antenna (DHLA) mode connected to the COTS Palstar HF-Auto tuner and its control unit [71]. The tuner is interfaced to a COTS 3 kHz HF radio [72]. Measurement equipment to get VSWR and impedance data from the antenna is set up close to the antenna in the command center. The antenna can be seen mounted on the metallic scaffolding with a wooden base used as a temporary support. All the parts made for the antenna were tested for tolerance and fit with its corresponding mating parts during the first assembly routine for the prototype. The structural integration also proved that the ceramic supports chosen for the build could support the entire weight of the antenna while still maintaining electrical isolation between the signal side connected to the antenna arms and the ground connected to the metallic scaffolding below the antenna. The setup for testing at the remote site is shown in Figure 3.12**.** The HF station was set up inside of a vehicle stationed next to the fan dipole antenna used for tests. The remote site was powered by a heavy-duty lead acid battery and a standby generator.

The link establishment tests were performed on various amateur radio frequency bands from 3.5 to 28 MHz for the prototype configured in the inverted-L mode, top loaded monopole mode and the loop mode with a minimum of 5 W and maximum of 100 W of transmit power using the CW and LSB modulation modes. NVIS contacts with the remote team as well as with numerous local amateur radio operators were established. Apart from this, long range skywave contacts with operators from other parts of the USA as well as with some international amateur radio stations were also established during these tests. The tests demonstrated successful integration of all components in the system and provided necessary operational training for the team. Impedance measurements performed during this preliminary testing phase pointed to high impact of parasitic reactance associated with

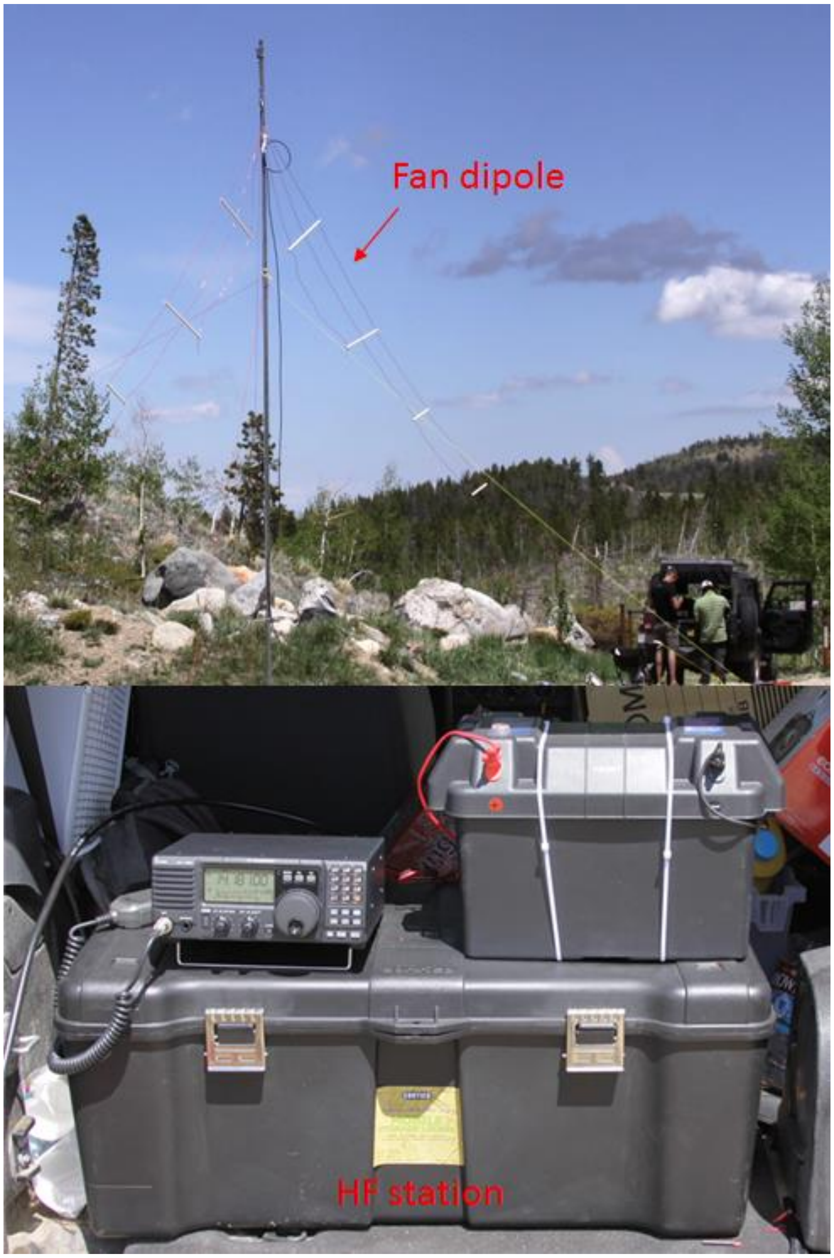

Figure 3.12: Setup for the HF station at the remote site for the preliminary testing of the two arms half-loop antenna at the University of Colorado Boulder.

surroundings on the antenna impedance and on the position of anti-resonance in particular. Note that the effects of parasitic reactance are not typically seen during these tests with regular sized, electrically large dipole antennas as much as they were seen with the electrically small prototype antenna.

3.5 Antenna Measurements on Platform Mockup

A few field tests focused on interfacing the 24 kHz wideband HF radio with the developed antenna system. These field tests were carried out before integrating the antenna system on the M-ATV. These antenna measurement and system integration campaigns were performed between January and September 2015. The antenna pattern measurements were performed at the SPAWAR Antenna Pattern Range (APR) measurement facility at the Point

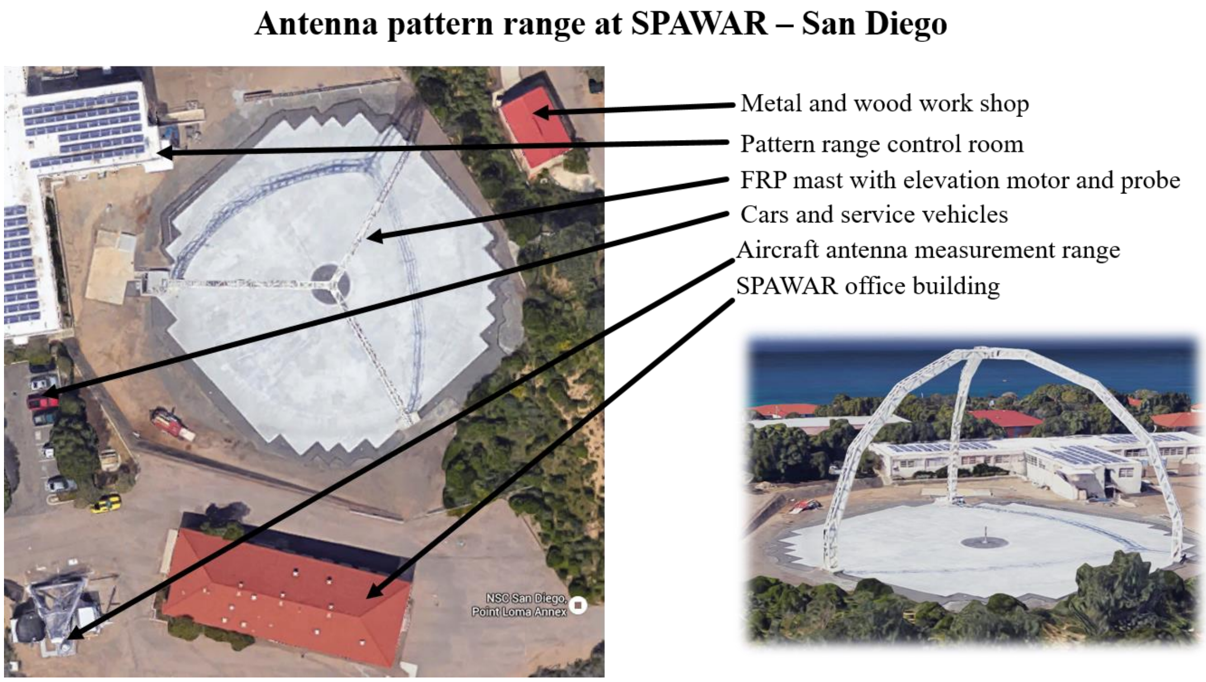

Figure 3.13: Aerial Rendering of the SPAWAR HF Antenna Pattern Range at the Point Loma Naval base in San Diego, California [74].

Loma Naval Base in San Diego [73]. The details of the APR site are shown in Figure 3.13 [74]. The purpose of the antenna pattern measurements was to evaluate the performance of the antenna and validate the performance computed from the computational modeling exercise. Results of the measurements conducted demonstrate the validity of the developed design and showcase their utility for integration into the future HF OTM platforms.

3.5.1 Integration on Platform Mockup

The developed antenna system was mounted on a mockup platform made from a rectangular aluminum box. The mockup platform was used to simulate the antenna mounted

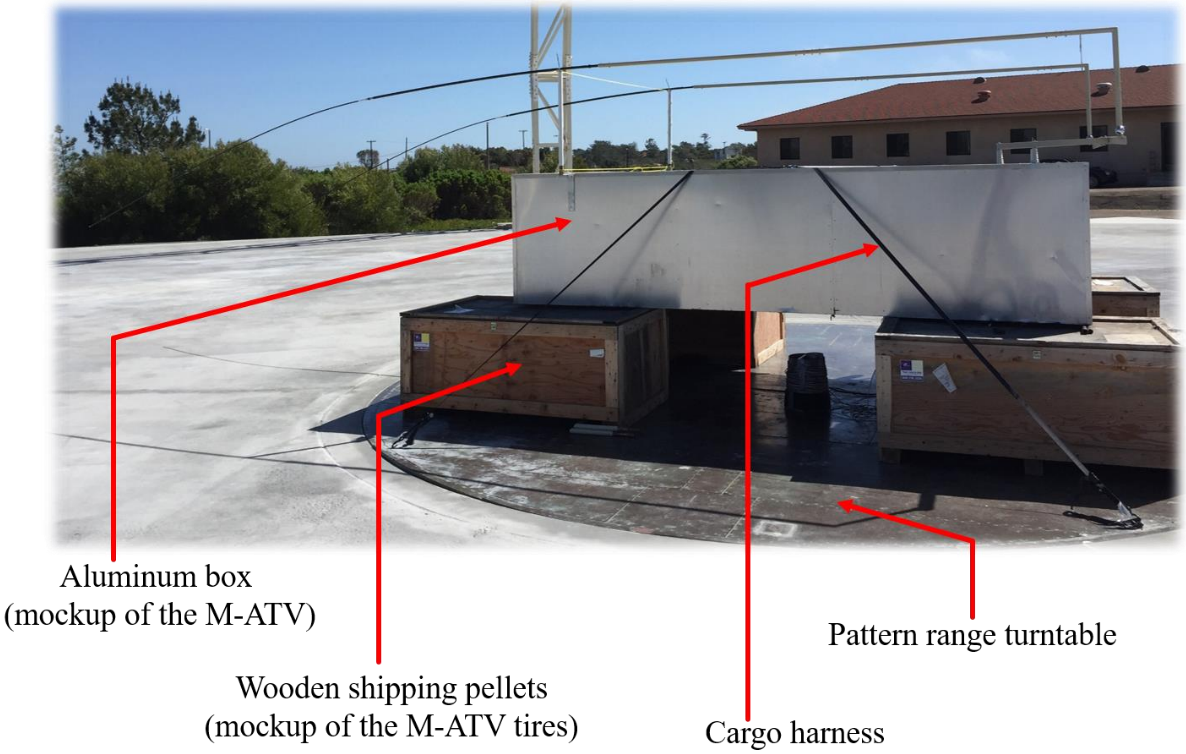

Figure 3.14: Setup for pattern measurements of the full scaled two arm inverted-L antenna mounted over the M-ATV mockup platform at the SPAWAR HF Antenna Pattern Range located at Point Loma Naval base in San Diego, California [75][76].

on the M-ATV and provide similar operational environment. The size of the aluminum box used for the mockup platform is 4 m (L) x 2 m (W) x 1 m (H). The box is raised on four wooden shipping crates with dimensions of 1.5 m (L) x 1 m (W) x 0.8 m (H) to simulate the effect of electrical isolation between the metal body of the M-ATV and the ground as it is mounted on four tires. The rear end of the mockup platform was made to have the same mounting structure and hole pattern as would be used in the actual M-ATV to check for fit and functionality of the designed mechanical mounts and fixtures. The feed is realized using the ceramic feed through posts that separate the signal and ground side of the antenna. The tuner box is housed inside the aluminum mockup platform box. The entire assembly is placed over a rotating turntable at the center of the APR for the pattern and gain measurements. The Palstar HF-Auto COTS tuner is installed inside the tuner box and the RF coaxial cable feeding the antenna and the control cable for the tuner are routed to the tuner box through a rotary joint located under the APR turntable. The antenna arms are supported in the front using two CPVC supports, similar to the case when it would be mounted on the M-ATV. The pattern measurement setup is shown in Figure 3.14.

3.5.2 Pattern Measurements

Pattern measurements for the full scaled antenna prototype configured in inverted-L mode as well as the loop mode, mounted on the M-ATV mockup platform were performed. There were several objects electrically close to the range behaving as scaterers, and thus special post-processing and time gating is used to filter out reflections from nearby

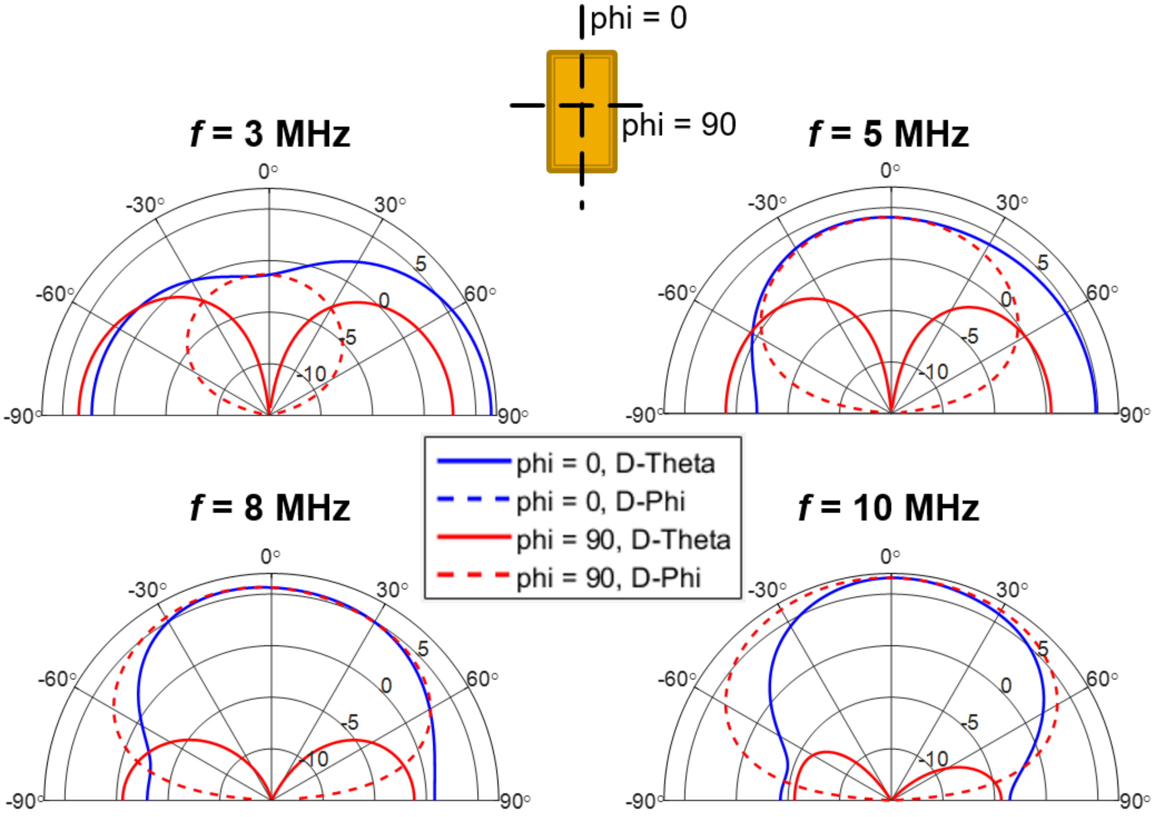

Figure 3.15: Measured directivity of the full scaled two arm inverted-L antenna mounted over the M-ATV mockup platform at the SPAWAR HF Antenna Pattern Range located at Point Loma Naval base in San Diego, California.

structures. The measured directivity patterns for the inverted-L mode are shown here in Figure 3.15.

The measured zenith gain for the Inverted-L mode are shown in Figure 3.16. From the two results we can see that the null at zenith at lower frequencies has been weakened significantly owing to the energy redirected from the large conductive ground below the antenna. The peak gain over the 3 to 10 MHz NVIS band saturates at -9 dB while the zenith gain is -18.4 dB at 3 MHz increasing to -10 dB at 10 MHz.

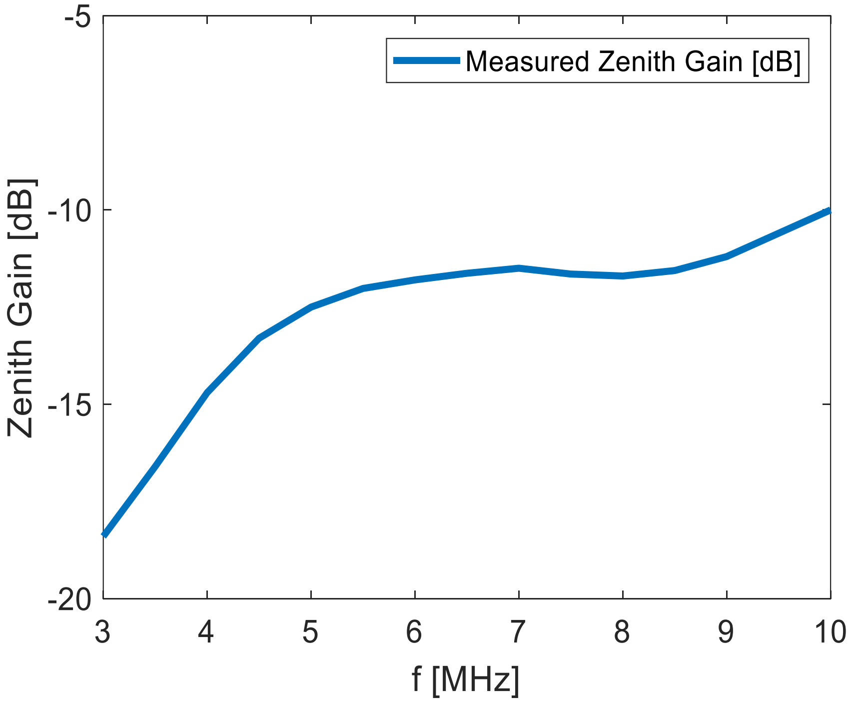

Figure 3.16: Measured Zenith gain of the full scaled two arm inverted-L antenna mounted over the M-ATV mockup platform at the SPAWAR HF Antenna Pattern Range located at Point Loma Naval base in San Diego, California.

3.6 Vehicular Integration

The proposed antenna is integrated onto the M-ATV with other existing vehicular antenna systems in situ. Not a single modification of preexisting antennas and other systems present on the M-ATV was allowed, thus making this assembly even more challenging. The full scale prototype can be seen in Figure 3.17. Aluminum is chosen as a compromise between weight, machinability and structural strength. Feed region is established at the rear center of the vehicle. The antenna is mounted on the M-ATV using fixtures that secure a mounting plate on the rear chassis of the M-ATV. The details of the integration achieved using the individual parts of the antenna are shown in detail in Figure 3.18. The mounting plate houses the tuner box and the feed region of the antenna (Figure 3.18 (a)). Antenna is fed against the vehicle body and is electrically isolated from the vehicle at the feed using four 7.5 cm diameter, 12 cm tall ceramic insulators. The tuner's signal line was connected to the antenna structure through a feed post running through one of the ceramic insulators, and the antenna ground was connected to the tuner box housing which in turn connects to the homogenous vehicular ground through the chassis. The feed layout is done so that the peak electric fields are well below breakdown for 400 W of input RF power in the worst-case scenario. Rear base of the antenna is made from rigid aluminum framework made from 6.5 cm wide square busbar tubing while the inverted L sections are made from 3.5 cm diameter round tubing. Copper interconnecting sleeves are used for joining the aluminum tubes (Figure 3.18 (b)). Such a flexible assembly allowed for fine adjustment of the antenna structure dimensions on

Figure 3.17: Full scale prototype of proposed antenna deployed on M-ATV.

the platform as described before. Since the aluminum and copper sleeve joints are prone to oxidation and corrosion, they were polished before each set of measurements. To use the joints over the duration of several measurements without deteriorating the contact due to oxidation, oxide inhibiting electrical joint compound called 'Penetrox-13A' was used at the sleeve joint interface [77]. The signal and control cables are routed from the side of the tuner box (Figure 3.18 (c)). The tapering tips of two arms are made from COTS PRC series HF collapsible whips. The front tips of the whips are secured by means of a nonconductive cord to the front bumper of the vehicle for stability. The cantilever beam formed by each arm is supported by 5 cm diameter CPVC columns mounted on brackets located at the front of the vehicle. These brackets are mounted at the base of the fog lights at the junction of the roof and the A-pillar of the M-ATV.

(a) (b) (c)

Figure 3.18: Details of the various parts used in the integration of the 2-arm inverted-L antenna prototype with the M-ATV: (a) mounting of the tuner box and antenna on the M-ATV chassis. Also shown is a close up view of the feed region, (b) modular aluminum tube sections connected using copper sleeve joints, (c) tuner interface with signal, DC power and remote-control cables.

3.6.1 Preliminary Impedance Measurements

Flexible, low loss LMR 400 coaxial cable was used to connect the radio with the antenna. The antenna tuner box housing the COTS Palstar HF Auto tuner at the feed was sealed using silicon based epoxy resin for weather protection against rain, moisture, dust and dew. The location of the tuner at the feed of the antenna itself, helps for precise tuning. The antenna was driven from a remote location, to better facilitate inter-operability with the radio, network, data and other engineering teams. This also allowed for operating under changing weather conditions as most of the equipment except the tuner could be housed indoors. To achieve this, the radio, tuner control unit and antenna measurement equipment were placed either inside a nearby building or inside a mobile laboratory setup inside a large van. Both these locations were at about 200 feet from the antenna prototype mounted on the

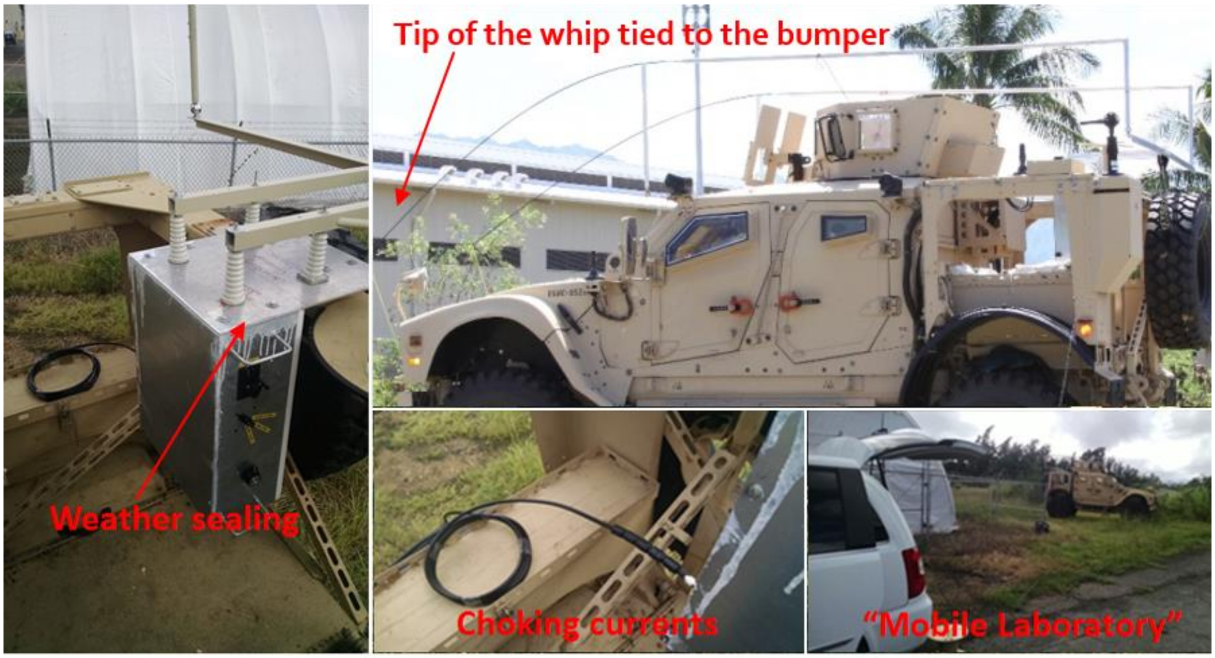

Figure 3.19: Details of the measurement setup used on the field for the antenna prototype mounted on the M-ATV.

M-ATV. The coaxial cable feeding the antenna was choked using ferrite beads and a large air core inductive coil choke to prevent any uncontrolled and undesired radiation from return currents flowing on the outside of the coaxial cable shield. The drooping tips of the whips protruding from the two arms of the inverted-L antenna are tied to the front bumper using non-conductive cords for maintaining stability throughout the measurements. The details of the measurement setup mentioned above are shown in Figure 3.19. Impedance measurements for the inverted-L mode of operation are shown in Figure 3.20. The impedance measurements of the antenna confirmed the expectations – the impedance goes through a series resonance at 7.5 MHz and anti-resonance at 14.5 MHz. This corresponds to a 0.5 MHz

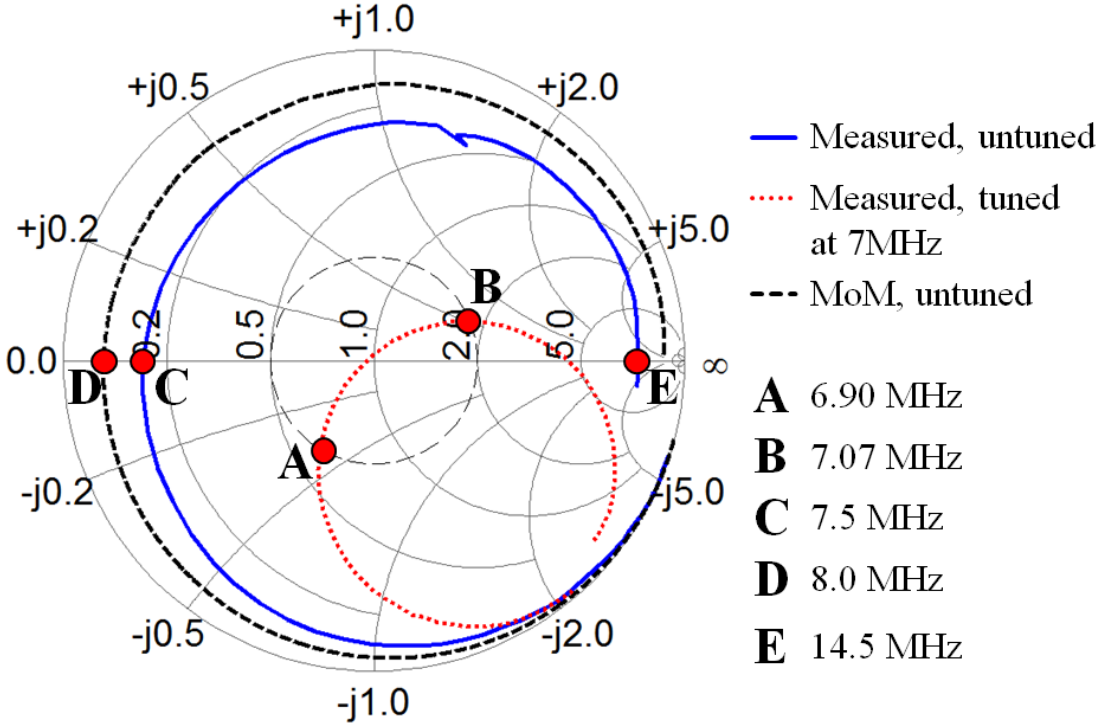

Figure 3.20: Measured and modeled antenna input impedance of the inverted-L antenna prototype mode mounted on the M-ATV. Untuned impedances are shown from 2 to 15 MHz. The dashed circle indicates the 2:1 VSWR condition.

drift in the resonance and antiresonance locations of the measured antenna compared to the computational model predictions. The drift can be attributed to the limited knowledge of materials used in the M-ATV, the difference in the modeled and actual dimensions of the M-ATV, the impact of paint and other platform related entities on the antenna performance and the variation in the deployed antenna environment compared to the modeled wet and dry ground scenarios. Practically, this drift in impedances did not matter on the field as the tuner attached to the antenna was capable of operating the antenna over a wide range of frequencies, including at antiresonance. The antenna was thus able to be operated in a tuned configuration when connected to the radio at the desired frequency of operation.

3.6.2 Field Demonstration

The developed antenna prototype was showcased and demonstrated as part of the ONR's annual technology demonstration event called "Agile Bloodhound 2015 (AB-15)" at the Marine Corps Base Hawaii (MCBH), Hawaii. As part of the technology evaluation, it was demonstrated that all the modes of operation of the antenna, the inverted-L mode, loop mode and the top loaded monopole mode were tuned by the COTS tuner. A set of tests with WB HF Trellisware radio were also conducted [78]. The antenna was successfully integrated with the 24 kHz wideband radio in the loop mode and the inverted-L mode of operation. The developed half-loop antenna system on the M-ATV was demonstrated and wideband HF connectivity between two testing locations was established using 24 kHz wideband waveforms. Link between the two sites separated by 14.5 km (9 mi) was established at 8.006 MHz. Analysis of time delay of arrival and signal strength of received raw data information over the HF link over the proprietary interface of the WB HF Trellisware radio was used to determine that the main communication mode was NVIS [78]. With an average input power of 30 W (230 W peak) a file of 99196 bytes was transmitted from the OTM half-loop to a horizontal half-wavelength dipole in about 200 seconds, which corresponds to average data transfer rate of 4 kbps. The maximum bitrate was seen up to 40 kbps. A long range skywave link over 7000 km was established at 14.243 MHz from Hawaii to Indiana, by using a conventional 3 kHz radio and input power of 100 W [72].

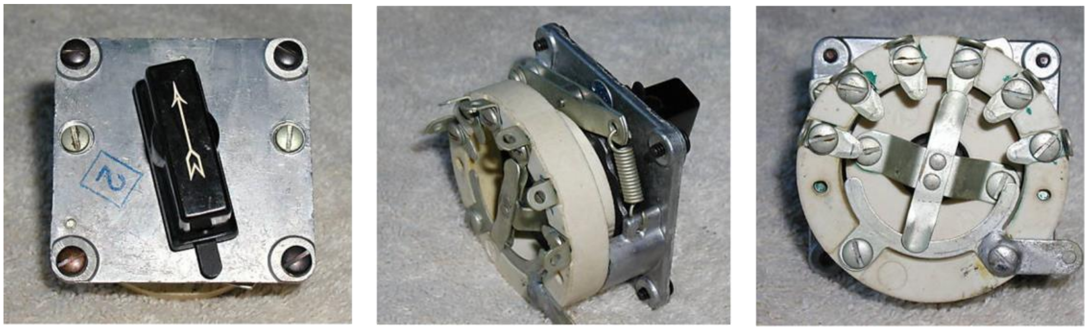

Ceramic Rotary Switch (Front)

Ceramic Rotary Switch (Back)

Fabricating aluminum adapters

4-way Electrical Junction Box

Machining Switch box (Rear)

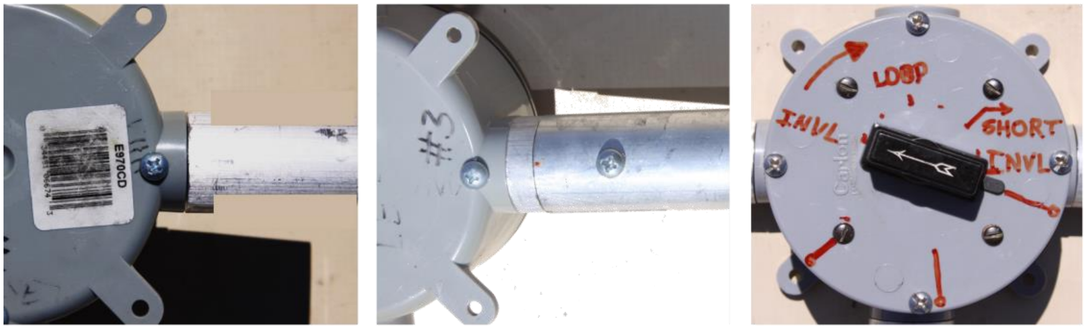

Attaching adapters

Attaching Antenna tubes to adapter

Switch box (Front)

Figure 3.21: Fabrication details of the reconfigurable half-loop / inverted-L antenna switch box using standard hardware parts and switches.

3.7 Switched Reconfigurable HF Antenna Concept

The combination of inverted-L and half-loop antenna designs into a reconfigurable switchable antenna structure would have the benefits of the performance advantages and

Front view

Rear view

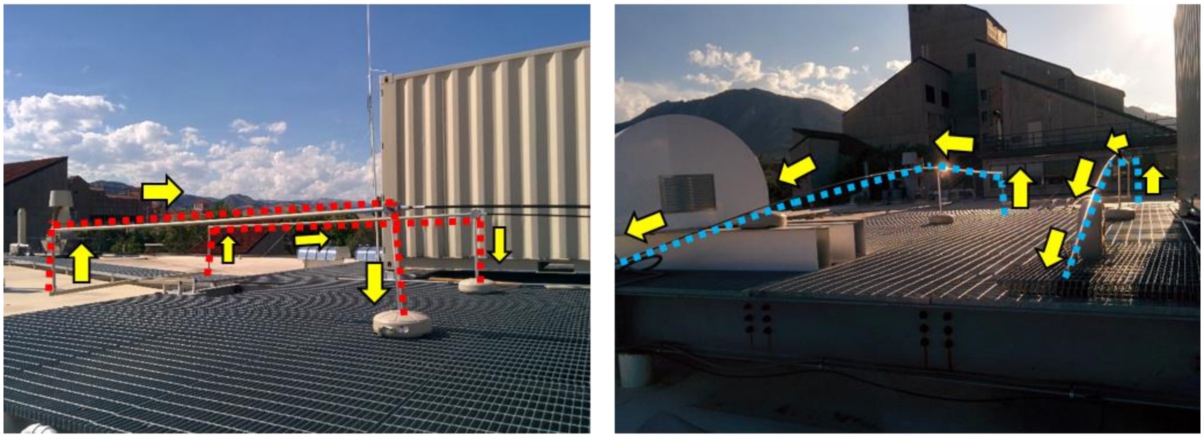

Representation of current flow
(Half-loop mode)

Representation of current flow
(Inverted-L mode)

Figure 3.22: Full installation of the reconfigurable antenna system on the roof of engineering center at the CU Boulder. Metallic scaffolding provides a ground for the antenna. The lower part of the figure virtually depicts the flow of current in the two different operational modes of the antenna.

discussed peculiarities of both these antennas in a single superstructure. The inverted-L and half-loop antennas proposed in this chapter have their respective benefits and challenges. For instance, inverted-L antenna has better omni-directionality within the NVIS frequency range, which is important for ground wave communications while the half-loop antenna has features that can better support NVIS communication. Switching between different antenna modes under specific operating conditions, ionospheric conditions or communication requirements allows for improved overall antenna performance at the expense of added hardware complexity and sophisticated concept of operation.

3.7.1 Utilization of Existing Antenna Hardware

The hardware for this reconfigurable antenna design has been borrowed from the antenna system developed and used for the Agile Bloodhound 2015 demonstration as it is described previously. The reconfigurable antenna however, is fabricated by combining the two antenna concepts into a one operational structure, where the half-loop and the inverted-L modes are switched using a rotary position switch. Mechanical switch is utilized for the proof of concept purpose; in the final design, electronic switching can be realized. Each arm houses the rotary position switch at the junction of the half-loop mode and the inverted-L mode joints. The exact fabrication and assembly of the reconfigurable mode switch box is illustrated in Figure 3.21. The rotary switch is used as a best choice for handling high currents that would exist during operation on the arms of the antenna in the half-loop mode.

The antenna is tested at the University of Colorado Boulder over large metallic scaffolding on the engineering building roof, which was used as a mounting base in place of the M-ATV body. Once the switch box is fabricated, it is internally wired with 8 AWG multi stranded flexible wire soldered on to the rotary switch to establish the connection at appropriate switch poles, such that it connects the antenna arm connected to the feed to the inverted-L or the half-loop mode extensions to reconfigure the antenna on the move. The complete installation of the antenna is shown in detail in Figure 3.22 with the virtual representation of current flow when the antenna is switched for use in either inverted-L mode or the half-loop mode.

3.7.2 Computational Modeling and Measurement Results

The switched reconfigurable antenna is modeled in Altair FEKO. Each of the antenna arms are modeled with a 0.8 Ω series resistor placed at the switch. The 0.8 Ω series resistor corresponds to the contact resistance offered by the switch in the connected state. For the switch position combinations, two computational models are created. The first model configures the antenna in the inverted-L state while the second model configures the antenna in the loop mode of operation. The computational model for the inverted-L mode is solved with the switch on the antenna arm connecting the feed side of the antenna to the long whip

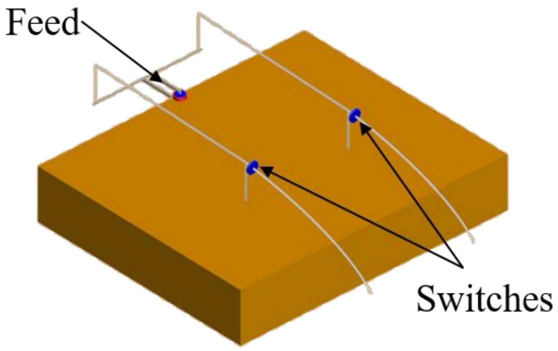

Figure 3.23: Computational model used in Altair FEKO to verify the operation of the switched reconfigurable antenna.

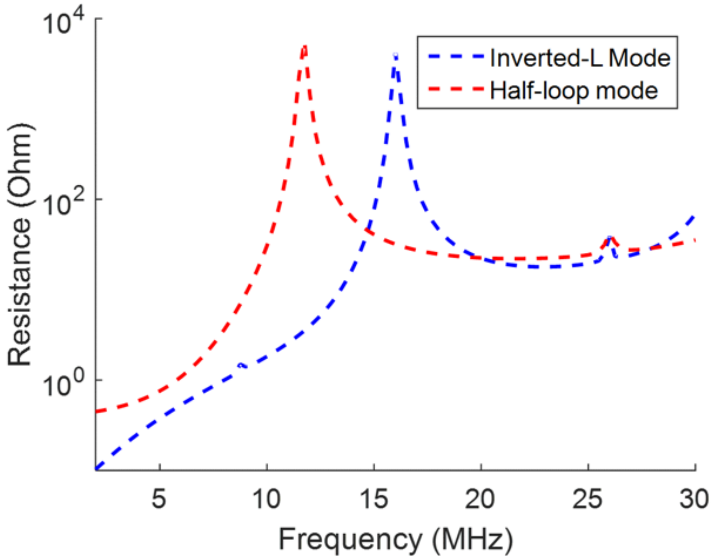

Figure 3.24: Input resistance of the two-arm switched reconfigurable antenna mounted on the steel pedestal with 0.8 m profile and 6 m length. Additional 0.8 Ω switch resistance is taken into account for both the switches housed on the antenna arms.

section and disconnecting the shunting leg. For the loop mode of operation, the switch connects the feed side of the antenna to the shunt legs of the half loop antenna while disconnecting electrical contact from the long whip sections. For the computational model, the vestigial elements are also modeled even if they are electrically disconnected to capture their impact on the antenna due to parasitics. The antenna model is simulated on a steel pedestal 5 m (L) × 7 m (B) × 0.8 m (H). This pedestal corresponds to the metal grill platform that would be used to mount the antenna during actual field tests at the Engineering center at CU Boulder. The computational model used for this analysis is shown in Figure 3.23. The antenna dimensions – 0.8 m profile and ~6.5 m length with 2.4 m width are maintained the same. The antenna hardware parts and material properties are also modeled same as previously described in section 3.3 through 3.6. This model does not include the considerations for effective tuner resistance but includes the switch contact resistances to

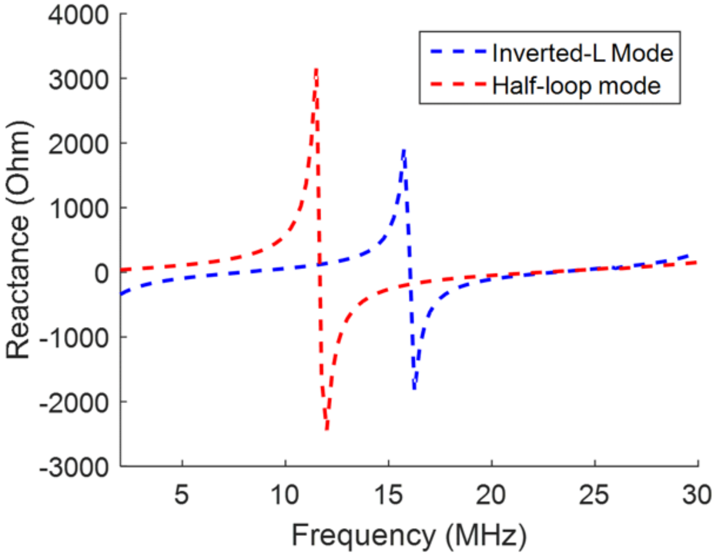

Figure 3.25: Input reactance of the two-arm switched reconfigurable antenna mounted on the steel pedestal with 0.8 m profile and 6 m length. Additional 0.8 Ω switch resistance is taken into account for both the switches housed on the antenna arms.

study the impact of the switching on the antenna. The computed resistance of the switched reconfigurable antenna in the inverted-L mode and the loop mode of operation is shown in Figure 3.24. The input resistance of the inverted-L mode of operation is seen to be higher than the loop mode of operation at the low frequency end. This will make tuning the inverted-L mode much easier at the low end and make it relatively less impacted by other losses from the environment as compared to the loop mode of operation at the lower frequencies. The input reactances for the switched reconfigurable antenna in the inverted-L mode and the loop mode of operation are shown in Figure 3.25. The input resistance is small at the low end confirming electrically small nature of the antenna. The ohmic loss from the switch impacts the input resistance in the case of the half-loop antenna while it does not contribute much to the loss at the low end in case of the inverted-L mode due to the continuity equation bounds, currents established through the switches in the two configurations, and the relative position of the feed compared to the location of the switches. From the impedance data, the antenna has an antiresonance at 12 MHz in the inverted-L mode of operation while the loop mode of operation has an antiresonance at around 18 MHz. The separation of these antiresonances in the frequency domain allows for a fallback option for the antenna to be operated in the other mode at these frequencies in case tuning at the antiresonance proves to be challenging due to rapid changes in the input resistance and reactance influenced due to changes in the environment as the vehicle moves.

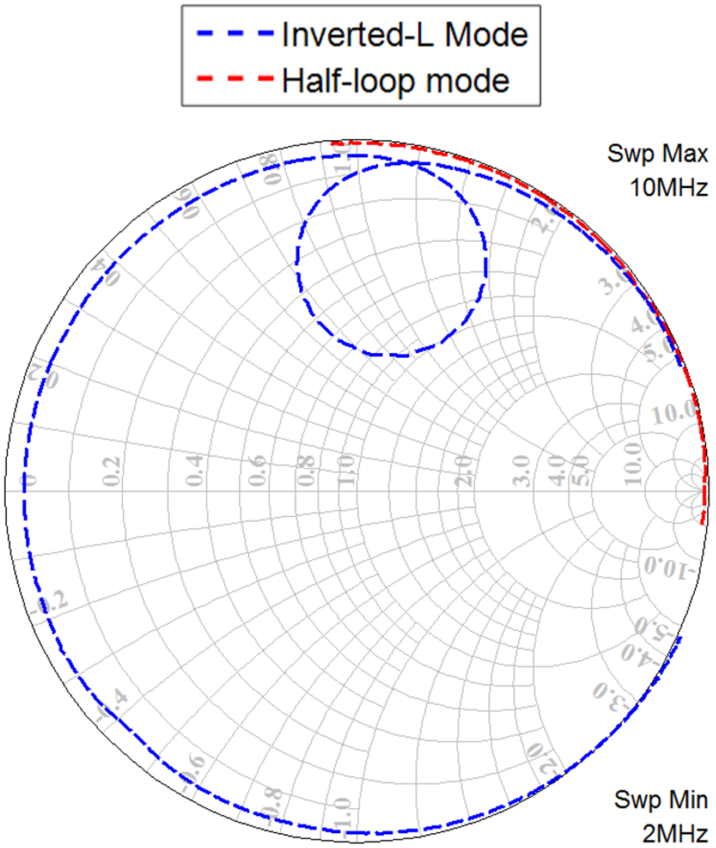

Figure 3.26: Measured impedances of the two-arm switched reconfigurable antenna mounted on the steel pedestal with rotary switches on the antenna arms.

3.7.3 Preliminary Measurements

The measured impedances of the two antenna modes are shown in Figure 3.26. As expected, the antenna is seen to be predominantly inductive for the loop mode and predominantly capacitive for the inverted-L mode of operation with the two configurations of the switches. The two modes of operation are tuned using the COTS Palstar tuner [71]. The tuned impedances for the reconfigurable antenna is measured for the half-loop mode of operation with the Palstar tuner. The antenna can be tuned all the way down to 2 MHz using the COTS Palstar HF-Auto tuner for the half-loop mode of operation. Figure 3.27 shows tuned impedance measurements for this mode over 3 to 10 MHz overlaid in one plot. Contrary to the half loop mode of operation, the inverted-L mode can only be tuned down to 2.7 MHz owing to the limitation of the shunt inductor range used in the Palstar tuner in this case. The tuned impedances measured over 3 to 10 MHz from the inverted-L mode of operation for the

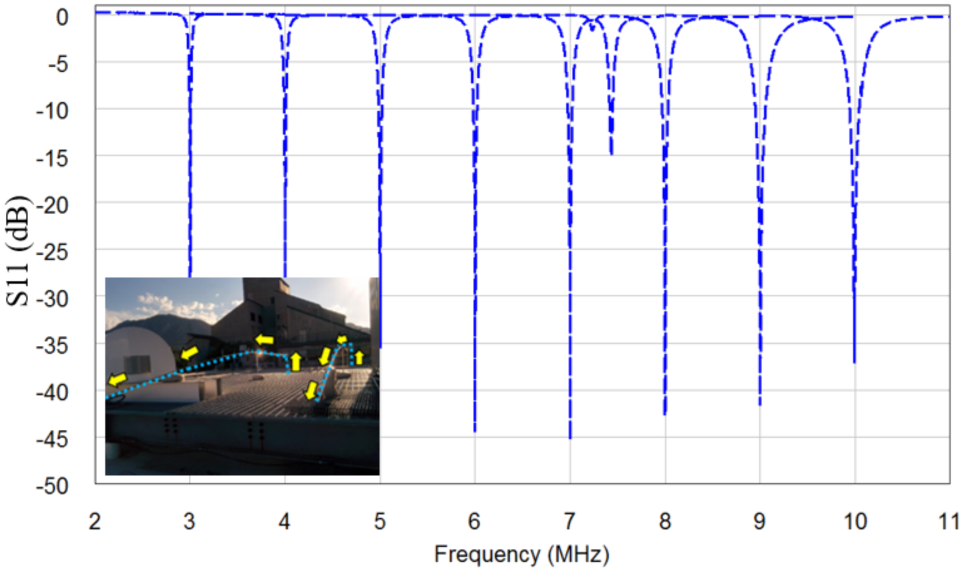

Figure 3.27: Measured S parameters of the two-arm switched reconfigurable antenna mounted on the steel pedestal with rotary switches on the antenna arms.

reconfigurable antenna with the Palstar tuner are shown overlaid in one plot in Figure 3.28.

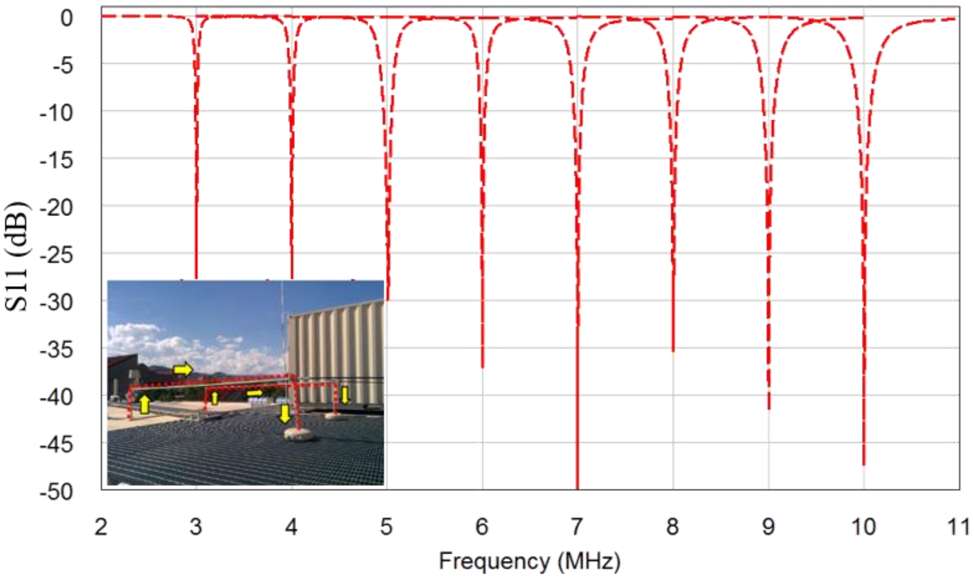

Figure 3.28: Measured S parameters of the two-arm switched reconfigurable antenna mounted on the steel pedestal with rotary switches on the antenna arms.

3.7.4 Discussion for Switched Mode Operation

The switched reconfigurable mode antenna looks quite attractive as a concept for application in vehicular HF antennas. Some important questions and challenges need to be addressed in this direction by a more thorough follow on study for a wholistic design analysis, including:

- Manual mechanical switching may not be suitable for OTM operation. More convenient automatic switching can be achieved with relays driven RF switches and the automatic tuning capabilities of the tuner.

- Switch is shown to introduce extra loss. This leaves less room for possible tuner loss in the half-loop mode. To maintain acceptable gain performance, half-loop size may need to be larger than the equivalent antenna without switches.

- Since HF NVIS OTM antennas are electrically small, significant currents and voltages can be established across the feed during operation. Simple straight switching may result in large power reflection back to tuner with possible damaging equipment. Concept of switchable operation should be carefully considered.

- In addition to the half-loop / inverted-L re-configurable antenna, switching between a monopole and half-loop can be another combination. In later case, antenna can be designed to be more compact in horizontal dimensions.

3.8 Summary

The design and full scale prototyping of a low profile, wideband, OTM capable vehicular HF antenna is discussed. Antenna shows promise to support all modes of HF communication. This study paves the way for the design of electrically small HF antennas over other land and ship based platforms in the future.

The design approach discussed in chapter 2 is adopted herein for the development on the M-ATV platform. The proposed antenna is made with mechanical reconfigurability in mind. For the inverted-L mode of operation for the M-ATV, the antenna has two arms with base feed. The antenna dimensions are: profile of 0.8 m (λ/125 at 3 MHz), 6.5 m length and 2.4 m width. The proposed antenna can be mechanically reconfigured on the vehicle in three modes of operation including the half-loop mode and the top loaded monopole mode, although this chapter focuses specifically on the inverted-L vehicular antenna design and development aspects. Each of the modes has its own set of benefits in terms of support of HF propagation modes, requirement of access to grounds on the vehicle, sensitivity to losses in the environment, ease of tuning and others. Majority of the antenna structure and features are maintained common between the three modes of operation to make mechanical reconfiguration easier.

Computational analysis of the antenna is discussed for the inverted-L mode. The results from the computational analysis show that the vehicular antenna can support the desired 24 kHz wideband HF operation with zenith gain better than -20 dBi over the M-ATV platform. Computed impedance over different grounds show that the impedance profile of the antenna is consistent with change in grounds and encourages the use of same tuning architecture over various grounds. The computed antenna patterns show that the antenna has a slight null in gain pattern close to zenith at low frequencies and this null gets weaker at higher frequencies.

The full scaled prototyping and fabrication process is discussed in detail. The evolution of the antenna from a concept to a computational model and then to an early stage prototype by adhering to the previously demonstrated design process is described. Practical aspects of antenna fabrication and fitting for various parts of the antenna on the vehicular host platform are considered to realize the antenna. Adjustable sleeve joints with the aluminum-copper-aluminum interface are shown to be a practical interface that provides an antenna structure with the desired dimensional flexibility for platform integration. The antenna is fed using feed through ceramic posts. The feed is demonstrated to work well from an electrical as well as structural point of view. Successful integration of a COTS tuner to tune the antenna over desired HF frequencies of operation is demonstrated. The use of COTS tuner over the entire range of frequencies, including the region of antiresonances shows that the antenna can be tuned and operated at anti resonance in static conditions. Modular mounting and integration provisions of the antenna are used to integrate the antenna onto various platforms such as a steel pedestal, the M-ATV mockup on the aluminum box, and the actual M-ATV without much modification to the antenna structure throughout the development and field testing process. Preliminary testing results and the process adopted to familiarize with the aspects of field operations and HF communications are shown. Use of mountainous terrain for separation between the AUT site located at the engineering building of CU Boulder and the remote test site is shown to ensure that NVIS mode of communication is established for all tests during the preliminary testing phase.

Antenna pattern and gain measurements are performed at the SPAWAR APR facility in San Diego, CA. An M-ATV platform mockup is used for these measurements due to limitations of the measurement facility and the lack of availability of an M-ATV vehicle at the testing site. The electrical and mechanical integration of the antenna on the platform mockup is shown. COTS tuner is interfaced with the antenna on the platform mockup for these measurements. The tuner is shown to tune the antenna over all frequencies from 3 to 30 MHz in a static case in both the tuning scenarios, first over the vehicular mockup and later over the M-ATV platform in spite of the presence of antiresonances. It is important to note that on-the-move conditions were not tested on the M-ATV, since OTM operation of the antenna system is prohibited due to safety and certification related constraints. It is expected that in a dynamic case, where the host vehicle moves, the antenna may need some re-tuning to counter the impact of the changing environment on the antenna impedance, irrespective of the proximity of the operating frequency to anti-resonance. The details of such dynamic on-the-move tuning for a vehicular HF antenna such as the one proposed herein are outside the scope of the current work showcased in this chapter. The gain and pattern measurement data confirm that the proposed antenna can support NVIS mode of propagation at the low frequency end and ground wave and long-range sky wave modes of propagation over the higher frequency ranges since it has significant radiation directed towards the horizon at higher frequencies. Quantitatively, the measurement results relate well with the computational analysis for the antenna placed over a PEC ground with the peak gain saturating at -9 dB in the 3 MHz to 10 MHz NVIS frequency range. The zenith gain is shown to be better than -18.4 dB at 3 MHz and increases to -10 dB at 10 MHz.

The computational design is validated by means of the full scaled measurements and field experiments. The vehicular integration of the proposed antenna is shown. The soldier friendly antenna can fit in a kit measuring 1.5 m (L) x 0.3 m (W) x 0.2 m (D) and weighs less than 12 kg. It can be deployed on the M-ATV within 15 minutes by a two person/soldier team as was done throughout the field demonstration campaigns. The antenna can work with all existing vehicular antennas and systems in place. Ferrite beads and choking coils are used to avoid any return currents on the coaxial cable from radiating. Impedance measurements on the M-ATV are shown to agree well with the predictions. This gives confidence in design tools used. There is a drift of 0.5 MHz between the measured and computed resonance and antiresonance locations and the difference is ascribed to the lack of accurate knowledge of materials on the M-ATV, the simplified computational model, grounds and the measurement environment.

The field demonstration of the antenna mounted on the M-ATV is performed. Successful integration with a WB HF radio is conducted. The antenna in half-loop configuration on the M-ATV is used to demonstrate wideband HF connectivity between two testing locations using 24 kHz wideband waveforms. The link is set up over a distance of 14.5 km (9 mi) at 8.006 MHz. Analysis of delay and signal strength confirms that the main communication mode was NVIS. With an average input power of 30 W (230 W peak) a file of 99196 bytes was transmitted from the OTM half-loop to a horizontal half-wavelength dipole in about 200 seconds, which corresponds to average data transfer rate of 4 kbps. The maximum bitrate up to 40 kbps is seen to be supported by the antenna system. For the inverted-L mode of operation of the antenna, a long range skywave link over 7000 km was established at 14.243 MHz from Hawaii to Indiana, by using a conventional 3 kHz radio and input power of 100 W.

The proof of concept validation for a switched reconfigurable mode vehicular HF antenna is demonstrated in the last part of this chapter. The existing antenna hardware is modified to house a switch on each arm to reconfigure the antenna in the inverted-L or the loop mode of operation. Computational modeling results show that the antiresonances of the two modes of operation are spread in frequency thereby giving the advantage of a fall back in case tuning the antenna around the antiresonance frequencies proves to be challenging in rapidly changing environments. Impedance measurements show expected results where the antenna is inductive for the loop mode and capacitive for the inverted-L mode of operation. COTS tuner is interfaced to this antenna and tuning over 3 to 10 MHz is demonstrated.

The practical challenges with the realization of this antenna are discussed in the concluding part of this section. From the discussion, it is clear that the design and development of an antenna with easy, practical and possibly OTM, electronically switched structure for the different modes of operation of the antenna would be highly desired despite the practical challenges. Such an antenna would truly be beneficial for flexible antenna reconfiguration to diverse communication conditions and operational scenarios in the future.

Chapter 4

Assembly Strategies for Isolation Improvement of Millimeter Wave Front Ends on Space Constrained Cylindrical Payloads

4.1 Introduction

The part of electromagnetic spectrum with frequencies between 3 Hz to 3 THz comprises of the radio spectrum [79]. Electromagnetic waves are used for various applications across the radio spectrum for modern telecommunications, sensing, weather forecasting, satellite operations, remote sensing, telephony, automotive applications and so on. Like most other resources, the radio spectrum is also a fixed commodity that is compartmentalized into various sub sections based on the range of wavelengths, atmospheric attenuation, and interaction for efficient management. Typical characteristics of the radio waves in a particular frequency range, and the local as well as national administrative guidelines laid out for governance and regulation influence such classification of frequencies into different bands. The allocation of various services across different radio frequency bands helps avoid interference of multiple services with each other. The international body that coordinates and presides over the shared global use of the radio spectrum is called as the International Telecommunication Union (ITU) [79], while radio spectrum is regulated in the USA by the Federal Communications Commission (FCC) [80]. The need to service emerging commercial applications, coupled with the proliferation of wireless technology has led to spectrum congestion and a push to migrate towards the unused spectrum at higher frequencies. The millimeter wave band, ranging from 30 GHz to 300 GHz is viewed as a potential resource for deploying new services [79]. Commercial and military applications at millimeter wave seek to exploit the wider fractional bandwidth and channel capacity. Propagation characteristics of millimeter waves allow for better spatial reuse and smaller wavelengths mean a scope for reduction in hardware size. Current allocation for millimeter wave frequencies include: fixed wireless, mobile wireless, space research, earth exploration, radio astronomy, fixed satellite, aeronautical radio navigation, radiolocation, satellite based broadcasting, amateur radio, amateur radio satellite, inter satellite communication, satellite based radiolocation, terrestrial broadcasting, satellite and terrestrial broadcast of standard frequency and time signals, and deep space communication and research [80]. Such a wide diaspora of services emphasizes the importance of millimeter waves. Typically, the frequencies from 18 GHz to 30 GHz exhibit most of the characteristics and benefits of the millimeter waves band and therefore are also regarded as millimeter wave frequencies in this work.

The frequency range of 18 GHz to 45 GHz form the focus of this chapter. Computational studies highlighting the impact of integration strategies for a horn antenna planned for deployment inside a space constrained cylindrical payload are shown. The system level integration and analysis of antenna and transmission line plumbing for a millimeter wave repeater system is discussed. The results of the antenna level analysis inspire the system level design methods. The system level analysis addresses the impact of internal RF leakage in a cylindrical payload on the overall system isolation performance. Practical, low cost mitigation techniques for curbing the identified internal RF leakages are demonstrated through isolation measurements. This chapter is organized into four major sections followed by the summary as described below.

- Section 4.2 discusses the research motivation for the work presented in this chapter. Typical millimeter wave front ends are described with a focus on their fabrication.

The challenges related to integration in a space constrained payload are shown.

- Section 4.3 discusses the fundamentals of shielding and RF leakage at millimeter wave frequencies.
- Section 4.4 discusses the antenna level analysis for integration and RF leakage. A horn antenna made from individual metal parts assembled together is considered. The impact of the seams on the antenna performance is discussed.
- Section 4.5 discusses the system level integration of a simple millimeter wave RF repeater system. An approach for the analysis of system level internal RF leakage is shown. Isolation measurements suggest that internal RF leakage can be a concern for the repeater operation. Mitigation technique to curb the internal RF leakage is proposed and the isolation results are shown through a series of measurements.
- Section 4.6 summarizes the chapter and lays out the important conclusions.

4.2 Motivation

The propagation mechanics for radio frequencies in the millimeter wave band can be understood based on four factors of transmission, reflection, diffraction and refraction [81]. The transmission losses experienced by an RF signal in free space are accounted by the free space path loss. For a simple setup with two antennas, one hooked up to an RF source and the other to a receiver on the other side, the free space path loss is given by [82]:

$$FSL_{dB} = 20\log_{10}\left(\frac{4\pi}{c}\right) + 20\log_{10} f + 20\log_{10} R - \mathrm{G}_{Tx} - \mathrm{G}_{Rx}, \qquad (4.1)$$

where, 'f' represents the frequency of the propagating signal expressed in Hz, 'R' is the line of sight distance between the transmitting and receiving antennas, expressed in meters, while 'c' represents the speed of light in vacuum expressed in m/s. The terms 'G_{Tx}' and 'G_{Rx}' represent the antenna gain in dB for the transmitting and receiving side respectively. From the equation, we can see that the free space path loss has a direct proportionality to the operating frequency 'f' and the distance between the two antennas 'R'. For instance, the free space path loss for two isotropic antennas separated by 1 m distance at 20 GHz is 58.5 dB. Similar analysis for a frequency of 40 GHz with isotropic antennas separated by 1 m distance gives a free space path loss of 64.5 dB. It is worth noting that as frequency is getting higher, the absorption of signals from atmospheric elements such as water vapor and oxygen starts becoming significant. The atmospheric attenuation of radio waves at sea level is shown in Figure 4.1 [83]. Other factors such as diffraction from edges, attenuation through hydrometeors like rain, fog, mist, flurries, hail or snow and blockage by foliage and scattering effects start becoming dominant for millimeter wave frequencies as compared to frequencies in the UHF range [84] [85]. The free space path loss increases with frequency, making the path loss a significant design parameter to be considered at millimeter

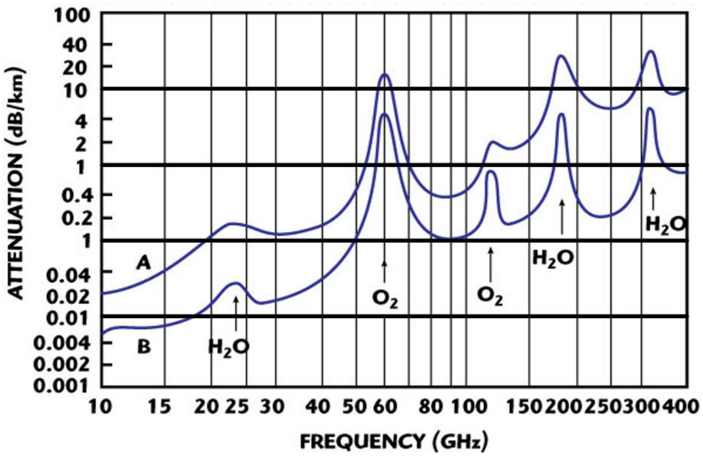

Figure 4.1: Average atmospheric absorption of millimeter waves [83]. Atmospheric conditions represented by trace A: Sea level; T = 20°C; P=760 mmHg; H_2O = 7.5 g/m^3. Atmospheric conditions represented by trace B: Altitude = 4 km; T = 0°C; H_2O = 1 g/m^3.

wave frequencies. However, for all practical purposes, millimeter wave systems look appealing because of the benefit of support for larger bandwidths and the promise of small system size compared to current systems operating at lower frequencies. Given the above background of millimeter wave systems, the design of large scale, reliable and practical millimeter wave wireless infrastructure needs to address the impacts of the path loss and other environmental losses. The propagation properties and atmospheric absorption suffered by millimeter waves therefore make it imperative to use repeaters for range extension and achieving uniform, reliable, and wide area coverage over millimeter wave frequency ranges.

4.2.1 Millimeter Wave Front Ends

The typical examples of antennas used in millimeter wave applications include travelling wave antennas as well as aperture antennas [86]. The antenna elements such as the monopole, dipole and loops are not readily used in millimeter wave applications owing to narrow bandwidth and integration challenges. The use of slots, patches and active antennas is common in millimeter waves. Traveling wave antennas at these frequencies include leaky wave antennas, slotted waveguide, tapered slot antenna, and loaded dielectric rod antenna [87]. The aperture antennas used in millimeter waves include horn antennas, and lens based or reflector based antennas [87]. Other variants such as the substrate integrated waveguide antenna, and planar Yagi-Uda arrays are also extensively used in millimeter waves [87].

The horn antennas are well known and widely used in the commercial and defense sectors at millimeter waves [88] [89]. Recent advances in additive manufacturing have supported the proliferation of light weight, low cost horn antennas on aerial platforms for communication and wideband sensing applications [90] [91] [92] [93]. The potential for millimeter wave horn antenna applications range from high power operations, highly directive systems, wideband phased arrays, space and satellite communications [94] [95]. It is important to note that horn antennas for satellite based applications often require integration of complex features inside the throat to support specific illumination profiles based on the desired service area for the satellite. Integrated injection probes, and complex feed structures that allow for multiband operation from the same structure are also desired in horn antennas for satellite applications. For instance, the K/Ka band antenna for earth observation mission can have multiple feeds and complex OMT integration [96]. The horn antennas for space applications need to be lightweight and compact with provisions for support brackets and mounting hardware built into the antenna body [97]. Satellite applications often use horn antennas either as radiators or as feed elements. The use of horn antennas allows to combine few bands together in one structure or incorporate a 'horn-in-horn' design with the high band horn element integrated into the center core of a low band coaxial horn [98] [99]. The complexity of these designs mentioned above is justified by the corresponding savings in weight, smaller size or the reduction in overall system level complexity on the satellite. However, it must be noted that such complex horn antennas require specialized manufacturing processes. Such horn antenna designs are often manufactured in two or more parts and are joined together with fixtures owing to the limitations of the conventional CNC and wire EDM tools, and to maintain simplicity in fabrication. This fabrication and integration approach of making the antenna in parts necessitates a radial cut in the horn antenna throat. Example of some fabricated horn antennas made from different parts integrated together with the cut feature along the throat are described in detail in the references [96] [97] [98]. The integration of a complex K/Ka band feed horn for satellite payload with three LP OMT's integrated at the feed for operating at 18, 24 and 36 GHz is shown in [96]. A lightweight machined corrugated feed horn antenna operating at C band is shown to be fabricated in two conical parts joined together for the antenna region and multiple waveguide plumbing parts joined together for the OMT connected to the antenna [97]. A multiband corrugated horn feed for satellite ground stations is shown to be made from multiple injection probe sections connected to two conical parts that are joined together using fixtures to form the complete antenna structure [98]. The impact joining parts and introducing seams and cut features on the horn antenna on its performance is studied in the first half of this chapter. Such integration approach for antennas to make the fabrication and integration easier can be a cause for concern in repeater applications where the antenna seams that joins the individual parts together becomes a cause for RF leakage which in turn deteriorates the system level isolation.

4.2.2 Space Constrained Payloads

Space constraint is a major challenge for satellite payloads and repeater applications. These payloads have strict power, mechanical and thermal specifications. The capability of handling high powers and low loss at millimeter wave frequencies makes the use of waveguide plumbing an ideal choice for transmission lines in these applications. The assembly of RF components using existing fabrication techniques is challenging due to the payload size constraints, and the complexity of the waveguide plumbing. Consequently, if the RF front end and waveguide plumbing is fabricated in parts and assembled step by step inside the payload to address the desired system level integration challenges, the concerns of RF leakage and system level isolation arise. An example of a satellite repeater system with the integration inside the payload is shown in [100]. From the description of the system, the tight integration of the RF components and the waveguide plumbing inside the space constrained cylindrical shell of the repeater payload is clearly seen [100]. The deterioration in system level isolation and self-coupling from RF leakages is highlighted as a potential problem. The system description also talks about the noise issues due to multiple reflections inside the metallic cylindrical payload.

It is required that the transmit and receive channels in a repeater are adequately isolated to avoid feedback that can cause magnitude and phase errors in the repeated signal or send the repeater into uncontrolled oscillations [101]. To maintain stable repeater operation, the total gain of the transmit channel needs to be set lower than the isolation level between the transmit and receive channels. Thus, the repeater gain is bounded by the isolation level achieved, meaning that high levels of isolation would be desired for operating the repeater at higher power levels. Typically, the isolation between Rx and Tx channels in a repeater is required to be higher than 85 to 90 dB [102]. Since the repeater is comprised of many parts connected together, RF energy leakages can occur at multiple levels in the repeater system. The coupling mechanism in repeater payloads works through three major paths: free space coupling, coupling through the surface currents on the payload and the coupling through the internal RF leakages from various sources. Potential ways to reduce the coupling may include treatment of the individual components as well as treatment of the entire integrated system. For instance, the free space coupling can be reduced by increasing the antenna separation, engineering the antenna patterns with low gain at horizon and by aligning orthogonal antenna polarizations when deployed on the payload. The coupling through surface currents can be addressed using absorber or by design of a reactive impedance surfaces that can suppress the surface currents flowing between the transmit and receive antennas [103] [104] [105]. Technique to mitigate the internal RF leakages from waveguide components is suggested with the use of a pin wall based design in [106]. It is vital to recognize that the impact of internal RF leakages on the system level isolation can be severe and that component level reduction in RF leakage alone is not enough for a complex repeater system. The measurement results shown later for the described payload show that internal RF leaks deteriorate the isolation to below 80 dB, making the repeater operation practically impossible. A low-cost solution for mitigation of internal RF leakages for millimeter wave and quasi millimeter wave repeater payloads is hereby presented with measurement results that prove its effectiveness.

4.3 RF Shielding Fundamentals

Use of RF shields is one of the way for mitigating the impact of RF leakages coming from the antenna and waveguide plumbing interfaces. It is worth noting that although traditional shields made from metal sheets can work at millimeter wave frequencies, they need to be installed very carefully for effective shielding. Integration of metallic sheets as shields is very cumbersome and complicated given the dense packing and complex cross sections of components inside the repeater payloads. Achieving the tight mechanical tolerances desired for good integration becomes very challenging in such scenarios. Small crevices and joints at the metal shield and host payload platform interface are undesired as they cause leakage of RF energy and deterioration in the shielding effectiveness. The shields would also need effective seals made from conductive sealant material at the seams between the shield and the payload body as an added measure to restrict leakage from the joint between the shield and the payload. Installing metal sheet shields also adds weight and inhibits any future modifications to the payload which might be undesired from maintenance and servicing perspective and not preferred in many use cases such as test beds, prototypes

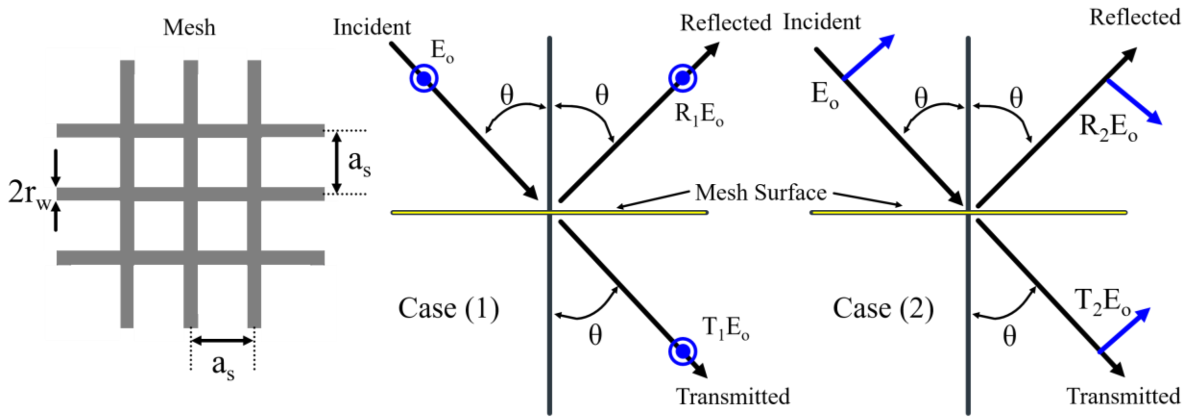

Figure 4.2: Geometry of the wire mesh considered for the analytical approach. The mesh grid is square and the wires forming the mesh are considered to be fused together at the junctions. The two considered cases of incident electromagnetic plane wave polarization (parallel and inclined) with respect to the lossless mesh are also shown alongside. The E field vector polarization is parallel to the mesh surface in case (1) and inclined to the mesh surface in case (2).

and modular repeater systems. To circumvent the problems with metallic sheets for use as RF shields, the use of flexible metallic meshes is proposed in this work as a mitigation approach for internal RF leakage. Metallic meshes are easier to integrate inside the payload. Achieving good shielding inside the payload is easier with metal mesh shields as their flexibility allows for changes to the payload configuration and parts. Metallic meshes allow for use of passive and active / forced air cooling inside the payload unlike sheet metal shields. Metallic meshes also have weight advantage compared to traditional sheet metal shields and are less prone to damage from shock and vibe in various operating environments.

A summary of the theory of scattering from wire grid structures is shown by Wait [107]. The low frequency analysis of apertures loaded with meshes is shown by Casey in [108]. Following this analysis, the analytical approach for the analysis of shielding effectiveness of metallic meshes is explained by Casey in [109]. The geometry of the wire mesh considered for this analysis is shown in Figure 4.2 (left). The mesh is considered to be lossless. The mesh wire radius is represented as 'r_w'while the inter wire spacing – center to center is 'a_s'. Two cases of plane wave polarization for the incidence on mesh surface are considered.

Casey developed expressions for shielding effectiveness of a mesh screen. The shielding effectiveness is a measure of the ratio of the incident field strength without a screen to the field strength with the screen interposed between the source and the measuring device. For the plane wave case, field effectiveness is a transmission (insertion) loss. Shield effectiveness for the two cases shown in Figure 4.2 is [109]:

$$SE_1(\theta) = -20\, log_{10} \frac{(2\omega L_s/Z_0)\, cos\theta}{\sqrt{1 + \, (2\omega L_s/Z_0)^2\, cos^2\theta}}, \tag{4.2}$$

$$SE_2(\theta) = -20\, log_{10} \frac{(2\omega L_s/Z_0)\,\left(1 - \frac{1}{2} sin^2\theta\right)}{\sqrt{(2\omega L_s/Z_0)^2 \left(1 - \frac{1}{2} sin^2\theta\right) + cos^2\theta}}, \tag{4.3}$$

where, 'Z_0' is the free space impedance and sheet inductance 'L_s' is:

$$L_s = \frac{\mu_o a_s}{2\pi} \ln(1 - e^{-2\pi r_w/a_s})^{-1} \,, \tag{4.4}$$

Casey also defined a polarization independent shield effectiveness 'SE_0' as:

$$SE_0(\theta) = -10\, log_{10} \left\{\frac{1}{2}\, |T_1(\theta)|^2 + \frac{1}{2}\, |T_2(\theta)|^2\right\}, \tag{4.5}$$

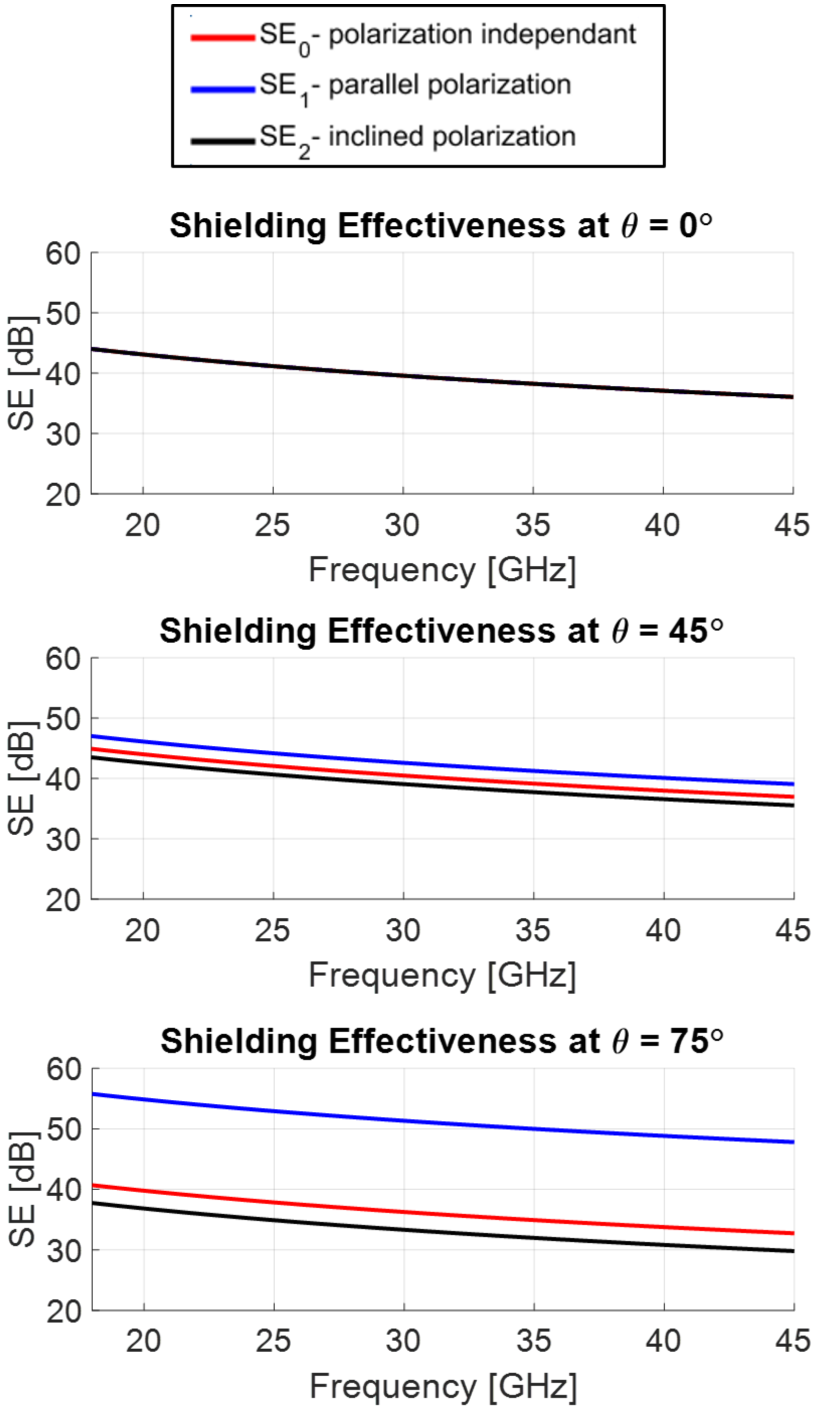

Figure 4.3: Shielding effectiveness of lossless wire mesh with plane wave incidence across frequency and for various angles of incidence. The mesh parameters used are: mesh grid size a_s = 195 µm; mesh wire radius r_w = 45µm. At normal incidence, $SE_0 = SE_1 = SE_2$.

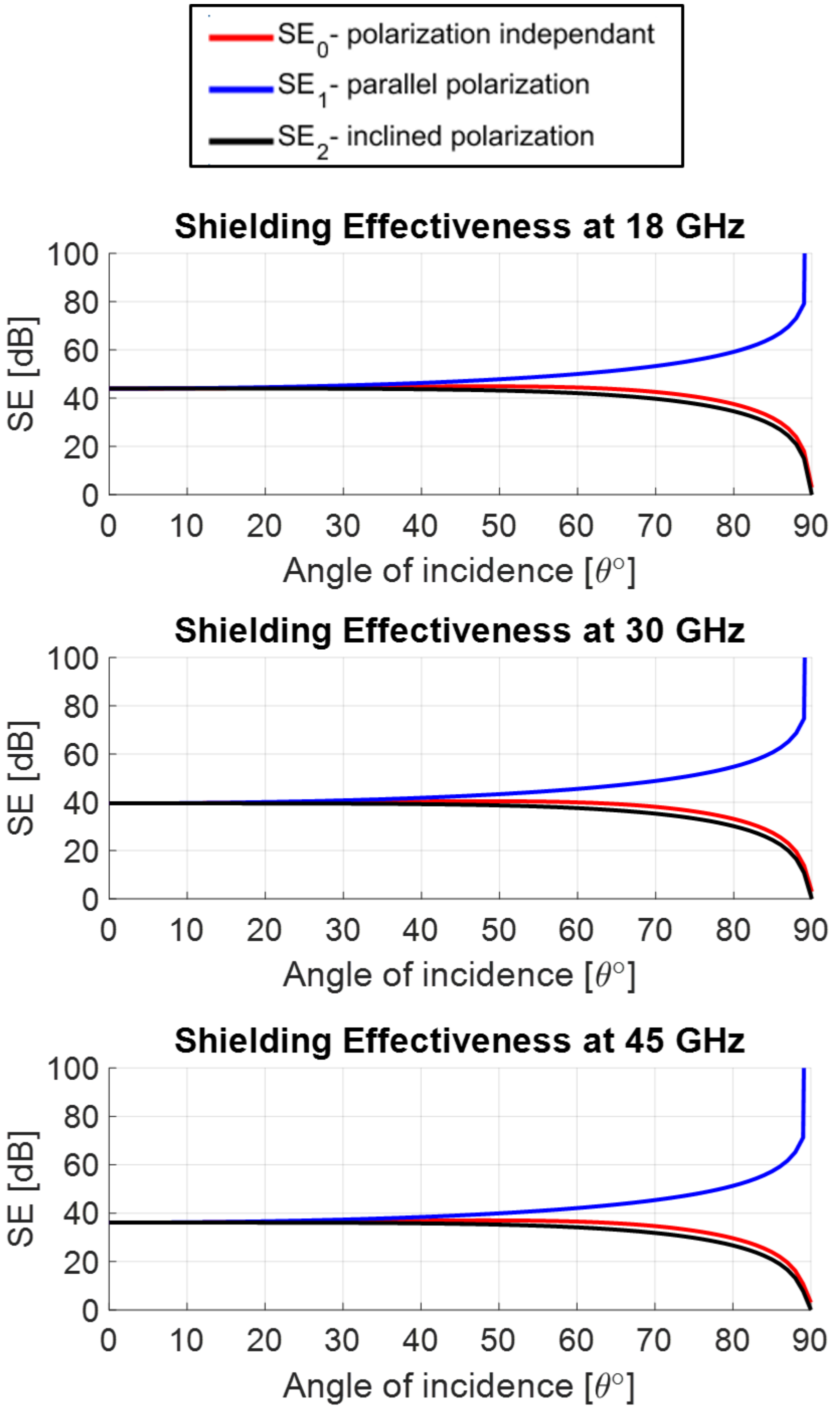

Figure 4.4: Shielding effectiveness of lossless wire mesh with change in incidence angle of the plane wave incidence for 18, 30 and 45 GHz. The mesh parameters used are: mesh grid size a_s = 195 µm; mesh wire radius r_w = 45µm.

The shielding effectiveness for a sample PEC mesh with mesh grid size a_s = 195 µm, mesh wire radius r_w = 45µm, and incidence of plane wave is shown in Figure 4.3. The parameters for the mesh shown here correspond to the parameters of the actual conductive mesh fabric used in the measurements. It is seen that the mesh can potentially improve isolation by 30 – 35 dB depending on the incident angle. The shielding effectiveness of the same mesh with change in angle of incidence for 18 GHz, 30 GHz and 45 GHz is shown in Figure 4.4.

From the plots shown above, we can see that the shielding effectiveness of wire meshes is a function of the incidence angle of the plane wave on the mesh surface. We can also see that the polarization independent shielding effectiveness first increases slightly with increase in angle of incidence and then decreases as we approach angle of incidence θ=90°. At angle of incidence of θ=90°, both the SE_0 and SE_2 asymptotically approach zero while SE_1 reaches a very high value. The analytical study helps us set some expectations of the performance and behavior of wire mesh shields for practical use as will be shown later in this chapter.

4.4 Analysis of horn antenna with cut plane

The impact of integration and fabrication provisions on the antenna performance is studied. The focus of this investigation is to assess the impact of a radial cut plane in the throat of a horn antenna. Fabrication limitations may necessitate the cutting the horn antenna at its neck for meeting payload integration requirements. Impact of such cutting on the antenna performance is discussed. Steps to model the impact of small cut features inside the throat of a prefabricated horn antenna on its electrical performance are demonstrated. Simulation results for the reflection coefficient of the prefabricated antenna with a purposely introduced, well defined air gap show good agreement with measurements. The corroboration between the simulation and measurement is used to validate the computational modeling process adopted for the antenna level studies performed thereafter.

Fabrication of horn antenna in parts introduces seams and air gaps at the mating interfaces. Impact of these air gaps formed between the metal parts of the horn antenna is investigated. Leakage of fields into the air gap formed due to the cut operation is shown. Analysis of horn performance for a uniform air gap model and a more practical, random air gap model is shown herein. Measures to mitigate the RF leakage from the horn body by using a shorting pin wall are discussed as part of the antenna assembly. The proposed path towards the development of an 18 – 45 GHz horn antenna designed to be integrated inside a space constrained cylindrical repeater payload is discussed [90]. Space constraints inside the platform and required conformal mating necessitate the development of the antenna as a modular two-part system. The possibility of RF leakage from the mating of the two parts of the horn antenna inside the platform motivates the development of the discussed mitigation strategies. The experimental validation of the impact of small cut features inside the throat of a prefabricated horn antenna is first shown as a means of validating the adopted computational modeling techniques. The computational modeling for this validation experiment is analyzed in an FEM solver, ANSYS HFSS and the results are validated through measurements [2]. The impact of the presence of a uniform air gap between the mating faces of the top and bottom parts of the integrated antenna is discussed. Modeling and analysis of horn antenna performance with a more realistic, non-uniform, random air gap is described in detail towards the end of this section.

4.4.1 Validation of Computational tools

The impact of small features on the throat of a horn antenna is computationally modeled and thereafter validated using measurements. The antenna used for this validation is prefabricated based on the design described in [110]. For purposes of validation, the horn antenna is modified with a cut pattern inside its throat region (Figure 4.5). Minute radially oriented sectorial gaps are introduced in its throat. The cutting operation is performed using a 0.4 mm (1/64") diameter milling tool. The antenna is mounted on a rotary table to achieve the cut operation. The description of the fabrication process is shown in Figure 4.6.

The computational model used is shown in Figure 4.5 along with the details of the horn antenna. The antenna is a flared quad ridge horn antenna with an aperture opening of 45.72 mm (1.8 in) in diameter and height of 76.2 mm (3 in) with a ground plane bezel of 71.12 mm (2.8 in) outer diameter. The cut operation performed on the prefabricated horn is replicated in the computational model. The antenna VSWR before and after introduction of

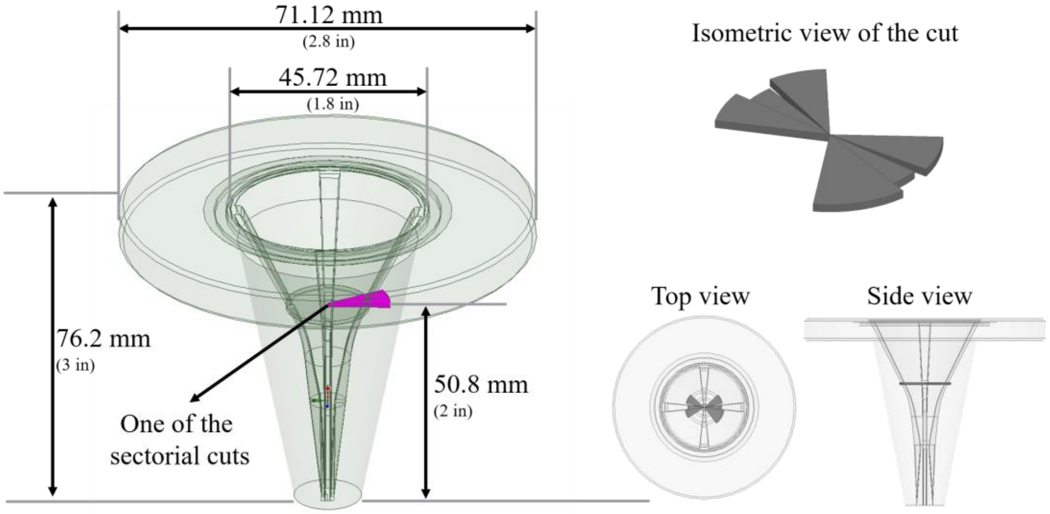

Figure 4.5: Computational model used to model the impact of a radial cut inside the throat of the horn antenna.

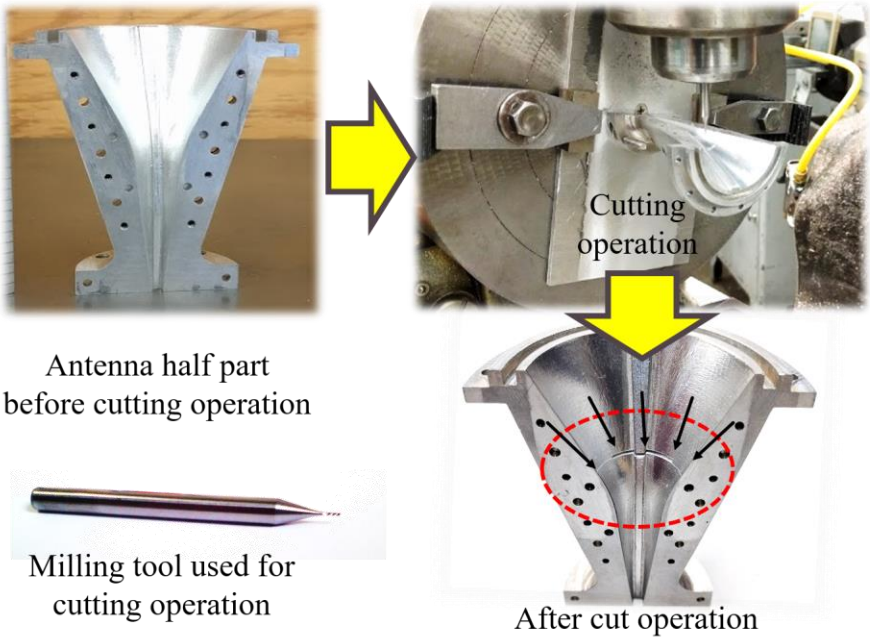

Figure 4.6: Fabrication process for introducing radial cuts in the throat of the prefabricated horn antenna. The antenna is used as a validation test bed to verify the modeling capability of the computational tool.

the cuts is shown in Figure 4.7. Cutting the antenna at the throat has significant impact on its match over the entire band of operation. There is good agreement between the measured and simulated results for the horn antenna with the cut along its throat. This gives us confidence in the computational model described herein as well as the computational tool used in this analysis. Good agreement between the measured and the simulated S-parameters shows the capability of the computational tool used to handle such complex problem involving small features inside the throat of the horn antenna. The agreement between the measurement and the simulation results lays the foundation for the studies performed on a more complex, realistic antenna shown in the following sections.

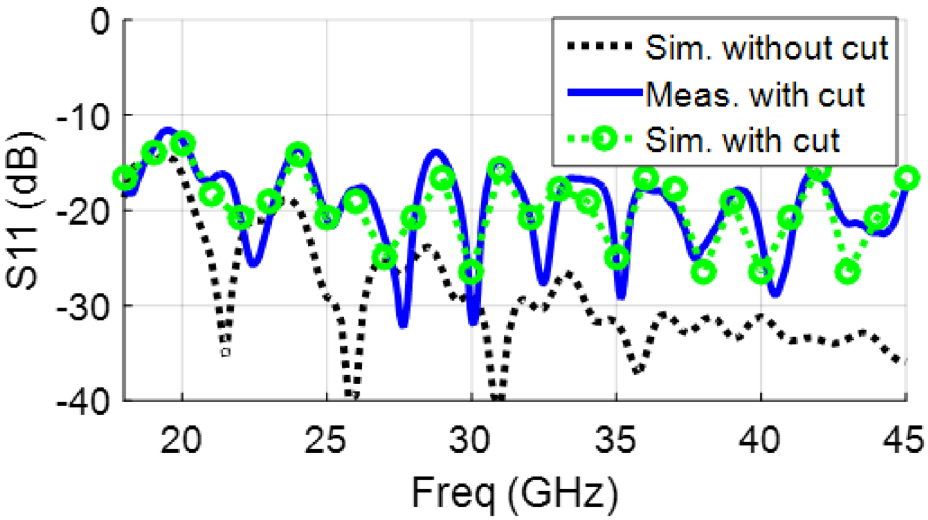

Figure 4.7: Impact of radial cuts on the antenna match. The comparison between measured and simulated performance of the antenna after cutting shows good agreement between the two.

4.4.2 Study on Flared Quad Ridge Horn Antenna

A more realistic and complex horn antenna considered for the assembly and leakage studies is shown in Figure 4.8 below. The total height of the flared horn antenna is 40.64 mm (1.6 in). The antenna aperture has a diameter of 36.83 mm (1.45 in). The antenna is divided into three parts for purposes of mechanical assembly and integration inside the payload. The top section houses the antenna aperture and is 12.7 mm (0.5 in) tall, the bottom section is 27.94 mm (1.1 in) tall and comprises of the antenna throat and the feed section. The pin wall assembly is sandwiched in between the top and bottom sections of the antenna. The assembly is made from 12.7 mm (0.5 in) long, 0.4 mm (1/64 in) diameter pins placed around the rim of the antenna interface joining the top and bottom sections. The pins are set at a diameter of 39.37 mm (1.55 in) with a 5° radial separation.

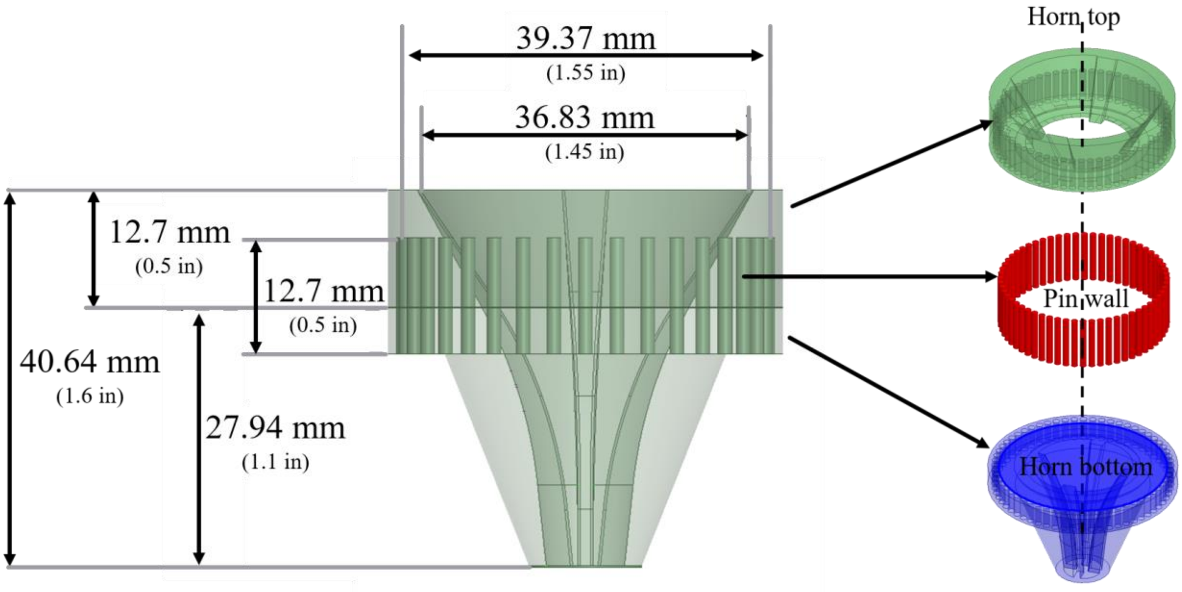

Figure 4.8: Proposed assembly scheme for the horn antenna integration inside the repeater payload.

4.4.3 Impact of Antenna truncation

The impact on the performance of a horn antenna due to a uniform air gap introduced between the mating faces of the top and bottom parts is considered in this section. The study is performed with a focus on the location of the cut plane that hosts the uniform air gap as well as the size of this uniform air gap. To move towards a more realistic integration scenario, the horn antenna is considered with the level of mechanical integration details as described in Figure 4.8. A pin wall is introduced between the top and bottom parts. The pin wall assembly provides dual function in this design. It serves as a mechanical feature for the alignment of top and bottom antenna sections and electrically acts as a shorting wall for the fields entering the air gap formed between the faces of the top and bottom mating sections. The distribution of normalized fields leaking inside the uniform 25.4 µm (1 mil) air gap formed between the mating faces of the top and bottom sections of the antenna at 45 GHz is

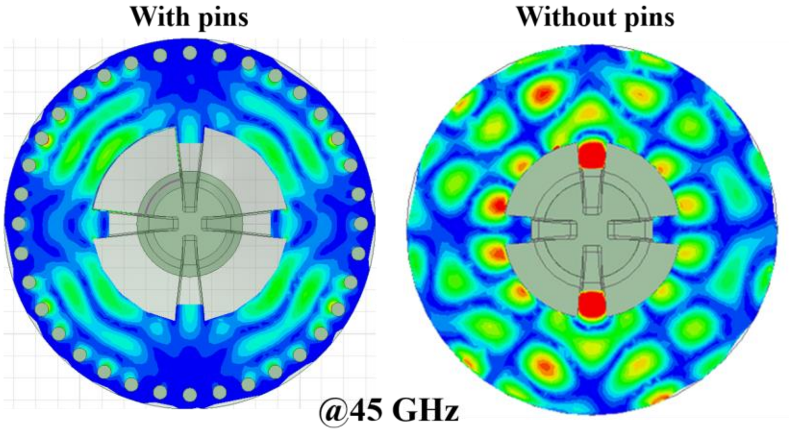

Figure 4.9: Field distribution inside a uniform 25.4 µm (1 mil) air gap formed at the interface between the mating faces of the top and bottom antenna parts. The normalized fields can be seen to be well bounded in the case of the pin wall assembly and fields leaking out of the antenna body can be seen for assembly without the pin walls.

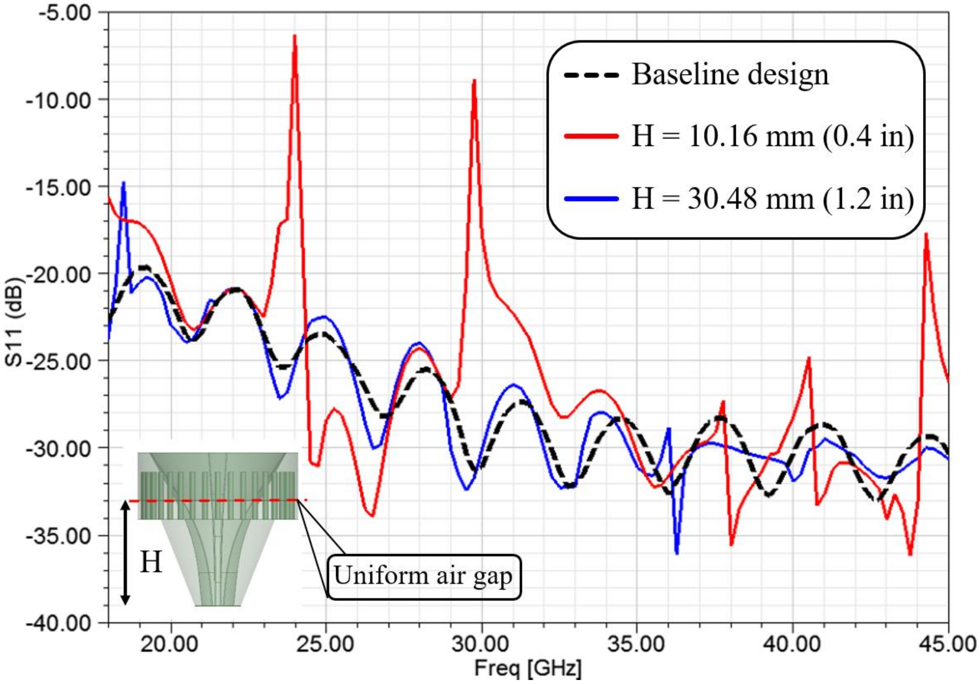

Figure 4.10: Impact of the cut plane location on the horn antenna match. Setting the cut plane location closer to the feed of the horn antenna has a deteriorating effect on the horn antenna performance.

shown in Figure 4.9. Majority of the fields are well bounded inside the shorting ring formed by the pin wall assembly in the case with the pin wall assembly while local hot spots with high concentration of fields can be seen near the edge for the case without the pin walls suggesting that the fields will leak outside the antenna body. The pin wall assembly thus shows potential to be used as a mitigation technique to avoid RF leakage from the seams and joints in the antenna body.

The impact of the cut plane location on the antenna performance is shown in Figure 4.10. The antenna cut plane location '*H*' for one case is set at 10.16 mm (0.4 in) from the feed while it is set to 30.48 mm (1.2 in) for the second case. Both the cases have a uniform 25.4 µm (1 mil) air gap between the mating faces of the top and bottom antenna parts. The two cases are compared to the baseline case where the antenna is made from one monolithic piece of metal. From the S_{11} data for the three cases, we can see that moving the cut plane closer to the feed of the horn antenna has a deteriorating effect on its match. The spikes seen in S_{11} occur due to high concentration of fields inside the uniform 25.4 µm (1 mil) air gap at certain frequencies. Such degradation in performance is highly undesired and makes the stable operation over the entire frequency band challenging. The high fields can lead to arcing, electro migration and severely reduce power handling.

Using the above computational study results and considering mechanical fabrication limitations for the thickness of the top part of the antenna, the cut plane location on the antenna is fixed at 27.94 mm (1.1 in) away from the feed as shown in Figure 4.10. Once the cut plane location is decided, the impact of the size of the uniform air gap is studied on the antenna performance. The performance of the antenna for a 25.4 µm (1 mil) and 50.8 µm (2 mil) uniform air gap at the interface between the mating faces of the top and bottom antenna parts is shown in Figure 4.11. The 50.8 µm (2 mil) uniform air gap degrades the antenna match and impacts the performance more than a 25.4 µm (1 mil) uniform air gap. This result

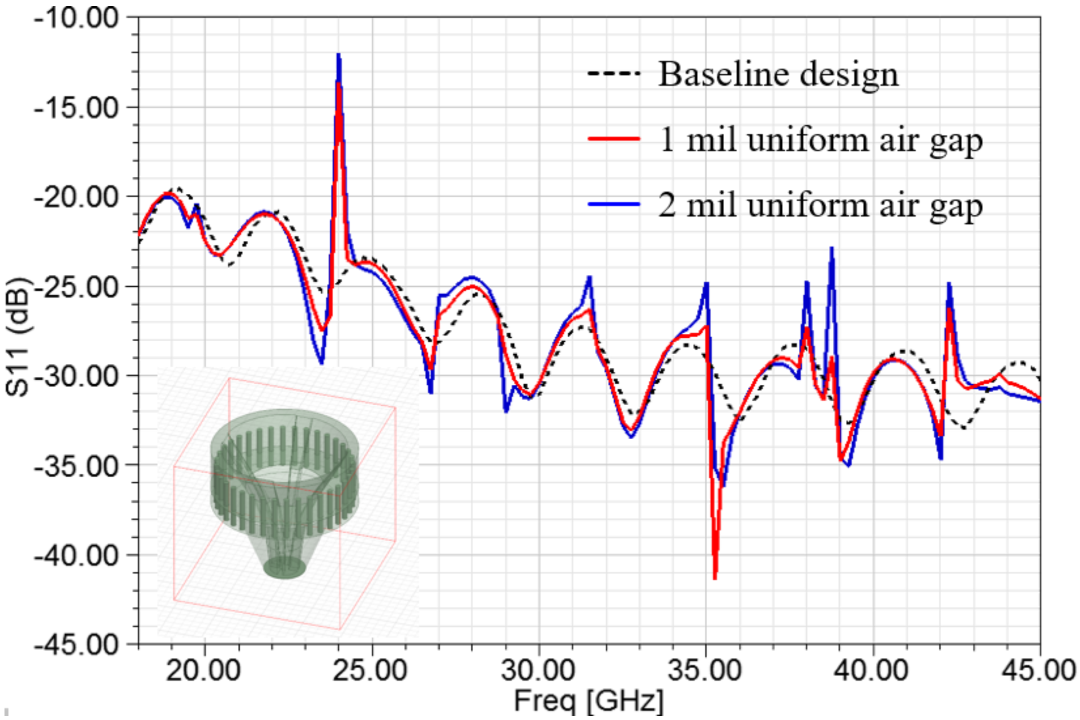

Figure 4.11: Performance of the horn antenna with a 1 mil and 2 mil air gap between the mating faces of the top and bottom parts of the antenna is compared against the baseline design. The baseline design assumes that the antenna is made from a single monolithic piece of metal. The study shows that 2 mil air gap has higher degradation (more spikes) in antenna S_{11} when compared to the case with 1 mil air gap.

lays emphasis on having a tight intimate contact between the two mating faces of the antenna top and bottom parts to ensure good overall performance. The results for the impact of the uniform air gap on the antenna performance motivate further detailed investigation of air gaps in the seams of a horn antenna due to integration artifacts in a more realistic scenario as discussed in the next section.

TABLE 4.1

Surface roughness of typical machining processes

Machining Process	Minimum surface roughness (mils)	Maximum surface roughness (mils)
Milling	0.01	1
Turning	0.008	1
Electro discharge machining (EDM)	0.3	0.5
Laser cutting	0.008	0.25
Fine saw	0.03	2
Planing	0.15	1
Shaping	0.15	1

4.4.4 Antenna Performance with Realistic Air Gap

Multiple machining operations need to be performed sequentially on the individual metal pieces to fabricate the individual antenna parts. The typical machining operations a part would undergo are listed in Table 4.1 along with the typical finish and surface roughness introduced by that machining operation on the machined face of the part [111]. It must be understood that for all practical reasons, the air gap between the mating faces of the top and bottom parts of the antenna is dependent on the machining operations performed on the individual parts during fabrication. The air gap will also be influenced by the compression forces applied by the fixtures that hold these parts together in the final assembly. To account for these factors and to model the antenna seams close to the real integration scenario, a non-uniform air gap is modeled between the mating faces of the top and bottom antenna parts.

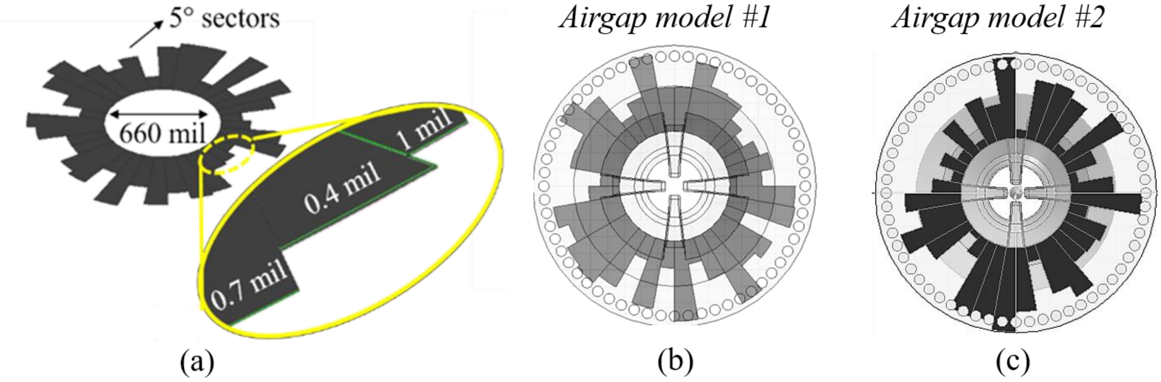

(a) (b) (c)

Figure 4.12: Non-uniform air gap introduced between the mating faces of the top and bottom parts of the antenna. The non-uniform air gap is expected to be a more realistic representation of the air gap formed between the two parts of the antenna. The details of the sectors forming the airgap are shown in (a). While an example with two random non-uniform air gap patterns generated using the adopted method are shown in (b) and (c).

The pin wall assembly is also included in the model of the antenna with a realistic, non-uniform air gap. The details of the non-uniform air gap are shown in Figure 4.12. The air gap is comprised of 72 sectors, each with a 5° angular spread and an inner radius of 8.382 mm (0.33 in). The outer radius of each sector forming the non-uniform air gap is randomly varied between 11.43 mm (0.45 in) and 20.32 mm (0.8 in), and the air gap thickness for each sector is randomly varied between 2.54 µm (0.1 mil) and 50.8 µm (2 mil) to account for the air gap features created due to the fixture placement and the various machining operations described in Table 4.1, that might be performed on the part. Parameters for each non-uniform air gap are generated in the specified range using a python script for a random function and the air gap is implemented in FEM solver ANSYS HFSS using python script [2] [112]. Thus, every non-uniform air gap is a unique combination of the various parameters described earlier. The performance of the antenna with a few different non-uniform air gap models is

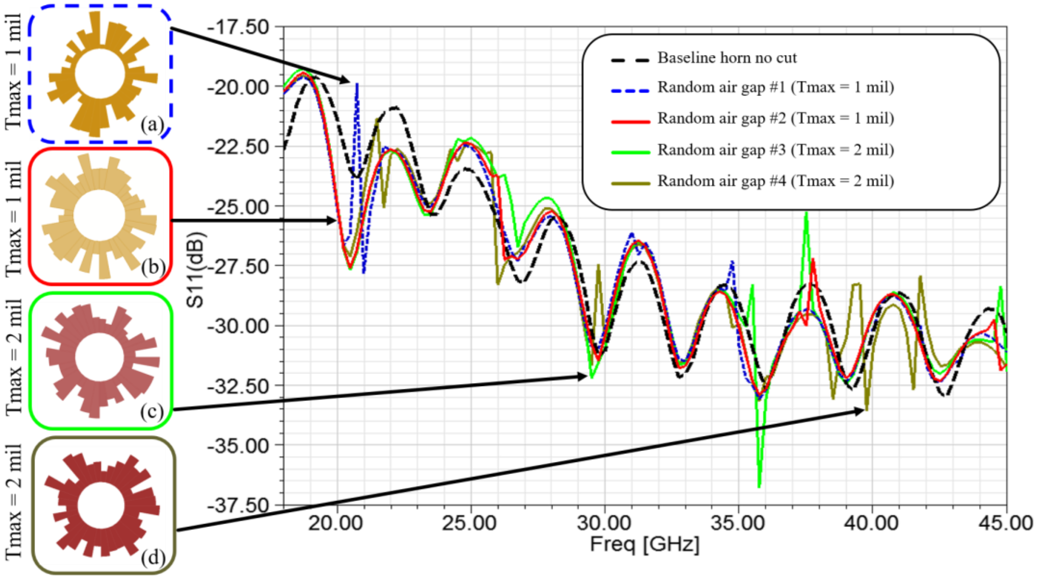

Figure 4.13: Antenna performance with four non-uniform air gap models is shown above. We can see that different random air gap models affect the antenna performance introducing undesired spikes in the S_{11} over the desired bandwidth.

shown in Figure 4.13. It can be seen that the antenna match is deteriorated at specific frequency points where there are local hot spots formed with the fields leaking into the air gap. It can also be seen that the location of such local field hot spots is truly sporadic and random for every air gap for the considered horn antenna assembly.

Furthermore, a detailed look at the fields inside the realistic air gap formed from the mating faces of the antenna show that the high concentration of fields developed inside the air gap creates undesired spikes for the antenna in S_{11}. The field concentration inside the air gaps disturbs the fields and currents inside the throat of the antenna resulting in the excitation of undesired higher order modes and standing waves. Theses higher order modes are seen to contaminate the radiation patter of the antenna at the frequencies where we observe the spikes in antenna S_{11}. An example of the field concentration inside the air gap is

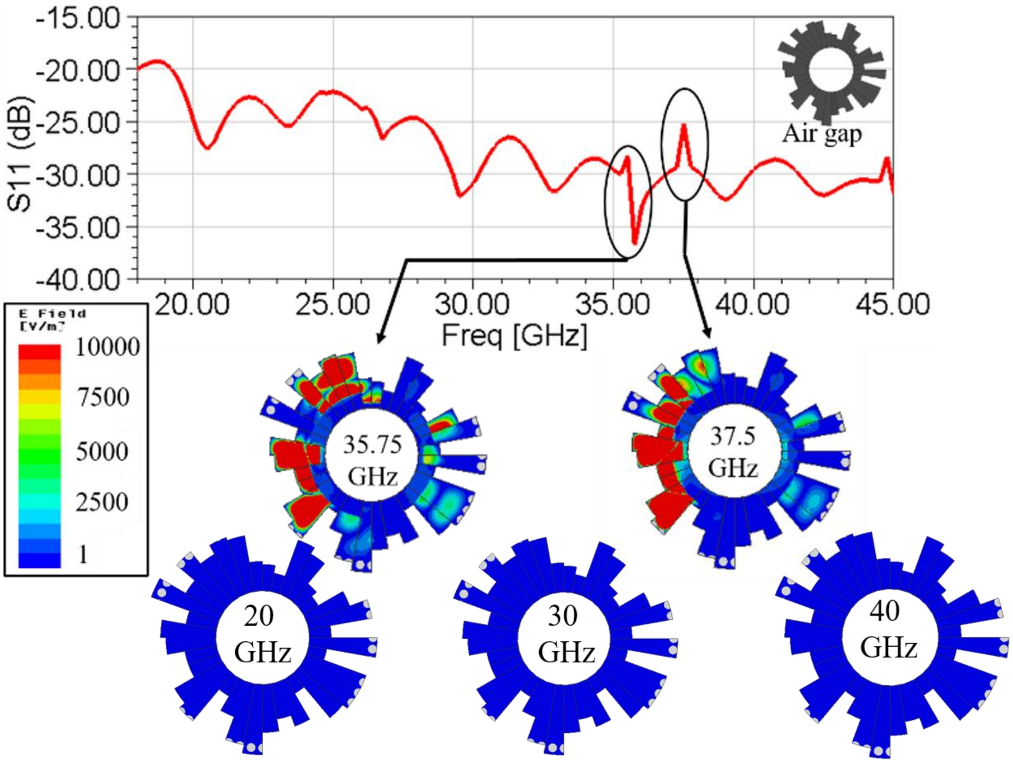

Figure 4.14: High concentration of fields formed inside the air gap cavities causing the undesired spikes in the antenna S_{11} performance.

shown in Figure 4.14. The E plane and H plane radiation patterns for the antenna are presented in Figure 4.15, and Figure 4.16, respectively.

The analysis of antenna with a radial cut on the throat of the horn antenna hereby shows that payload integration methods and techniques must be used very prudently with attention to RF leakage and antenna performance in mind. For a repeater-based application, especially when repeater performance under high power levels is desired, the design should be addressed from mechanical as well as RF standpoint. The integration of antenna from parts raises the risk of increased RF leakage from the seams. The performance of the antenna is impacted through sudden spikes in the antenna S_{11}, the high concentration of fields inside the air gaps formed at the seams, and the contamination of radiated patterns at these frequency points. Such performance deterioration may impact the stability and performance

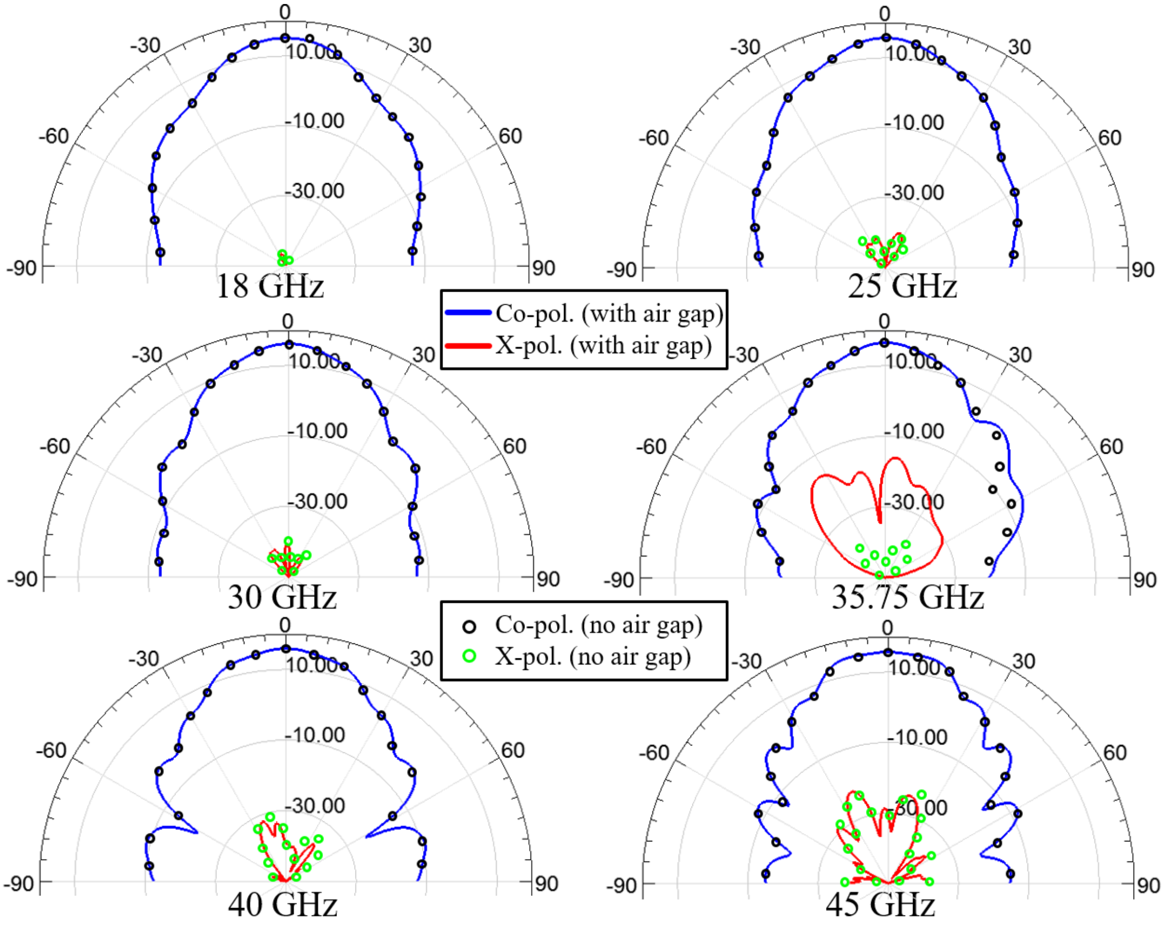

Figure 4.15: E-plane radiation patterns for the horn antenna modeled with the realistic air gap and with no air gap. Consistent patterns similar to the monolithic case are supported across the band except at 35.75 GHz and 37.5 GHz (not shown above), the points where the antenna S_{11} has spikes due to the high fields concentrated inside the air gap.

of the repeater system and set it into uncontrolled oscillations. In a real system, these issues must be addressed through careful design and analysis. Measures such as the use of seals and gaskets at the seams can be resorted to curb these undesired performance impacts due to presence of antenna seams. Computational results for antenna models having the air gap at the seams filled with conductive epoxy material or solder alloy material show that the detrimental impacts of the air gaps at the seams on the antenna S_{11} performance can be

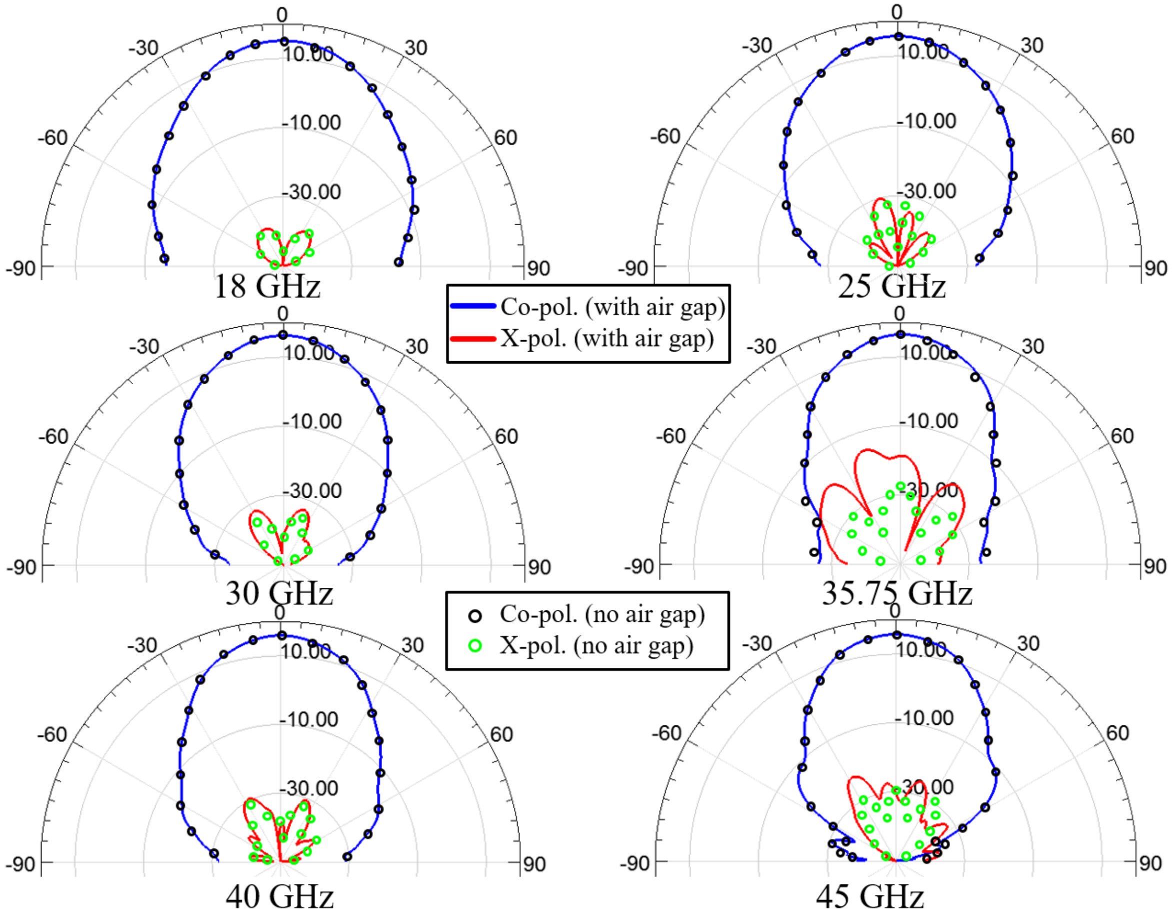

Figure 4.16: H- plane radiation patterns for the horn antenna modeled with the realistic air gap and with no air gap. Consistent patterns similar to the monolithic case are supported across the band except at 35.75 GHz and 37.5 GHz (not shown above), the points where the antenna S_{11} has spikes due to the high fields concentrated inside the air gap.

eliminated (not shown here). However, the use of such conductive filler materials has its limitations from an operational and maintenance standpoint. The issues of RF leakage may also need to be addressed separately in some cases when such filler materials are to be used as will be discussed in the following section of this chapter. The results shown for the impact of a cut plane in the throat of the horn antenna thereby form the motivation for the detailed system level RF leakage and isolation analysis in the next section of this chapter.

4.5 RF Leakage Analysis

RF leakage characterization is performed with a repeater model considered to be set inside a cylindrical payload. Various concerns and cautionary references have been mentioned in previous works related to RF leakage and self-coupling in literature in the past, and majority of these works have been on much lower frequencies [100] [101] [102]. The research presented in this work focuses on the characterization and mitigation of RF leakage for passive component suite aimed at operating as part of a millimeter wave repeater. The measurements are performed over 15 GHz to 40 GHz frequency range.

4.5.1 Measurement Setup

The measurement and analysis of the system level RF leakage is performed on a 1 m long metal cylinder with the transmit and receive antennas mounted at either ends of the cylinder on the curved cylinder walls. To study the impact of coupling from direct exposure of the victim antenna assembly to the source antenna assembly having RF leakage, the system level measurements are performed on an open-ended cylinder. Use of an open ended cylinder for RF leakage analysis also ensures that only the direct path coupling is accounted for in the measurement data and any higher order effects that may come from multiple bounces or echoes from the metal end caps of the cylinder are eliminated from the measurement. The source and victim antennas have a lip which is contoured at the aperture to match the inner curvature of the cylinder walls for achieving an intimate contact. Mounting fixtures are used to hold the antennas and passive waveguide suite in place against the cylinder walls. The passive RF assembly for the transmit and receive ends comprise of a horn antenna hooked up to an ortho mode transducer (OMT) and phase matched transmission lines based on the design suggested in [106]. The use of double ridge waveguide transmission lines with integrated pin wall assembly aim at reducing the RF leakage from the lines as compared to a split block approach without the use of pin wall assemblies. The antenna is fed using a custom made coaxial to waveguide adapter working over 18 to 45 GHz [106]. The passive RF assembly is connected to a VNA and the coupling (S_{21}) between the two ports is measured in different system configurations. The calibration plane of the VNA is set to the end of the coaxial cable used to connect the VNA to the coaxial to waveguide adapter used to feed the antenna assembly. Initial measurement setup is tested in the anechoic

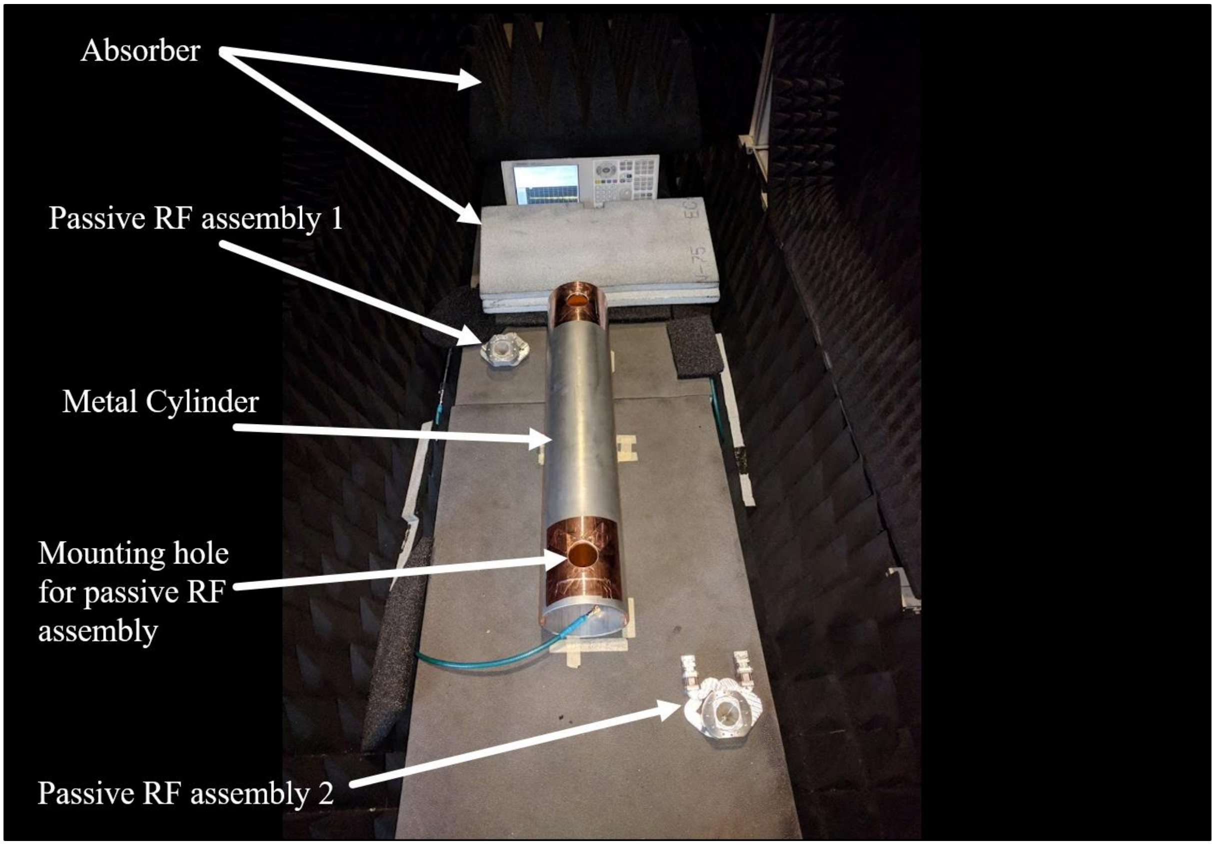

Figure 4.17: Measurement setup for characterization of internal RF leakage on a 1 m long metal cylinder used as a repeater platform. The setup shown in the image refers to the preliminary indoor measurements performed inside an anechoic chamber.

chamber to verify and eliminate the undesired measurement artifacts seen due to the poor calibration, unstable instrumentation setup, discontinuities in the transmission line and connector interfaces connecting the VNA to the antenna assembly, reflections from measurement environment, and impact of surface currents reflecting from the edges of the cylinder. Most of the above factors impacting the isolation measurements are eliminated through a step by step validation process. Clean measurements performed eventually inside the anechoic chamber however have a disadvantage of being contaminated by the reflections from the anechoic chamber ceiling, which impacts the quality of isolation results. Therefore, after achieving a stable measurement setup, the next set of measurements are done outdoors with the antennas facing upwards towards the sky to eliminate the coupling of reflected energy between the transmit and receive antennas. The measurement setup for the indoor testing performed inside the anechoic chamber is shown in Figure 4.17.

4.5.2 Baseline RF Leakage Measurements

The goal of the baseline RF leakage measurements performed indoors is to achieve a stable measurement setup before migrating to the detailed outdoor measurements. The indoor measurement setup helps in setting the right measurement parameters on the VNA to achieve enough sensitivity to capture the low coupled energy levels between the two antenna assemblies and to fine tune the setup to capture the coupling all the way down to the measurement system noise floor. The stable instrument configuration used for the indoor measurements comprise of 10 Hz IFBW, 0 dBm port power, start frequency of 15 GHz and stop frequency of 40 GHz (highest frequency of measurement is limited by the maximum frequency of operation of the VNA). The indoor measurements are conducted with 751 samples across frequency. This setup for the indoor measurements takes 3 minutes per sweep and 30 minutes for calibration. A Tacti-Cal model number TC-CK-24 calibration kit is used to calibrate the measurement setup. The measurement data of the coupling (S_{21}) is recorded and later post processed to transform it into the time domain ($S_{21}(t)$) using Fourier transform. The transformed time domain data is time gated to isolate the impact of the direct internal RF leakage using appropriately timed windows. For the indoor measurements, the time gating window is started at the fall of the first peak of the coupled energy level that corresponds to the energy coupled between the two antenna apertures and the window is stopped at the time corresponding to the rise of the second peak of the coupled energy level which corresponds to the energy coupled from the ceiling reflections. The inverse Fourier transform of the time gated data yields the impact of internal RF leakage on the system level isolation. The noise floor for the measurement setup is obtained by recording the S_{21} with the two measurement ports terminated into 50Ω loads of the Tacti-Cal TC-CK-24 calibration kit. For every measurement setup, the measurement system noise floor is recorded and used as a validation tool to achieve stable measurement environment before detailed isolation measurements are initiated. Evaluating the measurement S_{21} noise helps to ensure that the setup is configured properly and there are no errors in calibration or discontinuities in the transmission line path connecting the antennas to the VNA.

The result for coupling in the baseline setup with the two passive RF front ends mounted on the cylinder are compared against the measurement with the direct path between the two passive RF front ends being blocked with a 12.7 mm (0.5 in) thick metal shield and 101.6 mm (4 in) thick absorber slabs placed on either side of the metal shield are shown in Figure 4.18. The data for the measurement S_{21} noise is also plotted alongside. From the difference in the measured time domain coupling ($S_{21}(t)$), one can see that the baseline case shows higher energy levels between the first peak formed from the external free space

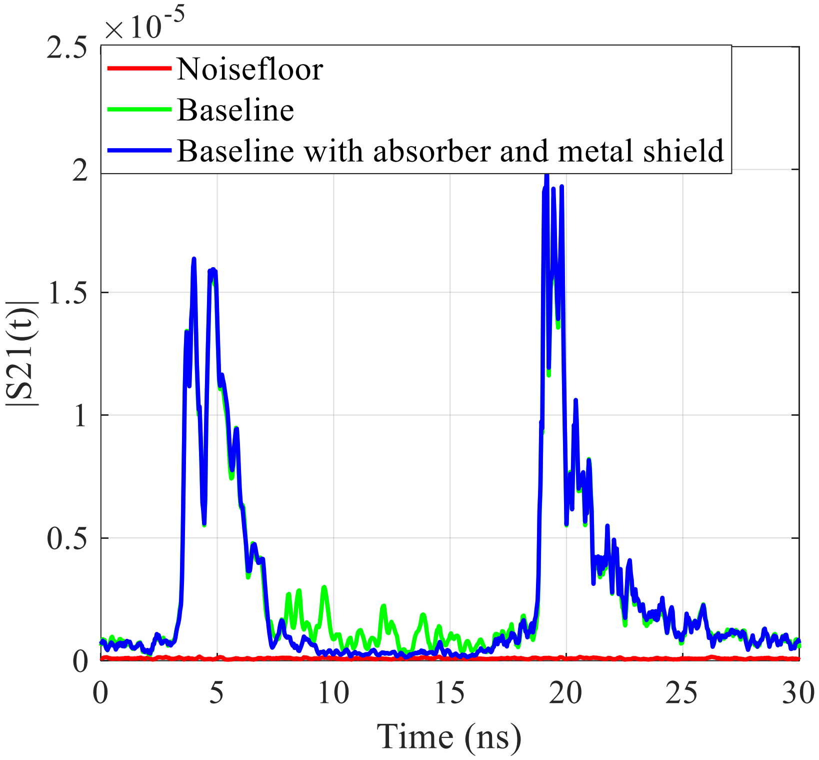

Figure 4.18: Preliminary indoor measurements for the baseline setup. The noise floor of the measurement system for the discussed set of measurement parameters is shown alongside the measurement of the baseline setup with metal shield and absorber slabs between the RF front ends inside the cylinder is shown.

coupling of the antennas and the second energy peak which corresponds to the energy reflected from the anechoic chamber roof and coupled back into the receive antenna. It is important to note that time domain coupling ($S_{21}(t)$) bears no units as it is a ratio expressed in linear scale. To further support the theory of reflection of energy from the roof of the anechoic chamber, the antenna aperture is loaded with a slab of absorber and measured. The result for the measurement with this configuration is shown in Figure 4.19. The suppression of the second peak in the measurement result proves the hypothesis that the second peak is manifested on account of the reflections from the roof of the anechoic chamber. Further validation of this fact is established through the change in time at which the reflected energy peak occurs in multiple isolation measurements where the cylindrical payload position is rotated so that the antennas face the anechoic chamber side walls changing the physical distance traveled by the energy before reflecting from either the roof or the saidewalls (not shown here). It is worth noticing the change in the magnitude and increased number of ripples in the $S_{21}(t)$ for the case of absorber loaded aperture compared to the unloaded case. Loading the aperture can cause reflections at the absorber – aperture interface resulting in formation of standing waves inside the antenna and transmission line assembly. The formation of such standing waves would alter the way energy is distributed along the path from the launch at the coaxial to waveguide adapter to the antenna aperture. The standing

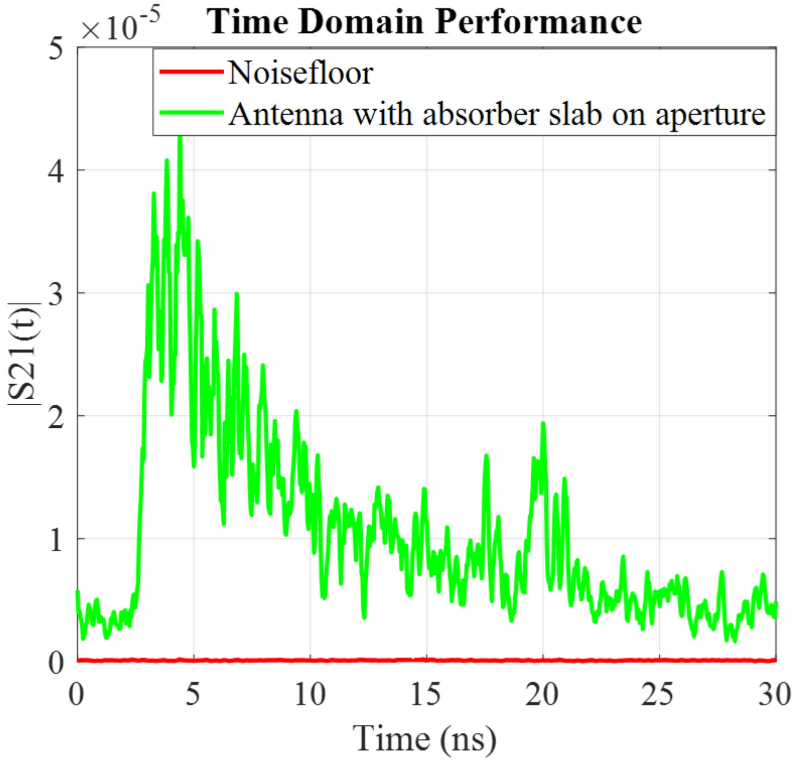

Figure 4.19: Measurement of the antenna aperture loaded with absorber slabs. The first peak at 5 ns is seen but the second prominent peak at 20 ns is prominently suppressed.

waves thus result in more energy being available over time to leak out from the interfaces compared to the unloaded aperture.

The measurement of passive RF front ends with baseline setup and the setup with absorber slabs placed on the edge of the metal cylinder are conducted to validate the impact of reflection of surface currents from the cylinder edges on the isolation measurements. The results for the measurement are shown in Figure 4.20. Consistent isolation profile between the baseline case and the case with absorber slabs placed on the cylinder edges show that there are no edge effects impacting the isolation inside the cylindrical payload. It is also important to note that substantial energy levels can be seen between the two major peaks in

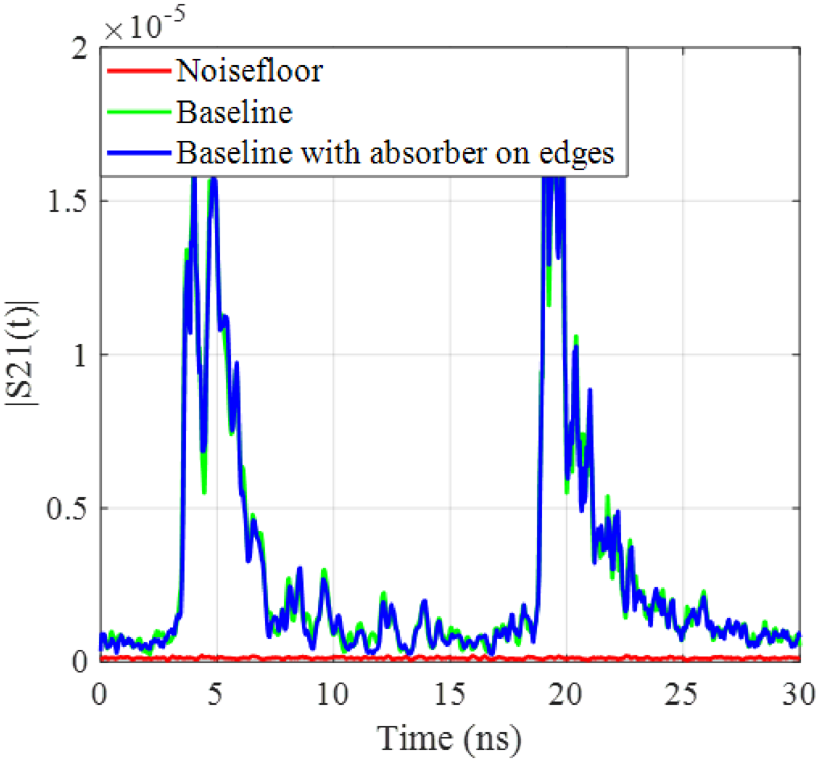

Figure 4.20: Measurement of the antenna aperture loaded with absorber slabs on the edges. The results show that there is not much difference in the two cases. This proves that there are no edge effects, energy levels between the two peaks are from RF leakage.

both the baseline measurements and the measurement with the absorber slab placed on the edge of the cylinder. This proves that the energy between the two peaks is from the direct path coupling between the two antenna assemblies inside the cylindrical payload.

After the preliminary indoor testing, where the measurement process is validated with the above-mentioned steps, the measurement of the cylinder is done outdoors for a more detailed look at the internal RF coupling with the repeater operation in mind.

4.5.3 Outdoor RF leakage Measurements

The measurement setup for outdoor measurements is put together based on the experience from the indoor measurements. The entire measurement apparatus was mounted

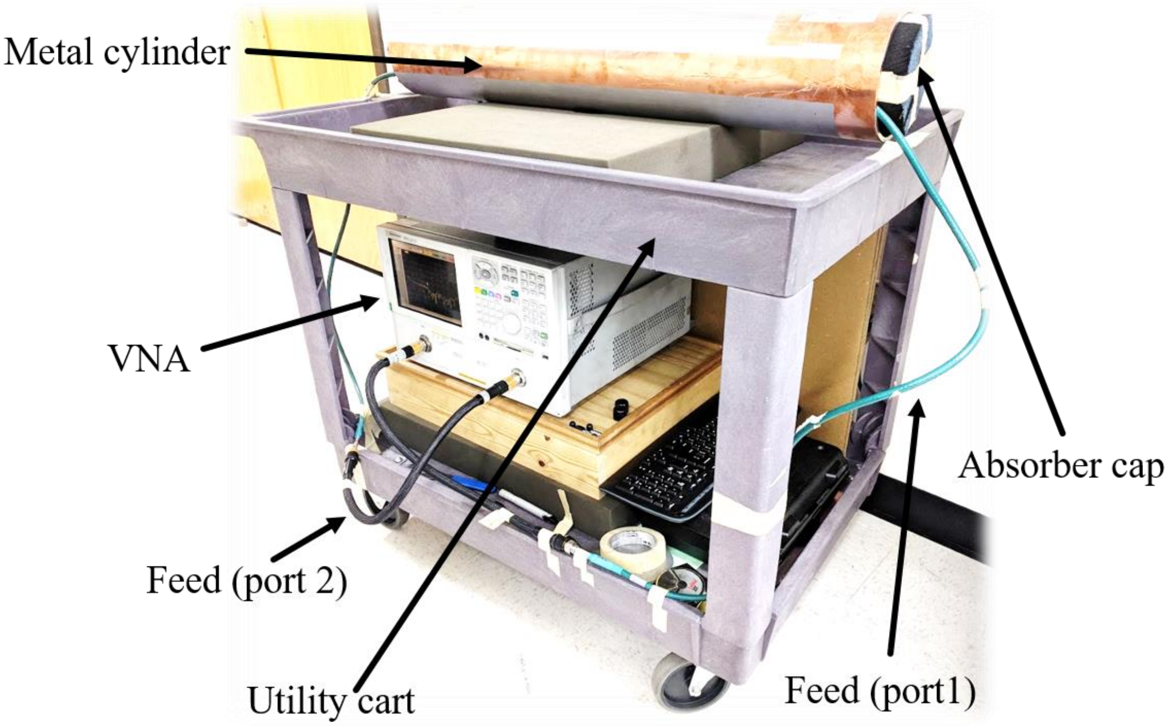

Figure 4.21: Measurement setup used for the outdoor measurements. A VNA is seen mounted on the lower shelf of the utility cart while the passive RF front ends are mounted on the cylinder placed on the top. Antennas are facing the sky in this setup.

on a flatbed utility cart. The VNA is placed on the lower shelf on the cart accompanied by provisions for routing the coaxial cables to the payload and routing the electrical connections to an outlet. The top shelf of the cart houses the cylinder with the passive RF front ends mounted inside in a similar fashion as described in the preliminary indoor measurements. The main goal for measurements performed outdoors is to eliminate the artifacts of reflection from the ceiling and to obtain cleaner measurements that are easy to analyze and help to quantify the impact of internal RF coupling. The measurement setup was kept the same as the indoor measurements except for one change. The outdoor measurement setup campaign uses 3126 number of samples. The other measurement parameters for the VNA were kept the same as the indoor measurements. With the higher resolution in the 3126 sample points

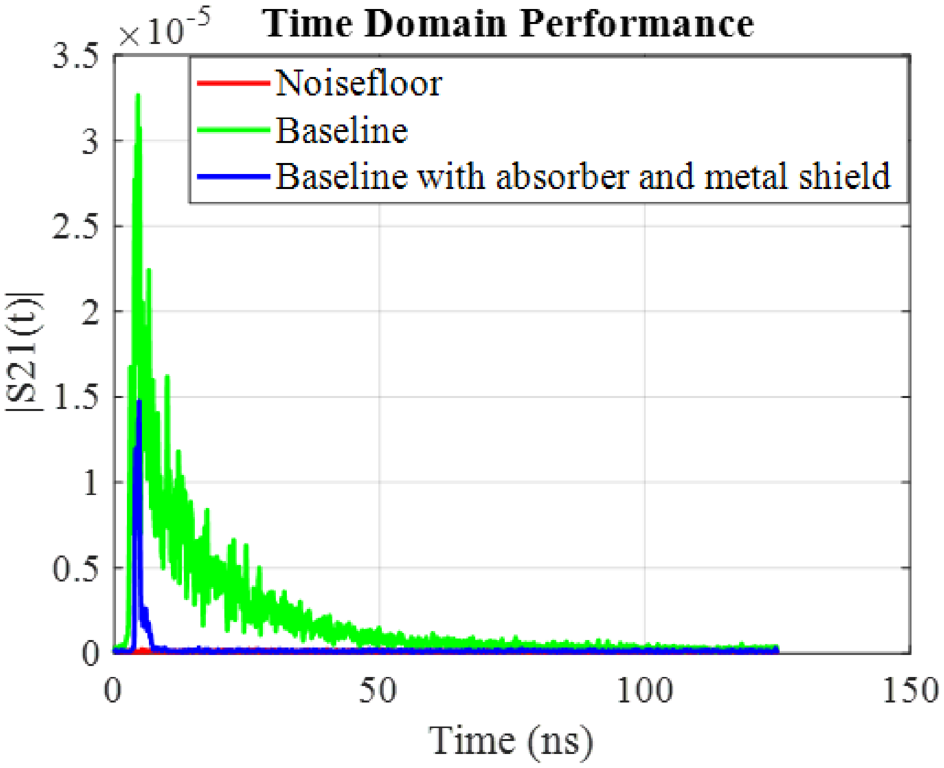

Figure 4.22: Measurement of the antenna aperture loaded with absorber slabs and metal shield in the center. The results show that the energy level seen in the baseline case is due to the coupling through internal RF leakage path.

for the frequency sweep, each sweep over the desired frequency range takes approximately 10 minutes. The measurement setup calibration takes 90 minutes in this case. The larger number of samples was iteratively fixed after multiple measurements where the goal was to increase the time span of the measured S_{21} in time domain for the energy levels from the internal coupling to decay down to the measurement S_{21} noise. This ensured that the time domain data could be gated over desired time intervals to see the time gated coupling from internal RF leakages without introducing any aliasing effects. A photo of the mobile measurement setup used for the outdoor measurements is shown in Figure 4.21. The data for the outdoor measurement with the baseline setup and the setup consisting of the metal shield and the absorber slabs placed in the center of the payload is shown in Figure 4.22. The

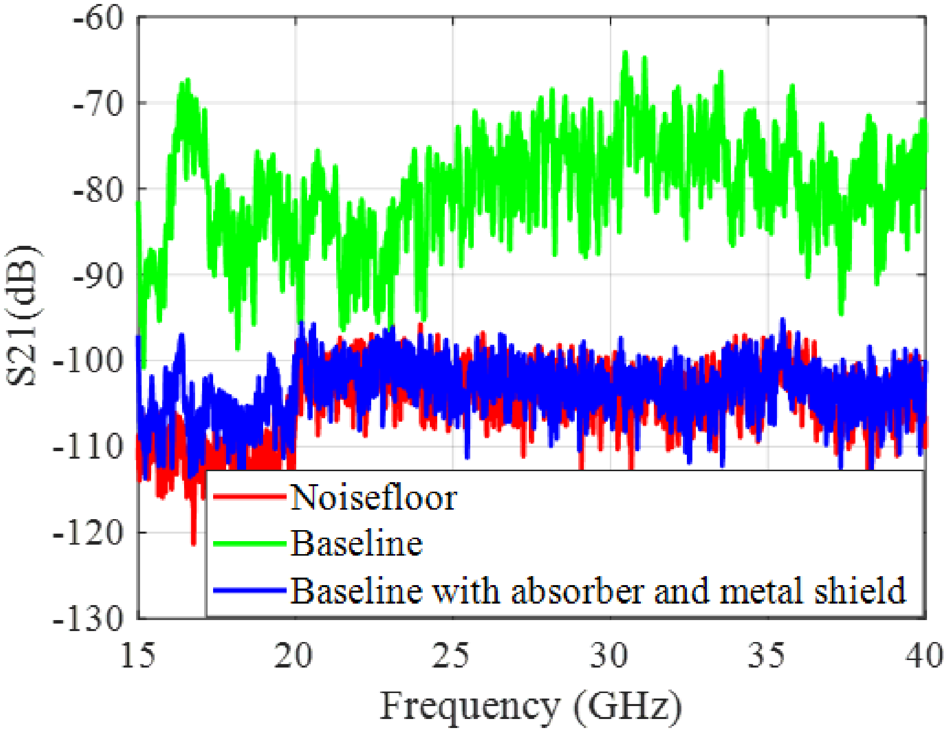

Figure 4.23: Time gated data for the impact of internal RF leakage on the coupling between the transmit and receive channels of the measured setup. The baseline design has significantly higher coupling compared to the case with absorber and the metal shield.

energy peak corresponding to the coupling due to ceiling reflections is eliminated as expected. More interesting to observe is the difference between the baseline case and the case with absorber and the metal shield suggesting that all of the energy coupled after the free space external coupling between the two antennas is due to the internal RF leakage inside the cylinder. The time gated data for the coupling shown in Figure 4.23 is processed from the sharp falling edge of the blue curve (7 ns) to the end of the time window (125 ns) for the available data. The result of the measurement shows that with a 1 m separation of the two antennas on the cylindrical platform, the contribution of internal RF leakage to the system deteriorates the isolation to be worse than 90 dB over majority of the band. This result is concerning for a repeater use case as this problem is expected to get worse with the cylinder end caps being used for practical applications. It is important to understand that the problem of internal RF leakage cannot be treated by the implementation of solutions that address the coupling through the free space path or through the surface currents. It is also important to note that RF leakage is reported in this system in spite of the precautions taken in the payload at the component level through the use of pin walls that reduce the RF leakage as suggested in [106]. This means that the RF leakage is also occurring at the multiple seams on the components and from the flanges that connect two components end to end. One of the ways to address the coupling is using compensation or cancellation techniques at the active level. However, keeping the repeater functionality in mind, one can see that such a system would ideally require a simple solution to address the issue of internal leakages since any level of additional compensation in the back end to improve the transmit and receive channel isolation will significantly impact the system level complexity.

4.5.4 Internal RF Leakage Mitigation

The problem of internal RF leakage described in the previous section can be mitigated using conventional techniques such as introducing a metal shield between the source and the victim. For instance, the measurement validation to prove the presence of internal RF leakage on the coupling uses a metal shield placed inside the cylinder payload at the center and is backed on both sides with absorber slabs. Another approach is to use conductive polymer gaskets at the flanges to treat the leakage from the mating interfaces. However, as discussed before, the metal shields or absorber stuffing are not the most practical in a

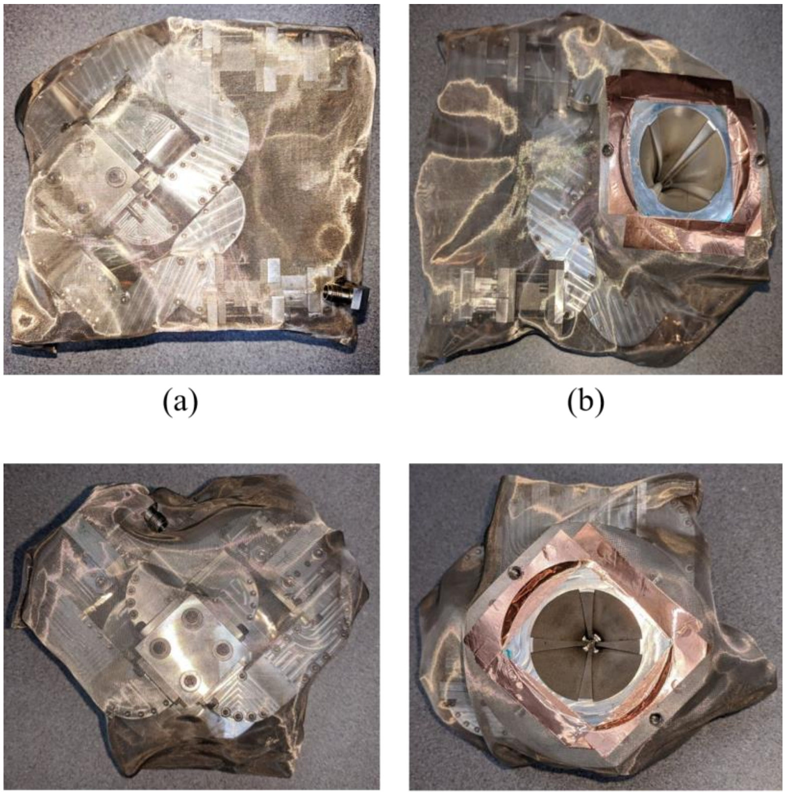
(a) (b)

(c) (d)

Figure 4.24: Transmit and receive channel passive RF front ends with proposed mesh based conductive RF sleeves. (a) Back side of the transmit RF front end, (b) front side of the transmit RF front end, (c) back side of the receive RF front end, (d) front side of the receive RF front end.

complex space constrained payload. The conductive gaskets may have limited operating flexibility and are not ideal for moisture, salt fog, extreme temperature swings, dust and other environments. Another measure for mitigating internal RF leakage is through the use of conductive epoxy and conductive sealants to seal the components. The use of conductive epoxy however prohibits device maintenance and the epoxied joints may be subjected to cracking and leakages over extended periods of time. It is apparent from this that conductive epoxies may not be effective and practical for initial testing and prototyping where constant changes to the payload are desired.

To address these concerns and to mitigate the impacts of internal RF leakage on the test bed with the cylindrical repeater payload used so far, we propose the use of conductive mesh fabric to be used as sleeves for the RF front ends. A photo of the RF front ends with the conductive RF sleeves mounted on them is shown in Figure 4.24. The passive RF front ends are covered in the custom made RF sleeves made from low cost conductive mesh fabric [113]. The mesh is made from polyester base, while there are metallic threads embedded in the base material with a composition of 23.4% Copper, and 10.9% Nickel by weight. The mesh thickness is 0.09 mm with a thread density of 130 threads pr square inch. The mesh has a loss (sheet resistance) of less than 0.1 Ω/sq (Ohm per square). The mesh is light in weight with a weight of 45 g/m^2. The total additional weight on both the RF front ends after the sleeves are mounted on them is less than 10 gm. The cost to implement the RF sleeves on both the RF front ends is less than $20. The two RF front ends with the RF sleeves mounted on them will be used for the measurements that follow. The sleeves are made by taking the projection of the RF front ends on three principal planes and then cutting mesh patches that match the projection shapes. The patches are stiched together using conductive steel thread. Coppertape is applied over the seams to ensure good contiguous electrical connectivity across the seam. Other validation tests performed to try out alternate means of reducing the impact of RF leakage on the coupling (not shown here) ascertain that the use of coppertape alone to seal and cover the component seams and flange interfaces inside the payload do not help to reduce the level of internal coupling inside the cylindrical payload. The measurement data for the payload with the mesh sleeves is shown in Figure 4.25. The time gated measurement data for the coupling with the sleeves mounted on the RF front ends is shown in Figure 4.26. From the data, we can see that the coupling is significantly reduced in the case when the RF sleeves are used on the RF front ends. The data is time gated with reference to the sharp falling edge of the energy peak (7 ns) that corresponds to external free space coupling for the

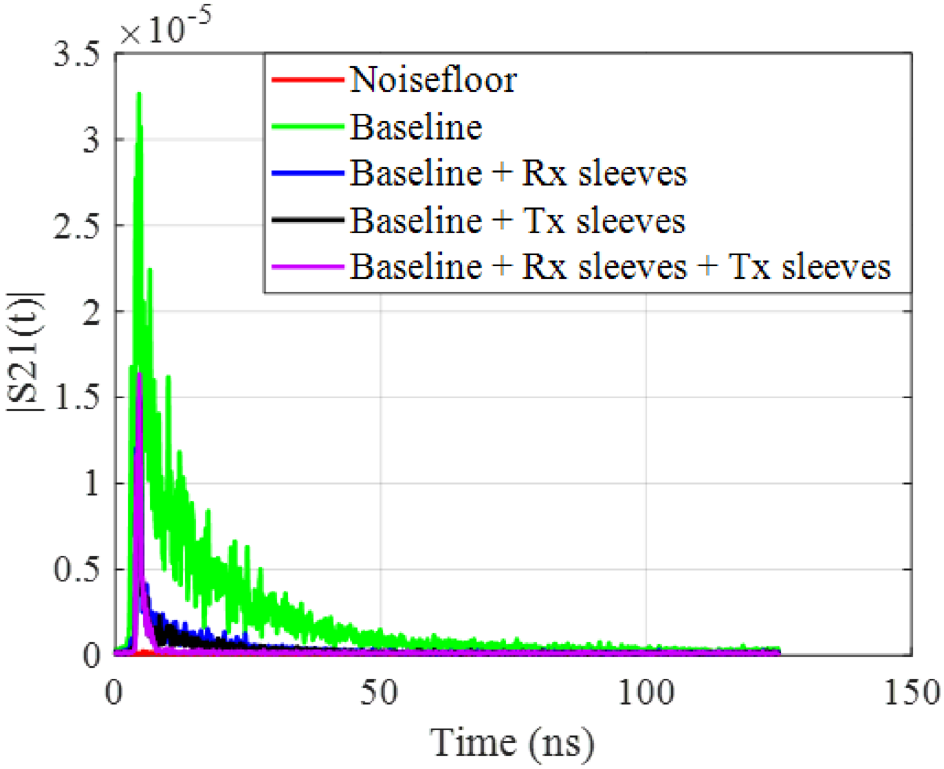

Figure 4.25: Coupling performance of the passive RF front ends with and without the conductive RF sleeves. We can see that the internal RF leakage is eliminated when both the transmit and receive side is covered with the conductive RF sleeves.

measurement of the RF front ends with sleeves. The time gating window is terminated at the maximum length of the available data (125 ns) where the coupling energy decays out into the measurement system noise floor. It is also worth noting that the data for RF front ends with sleeves on both sides agrees very closely with the Data for the RF front ends isolated using a thick metal shield and absorber slabs on either side of the metal shield (Figure 4.27). Such good agreement between the two cases proves the excellent RF shielding characteristics of the proposed method. The time gated data for the comparison of the measurement setup with the absorber slabs and metal shield compared against the baseline setup and the setup with the conductive RF sleeves is also shown alongside in Figure 4.28.

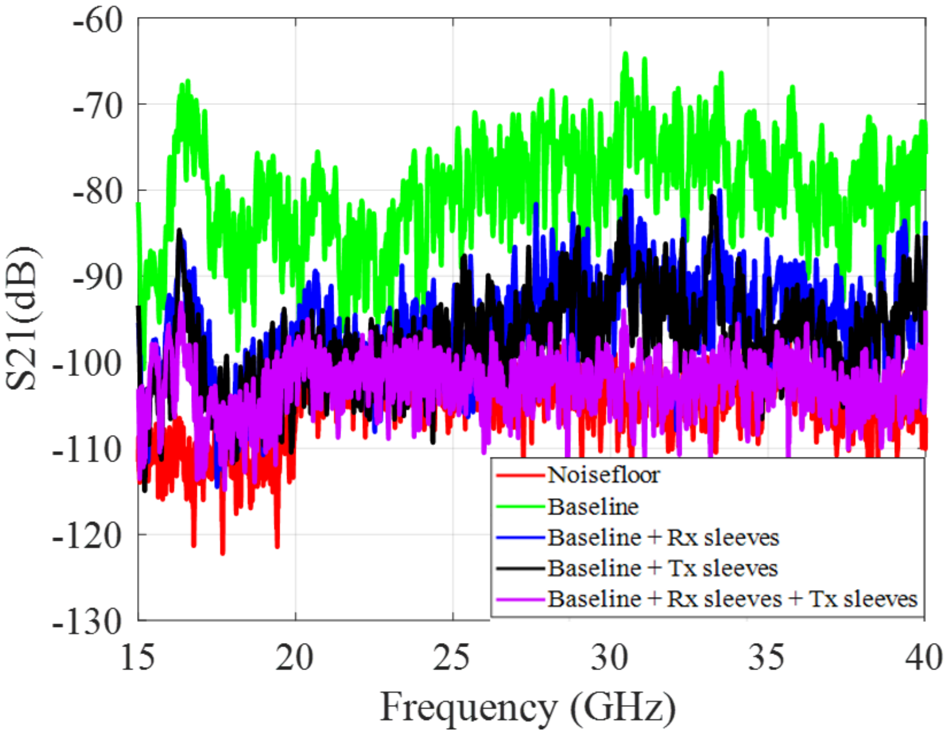

Figure 4.26: Time gated data for the impact of internal RF leakage on the coupling between the transmit and receive channels of the measured setup with and without the proposed RF sleeves. The baseline design has significantly higher coupling compared to the case with the sleeves.

After investigating the effectiveness of the conductive RF sleeves as a mitigation technique for internal RF leakages in a cylindrical payload, the effectiveness of the conductive epoxy as a potential mitigation resource for internal RF leakage is evaluated. A layer of conductive epoxy is applied to the entire RF front end assembly at the component seams as well as at the flange interfaces. Isolation measurements are performed with the same setup and at the same location to maintain consistency between the case with RF front

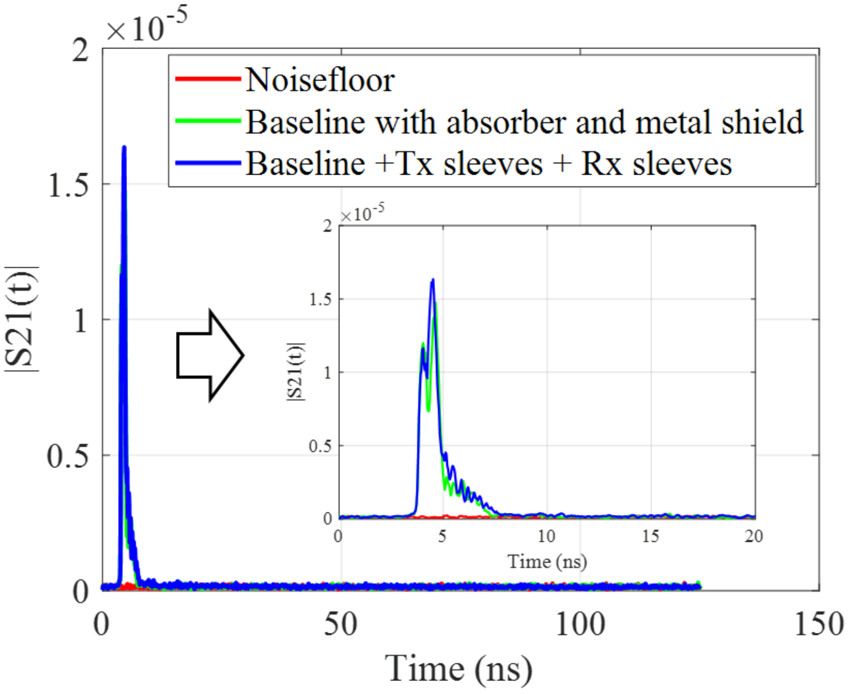

Figure 4.27: Comparison of the proposed RF sleeves against a metal shield backed on both sides by absorber slabs. Seen in the inset is a close up of the data for the measurement of the RF front ends with sleeves compared against the data for the RF front ends with a metal shield and absorber slabs placed in between the victim and aggressor. The data shows that the coupling for the RF front ends having the RF sleeves is very closely approaching the coupling in the case of the antennas with the metal shield and absorber slabs placed in between them.

ends mounted with the RF sleeves and the case with the RF front ends treated with the conductive epoxy seal coating. The comparison of the conductive RF mesh sleeves against the RF front end with the conductive epoxy is shown in Figure 4.29. The measurement with the RF front ends treated with conductive epoxy shows some traces of energy leaking between the 2 ns and 3.5 ns time frame. This leakage is attributed to the direct path leakage from the transmission lines before the energy gets to the external coupling path between the apertures. This leakage is not observed in the case of the conductive RF sleeves. Looking at the time axis past the coupled energy peak corresponding to the external coupling through

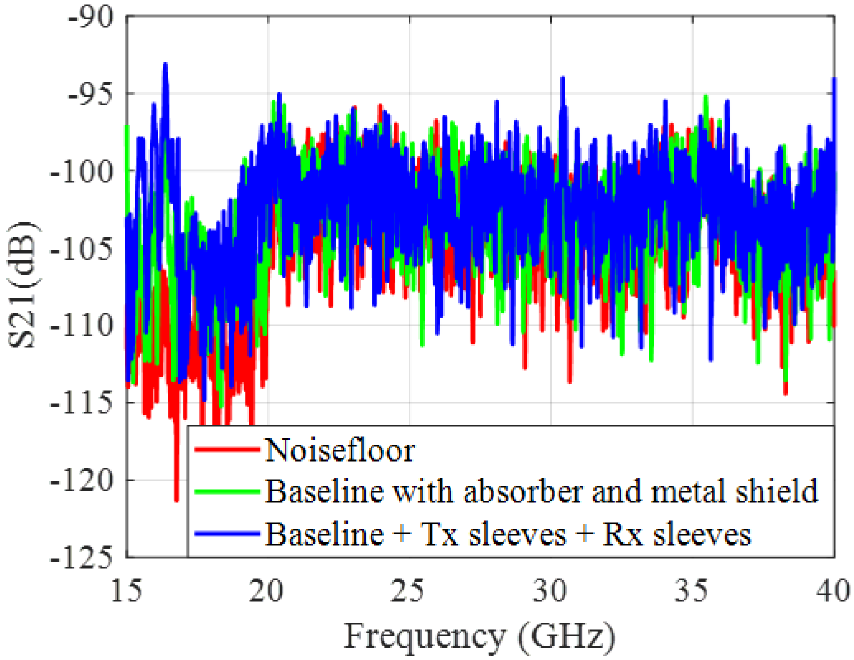

Figure 4.28: Comparison of the time gated frequency response for isolation with RF front ends mounted with the proposed RF sleeves against the measurement for a metal shield backed on both sides by absorber slabs. We can see that the proposed RF sleeves are effective in curbing the undesired impact of internal RF leakage.

the antenna apertures, one can see that the coupling level in the RF front ends treated with conductive epoxy can be seen to be slightly higher than the coupling level for the case with the RF front ends being covered in the conductive RF sleeves. These measurement results highlight the practicality of the use of conductive mesh based RF sleeves for mitigating deterioration in system level isolation due internal RF leakages. The proposed method is shown to mitigate the isolation deterioration to levels that are at par or slightly better than the conventional methods involving the use of an absorber backed metal shield or the use of conductive epoxy sealant coatings on the payload component seams and interconnect flanges.

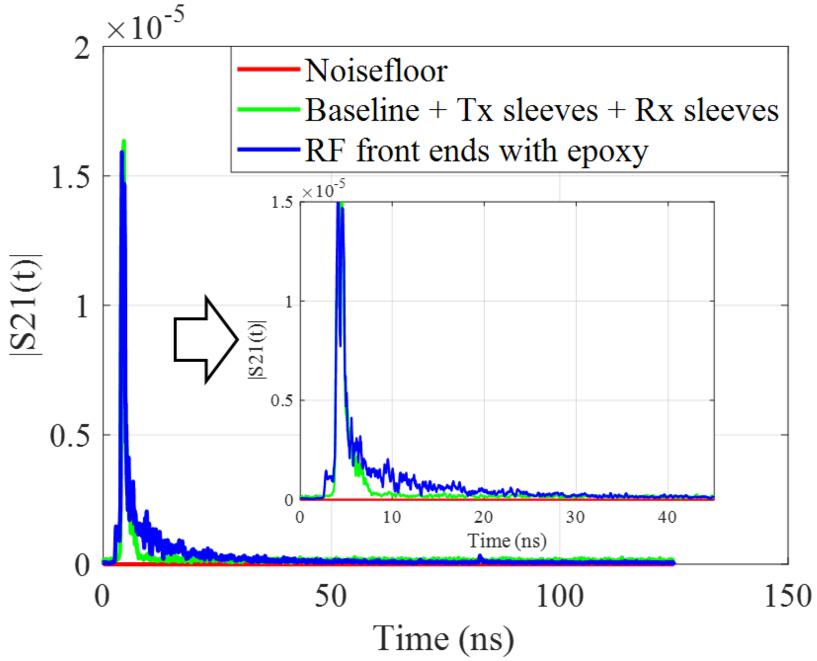

Figure 4.29: Comparison of the data with RF front ends mounted with the proposed RF sleeves and the measurement for the RF front ends treated with conductive epoxy to seal the seams and the interconnecting flanges. One can see that the isolation performance of the RF front ends with the epoxy treatment is slightly worse as compared to that of the RF front ends with the conductive RF sleeves.

4.6 Summary

The chapter is focused on investigating the impact of practical integration strategies and fabrication decisions on the performance of the horn antenna, followed by the analysis of the impact of internal RF leakages from the component seams and interconnect flanges on the isolation. The impact of a radial cut plane on the performance of a horn antenna is shown with validation of the computational model against the measured S_{11} for a prefabricated horn antenna. Good agreement between the computational results and measurements encourages the use of available computational tool to investigate the impact of cut plane location on a more realistic horn antenna. The results show that the cut plane should be located as far away as possible from the feed of the horn antenna where maximum dense fields exist. The effect of a uniform air gap is also studied on the performance of the antenna. The results for the uniform air gap study show that the antenna S_{11} deteriorates due to the presence of the uniform air gap since the air gap acts as a discontinuity in the horn antenna throat. Pin wall assembly is proposed as a measure to ease the integration process and aid the mechanical alignment of the antenna parts. The pin wall assembly also helps to curb the leakage of RF fields at the cut plane location of the horn antennas by shorting the fields inside the air gap.

The horn antenna performance is studied for a more realistic scenario with a randomly generated air gap comprising of several distinct sectors modeled together to form the gap. The parameters that define the sectorial dimensions of the randomly generated air gap such as the thickness and radius are randomly selected. The results of the random air gap study show that any cut along the throat of the horn antenna can significantly affect its wideband performance if the antenna is not properly integrated or if the air gaps so formed are not addressed in the final design. High field concentration inside the random air gaps is shown to cause the observed spikes in the antenna reflection coefficient. The impact of these fields on the contamination of antenna patterns is also discussed.

The characterization and mitigation of internal RF leakage is addressed in the second part of this chapter. The measurement setup comprises of two passive RF front ends with the antenna, OMT and waveguide transmission lines mounted 1 m apart on a metal cylinder. The use case of a repeater system is considered as a test bed to show the impact of internal RF leakage on the system level coupling. Baseline measurements of the two passive RF front ends establish the proof for existence of internal RF leakage and its detrimental impact on the coupling levels. The baseline measurements are performed indoors to first set up a stable measurement environment before detailed measurements are done outdoors. Since the level of coupling to be measured is very low, even measuring inside an anechoic chamber causes undesired measurement artifacts because of reflections from the chamber walls which causes contamination of the measured coupling data. The outdoor measurements are performed with the antennas facing towards the sky to eliminate any energy coupled between the two antennas through reflections. The outdoor measurements show that the isolation can deteriorate to as low as 65 dB only due to the contribution from the internal RF leakages. The presence of internal RF leakage is observed in spite of the use of pin walls as a precautionary measure in the design of the waveguide and transmission line components, suggesting that the leakage is occurring from the components, the flange interconnect interfaces between the two components, and the mating interface between the antenna and the metal walls of the cylindrical payload. A low cost, easy to install RF sleeve made from conductive mesh is suggested as a mitigation strategy to eliminate the internal RF leakage. Use of the conductive RF sleeves reduces the internal RF leakage and improves the system level isolation across the 18 to 40 GHz frequency range from 65 dB worst case to better 96 dB worst case, when only the internal coupling is taken into account. The technique to address the coupling issue due to internal RF leakage using components sealed with conductive epoxy is also discussed. The result of the RF front ends with the conductive epoxy are compared against the results of the conductive sleeves. The conductive sleeves are seen to perform comparable or better than the epoxied components. The prospects for future work related to this part of the research should be aimed at investigating and mitigating isolation deterioration from external coupling paths. Eventually, the techniques to improve isolation described herein can be combined with the techniques for isolation improvement from external path coupling so that a holistic approach to improve isolation can be developed.

Chapter 5

Summary and Future Work

5.1 Thesis Summary

The research showcased in this work moves across two major areas of expertise. The concepts of low profile, wideband support and high-power operation is seen to be the common underlying theme across the research areas presented herein.

The research shown in the HF frequency range is addressed towards the design of low profile vehicular HF antenna design. Full wave computational analysis is used to design the proposed antennas. The adopted design approach is shown to be validated through series of measurements performed on a scaled model prototype. The full scale antenna design is fabricated and evaluated through field tests and outdoor antenna measurements. The fabricated full scaled HF antenna is integrated on the vehicle and demonstrated by establishing HF links at different frequencies of interest.

The research on the millimeter wave RF front ends looks into the impact of integration strategies and accompanied fabrication provisions on antenna performance. The impact of integration strategies is approached from an RF leakage perspective. The focus of the analysis is to evaluate the impact on isolation due to internal RF leakage. Coupling measurements performed later show the detrimental effect of this internal RF leakage on the coupling. Mitigation techniques for improving the isolation are proposed using low cost conductive sleeves mounted on the RF component suite. The research outcomes for the work showcased in this thesis are summarized below.

5.1.1 Ultra-Low Profile Inverted-L Antenna for Vehicular HF Communications

The design process for a low profile, offset fed two arm inverted-L antenna is described in the thesis. The performance goal for the antenna is set at zenith gain better than -20 dBi and bandwidth more than 24 kHz. Profile of less than 1 m is desired based on the profile of currently fielded vehicular HF antennas. The proposed antenna design has a profile of 0.25 m which is λ/400 in electrical terms at 3 MHz. Fundamental performance limits are investigated for an electrically small antenna. Considering the size of the AAV and 1 m profile of the antenna over the AAV, the electrical size of the antenna is 'ka' = 0.3. The results from the analysis lay the performance expectations from such an electrically small antenna and highlight the acceptable loss in the antenna to maintain desired zenith gain and bandwidth performance. It is shown that the antenna supports 3 kHz bandwidth only if the radiation efficiency is less than 5%. To support 8 times wider (24 kHz) bandwidth, efficiency should be 8 times lower. A quick overview of inverted-L antennas shows that the antenna radiation pattern can be controlled using the aspect ratio of the vertical and horizontal arm length. Following this result, the antenna design is shown to evolve from a traditional whip antenna to a bent whip, *i.e.* base fed inverted-L antenna with lower profile. Offset feed is introduced as a means to improve the current on the horizontal section of the antenna and enhance zenith gain. In the last step of the evolution, a second arm is added in the offset fed configuration to improve the antenna bandwidth performance. The losses in the antenna from the vehicle and the environment are considered in the computational design by use of real material parameters for the vehicle and the grounds. The losses in the antenna tuner are taken into account by introducing a parameter called as effective tuner resistance. This parameter also sets the performance bounds on the tuner design. Results of the parametric study performed on the single arm and two arm offset fed design show that the single arm offset fed inverted-L antenna requires a minimum profile of 0.625 m while the two arm offset fed inverted-L antenna requires a profile of 0.25 m. The final antenna geometry has two arms, offset feed located at 5 m from the rear of the vehicle, 0.25 m profile, and 8 m length of the horizontal arms. The performance of this antenna is considered over various grounds in the NVIS frequency range. Consistent impedance characteristics above various grounds suggest that same tuning mechanism can be used to tune the antenna over different grounds and in diverse environments. Zenith gain is better than -20 dBi, which is comparable to existing COTS solutions. Good agreement between the computational results using method of moments as well as finite element method validate the computational approach. The antenna has better than 24 kHz tuned bandwidth over the operational frequency range from 3 to 10 MHz. Performance of the antenna under mechanical failure in one of the arms is investigated showing that antenna still supports communication but with lower bandwidth. The scaled prototyping of the antenna with a low-cost additive manufacturing process is introduced. Scaled prototype measurements are in very good agreement with the corresponding computational results in method of moments and finite element method packages. Tuning analysis on the scaled prototype is shown with support of better than 1.2 MHz bandwidth (24 kHz equivalent after scaling). Pattern measurements of the scaled prototype are shown to be in good agreement with the computational results.

5.1.2 Full Scale Prototyping and Platform Integration of Vehicular HF Antennas

The development of full scaled prototype is shown for the M-ATV. Design approach demonstrated in Chapter 2 is followed for this full scaled prototype. The main difference is that this antenna is designed as a two-arm base fed inverted-L antenna. This allows for reconfigurable approach to test multiple antennas on the platform using same feed structure and tuner integration method. With a desired profile less than 1 m over the M-ATV, the antenna electrical size is '*ka*' = 0.24 at 3 MHz. With this electrical size, the antenna efficiency needs to be less than 4.2% to support legacy 3 kHz bandwidth and less than 0.5% to support the desired 24 kHz bandwidth. Numerical studies demonstrate that the antenna supports better than 24 kHz bandwidth and -20 dBi of zenith gain, when effective tuner resistance is 2Ω. Antenna gain and pattern measurements are performed on the M-ATV platform mockup and the results show the measured gain performance of antenna to be better than -20 dBi, while the measured patterns are acceptable for NVIS, ground wave, and long-range sky wave propagation. Provisions for cable routing, choking of return currents on the cable, weather proofing and field measurement setup used on the field are discussed. Measured impedance agrees with the computational results. A 0.5 MHz shift in resonance and antiresonance position is observed. This is attributed to minor dissimilarities between the two cases. Integration of a switch is described for the antenna structure to reconfigure into loop mode or inverted-L mode. Preliminary measurements provide the proof of concept for the proposed concept. Tuning the switched reconfigurable antenna is also demonstrated using a COTS tuner.

5.1.3 Assembly Strategies for Isolation Improvement of Millimeter Wave and Quasi Millimeter Wave Front Ends on Space Constrained Cylindrical Payloads

The introduction of a radial cut plane in the throat of the horn antenna is described. The cut plane is necessitated by the practical integration requirements inside a cylindrical payload and by the capabilities of fabrication tools used to make such an antenna. The impact of radial cuts in the throat of a prefabricated horn antenna is shown to establish validation between computational tools and measurements. Following the validation, cut plane impact on a realistic horn antenna is shown with integration details. It is shown that the location of the cut plane must be kept as far as possible from the antenna feed. A uniform air gap is shown to introduce undesired spikes in the reflection coefficient. Concerns related to the antenna power handling and stable performance under such a scenario are discussed. To consider a more realistic integration scenario, the uniform air gap is modified into a practical air gap. The practical air gap is inspired by the fabrication finishes of typical fabrication processes performed on the antenna parts. The air gap thus considered is divided in radial sectors, with each sector having a random profile defined by the outer radius, and its thickness. The correlation between the undesired reflection coefficient spikes and high field concentration inside the air gap formed at the mating interface between the top and bottom antenna parts is shown. Good correlation is established between the spikes in the reflection coefficient, the fields concentrated inside the air gap at the frequency showing the spikes and contamination of the antenna radiation patterns.

Following the analysis on the proposed antenna, the analysis of the impact of internal RF leakage on the coupling between the passive RF front ends is shown. Indoor measurement setup is used to establish the presence of internal RF leakage in the prototype payload. Baseline S_{21} noise and coupling measurements of the RF front ends with and without thick metal shielding and absorbers used for isolation show the presence of internal RF leakage. The measurement with aperture loaded with and without absorber slabs validate the expected measurement physics and highlight impact of reflections from the anechoic chamber walls that contaminate the measurements. Following this result, clean outdoor measurements are shown to characterize the internal RF leakage. The effect of internal RF leakage is shown to decreases system level isolation to 65 dB. The mitigation of impact of internal RF leakage on the coupling is shown by use of proposed conductive RF sleeves. Measurement of RF front ends with conductive RF sleeves on both the transmit and receive components show worst isolation levels higher than 95 dB over the 18 GHz to 40 GHz frequency range. Alternative methods to curb internal RF leakage are discussed including use of conductive epoxy. Presence of internal RF leakage is seen in case of conductive epoxy layer on the RF front end components, with a substantial leakage from the transmission line when compared to the case with the proposed conductive RF sleeves. Techniques related to contrast photography and pneumatic inspection are also encapsulated with a focus on possible RF leakage from the components under test.

5.2 Original Contributions

The original contributions of this thesis are as follows:

- HF NVIS on-the-move antenna with 0.25 m (λ/400 at 3 MHz) profile is designed. The antenna has 8 times wider bandwidth, but maintains zenith gain similar to existing COTS products.

- Two arm inverted-L antenna is adopted to improve the antenna bandwidth, whereas the use of offset feed in HF antennas improves the antenna zenith gain for NVIS operation.

- Modular build of HF antenna is demonstrated using adjustable aluminum-copper sleeve joints with conductive lubricant for retarding oxidation effects. The proposed integration method provisions easy antenna integration on the vehicular platform.

- Path towards switched implementation of electrically small HF antenna structure is shown to operate the antenna in loop mode or inverted-L using the same installed antenna structure.

- The impact of introduction of a radially placed cut in the throat of horn antenna on its performance is shown. The cut features are introduced for ease of assembly, fabrication and integration inside a cylindrical payload.

- Mitigation of the deterioration in isolation between passive RF front ends inside a cylindrical payload using conductive RF sleeves is shown with improvement in worst case isolation from 65 dB to worst case isolation of 90 dB across the wide bandwidth of 18 GHz to 45 GHz.

5.3 Future Work

The work presented herein could be expanded upon in many directions leading to new and interesting research possibilities including:

- The tuning analysis and measurements shown in this work are performed in a static case. In a real-world scenario, the antennas need to be tuned as the vehicle moves across different grounds and changing terrain. The proposed designs of the two electrically small inverted-L HF antennas can be used as a test bench for research involving dynamic tuning of electrically small vehicular HF antennas for on-the-move applications.

- The proposed electrically small HF antenna design process can be applied to design other electrically small antennas for more complex platforms such as boats, aerial platforms and so on which require more careful consideration of the antenna environment and the mechanical forces acting on the antenna structure during operation.

- The design of a practical, efficient tuner for electrically small antennas based on the effective tuner resistance parameter given by the proposed antenna design approach will be an interesting and natural expansion of this work.
- The investigation of internal RF leakage and its impact on deterioration on the isolation must be extended into the 45 to 110 GHz frequency band. The bandwidth that the conductive RF sleeves can support must be ascertained, other mesh materials that can provide similar or better isolation must be investigated.

References

[1] Altair FEKO, Troy, MI, USA. (2014). FEKO V7.0.1, FEKO Suite 7.01. [Online] Available: https://www.feko.info/

[2] ANSYS, Inc, Canonsburg, PA, USA. (2012). HFSS V15.0.0, ANSYS HFSS. [Online] Available: http://www.ansys.com/products/ electronics/ansys-hfss

[3] *MATHWORKS Matlab*, http://www.mathworks.com/products/matlab/

[4] AWR Microwave Office, National Instruments, Austin, Tx, USA.

[5] *ARG Capabilities and Chamber,* Facilities, Antenna Research Group, University of Colorado Boulder, Boulder, Colorado, USA. [Online]. Available: http://ecee.colorado.edu/antenna/facilities/

[6] SAE Circuits Inc., http://www.saecircuits.com/index.shtm

[7] Rec. ITU-R V.431-7, "Nomenclature of the frequency and wavelength bands used in telecommunications," ITU, 2000.

[8] *ITU Handbook on Emergency Telecommunications*, Int. Telecommun. Union, Geneva, Switzerland, 2005.

[9] D. Bodson, "When the lines go down," *IEEE Spectrum*, Vol. 29, No. 3, pp. 40-44, Mar. 1992.

[10] A. Tang, D. C. Rai, D. Ames, C.V. R. Murty, S. K. Jain, S. R. Dash, H. B. Kaushik, G. Mondal, G. Plant, J. McLaughlin, M. Yashinsky, M. Eskijian, and R. Surrampalli, "Lifeline systems in the andaman and nicobar islands (India) after the december 2004 great sumatra earthquake and Indian ocean tsunami," *Earthquake Spectra* Vol. 22, No. S3, pp. 581-606, Apr. 2006.

[11] F. Lefeuvre and T .J. Tanzi, "Radio science's contribution to disaster emergencies," *The radio Sci. Bulletin*, Vol. 348, Mar. 2014.

[12] J. W. Nieto and W. N. Furman, "Improved data rate robustness of U.S. MIL-STD-188-110C appendix D wideband HF waveforms," in Proc. *12th IET Int. Conf. Ionospheric Radio Syst. Techn. (IRST' 12)*, pp. 1-5, May 2012.

[13] K. Davies, "Oblique propagation," *Ionospheric Radio,* Peter Peregrinus Ltd., London, UK, 1990, ch. 6, sec. 6.3, pp. 157-158.

[14] *AAV-7,* Amphibious Assault Vehicle, [Online]. Available: http://www.marines.com/operating-forces/equipment/vehicles/aav-7

[15] *Shakespeare 120-99,* Flexible HF Whip Antenna, [Online]. Available: www.Shakespeare-military.com, Shakespeare Military Antenna Products Brochure, 2010. pp-15.

[16] *Cobham 3160-99,* Cobham HF Vehicle Whip Antennas, [Online]. Available:http://www.masergroup.com/downloads/Cobham%20Half-Loop%20Demo%20Report%20Nov-Dec%202012.pdf

[17] *Stealth 9400c,* Super Skyrider – Mobile HF NVIS Magnetic Loop Antenna, [Online]. Available:https://www.stealth.ae/plugins/custompages/detinf.php?id=372&id_categories=136

[18] *RF-3134-AT003/5,* Harris OTM Loop Antenna, [Online]. Available: http://rf.harris.com/media/RF-3134-AT003-5%20Web_tcm26-19129.pdf

[19] *9350M,* Codan Automatic Tuning Whip Antenna, [Online]. Available: https://hf-ssb-tranceiver.at-communication.com/en/codan/hf_ssb_antennas_9350.html

[20] *Stealth 9420,* HF Loop Antenna, [Online]. Available: http://www.cntlwire.com/dealer_downloads/stealth-antennas/9420-datasheet.pdf

[21] M. Koubeissi, B. Pomie, and E. Rochefort, "Perspectives of HF half loop antennas for stealth combat ships," *Prog. Electromagn. Res. B*, vol. 54, pp. 167–184, 2013.

[22] "Monthly Report - June 2013," Marine corps center for lessons learnt, June 2013.

[23] *Harris RF-3134-AT003/5 OTM vehicular loop antenna,* Harris Corp., 2016. [Online]. Available: http://rf.harris.com/

[24] K. Koubeissi, “Private communication,” 2015.

[25] M. Ignatenko and D.S. Filipovic, "On the design of vehicular electrically small antennas for NVIS communications," *IEEE Trans. Antennas Propag.*, vol. 64, no. 6, pp. 2136-2145, June 2016.

[26] O. Langlois, “Wideband HF antenna - Cobham Plc.,” *HFIA 2015 meeting*, Brussels, Belgium, September 2015.

[27] M. B. McElroy, “Ionosphere and Magnetosphere,” *Encyclopedia Britannica,* 08th August 2012. [Online]. Available: https://www.britannica.com/science/ionosphere-and-magnetosphere

[28] NOAA, definition of ionospheric regions, [Online]. Available: http://www.ngdc.noaa.gov/stp/iono/ionostru.html

[29] A. Ghasemi, A. Abedi, F. Ghasemi, “Propagation engineering in wireless communications,” Springer, New York, NY, USA, 2012.

[30] B. Austin, "Near vertical incidence skywaves in world war II: an historical perspective," in *Proceedings of HF Radio Systems and Techniques Conference*, Conference Publications No. 474, 2000, pp. 225 - 229.

[31] S. J. Burgess and N. E. Evans, "Short-haul communications using NVIS HF radio," *Electronics & Comm. Eng. Journal,* vol. 11, pp. 95-104, 1999.

[32] B. Witvliet, E. van Maanen, G. Petersen, A. Westenberg, M. Bentum, C. Slump, and R. Schiphorst, "Near vertical incidence skywave propagation: elevation angles and optimum antenna height for horizontal dipole antennas," *IEEE Antennas Propag. Mag.,* vol. 57, no. 1, pp. 129-146, 2015.

[33] E. Johnson, E. Koski, W. Furman, M. Jorgenson, and J. Nieto, Third Generation and Wideband HF Radio Communications, Norwood, MA, USA: Artech House, 2013.

[34] *Low Profile Antennas for Vehicles On The Move*, Project Report, Antenna Research Group (ARG), University of Colorado Boulder, July 2016.

[35] P.372-12, Recommendation of International Telecommunication Union ITU-R, *Radio noise,* 2015.

[36] H. A. Wheeler (1947). "Fundamental Limitations of Small Antennas". *Proceedings of the IRE* 35: 1479–1484. doi:10.1109/JRPROC.1947.226199

[37] H. A. Wheeler, "The Radiansphere around a Small Antenna," Proceedings of the IRE, vol. 47, pp. 1325-1331, 1959.

[38] L.J. Chu, "Physical limitations on omni-directional antennas," *J. of Appl. Physics,* Vol. 19, pp. 1163-1175, Dec. 1948.

[39] P.527-3, Recommendation of International Telecommunication Union ITU-R, *Electrical characteristics of the surface of the Earth,* 1992.

[40] C. W. Harrison Jr., "Theory of inverted-L antenna with image," Sandia Corp. tech memo, report no. SCTM-11-58(14), April 1958.

[41] R. King, C. Harrison, and D. Denton, "Transmission-line missile antennas," *IRE Trans. Antennas Propag.*, vol. 8, no. 1, pp. 88–90, Jan. 1960.

[42] K. Fujimoto, Henderson A., Hirasawa K., and James J.R. Small antennas. Electronic & electrical engineering research studies: Antennas series. Research Studies Press, 1987.

[43] A. Andujar, J. Anguera, and C. Puente, "On the radiation pattern of the L-shaped wire antenna". Progress in Electromagnetic Research, vol. 6:pp. 91-105, 2009.

[44] A.D. Wunsch and S.P. Hu, “A closed-form expression for the driving-point impedance of the small inverted-L antenna,” *IEEE Trans. Antennas Propag.*, vol. 44, no. 2, pp. 236–242, Feb. 1996.

[45] Kraus J. Antennas. Electronic & electrical engineering research studies: Antennas series. Harper and Row, New York, 1988.

[46] S. A. Sanghai, M. Ignatenko and D. S. Filipovic, "Low-Profile Two-Arm Inverted-L Antenna Design for Vehicular HF Communications," in *IEEE Transactions on Antennas and Propagation*, vol. 65, no. 11, pp. 5710-5719, Nov. 2017.

[47] T. Yamashita and M. Taguchi, “Ultra low profile inverted L antenna on a finite conducting plane,” *Proc. International symp. on antennas and propagat.(ISAP),* pp.361-364, Oct. 2009.

[48] Y. J. Park, H. J. Ham, H. K. Ryu, K. S. Lee, J. M. Woo, “Low-profile inverted-L aircraft antenna with one folding using ground edge current,” *Electronics Lett.*, vol. 50, no. 17 Aug. 2014.

[49] Z. N. Chen and M. Y. W. Chia, "Broadband planar inverted-L antennas," *IEEE Proc. on Microwave, Antennas and Propagation,* no. 148, pp. 339-342, Oct. 2001.

[50] J. Y. Deng and L. X. Guo, "Double folded inverted-L antenna for access points," *IEEE Antennas Propag. Soc. Int. Symp., in Proc.*, pp. 1962-1963, Vancouver, BC, July 2015.

[51] A. D. Yaghjian and S. R. Best, "Impedance, bandwidth, and Q of antennas," *IEEE Trans. Antennas Propag.*, vol. 53, no. 4, pp. 1298-1324, Apr. 2005.

[52] M. Gustaffson, C. Sohl, and G. Kristensson, “Physical limitations on antennas of arbitrary shape,” *Proc. R. Soc. A*, vol. 463, pp. 2589 – 2607, July 2007.

[53] J.L. Volakis, C. C. Chen, and K. Fujimoto, Small Antennas: Miniaturization Techniques and Applications. *McGraw-Hill*, 2010.

[54] Comrod – APX52, HF Sectional Whip Antenna, Comrod Communications Group, Westlake, Ohio, 2017. [Online]. Available: https://www.comrod.com/wp-content/uploads/APX52.pdf.

[55] *Harris – SBv35 Vertical HF Whip Antenna*, Harris Corp., 2016. [Online]. Available: https://www.harris.com/sites/default/files/rf-products/SB-V16-SB-V35_tcm26-9214.pdf

[56] D. Sievenpiper, D. Dawson, M. Jacob, T. Kanar, S. Kim, J. Long, and R. Quarfoth, "Experimental validation of performance limits and design guidelines for small antennas," *IEEE Trans. Antennas Propag.*, vol. 60, no. 1, pp. 8–19, Jan 2012.

[57] Y. Geyi, "A method for the evaluation of the small antenna Q," *IEEE Trans. Antennas Propag.*, vol. AP-51, pp. 2124-2129, Aug. 2003.

[58] M. Ignatenko, S. Sanghai, G. Lasser, B. Allen, R. Smith, M. Notaros, and D. S. Filipovic, "Wide-band high-frequency antennas for military vehicles: design and testing low-profile half-loop, inverted-L, and umbrella NVIS antennas.," *IEEE Antennas and Propag. Mag.*, vol. 58, no. 6, pp. 64-74, Dec. 2016.

[59] M. J. Packer and R. I. Desourdis, "Rural and urban groundwave propagation in a desert environment," *Commun. on the Move, Military commun. conf. (MILCOM)*, pp. 634-638 vol.2, Oct. 1993.

[60] S. Sanghai, M. Ignatenko, and D. S. Filipovic, "Two arm offset fed inverted-L antenna for vehicular HF communications," *IEEE Antennas Propag. Soc. Int. Symp., in Proc.*, pp. 1604-1605, Vancouver, BC, July 2015.

[61] M. Ignatenko, G. Lasser, and D. Filipovic, "Wideband HF vehicular antennas for communications on-the-move," *Proceedings of the Antenna Applications Symposium,* pp. 502-519, 2015.

[62] D. M. Pozar, Microwave Engineering, 3rd ed., Hoboken, NJ, USA: Wiley, 2005.

[63] *Makerbot 5th Generation Replicator*, Makerbot, 2014. [Online]. Available: http://store.makerbot.com/replicator

[64] *USMC AAV C7A1 RAMRS*, 3D Warehouse model. [Online]. Available: https://3dwarehouse.sketchup.com/

[65] S. Sanghai, M. Ignatenko, K. Hassett, and D. S. Filipovic, "Scaled model measurements of HF antenna for vehicular platforms," Antenna Measurement and Techniques Assoc. Symp., Tuscon, AZ, Oct. 2014.

[66] N. Saleh, N. Hopkinson, R. J. M. Hague, and S. Wise, "Effects of electroplating on the mechanical properties of stereo lithography and laser sintered parts," *Rapid Prototyping J.*, Vol. 10. Iss. 5, pp. 305-315, 2004.

[67] *LMR-400: Flexible low loss communications coax*, Times microwave systems. [Online]. Available: https://www.timesmicrowave.com/documents/resources/LMR-400.pdf

[68] *M-ATV,* MRAP – All Terrain Vehicle, [Online]. Available: https://oshkoshdefense.com/vehicles/m-atv

[69] M. Ignatenko, S. Sanghai, G. Lasser, B. Allen, R. Smith, M. Notaros, and D. S. Filipovic, "Wide-band high-frequency antennas for military vehicles: design and testing low-profile half-loop, inverted-L, and umbrella NVIS antennas.," *IEEE Antennas and Propag. Mag.*, vol. 58, no. 6, pp. 64-74, Dec. 2016.

[70] *Typical Properties of PVC and CPVC,* International Polymer Solutions, [Online]. Available: http://www.ipolymer.com/pdf/PVC.pdf

[71] *Palstar HF-Auto tuner*, Palstar Incorporated, 2016. [Online]. Available:http://www.palstar.com/en/hf-auto/

[72] *IC-718 HF All Band Transceiver*, ICOM America Inc, 2018. [Online]. Available: http://www.icomamerica.com/en/products/amateur/hf/718/default.aspx

[73] A. Siripuram and M. Daly, "Near-field HF antenna pattern measurement with absolute gain calibration," *2016 USNC-URSI Radio Science Meeting*, Fajardo, 2016, pp. 91-92.

[74] *HF Antenna Pattern Range* (APR), SPAWAR, Point Loma Naval Base, San Diego, California. Downloaded from Google Maps, May, 2016.

[75] *University of Colorado Boulder Antenna Research Group (ARG), HF Prototype Antenna,* Approved for Public Release, SPAWAR Systems Center Pacific, Applied Electromagnetics Branch, Code 52250, San Diego, CA, October 2016.

[76] M. P. Daly, "Private Communication," October 2015, October 2018.

[77] *Penetrox A-13* ™ , PENA138 Oxide Inhibitor, Burndy, LLC., [Online]. Available: https://objects.eanixter.com/PD372804.PDF

[78] TrellisWare Technologies, Inc., [Online]. Available: http://www.trellisware.com/

[79] ITU-R Recommendation V.431: Nomenclature of the frequency and wavelength bands used in telecommunications. International Telecommunication Union, Geneva.

[80] *FCC Online Table for Frequency Allocations,* Office of Engineering and Technology Policy and Rules Division, FCC, Washington DC, USA. [Online]. Available: http://transition.fcc.gov/oet/spectrum/table/fcctable.pdf

[81] J.E. Freehafer, D.E. Kerr, "Elements of the problem", in propagation of short radio waves, Chicago (McGraw-Hill, Illinois, 1990)

[82] IEEE Std 145-1993(R2004), IEEE Standard Definitions of Terms for Antennas. New York, NY: The Institute of Electrical and Electronics Engineers, Inc. 1993. p. 14.

[83] *Millimeter wave propagation: Spectrum management implications,* Bulletin No. 70, Office of Engineering and Technology, New Technology Development Division, Federal Communications Commission, Washington, DC, USA, July 1997.

[84] B. Mahafza, "Radar Systems—An Overview", in Radar Signal Analysis and Processing Using MATLAB, CRC Press, New York, 2009.

[85] S. J. Dudzinsky, Jr., "Atmospheric effects on terrestrial millimeter wave communications," R-1335-ARPA, 3G10 Tactical Technology, DARPA Report, March 1974. [Online]. Available: http://www.dtic.mil/dtic/tr/fulltext/u2/780602.pdf

[86] A. W. Rudge, K. Milne, A. D. Olver, P. Knight, "The Handbook of Antenna Design," Vol. 1, Peter Peregrinus Ltd., London, UK. 1982.

[87] J. du Preez, S. Sinha, "Millimeter Wave Antennas: Configurations and Applications," Springer International Publishing, Switzerland, 2016.

[88] O. Sotoudeh, P-S. Kildal, P. Ingvarson, and C. Mangenot, "Dual band hard horn for use in cluster-fed multi-beam antennas in Ka-band," in 2005 IEEE Antennas and Propagation Symposium, 2005.

[89] T.-H. Tan, "Effectiveness of off-board active decoys against anti-shipping missiles," Thesis, Monterey, California. Naval Postgraduate School, 1996.

[90] C. K. Andrews, N. Jastram and D. S. Filipovic, "Gain and H-plane beamwidth stabilized millimeter wave horn antenna," *2016 IEEE International Symposium on Antennas and Propagation (APSURSI)*, Fajardo, 2016, pp. 1551-1552.

[91] S. Manafi, M. Al-Tarifi and D. S. Filipovic, "45–110 GHz Quad-Ridge Horn With Stable Gain and Symmetric Beam," in *IEEE Transactions on Antennas and Propagation*, vol. 65, no. 9, pp. 4858-4863, Sept. 2017.

[92] K. V. Hoel, S. Kristoffersen, J. Moen, G. Holm and T. S. Lande, "Characterization of a 3D printed wideband waveguide and horn antenna structure embedded in a UAV wing," *2016 10th European Conference on Antennas and Propagation (EuCAP)*, Davos, 2016, pp. 1-4.

[93] N. Jastram, “Passive front ends for wideband millimeter wave electronic warfare,” Ph.D. Dissertation, University of Colorado Boulder, 2014.

[94] L. Schulwitz and A. Mortazawi, “Millimeter-wave dual polarized L-shaped horn antenna for wide-angle phased arrays,”IEEE Trans. Antennas Propag., vol. 54, no. 9, pp. 2663–2668, Sep. 2006

[95] J. A. Gordon *et al.*, "An All-Metal, 3-D-Printed CubeSat Feed Horn: An assessment of performance conducted at 118.7503 GHz using a robotic antenna range.," in *IEEE Antennas and Propagation Magazine*, vol. 59, no. 2, pp. 96-102, April 2017.

[96] *K/Ka Feed Horn for MADRAS payload on board MEGHATROPIQUES Earth Observation mission (CNES / ISRO joint satellite)*, TRYO Group, Madrid, Spain. [Online]. Available: http://www.tryo.es/aerospace-products/antennas/

[97] *Lightweight machined corrugated feed horn antenna*, TRYO Group, Madrid, Spain. [Online Available]: http://www.tryo.es/aerospace-products/antennas/

[98] L. Cooper and H. Aintablian, "A multiband corrugated horn feed for satellite communication earth stations," 1985 Antennas and Propagation Society International Symposium, Vancouver, Canada, 1985, pp. 307-310.

[99] J. Teniente, I. Gómez-López, R. Caballero-Nagore, G. Crespo-López and A. Martínez-Agoües, "Quad band X/Ka horn antenna and feed chain designs," 2017 11th European Conference on Antennas and Propagation (EUCAP), Paris, 2017, pp. 3432-3436.

[100] C. G. Davis, P. T. Hutchison, F. J. Witt and H. I. Maunsell, "The spacecraft communications repeater," in *The Bell System Technical Journal*, vol. 42, no. 4, pp. 831-867, July 1963.

[101] W. T. Slingsby and J. P. McGeehan, “Antenna isolation measurements for on-frequency radio repeaters,” in *Proc. IEEE 9th Int. Conf. Antennas Propag.*, Eindhoven, The Netherlands, 1995, pp. 239–243.

[102] R. J. Jakubowski, "A new generation of high-power cellular repeaters," 40th IEEE Conference on Vehicular Technology, Orlando, FL, 1990, pp. 24-28.

[103] J. A. M. Lyon *et al.*, “Electromagnetic coupling reduction techniques,” Dept. Elect. Eng., Univ. Michigan, Ann Arbor, MI, USA, Tech. Rep. AFAL-TR-68-132, Jun. 1968.

[104] P. V. Prasannakumar, M. A. Elmansouri, and D. S. Filipovic, “Wideband decoupling techniques for dual-polarized bi-static simultaneous transmit and receive antenna subsystem,” *IEEE Trans. Antennas Propag.*, vol. 65, no. 10, pp. 4991–5001, Oct. 2017.

[105] B. F. Allen, N. Jastram and D. Filipovic, "A reactive impedance surface for enhancing antenna isolation on cylindrical platforms," *2017 IEEE International Symposium on Antennas and Propagation & USNC/URSI National Radio Science Meeting*, San Diego, CA, 2017, pp. 2661-2662.

[106] N. Jastram, M. A. Altarifi, L. Boskovic and D. S. Filipovic, "On the Split-Block Realization of Millimeter-Wave Ridge Waveguide Components," in *IEEE Microwave and Wireless Components Letters*, vol. 28, no. 4, pp. 296-298, April 2018.

[107] J. R. Wait, “Theories of scattering from wire grid and mesh structures,” in Electromagnetic Scattering, P.L.E. Uslenghi, Ed. New York: Academic, 1978, pp. 253-287.

[108] K. F. Casey, "Low-Frequency Electromagnetic Penetration of Loaded Apertures," in *IEEE Transactions on Electromagnetic Compatibility*, vol. EMC-23, no. 4, pp. 367-377, Nov. 1981.

[109] K. F. Casey, "Electromagnetic shielding behavior of wire-mesh screens," in *IEEE Transactions on Electromagnetic Compatibility*, vol. 30, no. 3, pp. 298-306, Aug 1988.

[110] N. Jastram, C. Andrews and D. S. Filipovic, "Design of circular dual and quad ridge horn antennas for millimeter wave applications," *2017 11th European Conference on Antennas and Propagation (EUCAP)*, Paris, 2017, pp. 764-767.

[111] J.T. Black & R. A. Kohser, “Degarmo’s Materials and Processes in manufacturing”, Wiley publications, 2003, pp. 227.

[112] *Python Programminig Language - Python Software Foundation.* Python Language Reference, version 2.7. [Online]. Available: http://www.python.org/

[113] *Radioscreen* ™ *,* Extremely fine shielding mesh, Mesh Products, EMF Fabrics, Less EMF Inc., 2017. [Online]. Available: https://www.lessemf.com/1240.pdf

[114] P. Sorells, “Weathering the Elements: how weather affects the network,” Wireless and Fixed Communications, ITS International – Advanced Technology for Traffic Management and Urban Mobility, Route One Publishing, Ltd. [Online]. Available: http://digital.itsinternational.com/2013/global/jul-aug/digital.html

[115] *A guide to the selection of RF coaxial cable,* Technical Notes, Times Microwave Systems, 2018. [Online]. Available: http://www.timesmicrowave.com/products/lmr/downloads/216-227.pdf

[116] I. Marchbank, "Radome manufacture-a review to date," *IEE Colloquium on Materials and Manufacturing Processes for Antennas*, London, 1990, pp. 5/1-5/4.

[117] E. G. Hoare and R. Hill, "System requirements for automotive radar antennas," *IEE Colloquium on Antennas for Automotives (Ref. No. 2000/002)*, London, 2000, pp. 1/1-111.

[118] S. P. Malashenkov, "Design of protective aerial complexes," *2005 5th International Conference on Antenna Theory and Techniques*, 2005, pp. 84-88.

[119] The Study of Foreign Object Damage Caused by Aircraft Operations on Unconventional and Bombdamaged Airfield Surfaces, Final Report, AFESC, Tyndall AFB, FL, June 1981.

[120] D. J. Kozakoff, "Analysis of Radome Enclosed Antennas," Ch. 11: Environmental Degradations in Analysis of Radome Enclosed Antennas, Artech House, 2010, pp. 217-228.

[121] *dBs 5100A-HS*, De-ice DME Antenna, dB Systems Inc., [Online]. Available: http://www.dbsant.com/images/500300-111_DME_HeatedRadome_Manual.pdf

[122] *The performance and Economics of Radome – Enclosed Antenna Subsystems,* Memo No. 134, 25 Meter Millimeter Wave Telescope, Electronic Space Systems Corporation and ESSCO Collins Ltd., January 1980. [Online]. Available: https://library.nrao.edu/public/memos/25/25M/25M_134.pdf

[123] R. H. Duhamel and D. Isbell, "Broadband logarithmically periodic antenna structures," IRE International Convention Record, vol. 5, pp. 119-128, Mar, 1957.

[124] R. H. DuHamel and F. R. Ore, "Logarithmically Periodic Antenna Designs," IRE International Conv. Rec., vol. 6, pp. 139–151, Mar, 1958.

[125] R. L. Carrel, "The Design of Log-Periodic Dipole Antennas," IRE International Conv. Rec., vol. 9, pp. 61–75, Mar, 1961.

[126] D. S. Filipovic and T. P. Cencich, "Frequency Independent Antennas," in Antenna Engineering Handbook, 4th ed., J. L. Volakis, Ed. New York: McGraw-Hill 2007.

[127] J. Ha, "High Power Wideband Antennas for Electronic Warfare Systems," Ph.D. Dissertation, University of Colorado Boulder, 2016.

[128] *Rogers 3003, RO3000 Series Circuit Materials,* High Frequency Laminates, Rogers Corporation, Chandler, AZ. [Online]. Available: https://www.rogerscorp.com/documents/722/acs/RO3000-Laminate-Data-Sheet-RO3003-RO3006-RO3010.pdf

[129] AWR Microwave Office, National Instruments, Austin, Tx, USA.

[130] *Power Rating for Coaxial Connectors,* Appendix in Product Catalogue, Southwest Microwave, Tempe, AZ, USA. [Online]. Available: http://mpd.southwestmicrowave.com/static/appendix.pdf

[131] E. M. Turner, “Spiral slot antenna,” U.S. Patent 2863145, 1958.

[132] R. Corzine and J. Mosko, Four-Arm Spirals, Norwood, MA, USA, Artech House, 1990.

[133] P. B. Green, “Advances in Spiral Antenna Technology”, RADC Proc. Of the Antenna Appl. Symp., Vol 1, pp. 227-248, Mar. 1984.

[134] S. Palreddy, R. Cheung, “Two Arm Archimedean Spiral Helical Antenna with Wrap Around Absorber”, 25th Ann. Rev. of Progress, In Appl. Computational Electromagnetics, March 2009.

[135] J. Bargeron, M. Radway, D. S. Filipovic, “5:1 Wideband High-Power Spiral-Helix Antenna”, in *Proc. IEEE Antennas Propag. Soc. Int. Symp. (APSURSI)*, Jul. 2012.

[136] M. Elmansouri and D. S. Filipovic, “Time and frequency domain analysis and design of circularly–polarized spiral antenna arrays,” in *Proc. IEEE Antennas Propag. Soc. Int. Symp. (APSURSI)*, Jul. 2013.

[137] T. Macnamara, “Introduction to Antenna Placement and Installation,” New York: John Wiley & Sons, Incorporated, 2010.

[138] *FCC Online Table for Frequency Allocations,* Office of Engineering and Technology Policy and Rules Division, FCC, Washington DC, USA. [Online]. Available: http://transition.fcc.gov/oet/spectrum/table/fcctable.pdf

[139] R. J. Fontana and S. J. Gunderson, "Ultra-wideband precision asset location system," *2002 IEEE Conference on Ultra-Wideband Systems and Technologies*, Baltimore, MD, USA, 2002, pp. 147-150.

[140] X. Qing, Zhi Ning Chen and T. S. P. See, "Sectored antenna array for indoor mono-station UWB positioning applications," *2009 3rd European Conference on Antennas and Propagation*, Berlin, 2009, pp. 822-825.

[141] K. Uchiyama and A. Kajiwara, "Vehicle location estimation based on 79GHz UWB radar employing road objects," *2016 International Conference on Electromagnetics in Advanced Applications (ICEAA)*, Cairns, QLD, 2016, pp. 720-723.

[142] J. Park and S. H. Cho, "IR-UWB Radar Sensor for Human Gesture Recognition by Using Machine Learning," *IEEE 14th International Conference on Smart City*, Sydney, NSW, 2016, pp. 1246-1249.

[143] S. Lee, Y. Jeon, S. Choi, M. S. Han and K. Cho, "Gigabit UWB video transmission system for wireless video area network," in *IEEE Transactions on Consumer Electronics*, vol. 57, no. 2, pp. 395-402, May 2011.

[144] C. Fumeaux, et.all, “Finite-Volume Time-Domain Analysis of a Cavity-Backed Archimedean Spiral Antenna,” IEEE Trans. Ant. Propagat., vol. 54, 844–851, 2006.

[145] *HFB152034,* High Frequency Ferrite with Cylindrical EMI core, Magnetic EMI Supressors, EMI and EMC Products, Laird Technologies Plc., London, UK. [Online]. Available: http://c1170156.r56.cf3.rackcdn.com/UK_LRD_HFB152034-000_1DS.pdf

[146] *IPP-7066-Surface Mount 90 Degree Hybrid Coupler,* Product Catalogue, Innovative Power Products, Holbrook, NY, USA. [Online]. Available: https://innovativepp.com/product/ipp-7066/.

[147] Random House Kernerman Webster's College Dictionary, 1997, 1991 by Random House, Inc, Copyright 2005, K Dictionaries Ltd, 2010.

[148] *Electrical and Electromagnetic Tests,* Engineering and Testing Services, Dayton T. Brown, NY, USA.

[149] S. Sanghai, M. Elmansouri, R. Sammeta, J. Bargeron, D. S. Filipovic, “Failure Mechanisms of Spiral-Helix Antenna under High Power Conditions” in IEEE Antennas and Propagation Society International Symposium, July, 2014.

[150] J. McCormick, H. H. Lin and L. Zakraysek, "Liquid Penetrant Testing for Microelectronic Package Hermeticity," *20th International Reliability Physics Symposium*, San Diego, NV, USA, 1982, pp. 207-213.

APPENDIX A

Low-Cost, Expendable Planar Log Periodic Antenna

A.1 Motivation

The research motivation for the proposed planar log periodic antenna design described herein is based on the desire to physically protect the antenna from environmental elements during operation. The wideband electrical properties and bi-directional nature of the planar log periodic antenna makes it ideal for many practical uses. The versatility of this antenna makes it ideal for deployment on various platforms. Typically, an antenna considered for such applications needs to be designed with an encasing shell or radome for environmental protection. Antenna ruggedization and planned deployment play a vital role in the success of the antenna system and its long operational life. The antenna must be able to handle harsh operational environment, exposure to the weather and abuse during field operations. An approach towards the use of a radome for the proposed planar log periodic antenna is thus motivated by the performance of the antenna under real world scenarios.

Antennas are often deployed in harsh environments where they are expected to operate over long duration without easy access for cleaning, maintenance, calibration and testing. In order for the wireless and RF infrastructure to achieve the maximum possible resilience to the environmental factors, each section of the system must continue to perform at its designed specifications. To achieve stable operation over a long duration of time, each RF component and interconnect along the RF path must be properly installed, verified in-situ and maintained [114]. It may not be practically possible to protect RF infrastructure and components against severe weather events such as tornados, hurricanes and floods but it is vitally important to ensure that they are proofed against the day to day weather if round the clock operation is desired. The antennas and other sensitive equipment mounted at most cellular and other point to point base station sites have to tolerate constant exposure to wind, rain, sleet, snow and even the UV exposure to the sun.

Ensuring isolation from moisture and water in antennas as well as the RF transmission lines is critically important to keeping the wireless networks operational. The typical points of failure at the antenna level include water ingress at various connection points for the antenna casing such as at the tower mounts and the fabrication joints, water ingress at the RF connection and feed interface of the antenna or the transmission line feeding it [115]. Water ingress inside the antenna is undesirable as it can cause deterioration in the antenna performance and consecutively affect the network performance. Long term weather and environmental exposure may often lead to slow degradation of performance due to rust, moisture, water ingress, salt fog and mist, and heavy wind gusts.

To counter these practical challenges, antennas are often designed with protective layers in front of the aperture. The purpose of this protective layer or the radome is to provide protection for the antennas and their associated systems without causing unacceptable degradation to the electrical performance. As such the radome design is a compromise between the physical need to place a protective barrier in front of the antenna and the desire for the same antenna to have a clear and unrestricted view of its target in an electrical sense [116]. Various types of radomes and its properties are discussed for antenna applications in [116]. Antennas used for the automotive radars employ radome that protects the aperture from the road debris, rain, snow and dust [117]. Large operational facilities such as doppler weather radars also employ radome over the antenna elements to protect them from the external environmental factors [118]. Foreign object damage is an important issue for nose cone mounted antennas in an aircraft [119]. Several documents of nose cone damage have been reported for aircrafts that encounter lightning, thunderstorms, hail, rain, dust or bird strikes during flight [120]. A radome loaded antenna with integrated heating element for deicing the antenna is shown as an example of how the radome can be used to add additional resilience to extreme weather [121]. It must be noted that although the radome adds protection to the antenna against weather and the environment, typical radome materials are extremely specialized and an antenna outfitted with a radome can often have a large upfront cost associated with it [122]. The radome design also needs to be as wideband as the operational range of the antenna itself, which can be a major challenge in some cases.

In most typical cases, a planar log periodic antenna is realized on a dielectric substrate. Leaving the antenna in its raw PCB form factor may expose the copper traces to the environment and cause potential deterioration in its performance. In extreme cases, it may lead to truncation in the operational life of the antenna due to corrosion, dust and environmental abrasion. Additionally, dielectric exposure to moisture would lead to absorption by the hydrophilic dielectric bulk and cause a change in the dielectric properties of the substrate which may affect the antenna performance. With all these challenges and perspectives, it is appropriate to recognize how a low cost, wideband, easy to fabricate radome for the expendable planar log periodic antenna forms the motivation for the first part of this research.

A.2 Overview of Planar Log Periodic Antennas

Raymond DuHamel introduced the log-periodic (LP) aperture in 1957 [123]. Subsequent research from DuHamel and Carrel established the LP design guidelines and operational details [124] [125]. A significant number of contributions related to the theory and practical designs have been reported for LP antennas since then [126]. The active region of the antenna comprises of primarily resonant teeth pairs changes with the operating frequency: the higher the frequency, the active region migrates closer to the inside, near the feed. When realized in planar configuration, these antennas radiate towards both front and back directions (with respect to the aperture) very consistently over a broad range of frequencies. The wideband behavior of LP antennas has been utilized in a wide variety of applications, both for defense and non-defense/commercial application related needs.

The antenna systems employed in the field demand a higher level of robustness along with compliance to the basic electrical performance. The mechanical and ergonomic design features of the antenna may have equal importance in this case. The radome design proposed herein yields an ergonomic, rugged and practical antenna ready for outdoor deployment, while still maintaining high degree of compliance with the desired wideband electrical performance.

$N = 12$

$\tau_n = R_n/R_{n-1}$

$\chi_n = r_n/R_n$

$R_{11} = 98$ mm

$\Delta = 12$ mm

$\alpha = 173.05°$

$\beta = (\pi-\alpha) = 6.95°$

$X_n = \sqrt{\tau_n}$

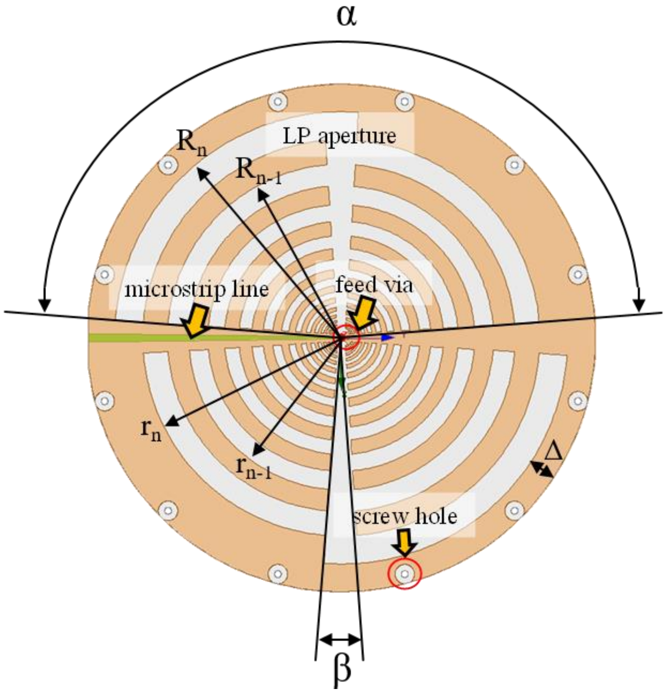

Figure A.1: Variables used to define the proposed planar log-periodic antenna.

The basic aperture shown herein has been developed by Jaegeun Ha. [127]. It must be noted that Ha adopted his design for high power applications by using wide boom, which contrasts it to most conventional planar log periodic designs.

An illustration of the log-periodic antenna with annotations is given in Figure A.1. The antenna is fed by a microstrip line, etched on the other side of dielectric (with respect to the aperture), and is fabricated using standard printed circuit board (PCB) process. Varying growth rate is applied to the inner teeth to keep the width of the innermost teeth larger than 0.8 mm. The boom is offset from the center of the antenna by 40 mm, thus increasing the minimum boom width to 1.2 mm which is much thicker compared to conventional log-periodic apertures. The antenna is designed on a 1.524 mm (60mil) Rogers3003 substrate [128]. The R03003 material results in comparatively lower nominal impedance of log-periodic antenna. The input impedance of the antenna is stabilized over wide bandwidth due to the variable growth rate used. A linearly tapered microstrip feed line impedance transformer with minimum line width of 0.8 mm is designed in AWR MWO [129]. The aperture has 12 teeth

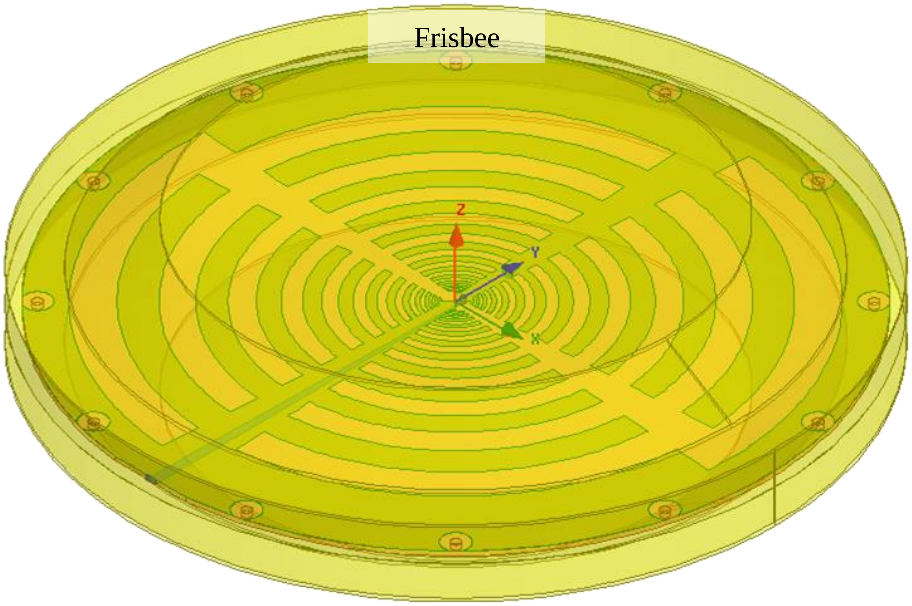

Figure A.2: Frisbee discs used as radomes for the proposed log periodic aperture.

pairs (N = 12) distributed over the antenna's diameter of 220 mm (R_{11} = 98mm and Δ = 12mm). The teeth from the 12th arm are fused with the surrounding copper ring in two quadrants as shown. Other adopted structural parameters are: growth rate τ = 0.7674; α = 173.05°; boom angle β = 6.95°. Mounting holes with 3 mm diameter are placed at a radial distance of 105 mm on the log periodic aperture to allow for radome integration using fixtures.

A.3 Estimated Impact of Radome

The computational analysis is performed in ANSYS HFSS. To provide a radome for the antenna aperture, two COTS Frisbees are used to enclose the aperture as shown in Figure

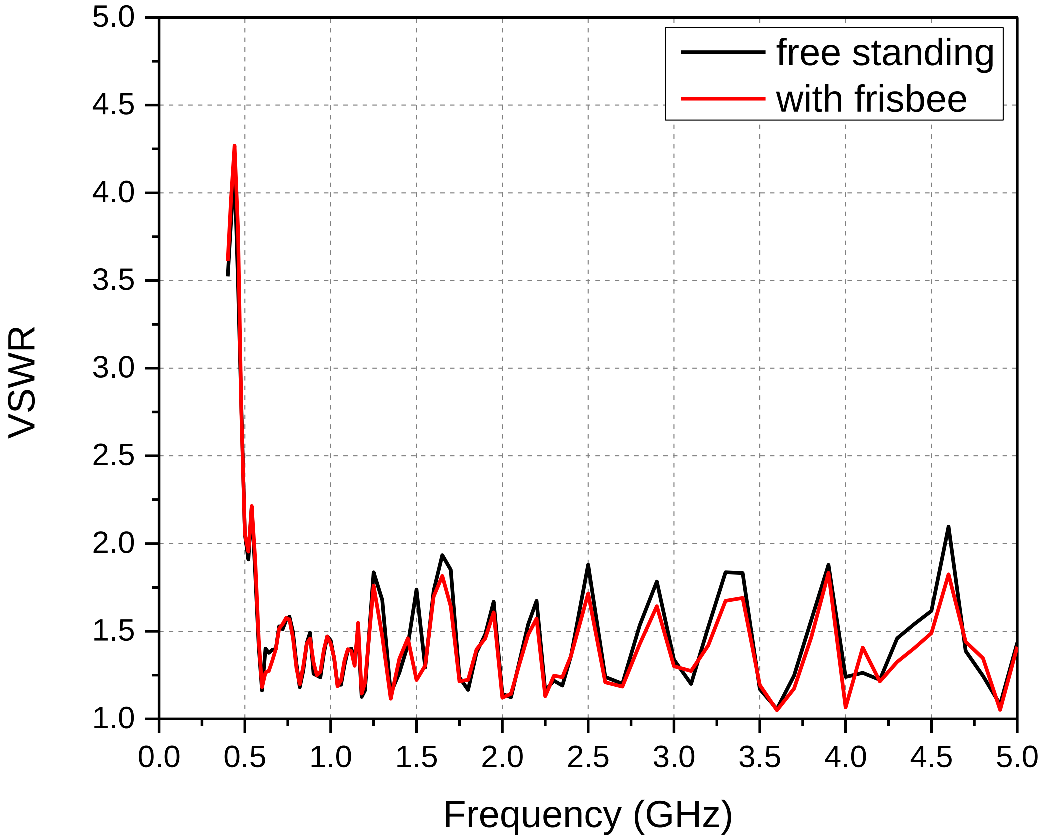

Figure A.3: VSWRs of the antenna with and without the Frisbee.

A.2. The Frisbees are made up of low-density polyethylene (LDPE) with permittivity ε_r=2.2 and loss tangent tanδ=0.0013, respectively.

Figure A.3 shows the simulated VSWR characteristics of the free standing and Frisbee loaded log-periodic antennas. The two curves agree with each other well except for the fact that the Frisbee loading slightly improves match over most of the operating bandwidth. In the simulation results with the Frisbee, the VSWR is below 2:1 from 550 MHz to over 5 GHz. Measurements shown later demonstrate that the small swing in VSWR at turn on is not present in the fabricated antenna. Figure A.4 shows the realized boresight gain and the front-to-back ratio of the free-standing aperture and the antenna with the Frisbee radome. As seen, in case of the VSWR the two configurations perform similarly for the boresight gain. The

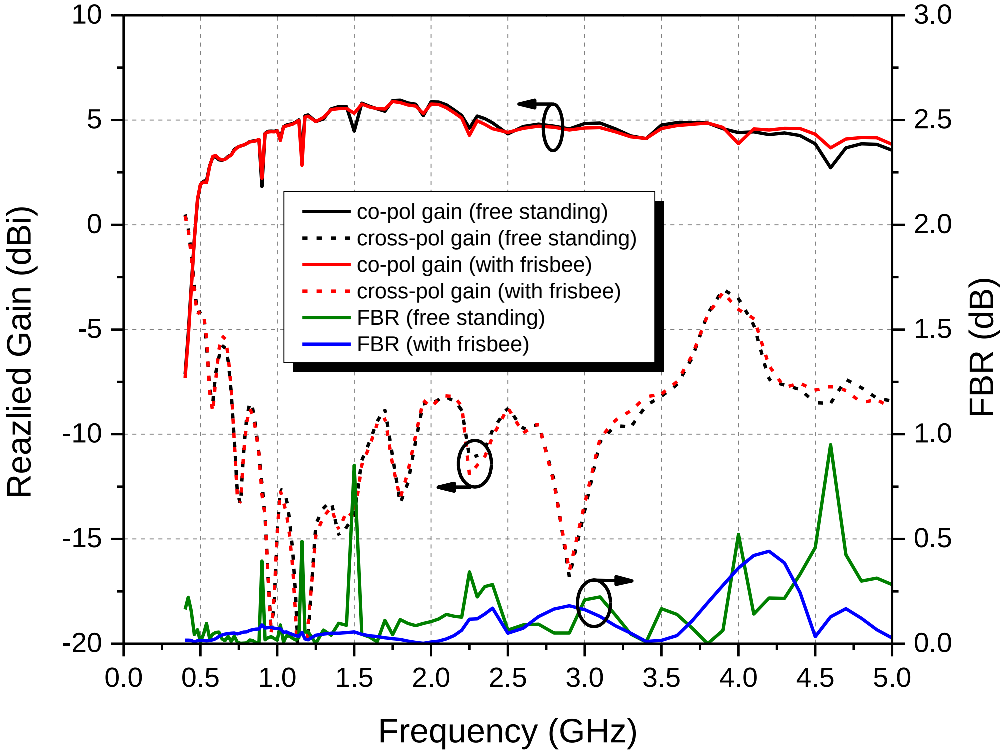

Figure A.4: Realized boresight gain and front-to-back ratio of the antenna with and without the Frisbee.

realized gain at the turn-on frequency is around 2.5 dBi and a stable gain performance is seen. The front-to-back ratio with Frisbee is below 0.44 dB over the entire bandwidth. The simulated radiation patterns in E-plane and H-plane (xz- and yz-planes, respectively) of the antenna enclosed by the Frisbee are shown in Figure A.5. A stable bi-directional pattern over a broad bandwidth can be seen, though a small beam squint in E-plane at 4 GHz is observed. Lastly, total efficiencies of the antenna for the two cases are shown in Figure A.6, and they are higher than 85% over the entire bandwidth. It is worth noting that the Frisbee does not decrease the efficiency drastically, owing to the impact from its dielectric losses.

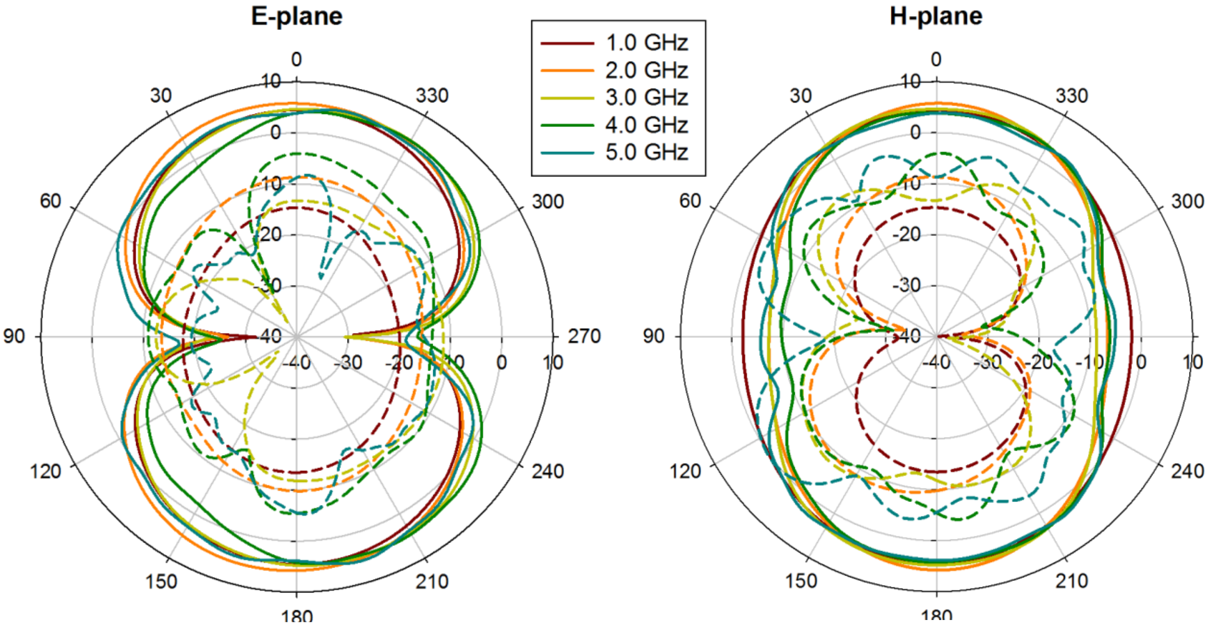

Figure A.5: Radiation patterns at two principal planes with Frisbee enclosure. Solid line: co-pol gain. Dotted line: cross-pol gain.

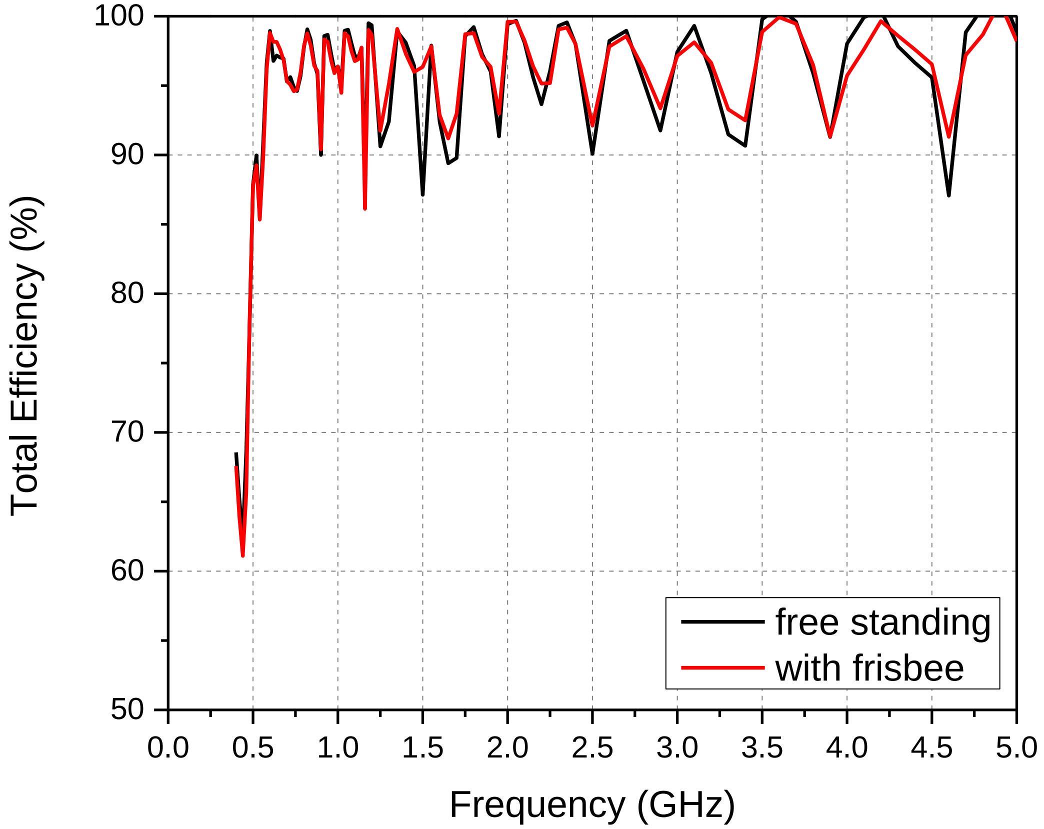

Figure A.6: Total efficiency of the antenna with and without the Frisbee.

A.4 Radome - Antenna Integration

The integration of Frisbees with the antenna includes customizing the Frisbee discs in accordance with the aperture design to mount the antenna aperture inside the Frisbee radome. The aperture is sandwiched between the two Frisbee disks as shown in Figure A.7. The entire antenna aperture is supported inside the Frisbee radome using right angled support columns inlaid on the inside walls of each of the Frisbee disk. The customized acrylic mounting posts for the Frisbee radome are set in accordance with the through hole pattern on the log-periodic antenna aperture. The mounting posts are fabricated out of transparent acrylic sheet of 1 mm thickness and a width of 10 mm. One arm of the right-angled mounting

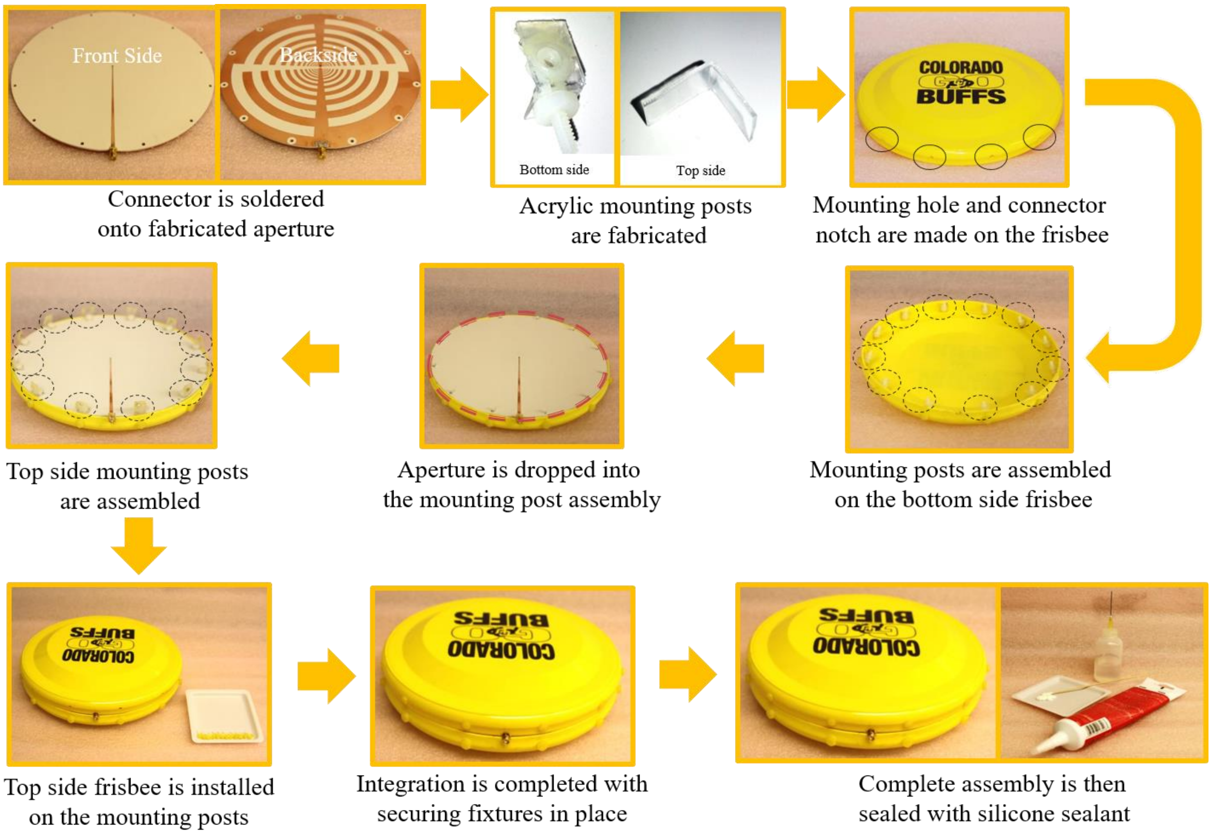

Connector is soldered onto fabricated aperture

Acrylic mounting posts are fabricated

Mounting hole and connector notch are made on the frisbee

Mounting posts are assembled on the bottom side frisbee

Aperture is dropped into the mounting post assembly

Top side mounting posts are assembled

Top side frisbee is installed on the mounting posts

Integration is completed with securing fixtures in place

Complete assembly is then sealed with silicone sealant

Figure A.7: General build process for the Frisbee antenna.

posts is bonded to the inner wall of the Frisbee. This arm is 20.3 mm long (equal to the inner height of the Frisbee disk). The other arm of the mounting post is 10 mm long with a center hole of diameter 5 mm drilled into it to house the mounting bolts that would harness the two Frisbees and hold the aperture in between them. The entire antenna aperture is harnessed to the Frisbee radome using 8-32 imperial sized nuts and bolts fastened onto 12 such mounting posts spaced at the periphery of the Frisbee disk with an angular separation of 30°. Additionally, each Frisbee disk has 12 supporting posts set in the space between two mounting posts to provide mechanical stability and enhanced support to the antenna aperture and to prevent it from warping and distorting in the event the Frisbee antenna experiences a mechanical shock or an accidental drop. The antenna aperture has an SMA type connector interface in order to maintain the compact and easy to assemble form factor.

Note that the concept can be realized with other high-power capable connectors, such as N- or TNC without major changes or any deterioration in antenna performance. However, for the purpose of this research, the SMA connector power handling capabilities suffice [130]. For operating frequency of 1 GHz, and 5 GHz, the SMA connector is rated for powers of ~600 W and >200 W, respectively [130]. The completed Frisbee antenna is sealed using silicone sealant paste applied to the joint connecting the two Frisbee discs thereby sealing any small air gaps or slits formed at the junction of the two Frisbee discs and adding to the mechanical integrity of the design. Use of sealant in this case holds a fair promise for future designs that are hermetically sealed or waterproof in nature. Such a design that isolates the antenna aperture from the external factors such as weather, moisture and dust would prove beneficial in increasing the durability and operational life of the antenna for many years as compared to the bare, exposed antenna aperture which would be subjected to the harsh external conditions.

A.5 Measured Performance

The measured VSWR of the free-standing aperture and the assembled prototype are shown in Figure A.8. The turn-on frequencies for VSWR = 2:1 are 500 MHz for both, free standing antenna and for the fully assembled prototype with a decade bandwidth performance (0.5 to 5 GHz) of VSWR below 2:1 is achieved, and the electrical size of antenna at the turn-on frequency is $0.373\ \lambda_0 \times 0.373\ \lambda_0 \times 0.09\ \lambda_0$ with the Frisbee radome. Note that the effect of the Frisbee on the antenna performance at these frequencies is not detrimental. The measurement of the radiation patterns and gain are conducted in a combined near-field/far-field measurement system at University of Colorado Boulder (Figure A.9). The antenna is placed on the AUT rotator mount with absorber backing using a Styrofoam spacer

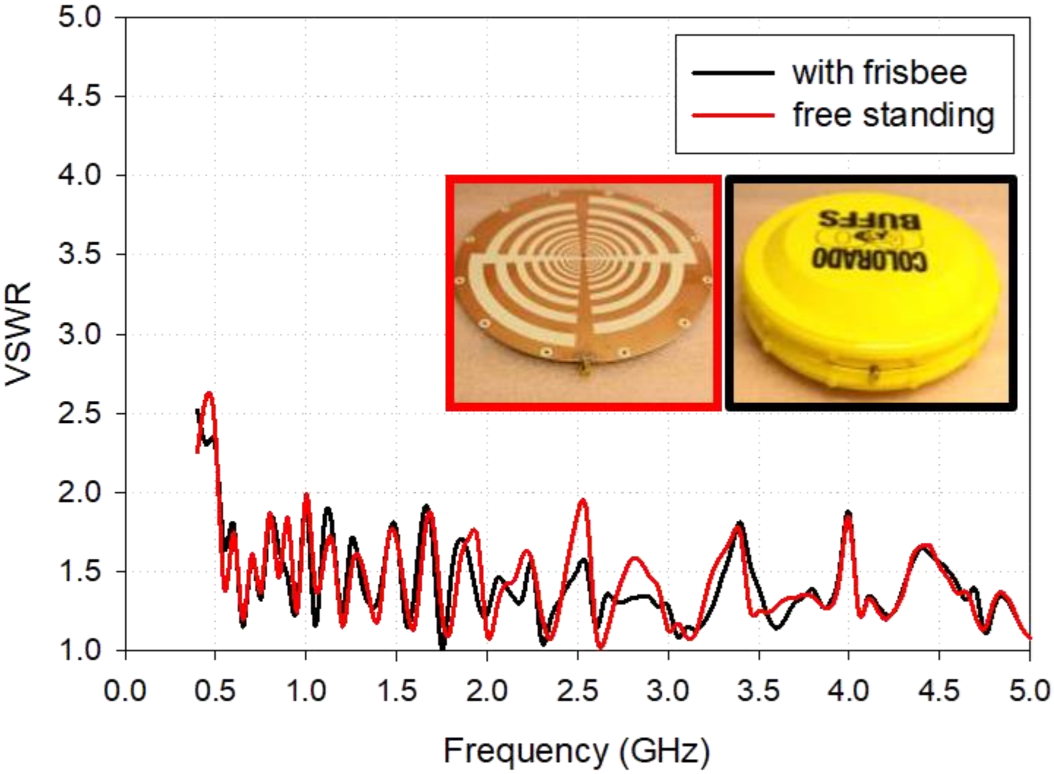

Figure A.8: Measured VSWR for the free-standing aperture and frisbee antenna.

to eliminate any impact of reflections on the measurements from the metallic rotator mounts. Note that in the real application, there will be no absorptive backing since this prototype is designed for the bi-directional application, there will be no absorptive backing since this prototype is designed for the bi-directional operation. A standard end-fire log-periodic antenna is used as the source for the performed far-field experiments.

The measured realized gain of the antenna is depicted in Figure A.10 and overall good consistency is achieved in the measurements and they track well with the simulation results. The measured realized gain at the turn-on frequency is 0 dBi and it is maintained higher than 2.5 dBi from 0.5 GHz to 4.6 GHz after which the radome impacts the gain causing it to drop close to 0 dBi over a narrow band range of frequencies around 4.7 GHz.

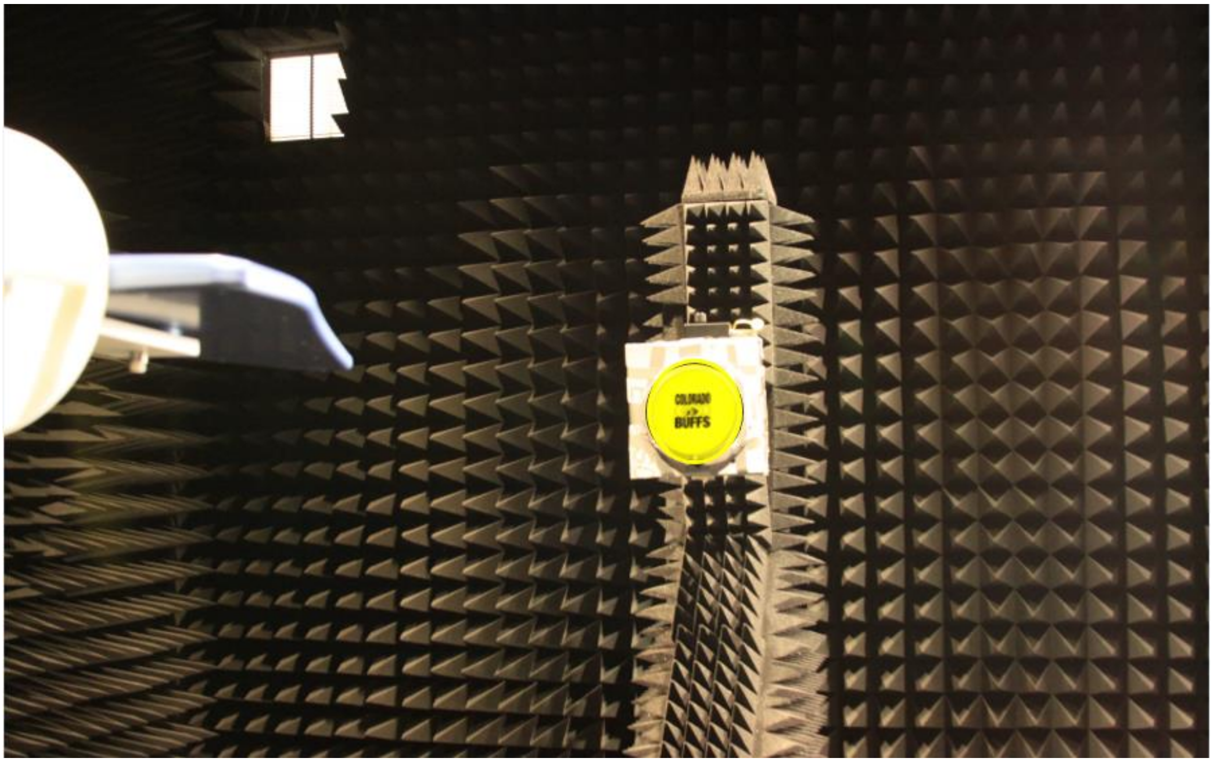

Figure A.9: Antenna setup used for gain and radiation pattern measurements.

The measured normalized radiation patterns of the antenna in E- and H-planes are shown in Figure A.11, and Figure A.12, respectively. Although the measured patterns are uni-directional due to the absorber used in the measurement, the antenna has bi-directional radiation in free-space. The patterns are stable over the frequency band of interest in terms of shape and beam width. Increased cross-polarization at the high end is partially due to the measurement setup used and due to the impact of the radome. The numerical and experimental results verify that the antenna has more than a decade impedance bandwidth, consistent radiation patterns, and good bi-directionality without noticeable deterioration in electrical performance in the presence of the proposed radome.

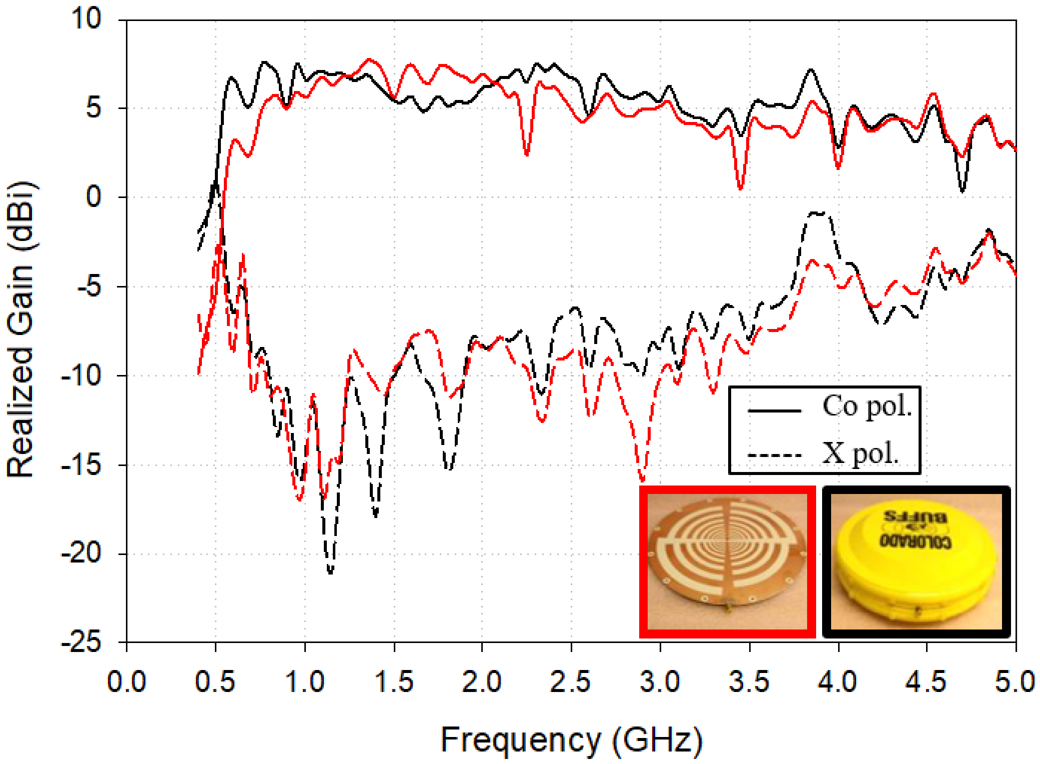

Figure A.10: Measured broadside gain of the fully assembled log-periodic antenna.

A.6 Summary and Discussion

The integration of a low cost, easy to fabricate log periodic antenna with a Frisbee radome is discussed. Good, consistent impedance and radiation pattern performance is shown with the Frisbee antenna over decade bandwidth. The simple mechanical mounting feature of the radome over the antenna aperture promises for the use of different types of apertures such as a log-periodic or a spiral inside the same radome. There is also the choice and freedom to design these apertures with different properties such as variation in the substrate thickness and microstrip transformer in order to make the design higher power capable while maintaining the same overall design for the antenna without changing much of its electrical performance. The only design constraints enforced onto the designer in such a case would be to limit the physical size of all the apertures intended to be fit inside the Frisbee radome in accordance with the diameter of the Frisbee disk if finding a cost efficient larger sized radome is not favored. The typical applications for the Frisbee antenna include its use as a (visually) covert jamming. The Frisbee antenna can also be used as an excellent RF target for various ballistic platform testing. Because of its potential to be waterproof, the antenna holds good promise to be deployed on water surface or for use as a communication antenna in harsh marine environments.

The future improvements for this design would include the implementation of a magnetically mounted aperture onto the Frisbee radome. This design would use rare earth permanent magnets mounted with reverse polarities on the Frisbee radome so that the two Frisbees are held together by the attraction between the two set of magnets. This would essentially sandwich the aperture between the two-magnet mount Frisbee radome. The use of magnets on the periphery of the aperture in place of the mounting posts would not much change electrical performance of the antenna while it would offer the design a complete field reconfigurable nature as opposed to the mechanically integrated Frisbee antenna design.

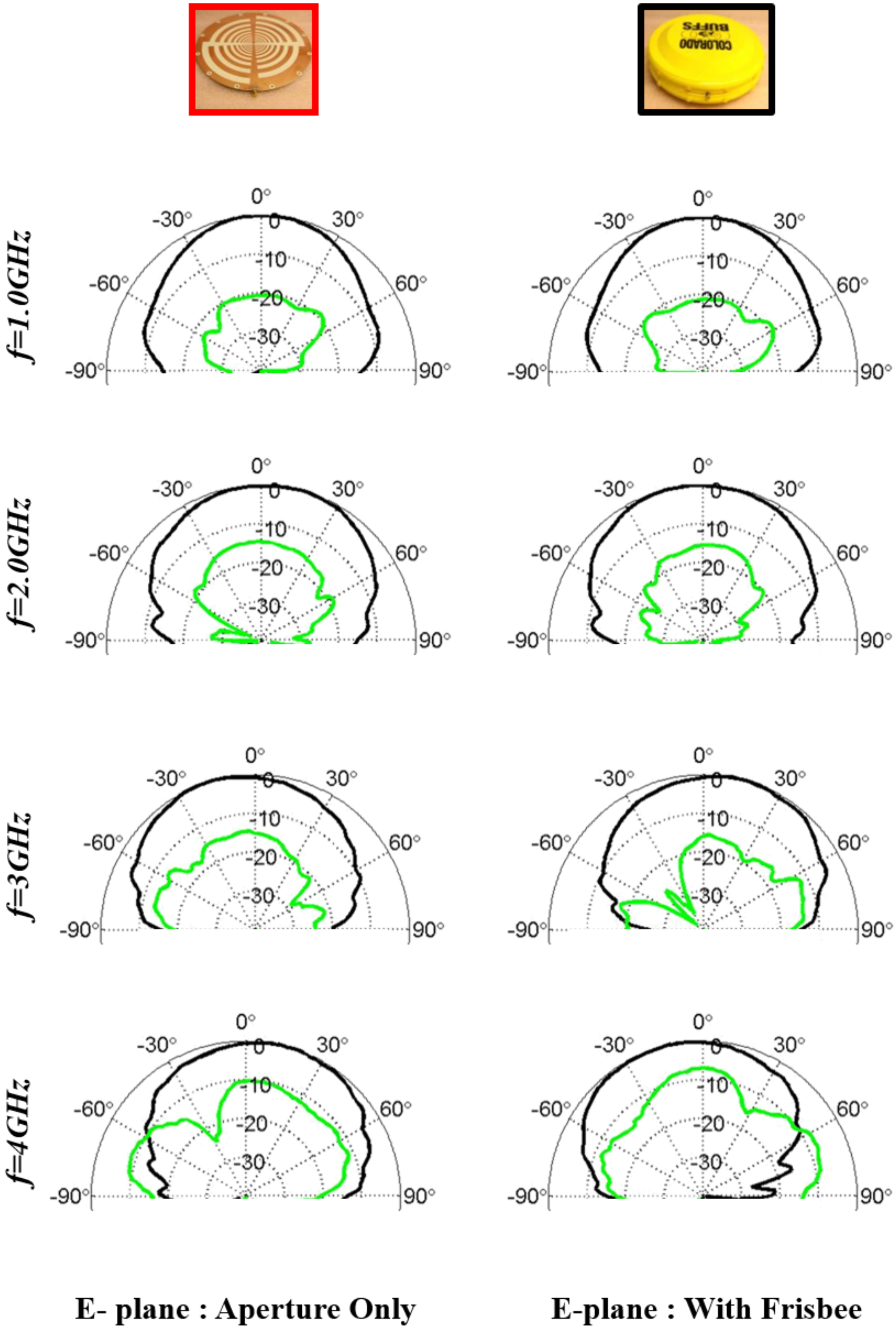

Figure A.11: Measured E-plane radiation patterns.

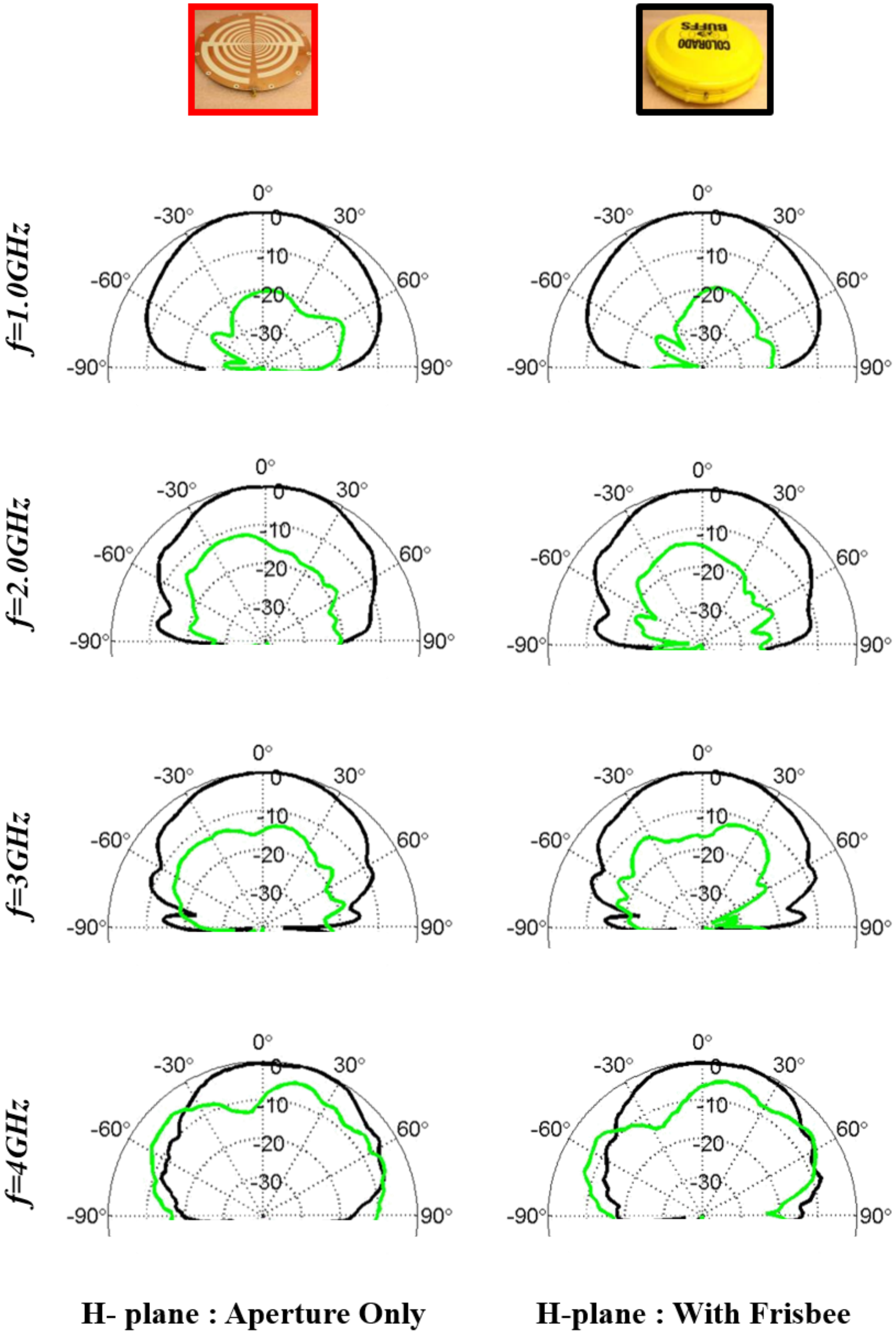

Figure A.12: Measured H-plane radiation patterns.

APPENDIX B

Failure Analysis of Compact Spiral-Helix Antenna Under High Input RF Power

B.1 Introduction to Spiral Antennas

The exponential spiral antenna introduced by E. M. Turner in 1958 [131], is the most widely used FI antenna due to its well understood operating principles and relative ease of construction [126]. This appendix performs failure analysis of a four-arm cavity backed spiral-helix antenna. A typical two arms spiral antenna may be absorber-backed to achieve very wide bandwidth. However, the power handling of this antenna is limited by the use of such absorber. This may be improved by considering a metal-backed spiral antenna design as an appealing candidate for high power applications. Addition of the helix helps to miniaturize antenna, and thus improve its performance at lower frequency end [132] [133] [134]. The helix makes use of the available real estate on the vertical profile of the antenna between the cavity and the spiral aperture improving the low frequency response of the antenna. The combination of the helix element at the end of the spiral arms with resistive termination (i.e. spiral-helix antenna [135]) allows for minimized reflections from the antenna arm ends while still contributing towards improvement of performance on the low end. Another challenge with this antenna design is the complexity of the beamformer. The complexity of the beamformer can be addressed by introducing a microstrip feed configuration with a simple integrated beamformer using a single 90° hybrid [136].

The spiral-helix antenna is thus built to meet requirements of good wideband performance, low cost, and high-power operation at a size that is smaller in diameter than a conventional spiral antenna. The design of the spiral helix antenna featured in this appendix was done by J. Bargeron and M. Elmansouri [135]. All the necessary design steps and precautions are followed during the antenna design process. However, the antenna suffers failure at the low-frequency during high power operation on account of a number of factors that could not have been foreseen or addressed in the design process through simulations or through traditional antenna testing processes without subjecting the antenna to high input power. In this section, a method of performing an autopsy that investigates the failure mechanism of the antenna is considered. By studying the antenna autopsy results, the specific parts of the antenna that led to the overall system failure are identified and the respective failure mechanisms are discussed. In the discussion that follows the autopsy, improvements to the antenna design are suggested to avoid a future failure under similar high power operating conditions. The overall focus of the antenna design shown in this appendix is to highlight the importance of practical details in the design process of an antenna, especially for the case when high power operation is concerned.

B.2 Motivation

Numerous RF systems performing many complex functions, employing multiple antennas are often found deployed on a single platform such as an aircraft [137]. A similar scenario can be observed for a ship, or a land vehicle that is required to support a large list of functions related to communications, navigation, radar-based detection and so on. Electronic warfare (EW) systems are typically employed to work in the UHF bands due to the threat from cellular and other wireless technologies working at those frequencies [138]. Based on the operational requirements, EW systems and antennas must offer the required adaptability and flexibility to cover a wide portion of the spectrum across the UHF band where imminent threats may appear. Use of FI antennas offers the incentive and possibility of replacing multiple antennas on such platforms with fewer, wideband antennas. In the commercial world, there is an ever increasing requirement for wider bandwidth systems for applications such as UWB based geolocation systems [139], UWB indoor positioning systems [140], UWB radar for autonomous vehicles [141], UWB radar based gesture recognition [142], and high fidelity wireless video relay links [143]. Naturally, the performance of FI antennas offers a path towards appropriate use in these applications. However, these antennas need special consideration for design, fabrication and deployment when used for specialized high power applications on various platforms. Prominent among these aspects is the ability of achieving sustained high power operational capability without affecting the electrical performance of the antenna. Higher power handling capability would translate to enhanced communication prospects such as reliability, longer range and spectrum dominance on top of the wideband performance offered by the FI antenna. Requirement to support high power operation further adds to the design challenges of an FI antenna. For purposes of practicality and versatility, the high power operation capability needs to be addressed as part of the design process. The high power performance of the antenna is impacted by its electrothermal design features meaning that the antennas often need to be tested under high power levels and the design further improvised to realize a truly high power capable, wideband, FI antenna. Increment in power handling capacity of FI antennas can make them appealing for a large number of versatile applications across communications, jamming, directed energy, spectrum sensing, and UWB applications. The research motivation for the compact high power capable spiral helix antenna under study in this appendix section B therefore comes from the performance deficiency of typical FI antennas in the power domain. The objective is to improve the ability of FI antennas to achieve similar or better performance in power domain while maintaining desired electrical performance over a wide bandwidth.

B.2.1 Power Handling

Unidirectional radiation can be obtained from a planar FI antenna by using a lossy absorber loaded cavity-backing which reduces the antenna efficiency and limits their continuous wave (CW) power handling capability to typically a few watts [144]. The most important limiting factor in an absorbing cavity backed FI aperture is the carbon-loaded foam absorber which absorbs the back radiation to prevent the radiated energy from reflecting from the cavity bottom and destructively interacting with the antenna radiation coming from the top side of the aperture. The use of carbon-loaded absorber filled cavities help maintain consistent antenna performance across wide range of frequencies at the cost of efficiency. Higher power handling absorbers are available and can be used in this concept to improve the power handling of the antenna. These higher power handling absorbers may be expensive, bulky, hard to integrate, heavy, and require careful heat-sinking strategy. It is important to note that the typical efficiency of a good absorber-backed FI antenna is less than 50% as half of the radiated power directed towards the cavity bottom is absorbed and lost in the carbon loaded foam absorbers. Such efficiencies are too low and make no practical sense for use in real world high-power applications. The evolution towards a practical, high power capable FI antenna would therefore mean that the antenna supports uni-directional properties and is able to avoid the use of carbon loaded absorbers.

End-fire log-periodic antennas can be considered for unidirectional radiation with high-power performance. However, end-fire log periodic antennas are long. Another common approach used to achieve uni-directional performance of FI antennas with efficiencies better than 50% is based on adopting a conical configuration. With a suitable design consisting of a proper selection of the cone parameters of the apex angle, and cone height combined with a suitable antenna growth rate, a consistent high-quality uni-directional beam may be obtained with these antennas. Since the loading absorber is not required in this design, these antennas are capable of handling higher CW powers. A known drawback of the conical design is the antenna height. For turn on frequencies in the UHF domain, the height of a conical spiral design might not be as small as desired for platform mounted or flush-mounted applications. Additionally, copper plating and fabrication of conical spiral antennas is not straightforward and while it may be done by different manufacturing processes, it is very expensive compared to the costs of standard PCB fabrication processes used to fabricate planar spiral apertures. The high-power handling capabilities of these antennas are also limited by the utilized balun/feed network, thin conductor traces throughout the structure (particularly in case of the tightly wrapped spirals), arm count selection, and very tight feed region. Since these antennas are typically intended for multi-octave bandwidths with the highest frequency of operation in the millimeter wave regime and nominal impedance > 100 Ω, the balun lines need to be narrow which limits their current carrying capacity (and thus power handling). Spiral antennas are often built with a tight wrap to enhance the quality of the radiated field while two arms are preferred to reduce the feed network complexity. Both these features limit their high-power handling capability. Noting these structural niceties of the typical FI antennas makes us realize that design of a high power capable FI antenna must be done with some compromise at the antenna level. The increase in its inherent power handling capabilities may come at a corresponding impact on its electrical performance.

B.3 Antenna Design

The spiral-helix antenna chosen as a candidate for the antenna autopsy was designed by J. Bargeron, inspired from the good measured performance of the larger spiral helix antenna [135]. The antenna aperture is a single-turn planar microstrip-fed four-arm spiral with outer radius $r_{out} = 94$ mm , and inner radius $r_{in} = 2$ mm. Spiral is fabricated on a 1.52 mm Rogers RO 3003 substrate ($\varepsilon_r = 3, \tan\delta = 0.0013$) chosen for its favorable thermal properties; specifically, low loss tangent, high thermal conductivity, and low thermal expansion coefficient which closely matches that of the copper in the substrate plane leading to better power handling [128]. The designed quadrifilar helix has two turns and height of 39.12mm with arm width of 2.46 mm. It is printed on 0.254mm Rogers RT 5880 substrate and wrapped around hollow Teflon cylinder (Figure B.1). The antenna is well matched with VSWR less than 2.6 from 0.5 to 3 GHz (6:1 bandwidth). The coupling between the antenna's ports is less than -20 dB. The antenna has positive realized gain from 0.9 GHz and higher. The maximum measured gain is 7 dBic, minimum measured gain is -3 dBic.

B.3.1 Antenna Fabrication

The antenna is fabricated on a small hexagonal ground plane, since multiple of these elements can be arranged next to each other in an array configuration that has a hexagonal grid. The helix top ends are soldered to the spiral arms (Figure B.1). In order to provide stable far field performance over the frequency range of operation, lumped resistive loading is applied to the bottom arm ends of the quadri-filar helix. Resistors of 75Ω, 100W rating (one resistor per arm) are utilized. Metallic inset of 15.75mm height is placed inside the Teflon cylinder to extend the high-frequency operation of the antenna. Ferrite beads are placed around the coaxial feeds and the dummy posts to choke any currents on the outer conductor [145]. The SMD 90° hybrid (rated up to 125W) is used to excite the antenna. For ease of

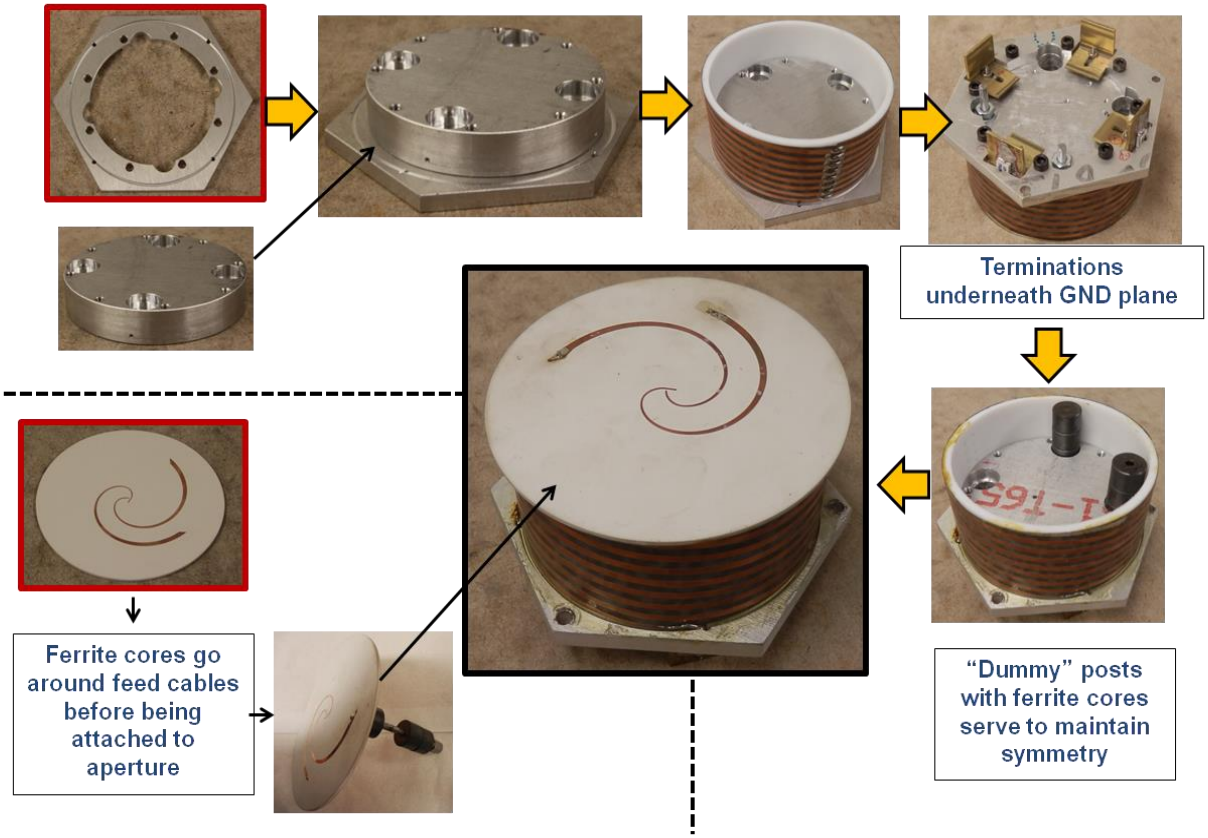

Figure B.1: Fabrication and assembly details of the spiral-helix antenna element. Shown in the top inset is the hexagonal augmented ground, the cavity bottom inset, Teflon cylinder used to mount the helix arms and the resistive terminations under the augmented ground. Ferrite beads are slid over the feed coaxial cable and the dummy coaxial cable before mounting the aperture onto the helix element.

integration, practicality and desired power/bandwidth the chosen 90° hybrid is surface mountable IPP-7066 which operates over 0.8 - 4.5 GHz range with reflection coefficient less than -20 dB, isolation is better than 20 dB, power loss is less than 0.75 dB, amplitude and phase imbalances are less than 1.5 dB and 5°, respectively [146]. It must be noted that the

TABLE B.1
Mechanical design parameters of the fabricated antenna.

Parameter	**Value**
Aperture Diameter	94 mm
Operating Frequency	0.5 – 3 GHz
Metal to slot ratio (MSR)	2.6:1 (72/28)
Minimum microstrip width	0.533 mm (21 mil [127 Ω])
Minimum slot width	0.533 mm (21 mil [at the center])
Aperture substrate	RO-3003
Substrate thickness	1.524 mm (60 mil)
Helix Height	39.12 mm (1.54”)
Helix arm width	2.46 mm (97 mil)
Termination	75Ω; 100W (4 resistors, one per arm)
Antenna weight	Less than 5 lb.

antenna element itself has a slightly wider coverage compared to the rated coverage of the chosen 90° hybrid. The mechanical details of the antenna are shown in Table B.1.

Figure B.2: Measurement setup for the high power test of the 94 mm diameter aperture planar spiral-helix antenna.

B.4 Antenna Autopsy

The term ‘autopsy’ is defined as a critical analysis of something performed after it has taken place or has been completed [147]. Based on this definition, the analysis of the antenna failure mechanism after its failure under high power operation is referred to in this work as ‘antenna autopsy’. The candidate antenna is subjected to high power operation. The antenna failure during the high power operation is studied based on the test data, available evidence and the antenna performance characteristics. The antenna is dismantled post the high power test and the internal components are inspected one by one to establish the series of events that may have led to the antenna failure. Different methods to improve the power handling capability of the candidate antenna are proposed thereafter.

B.4.1 High Power Test

The candidate spiral-helix antenna is put under high-power tests at Dayton T. Brown Engineering and test division, in Bohemia, New York [148]. The test setup is shown in Figure B.2 [149]. The setup consists of the test antenna connected to a directional coupler and fed by a high-power source. CCTV camera is used to record visuals during the test. Temperature on various antenna parts are captured through thermocouples. An E-field probe above the aperture is used to measure the radiated fields in real time. Throughout the test, the antenna’s performance is continuously monitored through the measurement of forward and reflected power at the antenna input, electric field strength at boresight, and thermocouple readings from non-radiating elements. The antenna is first tested at 3GHz where it readily handled 100W CW for 60min without any issues. Then the high-power test is performed at low frequencies specifically at 800MHz where the antenna fails to pass the test. Figure B.3 shows the temperature profile of the antenna during the 800 MHz test. The test is started at time t=0 with the input power set to 50W. The antenna is soaked at this power level for close to 20 minutes and gradual increase in the measured temperatures is seen (Figure B.3) at all locations due to thermal losses. No anomalous behavior is seen and at point 'A' in Figure B.4, the power level is increased to 100 W. However almost immediately fluctuations in both, probe E-field values, and reflection coefficient are noticed giving preliminary hints of antenna malfunction. From 'A' to 'B' the fluctuations continue and the input power is dialed down at 'B' to 10W as a precaution against complete destruction of the antenna.

With lower power now entering the antenna from 'B' to 'C' one can expect all the measured temperatures to drop as is observed in Figure B.3. From 'B' to 'C' the antenna's behavior is found to be stable once again and thus the power is increased back to 80W at 'C'. The temperatures show an expected rise from 'C'; however, once again fluctuations in the probe field values and reflection coefficient are noted. The power level is reduced again to 10W at the peak between 'C' and 'D' to protect the antenna. As before, at these low power levels,

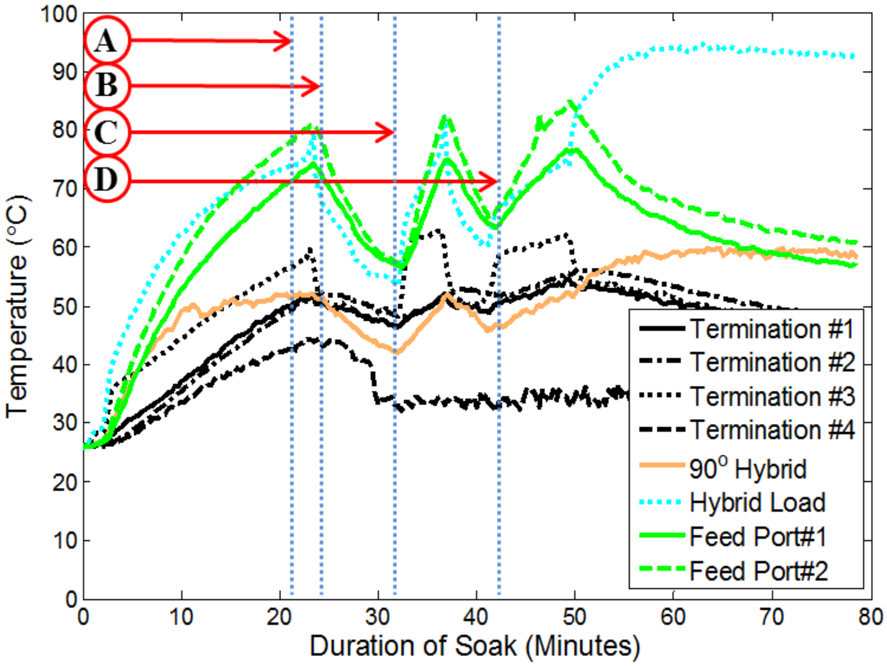

Figure B.3: Readings of the thermocouples at 800 MHz versus the soak period.

the antenna is stable. In order to find a higher power level where the behavior of the antenna is stable, the power is reverted back to 50W at ‘D’. However, at this point the reflection coefficient increases from previous value of -25 dB (around which large oscillations are observed) to a stable value of -6 dB and the probe field value drops to very low levels indicating an irreversible breakdown in the antenna. It is interesting to note the diverging nature of the temperature profiles in Figure B.3 from ‘D’ onwards. This suggests an asymmetric nature of breakdown in the antenna. The asymmetric antenna breakdown is supported by observations and findings about the internal parts of the antenna when these parts are investigated after the high power test.

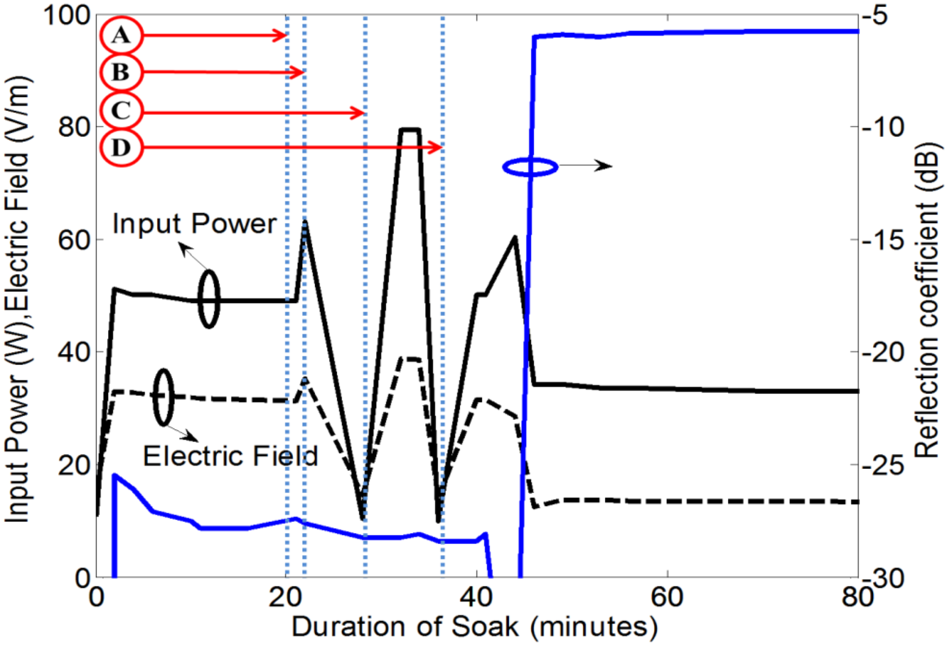

Figure B.4: Measured input power and electric field readings above the antenna at 800 MHz versus the soak period.

B.4.2 Antenna Autopsy Results

During the antenna autopsy, a physical inspection of the antenna and its parts is performed followed by correlation of the electrical and thermal data from the high-power test with the observations from the antenna parts. From the inspection of the candidate antenna after the test, the antenna is found to be mechanically intact from outside. There are no visible external burn marks or solder reflow or signs of structural damage on the antenna body (Figure B.5). Preview of the antenna after dismantling is shown in Figure B.6. The antenna assembly is initially performed with some adjustments to the original plan to account for machining imperfections in the antenna parts. The assembled antenna is then

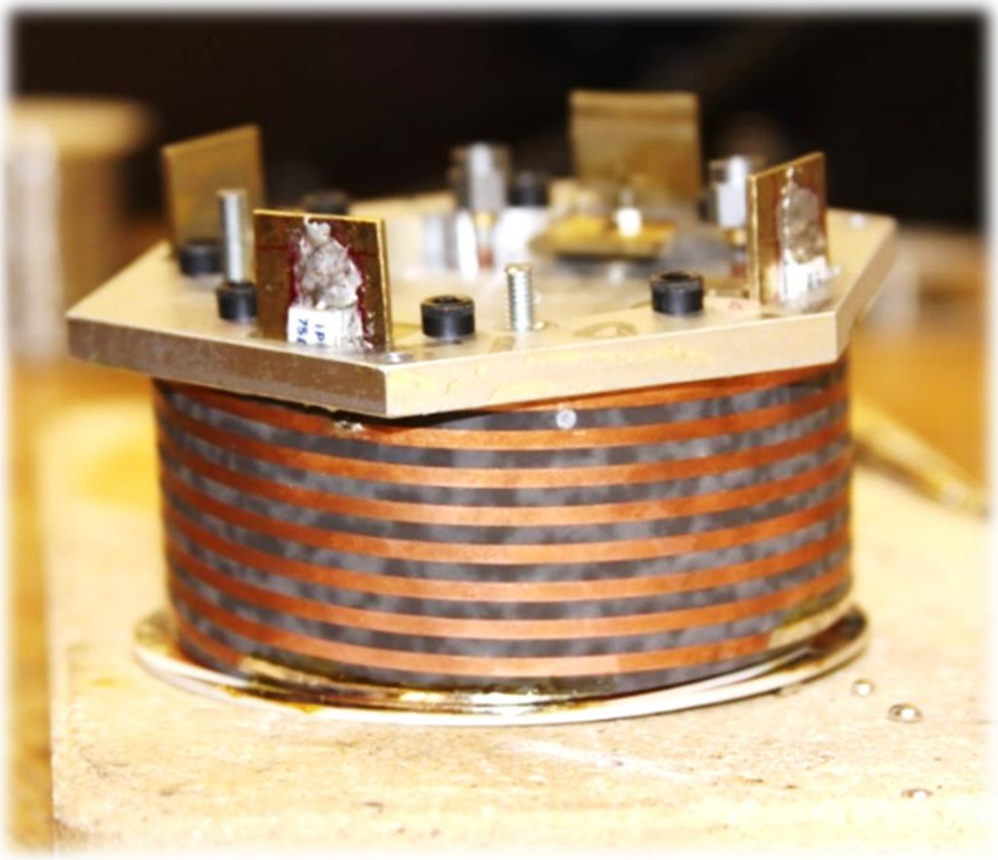

Figure B.5: Spiral-helix antenna after high-power test.

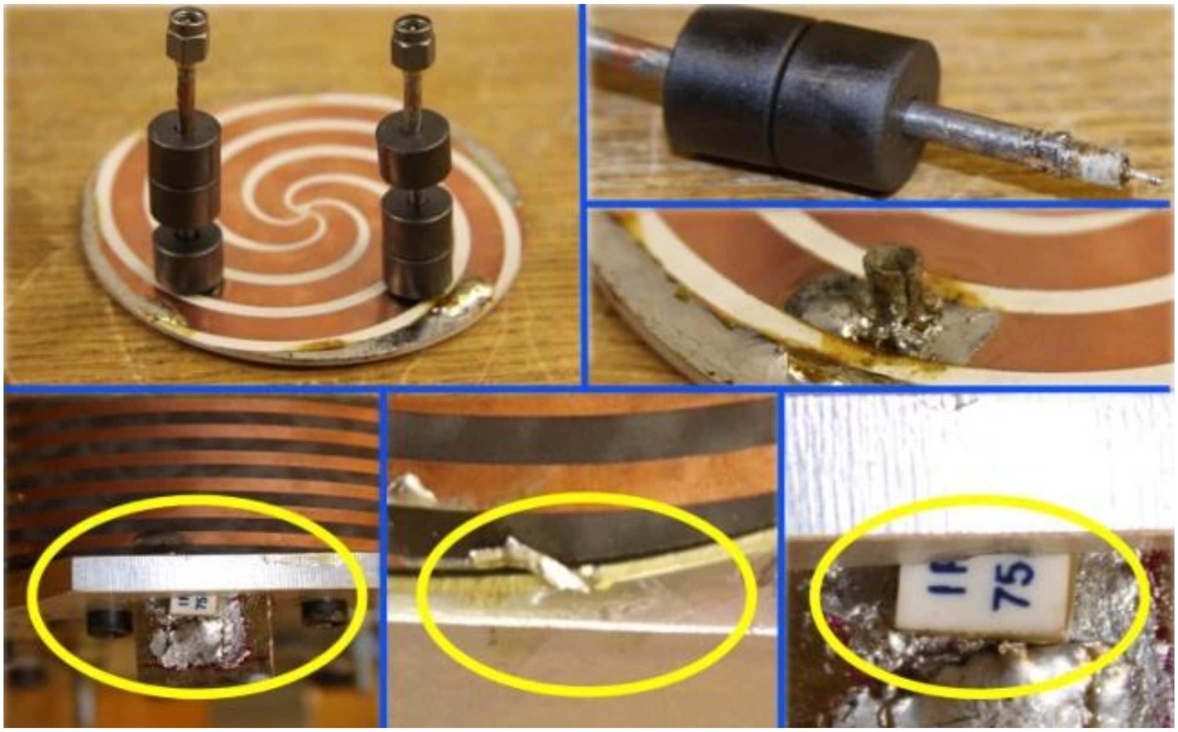

Figure B.6: Spiral helix antenna dismantled after the high-power test as part of the antenna autopsy investigation. Contribution from each part of the antenna led to the catastrophic failure of the antenna during the high- power tests.

subjected to high power tests. It is eventually found that the small adjustments in the antenna assembly result in poor power handling capacity.

The ferrite beads on the feed posts of the antenna and the copper on the antenna aperture near these ferrites are found to be discolored. There is clear discoloration of copper traces and carbon deposit on the underside of the spiral aperture due to sustained heat buildup near the ferrite post contact points. There is mild discoloration observed at points of high current density on the antenna aperture. This implies excess heat development at the ferrite posts and the aperture in a localized manner during the high-power tests (Figure B.7).

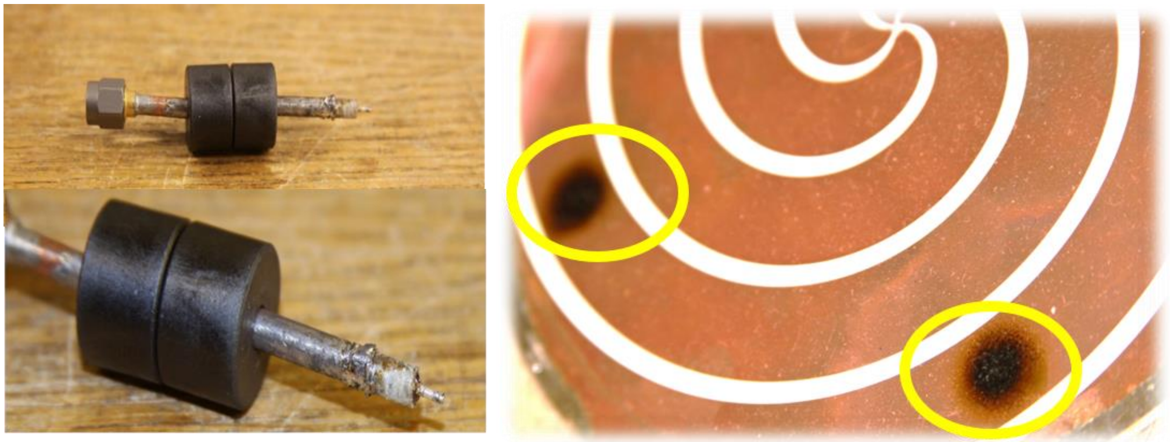

Figure B.7: Damaged feed ports with discolored ferrites and carbon deposit on the antenna aperture near the ferrite bead region. The localized carbon deposit on the antenna aperture near the ferrite beads suggests very high temperatures were developed in these areas during the test.

The joint between the feed port and the aperture is observed to have failed because of the localized heat developed from the ferrite beads. Also, the brass fixture used to solder the coaxial feed at the aperture is found to have traces of burnt dielectric from the feed cable along with solder flux residue and some signs of solder reflow. The excessive heat on the outside of the coaxial feed port may have caused the dielectric inside it to expand and exert pressure on the joint between the coaxial feed and the aperture thereby completely disconnecting one of the feed ports from the antenna aperture. At the time of the investigation, no DC electrical connection is found between the shield of the feed port coax cable and the antenna ground due to the damaged solder joint at that port (Figure B.8). This port where the local heating artifacts described above are observed is the same feed port that yielded erroneous results during the high-power tests.

A close inspection of the antenna terminations reveals that the resistors placed on the spiral-helix are soldered onto brass heat sinks on the underbelly of the ground plane with

Figure B.8: Localized heating of the ferrite beads around the coaxial feed cable caused the feed cable dielectric to expand. The pressure from the increased volume of the expanding dielectric inside the coaxial cable and solder reflow at the joint between the coaxial cable and the aperture caused an electrical disconnect of the feed cable consequently resulting in a total asymmetric antenna failure.

bent leads and skewed orientation to compensate for the aforementioned machining errors and misalignment of the antenna fixtures (Figure B.9). This is seen as another factor that may have affected the antennas capacity to dissipate power in the resistors efficiently. Due to the possibly poor terminations, most of the residual power would have been reflected back into the system instead of being terminated. The reflected power would then make its way eventually in to the antenna bulk in the form of heat. One of the resistors is also found to be broken at the lead contact. Furthermore, these resistors are found to have been cold soldered onto the heat sink (Figure B.10). The cold soldering may have happened during the assembly process when a large area of brass metal would have to be heated using a small soldering iron for the integration of these resistors.

These observations about the design and integration deficiencies and their contribution to the thermo-electric runoff based failure of the antenna corroborate well with

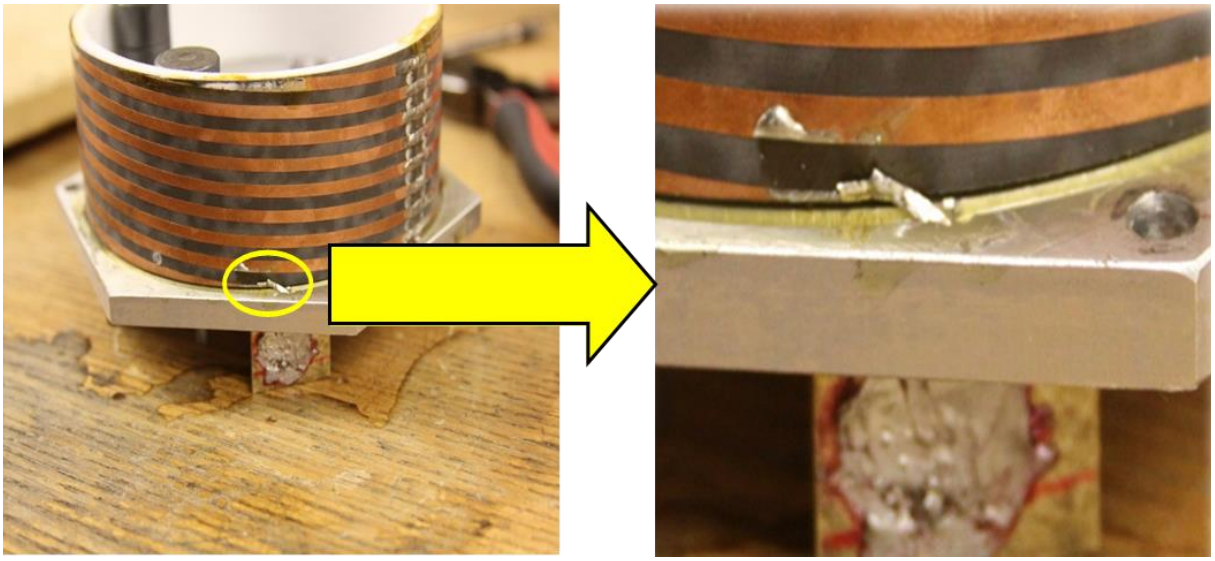

Figure B.9: A close-up view of one of the resistor used as termination on the spiral helix antenna showing bent connecting leads used to compensate for fabrication errors and misalignment of parts.

the hypothesized asymmetric failure mechanism of the antenna and the corresponding high reflection coefficient observed during breakdown. Based on the autopsy, the thermal hotspots are attributed to ferrites and possibly to the poor heat dissipation at the resistive terminations. The thermal expansion of the dielectric in the coax at the feed point can be tied to the artifacts of thermal hot spots being observed near the coaxial breakdown point at the aperture. The heat developed at the breakdown point may have aided the solder joint to weaken and excessive pressure on the feed – aperture joint from the expanding dielectric core would have resulted in an electrical disconnect.

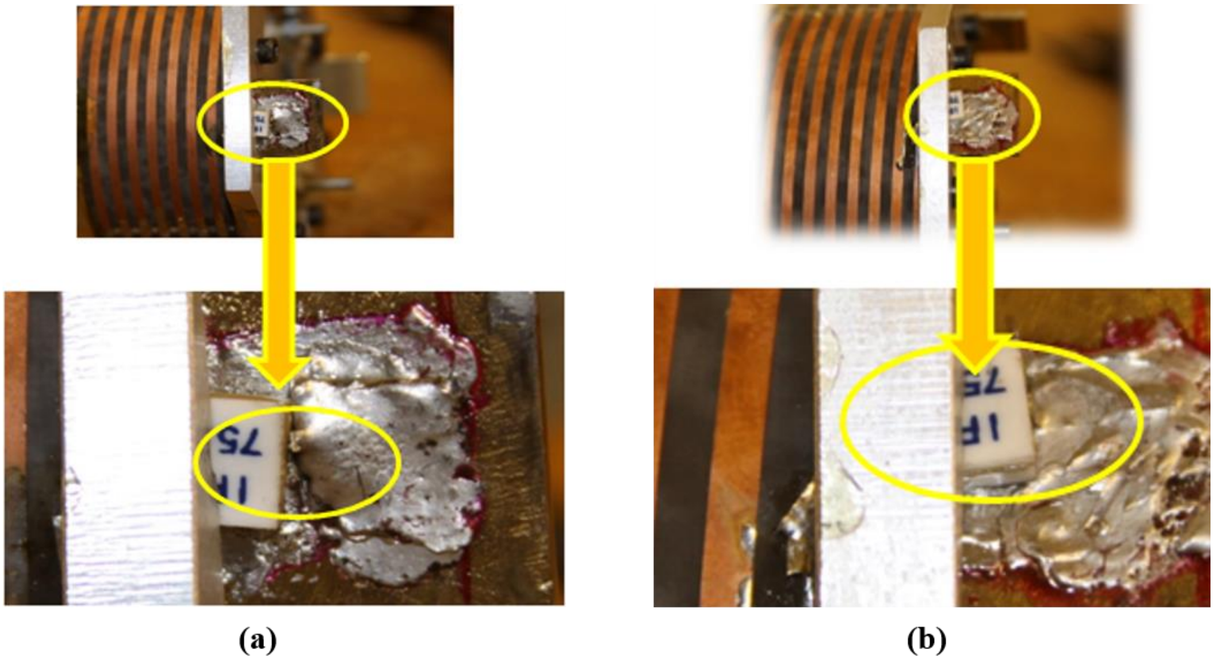

(a) (b)

Figure B.10: Cold soldered resistive terminations on the underbelly of the spiral helix antenna. (a) and (b), Two of the four resistive terminations are shown here for reference. (a) The discussed broken resistive termination can also be seen in this picture on the left image (a).

B.4.3 Design Improvements

To address the antenna deficiencies and issues discovered through the autopsy, the brass heat sinks are replaced by copper heat sinks which have three times higher thermal conductivity. The antenna feed posts are connected to the aperture by means of COTS bulk SMA through hole connectors instead of connecting by means of soldered brass mounting posts to ease antenna assembly process, and thus reduce chances for assembly errors. Soldering of terminations on the heat sinks is proposed to be done at a higher temperature to avoid cold soldered joints. The cables that are used to make the feeding posts are preheated before installation. Preheating the coaxial cables to 400º C before the installation causes the thermal curing of the dielectric core. Excess dielectric coming out of the cable due to thermal expansion is removed as part of the preheating treatment. Two out of the three ferrite beads mounted on each feed post are sunk into the metallic ground plane to provide for additional heat sinking through the metal mass of the antenna cavity bottom. Soldering at the thermal hotspots on the antenna is done using a solder alloy with higher melting temperature as per the improvised integration plan. The small incremental changes in the fabrication and integration techniques adopted to make the antenna are targeted at the identified weak spots in the antenna design. These small but important design changes are aimed at significantly improving the overall build quality and mechanical and electrical robustness of the antenna.

B.5 Summary and Discussion

The antenna autopsy process is introduced in this section. The antenna failure under high power is studied and series of events that led to its failure are investigated. The thermal data obtained from the high-power tests supports the deterioration in the antenna performance during the high-power tests. The design features that led to the antenna failure are improved to mitigate the prevailing flaws. The primary reason for antenna failure is attributed to its inherent mechanical integration and thermal design flaws. The antenna is overhauled with some critical design changes post the high power test on the basis of the findings given below from the autopsy performed on the candidate antenna. For the future exploration of proposed antenna autopsy research and its potential applications, enhancement in the thermal/high power performance of FI, resistively-loaded antennas is suggested by addition of low cost, and lightweight active cooling systems that can be easily integrated with the antenna. An illustration is shown for this concept in Figure B.11. This suggested solution is based on using small fans as sidewalls for the 7 – element spiral antenna array is built with the integration principles elaborated in the above discussion section. In the actively cooled design, one set of fans would pump the air in to the air gap between the antenna aperture and the backplane and the other set of fans on the opposite wall would move the air hot column out of the antenna structure. A small DC rechargeable battery or an integrated power supply can be used to run these fans when the antenna unit is under operation. Alternatively, thermal sensors can be used to automatically regulate the fan when the temperature reaches certain level. Passive cooling approach by adding heat sinks to the resistive terminations to dissipate the generated heat at the source can also be considered. Testing the high-power capability of such antennas with ferrite-loading and active cooling is also important aspect of the future work.

Figure B.11: Resistively-loaded, FI array made from spiral antenna elements with active cooling fans mounted on the antenna sidewalls.

APPENDIX C

Techniques for Preliminary Component Inspection from an RF Leakage Perspective

C.1 Introduction

The approach to investigate internal RF leakages has been demonstrated in Chapter 4 of this thesis. The results of the internal RF leakage measurements point to a possibility of significant impact of the RF leakage on the system level isolation depending on fabrication approach. The component seams and joints as well as flanges used to connect multiple components together are hypothesized to be one of the root causes of RF leakage. For practical purposes, it is desired that potential causes of RF leakages from components and RF systems are identified. One of the first steps towards this would be the ability to inspect the RF components from an RF leakage perspective. Contrast photography method and pneumatic testing approach is shown as a path towards such preliminary component investigation.

C.2 Component Inspection Against Bright Light

Contrast photography principles are used as a tool to identify miniature openings in the component seams. This method proposes to investigate the potential leakages by the use of a high power light source placed against the part under study. A double ridged waveguide transmission line section is used to demonstrate the adopted approach. By testing the seams of the component against the light from different exposure angles, the potential defects, misalignments and air gaps can be identified. Possible reasons for the manifestation of these potential RF leakage spots can be attributed to fabrication burrs, tooling finishes and minor

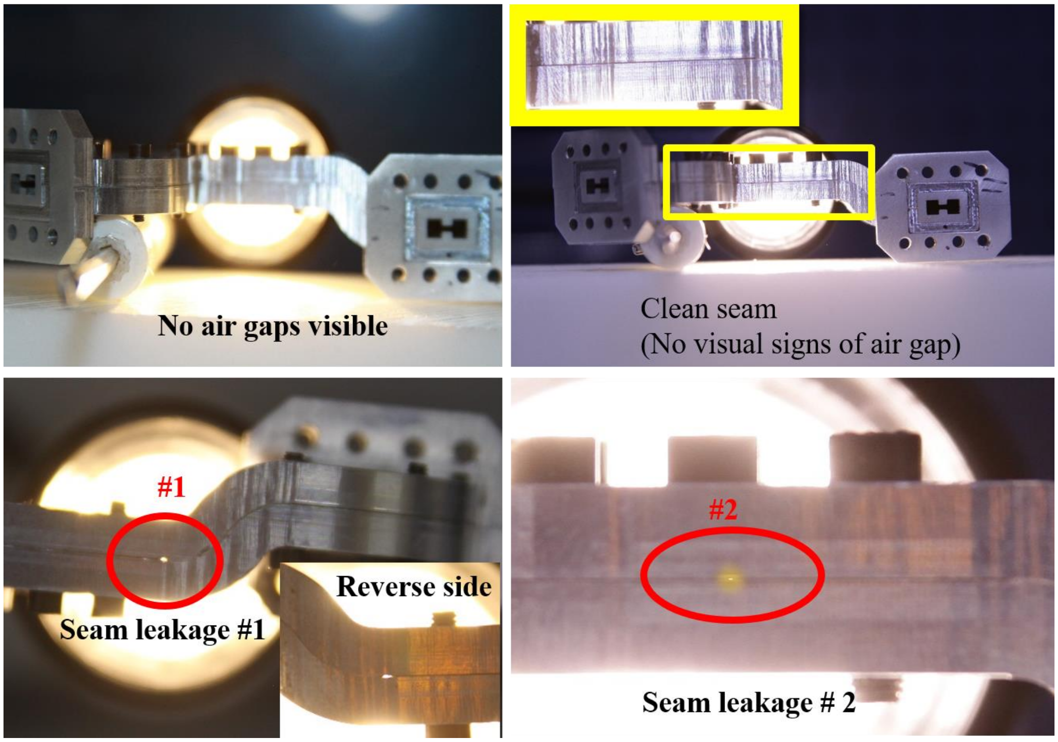

Figure C.1: Example of component inspection of a short section of waveguide transmission line for compromised seams and fabrication errors against a high intensity light source. Shown in the picture are good and bad seams are identified by the use of this test.

blemishes formed on the finished part. The areas where the seams are compromised, and air gaps or defects are present light up against the darker background as seen in Figure C.1. These areas could potentially be sources of RF leakage when integrated inside payloads.

C.3 Component Inspection Using Pneumatic Method

The same transmission line used in the contrast photography inspection technique is also inspected using a pneumatic method. The line is submerged in water, and pressure between 0.5 and 1 psi is applied against the component on one end, whereas it is plugged with a sealing adapter plate on the other side. Once the pressure is turned on, bubbles of air

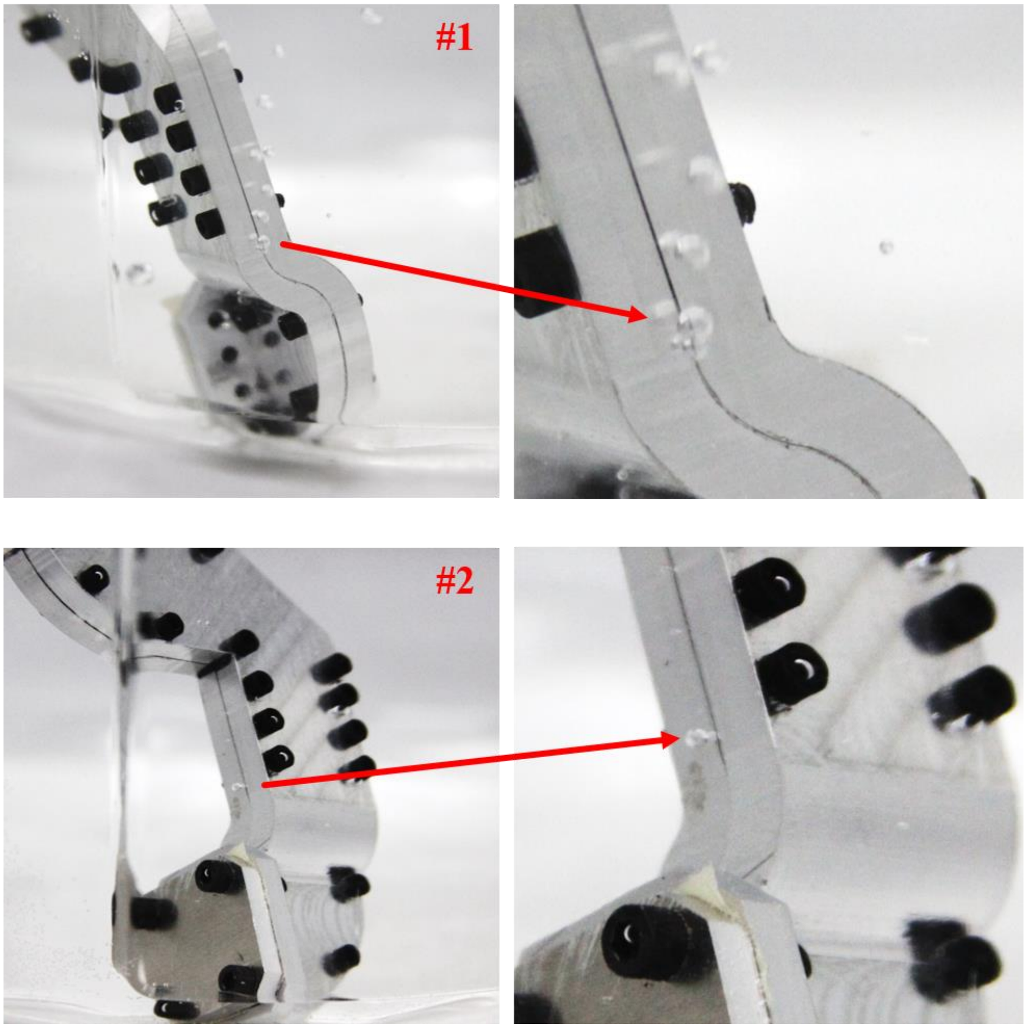

Figure C.2: Potentially leaking seams are identified in a waveguide transmission line using the pneumatic method.

are seen to leak out of the component in places where the seam is compromised or where there are misalignment errors creating a miniature air gap (Figure C.2). Care must be exercised while performing this inspection, since the entire component may start leaking air above a particular pressure threshold and masking the potential source of RF leakage. In this case, identifying the actual location of potential RF leakage due to air gaps in the seam can become difficult. Experimental results show that this method can identify miniature or hairline cracks and fine air gaps suggesting that the detecting resolution is higher compared to the contrast photography method.

C.4 Summary and Discussion

Path towards component analysis and preliminary inspection for RF leakage is shown through the contrast photography and pneumatic methods. Another possible method for identifying potential RF leakage spot is through the use of liquid penetrant dyes. These dyes are extremely low viscosity and are used to identify cracks, hairline ruptures, welding defects and seizures in plumbing, oil and gas and many other industrial applications [150]. The use of the liquid penetrant can be analogously applied in the use case of antennas to identify similar hairline cracks and ruptures in the component seams that may be a cause for RF leakage. The discussed component inspection techniques should be put through additional trials and tests for applicability towards quantitative as well as qualitative analysis of RF leakage from components. Such a detailed analysis would be appropriately suited for study as part of future work.